Toward the Detection and Characterization of Sub-Neptune Exoplanets Orbiting Nearby M Dwarfs

by

W. C. Waalkes

B.S., University of Michigan, 2016

M.S., University of Colorado Boulder, 2020

A thesis submitted to the
Faculty of the Graduate School of the
University of Colorado in partial fulfillment
of the requirements for the degree of
Doctor of Philosophy
Department of Astrophysical and Planetary Sciences
2023

Committee Members:
Zachory Berta-Thompson, Chair
Meredith MacGregor
Benjamin Brown
Kevin Reardon
Adam Kowalski

Waalkes, W. C. (Ph.D., Astrophysical and Planetary Sciences)

Toward the Detection and Characterization of Sub-Neptune Exoplanets Orbiting Nearby M Dwarfs

Thesis directed by Prof. Zachory Berta-Thompson

The last 20 years have seen a boom in the number of known exoplanetary systems, and many of the temperate sub-Neptune planets we study orbit low mass M stars. M dwarf stars can host temperate worlds with periods short enough for rapid followup and precise characterization but these stars are also extremely active, subjecting their planets to harsh XUV radiation and frequent flares that can sterilize and evaporate planetary atmospheres. Follow-up studies of potentially rocky planets in these systems have so far provided only tenuous evidence for their atmospheres and in some cases what are likely false positive detections caused by stellar active regions like starspots. Starspots are ubiquitous on M dwarf photospheres and introduce molecular features in the disk-average stellar spectrum which, if uncorrected, can be mistaken for absorption of molecules like H2O and TiO in the planet's atmosphere. With the successful launch of JWST and the promise of studying exoplanet atmospheres in greater detail than ever before, it is vital that we mitigate the problem of starspot contamination in exoplanet transmission spectra. How does stellar activity affect the atmospheres of short-period planets? Do temperate and warm sub-Neptune planets orbiting M dwarfs retain their atmospheres? To what extent do stellar active regions like starspots contaminate our observations and obscure the evidence of atmospheric absorption? How can we accurately measure spot characteristics and mitigate their effects on exoplanet observations? These questions have motivated the research I present in this thesis, where I describe how I used space- and ground-based observations to validate new exoplanets found by TESS, search for atmospheric escape from a nearby terrestrial world, and characterize starspots on the young exoplanet host AU Microscopii.

Dedication

To my parents Marie and Dave and my sisters Katie and Sara for instilling me with intellectual curiosity, a strong sense of justice, and respect for the importance of books.

Acknowledgements

It takes a village to raise a PhD and I have many people to thank for their help and support and encouragement throughout the years. First I thank my advisor Zach Berta-Thompson for his encouragement that if I kept my focus on the joy of doing science, the rest would follow. I thank my partner Chisom Nwizu for her love and support as we shared in the thrills and disappointments of the last year, her family for ensuring I never lacked for a home, fried plantain, or glass of wine, my friend Hannalore Gerling-Dunsmore for reminding me why I started down this path in the first place and that I was gonna make it through this year, if it killed me. I thank Dennis Tilipman for being by my side each step of the way from the sour start to the oak-y finish of grad school, and Girish Duvvuri for his good humour and occasional help with LaTeX at the 11th hour. I thank my friends Luke Peterson, Whitney Powers, Jay Chittidi, and Carl Pérez for being part of a community that made the pandemic bearable and Tia Mohacsi for gifting me a book about planets 23 years ago that apparently left a big impact. I thank my friends Karl and Ryan Campbell, who proved the importance of joy in the middle of struggle, my undergraduate research advisors Daniel Bergman, OJ Tucker, Viviana Guzmán, Karin Öberg, and Ted Bergin for putting me on the trajectory to be a scientist. I thank Tom Rice, Bryan Terrazas, Jessica Libby-Roberts, Andrew Sturner, and Ward Howard for their support and mentorship, Eric Swack for helping me navigate some precarious times in the last 6 years and reminding me the importance of being deliberate, and my peers who made the undergraduate journey through physics and astrophysics at U of M every bit as weird and fun and exciting and unpredictable as becoming a young scientist should be. Lastly I thank my dog Samwise for reminding me to go outside several times each day and touch some grass.

Contents

Chapter

4 Quantifying the Transit Light Source Effect: Measurements of Spot Temperature and Coverage on the Photosphere of AU Microscopii with High-Resolution Spectroscopy and Multi-Color Photometry **78**

Tables

Table

Figures

Figure

Chapter 1

Introduction

“Every star may be a sun to someone” - Carl Sagan, *Cosmos*

Planets in our solar system and others have long captured the curiosity and imagination of humanity, forcing us to reckon with the knowledge that ours may not be the only home for life. Planets are *places* we can imagine visiting one day, and that sparks our fundamental human need to explore and discover and understand that which no one ever has. Only in the last few hundred years have we begun to study planets in the solar system, and only 3 decades ago were planets around other stars first confirmed.

My study of planets has inspired the following questions in me:

- What are the surfaces and atmospheres of other planets like?
- Are there terrestrial exoplanets like Earth which have atmospheres amenable to life?
- What could life, and observational evidence of it, look like on other planets?
- What types of stars are most likely to host habitable exoplanets?
- How does the complex physics of low-mass stars affect planetary formation, evolution, and habitability?
- How far can we develop our understanding of exoplanetary systems with current technological limitations?

Not all of these questions will be answered within my lifetime, but the exoplanet community has made great strides in characterizing exoplanets and is closing in on the ability to detect atmospheric biosignatures in the atmospheres of Earth-like planets.

The discovery of life or evidence of biological processes on another planet has scientific and philosophical implications for humanity that we can hardly predict, and must be treated with careful and deliberate scientific inquiry. Like all important discoveries, we have to first build our way to them and lay the important theoretical and observational groundwork which will support the eventual unambiguous detections of complex atmospheric chemistry in the atmospheres of habitable worlds. To develop our ability to one day answer those questions, I have addressed some tractable problems using a combination of space- and ground-based observations to characterize M dwarfs and their transiting planets.

Transiting exoplanets (Section 1.1) are those which we can detect when they pass in front of the face of the star. From these *transit light curves* (Section 1.2) we can learn a lot about planetary characteristics such as the relative size of the planet compared to its star and the period of the planet. M dwarf stars (Section 1.3) can host temperate worlds with periods short enough for rapid followup and precise characterization (covered in Section 1.4, making these systems particularly useful for atmospheric studies of small exoplanets. However, these small cool stars are also highly active and the characteristics of their activity (1.5) are extremely relevant to the formation, evolution, and habitability of their close-in temperate sub-Neptune worlds. Improving our ability to account for stellar activity in our observations (Section 1.6) and our understanding of exoplanets requires a firm connection between the theoretical background stellar surface and how we interpret stellar observations within that theory (Section 1.7).

The rest of this thesis is laid out as follows: In Chapter 2 I report the discovery of two exoplanets, TOI 122b and TOI 237b, two warm sub-Neptune exoplanets orbiting inactive stars straddling the fully-convective limit. These planets do not have measured masses, but could be viable targets for mass measurements and atmospheric study with sufficient time commitment on current or future instruments.

In Chapter 3 I search for a Lyman-α absorption signature in and around the transit of nearby terrestrial exoplanet GJ 1132b with Hubble Space Telescope Wide Field Camera 3 (HST/STIS) UV data which, if detected, would have indicated an extended cloud of neutral H outflowing from the planet. This is a terrestrial world orbiting a fully-convective nearby M dwarf, making it a keystone system in our study of exoplanet atmospheres. Unfortunately there is still no conclusive evidence showing an atmosphere on this planet, perhaps a bad omen for the long-term retention of atmospheres on M dwarf planets.

Before we can conclusively determine the presence or characteristics of planetary atmospheres, we need to solve the outstanding questions of how stellar heterogeneities bias our transit measurements. Starspots introduce anomalous features in the stellar spectrum which contaminate our measured stellar and planetary parameters in ways that are unique to stellar spectral type and activity level, so a robust understanding of stellar photospheres and activity is necessary for studying planetary atmospheres. In Chapter 4 I report measurements of spot temperature and filling factor for the nearby pre-main sequence star AU Mic. This active flare star has multiple transiting planets with primordial atmospheres we should be able to detect in transmission, but stellar contamination will be affecting the observed transit signals of AU Mic b and c at all wavelengths in ways that depend on the spot coverage fraction at the time of transit, the coverage fraction on the transit chord at the time of transit, and the spot and ambient photosphere spectra (assumed to be time-independent outside of stellar-evolutionary changes in the stellar flux over long timescales). This is part of an effort to disambiguate the atmospheric signal from stellar contamination in the HST/WFC3 transmission spectrum of AU Mic b, which is a current work in progress, discussed in Chapter 5.

1.1 A Brief Overview of Transiting Exoplanets

Exoplanetary systems are randomly aligned to our line of sight, and when a planet's orbit is aligned such that we observe it cross the face of the star, we can measure the amount of light blocked by the planet. The probability of a given star-planet system to transit given by $\frac{R_*}{a}$, the

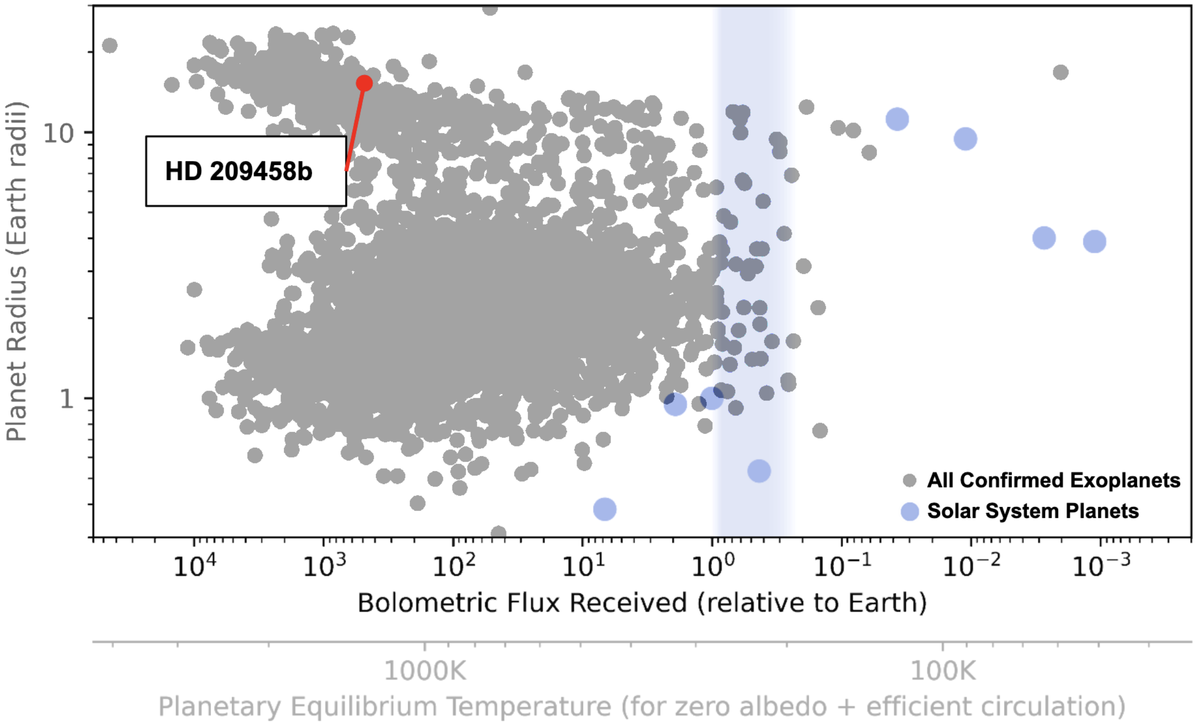

Figure 1.1: Radius-Insolation plot for all confirmed exoplanets downloaded from the NASA Exoplanet Archive on 19 Oct. 2023 (gray), the solar system planets (blue), and HD 209458b, the first transiting exoplanet discovered. The vertical blue bar represents the circumstellar habitable zone.

ratio of the radius of a star to the semi-major axis of its planet. Transit light curves contain other clues about the star-planet system such as orbital elements like period and eccentricity, the existence of other planets in the system, the presence and composition of a planetary atmosphere, and the structure and brightness of the stellar surface.

Transits are the most prolific method for planetary discovery, having surpassed other detection methods with the launch of Kepler (Borucki et al., 2003), the Transiting Exoplanet Survey Satellite (TESS Ricker et al., 2015), and a number of ground-based transit surveys. As of September 2023, there are 3718 confirmed exoplanets on the NASA Exoplanet Archive (2778 from Kepler, 548 from K2, 392 from TESS), with nearly 2000 additional unconfirmed planet candidates. Of the 5523 total confirmed and unconfirmed candidates, 4122 are transit method detections, with the next most prolific method being radial velocities (RV; the measurement small Doppler shifts in a stellar spectrum due to an orbiting object), with 1065 detections. Transiting planets with masses well constrained by RV measurements become viable candidates for atmospheric observations. As transit surveys have now returned many of what will forever be the best targets for atmospheric characterization around nearby stars, there is a shift in focus from detection to characterization, and a drive to extract as much information from our transit light curves as possible.

The first transiting planet discovered was HD 209458b (Charbonneau et al., 2000), a hot gas giant orbiting a G0-type star in a close 3.5 day orbit (see Figure 1.1). This gas giant was the first transiting planet to have an RV mass measurement (Mazeh et al., 2000) and subsequently the first exoplanet whose atmospheric absorption was measured (Charbonneau et al., 2002). While HD 209458 is not a particularly active star, HD 209458b is heavily irradiated on its short orbit and has been extensively studied to measure outflowing atmospheric species, being the first system where Lyman-α observations were used to study atmospheric outflow (e.g., Vidal-Madjar et al., 2003; Linsky et al., 2010). Since its discovery, this heavily studied systems represents a controversial benchmark in atmospheric studies of transiting gas giants. The detection of sodium in this planet's atmosphere (Charbonneau et al., 2002; Vidal-Madjar et al., 2011) has been contested in a more recent study by Morello et al. (2022) which took a careful approach to combining data sets and found no evidence for sodium. Similarly, the detection of molecules in the atmosphere of HD 209548b like H_2O and CO_2 are detected in transmission (Sánchez-López et al., 2019; Snellen et al., 2010) but not emission (Evans et al., 2015; Schwarz et al., 2015); an unresolved mystery which may be due to atmospheric evolution, stellar spectral features, weak emission features due to a shallow temperature-pressure profile, or the sensitivity of our results to different techniques, assumptions, model libraries, and reduction pipelines (e.g., Deming & Sheppard, 2017; Iyer & Line, 2020).

1.2 What Do We Learn from Transits?

When a planet transits its star, the first pieces of information we get are the planet-star radius ratio, the stellar limb-darkening profile, and if more than one transit is observed, the orbital period. Transits, first characterized analytically by Mandel & Agol (2002), also inform us on the eccentricity of an exoplanet (Price et al., 2015) or the stellar density (ρ_*, Seager & Mallén-Ornelas, 2003a; Winn et al., 2010) (without RV measurements, stellar density and orbital eccentricity are degenerate), and the possible existence of other planets in the system through transit timing variations (e.g., Ballard et al., 2011). Being able to measure stellar density (ρ_*) from the transit light curve provides us with a powerful check on stellar mass and radius. For sub-Neptune planets where $M_p << M_*$, the density is calculated as follows:

$$\rho_* = \frac{3\pi}{GP^2}\left(\frac{a}{R_*}\right)^3, \tag{1.1}$$

where G is the gravitational constant, P is the planet's orbital period, and $\frac{a}{R_*}$ is planet's semi-major axis in units of stellar radii (for reference, this value is about 200 for the Earth-Sun system, and between 10-100 for most warm or habitable-zone sub-Neptune planets in M dwarf systems. The scaled semi-major axis is measured from the transit duration as:

$$\frac{a}{R_*} = \frac{P_{orb}}{\pi T_D}, \tag{1.2}$$

where P_{orb} is the planet's orbital period (measured from successive transits and/or RV measurements) and T_D is the transit duration, shown in Figure 1.2.

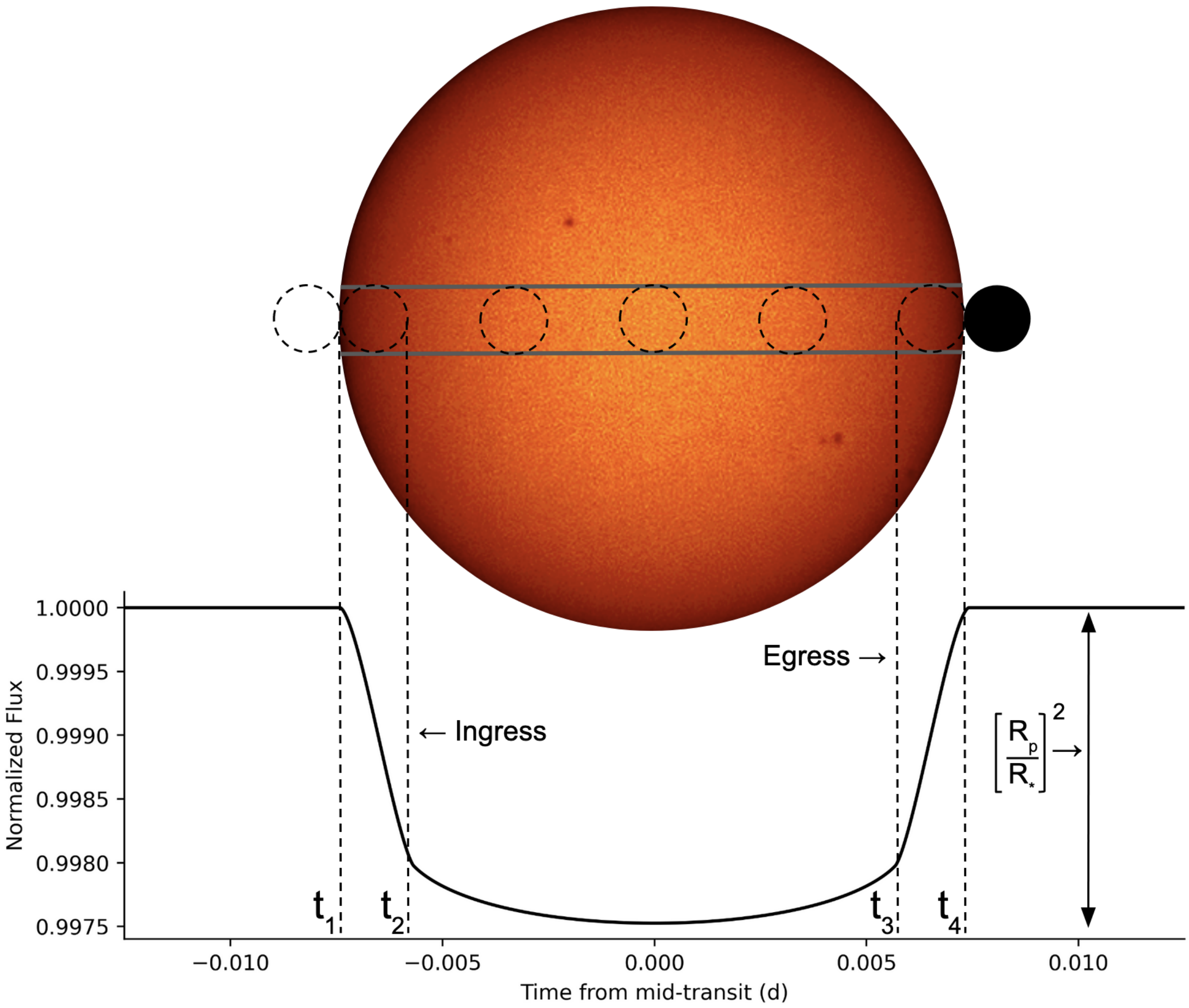

Figure 1.2: Diagram of a transit light curve showing the ingress (from first contact, t1, to second contact, t2) and egress (third contact, t3, to fourth contact, t4). The duration of transit is t4-t1, and the mid-transit depth is the ratio of the light blocked by the planet to the total light of the star. Transit model created with `batman` (Kreidberg, 2015).

For a circular orbit, the transit duration depends upon the speed with which the planet is traveling in its orbit and the distance it travels across the stellar face. This distance is 2 × R_* if the planet transits perfectly across the full face of the disk, but in reality most systems have some observed inclination slightly less than 90 degrees (which would be fully edge-on) that reduces the transit duration. To include that in our transit models, we define the *impact parameter*, b, calculated as:

$$b = \frac{a}{R_*} \cos i, \tag{1.3}$$

where i is the exoplanet's observed inclination. We can write a more accurate expression for the transit duration (or re-arrange it to solve for a/R_*) with this impact parameter:

$$T_D = \frac{P_{orb}}{\pi} \frac{\sqrt{(R_* + R_p)^2 - (bR_*)^2}}{a}, \tag{1.4}$$

with the addition of R_p to account for cases where the transiting object is so large that the ingress and egress of the transit are a significant fraction of the duration of transit.

Observing transits in multiple narrow wavebands is called transmission spectroscopy, and allows us to measure diatomic and molecular species in a transiting planet's atmosphere (Seager & Sasselov, 2000a). The transit depth and apparent radius of the planet will increase as species in the terminator of a planet's atmosphere absorb stellar flux. Longer wavelengths probe molecular features in planetary atmospheres while atomic absorption from species like H occurs at shorter wavelengths and can reveal escaping atmospheres that help us understand the radiative environment of the system. Toward optical wavelengths, Rayleigh scattering in exoplanet atmospheres can create a rise in observed transit depth (e.g., Robinson et al., 2014) and be a further indicator of the presence of a planetary atmosphere for the same reason a blue sky is evidence of the Earth's atmosphere. An additional (sort of) observable piece of evidence of exoplanet atmospheres is the the presence of clouds (Seager & Sasselov, 2000b) or hazes (Morley et al., 2015). The presence of clouds and hazes increases the altitude at which the planet's atmosphere is optically thick at all wavelengths (like Venus compared to the Earth) and effectively mutes the strength of transmission features. In practice, it is still challenging to distinguish the lack of an atmosphere from an atmosphere with a high cloud deck or significant haze coverage though this is likely an observational challenge that will be solved as our understanding of the range of possible exoplanet atmospheres grows.

1.3 M Dwarfs and Their Planets

M stars are the most numerous in the galaxy (Bochanski et al., 2010) and populate the main sequence between 0.08-0.5 $M_\odot$, with much longer main sequence lifetimes than more massive stars as nuclear burning rate scales with mass and is slowest for M stars (Tarter et al., 2007). Given what we now know about the occurrence rate of exoplanets, we expect most stars to have planets and indeed compact multi-planet systems are ubiquitous around M dwarfs (Dressing & Charbonneau, 2015; Hardegree-Ullman et al., 2019). M dwarfs are favorable targets for exoplanet transit and transmission studies because the depth of transit features scales as $(R_p/R_*)^2$, which is to say that for a planet of a given size, its transit depth and atmospheric absorption features will be deeper around a small star than around a larger star. M dwarfs are also cooler, which has a particular significance in that their liquid water habitable zones (e.g., Kopparapu et al., 2019) are much closer to the star and we can detect and study exoplanets with periods of 10s of days in their star's habitable zone. A closer habitable zone also means that temperate or cool planets orbiting M stars have a higher transit probability than around more massive stars. However, while all stars display some or many forms of stellar activity, M stars are particularly active in ways that throw the persistence of terrestrial atmospheres into question for these systems.

The activity of low mass stars has been studied for a long time, with Reiners & Basri (2007) demonstrating the first measurements of magnetic field strength on stars later than M4.5. They studied the variability of FeH molecular bands with stellar rotation and associated shorter rotation with greater activity. While all stars decrease in activity with age, these late M stars were found not to decrease in magnetic activity similar to other stars, but to remain relatively active even at slow rotation, late into their lives. West et al. (2015) expand on the age-activity relation for M stars, finding that old late-type stars are more magnetically active than old earlier-types. This implies that the latest M type stars, one of the most numerous exoplanet host types in the galaxy

(Laughlin et al., 1997), have characteristically different dynamo properties and magnetic activity than more massive stars. In this regime, stars are fully convective and even as they spin down, the convective turnover time scale can be much longer than the rotation period, resulting in unique but as-yet poorly understood magnetic properties for these stars.

The first known terrestrial exoplanet around an M dwarf star was GJ 1132b. Berta-Thompson et al. (2015) discovered this Earth-like ($R = 1.130 \pm 0.056 R_E$, $M = 1.66 \pm 0.23 M_E$; Bonfils et al., 2018)) exoplanet on a 1.6-day orbital period around a nearby fully-convective low-mass star with $M = 0.21 M_{\mathrm{sun}}$ (Bonfils et al., 2018) with the MEarth ground-based transit survey (e.g., Irwin et al., 2009; Berta et al., 2012). Since its discovery, this planet has been target of interest for its potential to have an observable atmosphere (Schaefer et al., 2016; Morley et al., 2017) and attempts to detect an atmosphere have provided controversial and contradictory results. Chapter 3 covers the non-detection of an *escaping* atmosphere, but longer wavelength observations from both ground- and space-based observatories haven't found consistent evidence of any sort of atmosphere. Southworth et al. (2017) and Swain et al. (2021) claim detections of atmospheric species from the ground and HST/WFC3 transmission spectra, respectively, while ground-based transmission observations from Diamond-Lowe et al. (2018) and independent analyses of HST/WFC3 transmission spectra by Mugnai et al. (2021) and Libby-Roberts et al. (2022) show GJ 1132 b's transmission spectrum to have no significant atmospheric absorption. May et al. (2023) recently analyzed two transits of GJ 1132b with JWST NIRSpec and found the first transit consistent with either atmospheric absorption or stellar contamination, while the second transit showed no significant deviation from a flat transmission spectrum. This continued mystery particularly highlights the importance of using multiple observations, instruments, and methods before reporting detections of atmospheric species in M dwarf exoplanet atmospheres.

1.4 The TESS Followup Observing Program

In 2018, TESS successfully launched and began observing the light curves of bright nearby stars, eventually surveying 75% of the sky by the end of its initial two-year mission. This telescope has the explicit purpose of monitoring hundreds of thousands of bright nearby stars to observe as many transiting systems as possible, especially sub-Neptune exoplanets on temperate orbits around M dwarf stars, a demographic undersampled in the Kepler catalog as Kepler targeted a narrower and deeper field more sensitive to far away solar- and more massive type stars.

To handle the amount and variety of observational followup needed, the TESS Followup Observing Program (TFOP), hosted alongside TESS at MIT, was set up to organize the incoming planet candidates and followup observations from teams around the world. I led several ground-based observing campaigns to validate as many TESS Objects of Interest (TOI) as possible with ground-based transit followup, with some of the discoveries I contributed to highlighted in Figure 1.3. I mostly targeted the smallest planet candidates with the lowest mass stellar hosts, contributing data to the discovery and validation of LHS 3844b (Vanderspek et al., 2019), LP 791-18 b, c, and d (Crossfield et al., 2019; Peterson et al., 2023), and TOI 269b (Cointepas et al., 2021); three nearby M dwarf systems with sub-Neptune and terrestrial exoplanets which are viable targets for transmission studies. Overall I contributed 38 light curves for 26 different TESS Objects of Interest to Exo-FOP using a ground-based observation campaign I led using the Las Cumbres Observatory (LCO).

1.5 Stellar Activity and Atmospheric Escape

The base concern of stellar activity is its effect on planetary atmospheres and habitability. These stars exhibit some of the most significant stellar activity and typically have XUV-bolometric luminosity ratios of an order of magnitude greater than solar (France et al., 2013). In the first few Gyr of an M dwarf's life it bombards its planets with high energy radiation, flares, stellar winds, and other effects.

Flares are known to have a greater effect on atmospheric loss for planets around M stars than around G or K stars (Chadney et al., 2017), with Atri & Mogan (2021) finding that M0-M4 stars are likely to erode both primary and secondary atmospheres of terrestrial planets in the HZ through extreme XUV activity and flaring. Louca et al. (2023) model the effects of recurrent flaring from

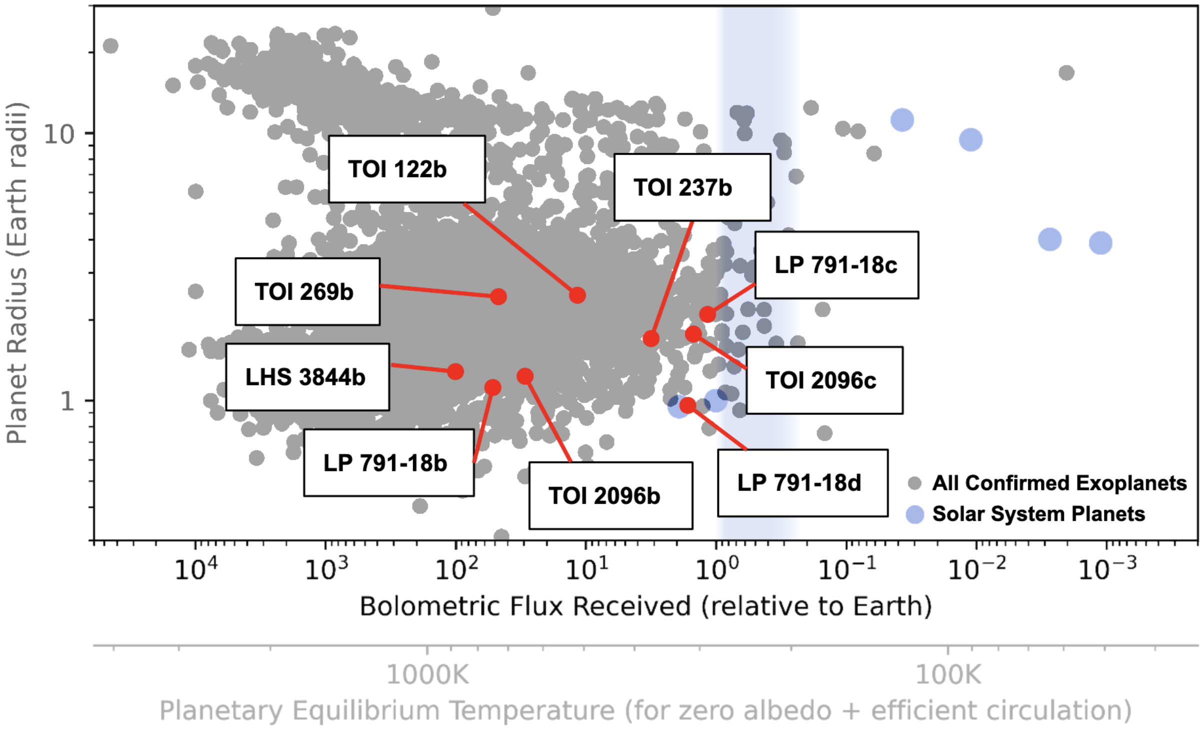

Figure 1.3: Radius-Insolation diagram of known exoplanets, pointing out those I have published or helped discover. Insolation is the amount of bolometric stellar flux received by the planet relative to the solar flux received by the Earth. The vertical blue bar represents the circumstellar habitable zone.

early and mid-M dwarfs on sub-Neptune exoplanet atmospheres and find that on the timescale of a few weeks, flares alone significantly alter atmospheric chemistry. Interestingly, they found this to not have significantly affected the methane chemistry or detection for the larger planets.

Modi et al. (2023) studied the effects of both stellar wind and EUV flux on planetary atmospheres and found that stellar winds were ultimately not very effective at stripping planetary atmospheres and EUV flux was the primary driver of atmospheric loss. They find that planets orbiting > 0.1AU from active late-type stars are most likely to retain their primordial atmospheres. Lobo et al. (2023) modeled the evolution of tidally locked sub-Neptune planets in the habitable zones of active M stars and found that water worlds will experience runaway greenhouse effects at young system ages but that there is a chance for habitable conditions on the terminator region of terrestrial worlds.

Several planets have been observed to have deep and extended transits at Lyman-α, attributed to outflowing gas photo-ionized by the XUV radiation of the host star, like HD 209458b (Vidal-Madjar et al., 2003; Ehrenreich et al., 2008), HD 189733b (Bourrier et al., 2013), Gl 436b (Ehrenreich et al., 2015; Bourrier et al., 2015; Bourrier et al., 2021), the TRAPPIST-1 system (Bourrier et al., 2017c) and GJ 3470b (Bourrier et al., 2021). This is one of the best probes for inferring atmospheric loss from transiting exoplanets, and from the depth and duration of the transit we can learn about how quickly neutral hydrogen in the outflow is photo-ionized, the radiative and tidal forces of the star, and the processes driving escape (e.g., Waalkes et al., 2019; Owen & Altaf, 2021).

If we come to find that terrestrial planets in the habitable zones of M stars rarely retain their atmospheres, the prospects for life in the galaxy (and our ability to find it) become somewhat bleak until we are able to detect and study large numbers of habitable-zone planets in sun-like systems, like with the proposed Habitable Worlds Observatory, which is a telescope combining the designs and scientific goals of the previously proposed LUVOIR (The LUVOIR Team, 2019) and HabEx (Gaudi et al., 2020) missions. However, this is not (yet) the case, and the search for atmospheres in these systems is only beginning, with active and spotted young systems like AU Mic (see Figure

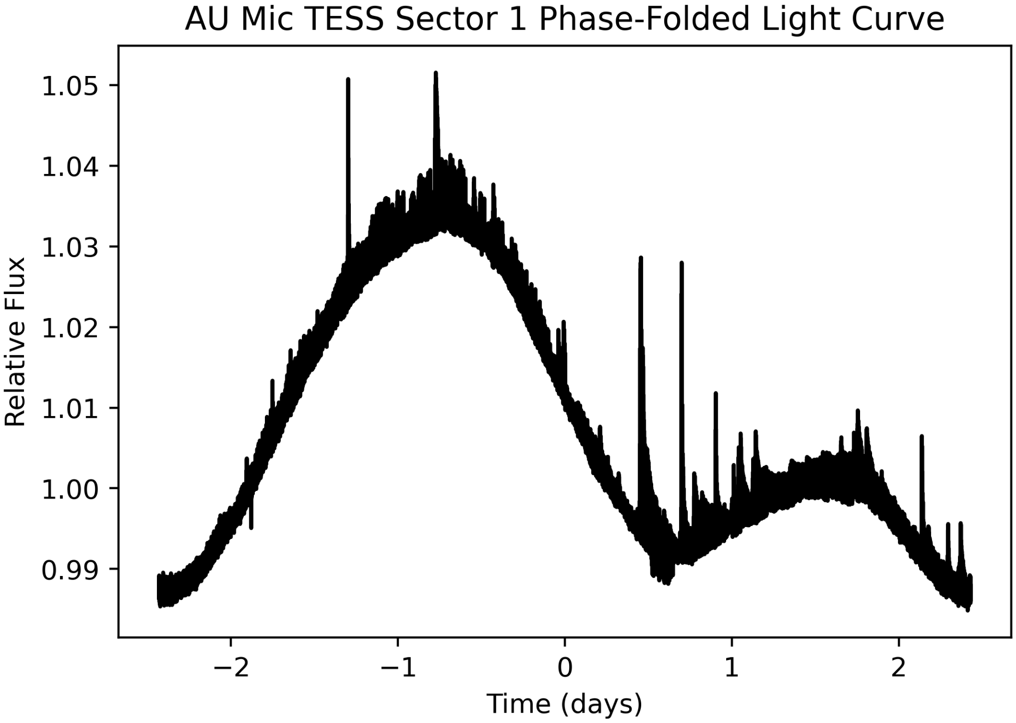

Figure 1.4: A phase-folded lightcurve of AU Mic from TESS sector 1, showing complex rotational modulation from surface heterogeneities and spikes in flux from flares.

1.4) allowing us to study planets which still have their primordial atmospheres in high-activity environments. The challenge for these systems then becomes the issue of disentangling stellar contamination from signals due to atmospheric absorption.

1.6 Observational Biases Introduced by Starspots

Stars with convective outer envelopes will exhibit starspots and faculae in regions where magnetic field lines pass through the photosphere. A sufficient concentration of magnetic field lines creates a region where magnetic pressure counteracts gas pressure, reducing opacity and increasing the flux emanating from deeper in the photosphere, creating a bright region known as a facula. When the concentration of magnetic field lines is great enough, convection is inhibited and instead of an increase in flux, the magnetic region is cooled via radiation and appears as a dark spot with temperature that depends on the strength of the magnetic field (Kopp & Rabin, 1992).

As spots on the stellar surface rotate in and out of view they create spectro-photometric variations in phase with stellar rotation and impart unique spectral features into stellar spectra. Spots occulted by transiting planets can appear as a bump in the light curve where the flux contrast and shape of the bump provides clues about the spot morphology, location, and spectrum. Unocculted spots, however, impart spectral signatures in the disk-averaged spectrum that create λ-dependent changes to the exoplanet transit depth in what is now known as the transit light source effect (TLSE; Rackham et al., 2018). Below about 4000 K, absorption features for molecules like H_2O and TiO begin to appear in stellar spectra which may be mistaken for atmospheric signatures in planetary transmission spectra if the spot coverage on the transit chord is not representative of the disk-averaged spot coverage. Iyer & Line (2020) find that H_2O absorption is widespread in archival WFC3 spectra, a phenomenon that may, in many cases, be due to unocculted spots. Starspot contamination increases in magnitude at bluer wavelengths (see Figure 1.5) as spot contrast against the surrounding photosphere increases, the relative stellar background flux decreases, and the apparent planetary radius increases. In observation, this can appear similar to Rayleigh scattering in a transiting exoplanet's atmosphere.

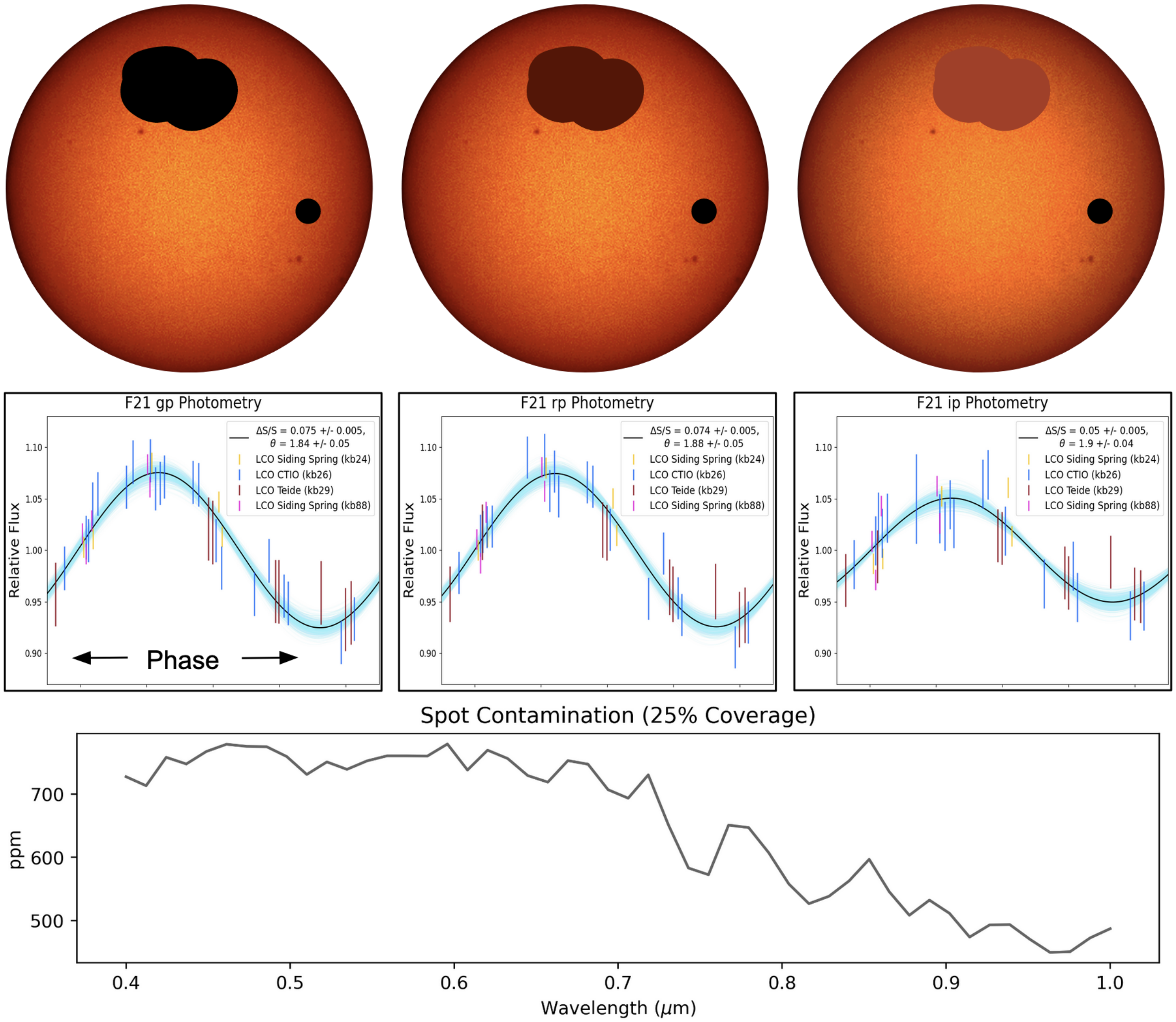

Figure 1.5: Spot contrast against the photosphere is greatest at blue wavelengths and decreases toward redder wavelengths (top panel). This corresponds to a decrease in photometric variability (middle panel) as well as a decrease in spot contamination with wavelength.

Spots are ubiquitous on stars with convective outer envelopes, which includes all but the most massive stars. The greatest spot coverage fraction measured for the sun is about 0.06% (e.g., Penza et al., 2021) but the sun is a relatively inactive star compared to other solar-type stars, and is less active than nearly every single M star (e.g., Basri et al., 2013). Lower mass stars have much higher coverage fractions of spots, but tend to be spot-dominated instead of facula-dominated like solar-type stars (Rackham et al., 2018).

Photometric variations in stellar rotation have long been recognized as a measurable effect of spot coverage, with direct links to spot coverage and spectrum (Budding, 1977; Spruit, 1982). When spots lie on the transit chord and are occulted by a planet, a bump can be found in the transit which is used to study the shape and extent of spots, their spectral contrast, planetary obliquity, and stellar differential rotation (e.g., Budding & Zeilik, 1987; Silva-Valio, 2008; Araújo & Valio, 2023). There are now over a dozen known systems with spot crossings, with vast potential for studying spots on these stars and learning more about spot spectra, location, evolution, and morphology.

Spots and the rotational variations they cause can introduce biases into our measurements of stars and their planets. Lanza et al. (2008) found that magnetic active regions can shift the star's photocentre, causing false detections of transiting planets in astrometry. Similarly, Newton et al. (2016b) show that when a planet's orbit is on a similar period to the stellar rotation, radial velocity measurements and detections can be obscured, most significantly affecting RV measurements for habitable-zone exoplanets around early (M4V-M1V) M stars, and being less of a problem for habitable-zone planets around later-type stars. Stars with very short rotation periods (P<1 day) obscure transit signals regardless of stellar type (Miyakawa et al., 2022), but this effect is less at redder wavelengths where stellar photometric variability amplitudes decrease.

If spots are left unaccounted for, atmospheric depths can be biased and planets mischaracterized in multiple ways. Unocculted spots increase the measured transit depth of the planet with a chromatic effect and an increasing trend toward bluer wavelengths, making the planet appear larger than it is in both broadband and high-resolution observations. Czesla et al. (2009) found

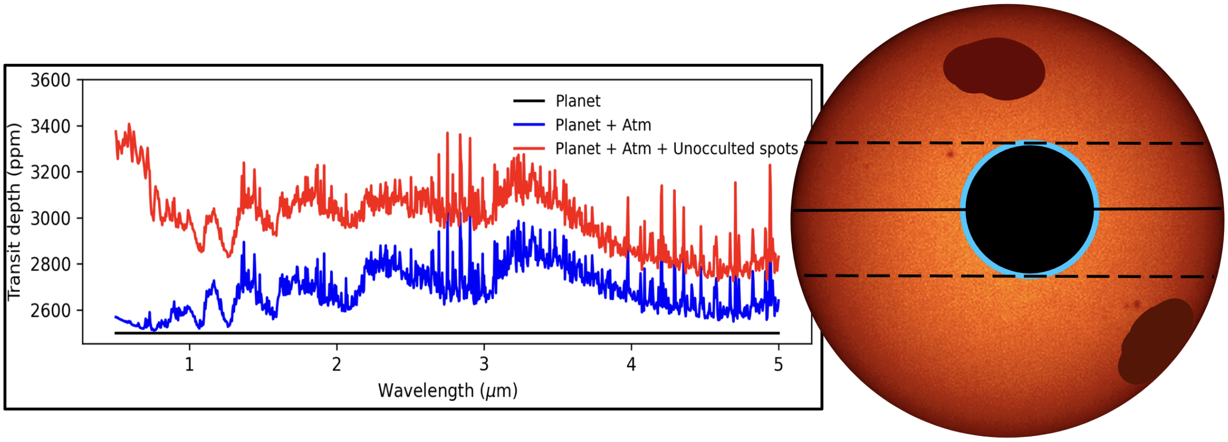

Figure 1.6: A cartoon model of the relative effects of atmospheric absorption and unocculted spot contamination for a planet like AU Mic b around a star like AU Mic.

that occulted and unocculted spots can both affect transit measurements and that stellar activity cannot be ignored in exoplanet studies. Other studies have also confirmed this effect, found to behave differently depending on the resolution of our spectra (Deming & Sheppard, 2017) and also adding bias to transit duration and TTV signals (Oshagh et al., 2013). Studies have shown that transit depths can be biased by spots in broad photometric bandpasses (e.g., Ballerini et al., 2012) as well as in medium- and high- resolution spectra, with the potential to cause both false-positive and false-negative detections of atmospheric absorption (e.g., Zhang et al., 2018; Rackham et al., 2018, 2019; Wakeford et al., 2019; Iyer & Line, 2020). Iyer & Line (2020) investigate the issue of spot contamination and find the TLSE is negligible for stars with spot coverage less than about 1%. Unfortunately, spot coverage fractions this low are uncommon or even rare for low mass exoplanet hosts.

This effect has become a real problem for state-of-the-art observations of sub-Neptune exoplanet atmospheres with HST and JWST, with possible spot contamination obscuring our interpretation of atmospheric absorption for M dwarf sub-Neptunes TOI 270d (Mikal-Evans et al., 2023), K2-33b (Thao et al., 2023), Gl 486b (Moran et al., 2023), L 98-59c (Barclay et al., 2023), and the TRAPPIST-1 system (Zhang et al., 2018; Wakeford et al., 2019; Lim et al., 2023) - all nearby planets on temperate orbits that are promising targets for atmospheric study. Transmission observations of these planets show features consistent with spot contamination and/or atmospheric absorption, with signals entangled until we have a detailed understanding of the stellar surface of each of those stars at the time of transit. Moreover, Luque & Pallé (2022) report that sub-Neptune planets in M dwarf systems can be characterized into three distinct groups based on density; rocky worlds, water-rich worlds, and gaseous worlds. If densities are highly indicative of distinct planet types, then the accurate calculation of planetary radii from multi-wavelength transit observations that also account for starspots is crucial for even the broadest interpretation of transiting sub-Neptune observations.

1.7 A Deep Investigation Into An Active, Spotted Star

My current research builds off of the research presented in Chapter 4 to lay the groundwork for the discovery and characterization of M dwarf exoplanet atmospheres by studying starspot contamination for the young active planet host AU Microscopii. This very young (24 Myr; Mamajek & Bell, 2014) and very close (9.71 pc; Gaia Collaboration et al., 2023) star is a closely studied star historically for its high level of activity and significant photometric variabilities (e.g., Hebb et al., 2007), and is now an exoplanet host of high interest for its planetesimal-containing debris disk (e.g., MacGregor et al., 2013) and two transiting warn Neptunes (Plavchan et al., 2020; Martioli et al., 2021; Szabó et al., 2021; Zicher et al., 2022; Donati et al., 2023). Because of the young age and proximity of this system, it presents exoplanet transmission targets which we expect to have atmospheric absorption signatures more detectable than nearly every other sub-Neptune exoplanet. These planets have not yet lost their primordial atmospheres, and are likely inflated from only recently being formed, with hydrogen-dominated atmospheres.

This is an extremely active early-type M star (M0Ve) with a well-studied magnetic field. AU Mic has been found to have an asymmetric global magnetic field with a mean field strength of 90 Gauss and spotted magnetic field strengths of 2-3 kG (Kochukhov & Reiners, 2020; Reiners et al., 2023; Cristofari et al., 2023; Donati et al., 2023). Donati et al. (2023) measured magnetic field strengths of 2-2.3 kG with a corresponding spot filling factor of $24 \pm 3\%$, somewhat smaller than the $40 \pm 4\%$ coverage we measured in Chapter 4. In the first order assumption that the empirical relation derived by Kopp & Rabin (1992) for sunspot temperature and magnetic field strength holds somewhat true for AU Mic, field strengths between 2-3 kilo Gauss (kG) should correspond to spot-to-photosphere temperature ratios of 0.5 (at 3 kG) to 0.9 (at 2 kG), which encompasses our measurements of spot temperature ratios of between 0.75-0.80 ($\mathrm{T}_{\mathrm{spot}} = 3000 - 3100\mathrm{K}$) for AU Mic.

AU Mic's flaring and XUV activity level may spell doom for the atmospheres of AU Mic b and c, but the young age of the system implies those atmospheres are still observable and have not been photoevaporated. Some evidence of atmospheric escape from the atmosphere of AU Mic b was found by Rockcliffe et al. (2023), with inconsistent measurements which might tie atmospheric escape to specific mechanisms or high energy events. Studying this system in depth allows us to glimpse into the very early stages of atmospheric absorption and evolution under an active flare star which represents a young version of many other exoplanet host stars with transmission targets. The insights we gain about the atmospheres of AU Mic b and c will help us better understand the prognosis for sub-Neptune atmospheres subjected to a lifetime of M dwarf stellar activity.

To successfully disambiguate stellar contamination from the HST/WFC3 transmission spectrum of AU Mic b, we will need to develop a novel approach which integrates all of our ground-based and WFC3 data. Iyer & Line (2020) demonstrated that simply having priors for spot contamination does not improve atmospheric retrieval for contaminated spectra, but that a joint inference of both stellar and planetary parameters is more reliable. Based on this, we will model AU Mic b's transmission spectrum using an atmospheric retrieval framework that simultaneously models spot characteristics similar the model we developed in Chapter 4. The precise constraints we place on spot characteristics in that chapter gives us optimism for the success of measuring AU Mic b's atmospheric absorption, but it may also be the case that the uncertainty on contamination level obscures a significant absorption signal, which will give us insight into the challenge we are up against for measuring planetary atmospheres in more distant systems with even weaker atmospheric signals.

If there are signs of biological processes in the atmospheres of other worlds, then it is a matter of time until we discover them. Many of the best targets for atmospheric characterization have been or will soon be found, but there is no shortage of challenges we need to overcome in order to robustly detect planetary atmospheres and disentangle them from the complex spectrum of the background star. The following chapters chart a path through observations of transiting exoplanets and low mass host stars that have left me with many burning questions and several new ideas on how to answer those questions so that I can help lay the groundwork for the eventual unambiguous detections of molecular and biogenic species in the atmospheres of temperate and habitable worlds.

Chapter 2

TOI 122b and TOI 237b, two small warm planets orbiting inactive M dwarfs, found by *TESS*

This chapter has been published in the Astronomical Journal as: W. C. Waalkes, Z. K. Berta-Thompson, K. Collins, A. Feinstein, B. Tofflemire, B. Rojas-Ayala, M. Silverstein, E. Newton, G. Ricker, R. Vanderspek, D. Latham, S Seager, J. Winn, J. M. Jenkins, J. Christiansen, R. Goeke, A. Levine, H. Osborn, S. Rinehart, M. Rose, E. Ting, J. Twicken, K. Barkaoui, J. Bean, C. Briceño, D. Ciardi, K. I. Collins, D. Conti, T. Gan, M. Gillon, G. Isopi, E. Jehin, E. Jensen, J. Kielkopf, N. Law, F. Mallia, A. Mann, B. Montet, F. Pozuelos, H. Relles, J. Libby-Roberts, C. Ziegler, *TOI 122b and TOI 237b, two small warm planets orbiting inactive M dwarfs, found by TESS*, The Astronomical Journal, 2021, 161, 13.

Specific contributions include: W. C. Waalkes led the data analysis and model fitting, Z. K. Berta-Thompson provided the finder charts for both systems and PI'd an proposal with which some of the ground-based light curves were observed, K. Collins organized the TESS Followup Observing Program (TFOP) which organized various contributions from many sources. B. Tofflemire provided systemic radial velocities and A. Tokovinin (who chose not to be a co-author on the publication) provided the SOAR speckle imaging.

2.1 Preface

We report the discovery and validation of TOI 122b and TOI 237b, two warm planets transiting inactive M dwarfs observed by *TESS*. Our analysis shows TOI 122b has a radius of 2.72±0.18 R_E

and receives 8.8±1.0× Earth's bolometric insolation, and TOI 237b has a radius of 1.44±0.12 R_E and receives 3.7±0.5× Earth insolation, straddling the 6.7× Earth insolation that Mercury receives from the sun. This makes these two of the cooler planets yet discovered by *TESS*, even on their 5.08-day and 5.43-day orbits. Together, they span the small-planet radius valley, providing useful laboratories for exploring volatile evolution around M dwarfs. Their relatively nearby distances (62.23±0.21 pc and 38.11±0.23 pc, respectively) make them potentially feasible targets for future radial velocity follow-up and atmospheric characterization, although such observations may require substantial investments of time on large telescopes.

2.2 Introduction

The Transiting Exoplanet Survey Satellite (*TESS*, Ricker et al., 2015) follows the 8 year missions of *Kepler* (Borucki et al., 2010) and *K2* (Howell et al., 2014), which discovered thousands of planets. While *Kepler* typically found planets orbiting faint and distant stars, *TESS* is examining the brightest and nearest stars for evidence of exoplanet transits. Over the course of its 2-year primary mission, *TESS* has surveyed 85% of the sky, looking at over 200,000 nearby stars with a 2-minute cadence and many more stars with the 30-minute full frame images (FFIs). *TESS* is expected to find up to 4500 planets, 500-1200 planets orbiting M dwarfs, and about 50 planets within 50 pc (see Sullivan et al., 2015; Barclay et al., 2018; Ballard, 2019).

M dwarfs are interesting targets for transiting exoplanet studies as they provide the best opportunity for finding temperate terrestrial planets (Nutzman & Charbonneau, 2008; Blake et al., 2008). All main sequence stars less massive than 0.6 $M_\odot$ fall into the M dwarf category, and they are the most numerous stellar type in the universe (e.g., Chabrier & Baraffe, 2000). These stars are very cool (2000 K$<T_{\rm eff}<$4000K) and very small, so cool planets have shorter periods, higher transit probabilities and deeper transits than they would around larger stars.

M dwarfs tend to host terrestrial exoplanets more often than gas giants (Mulders et al., 2015; Bowler et al., 2015), and these terrestrial planets can more readily be found at lower insolations given the low luminosities of M dwarfs. Finally, M dwarfs have such long lifetimes that not a single M dwarf ever formed has yet evolved off the main sequence (Laughlin et al., 1997), making these stellar systems interesting laboratories for very long timescale planetary evolution. For a comprehensive review of M dwarfs as exoplanet host stars, see Shields et al. (2019). While the habitability of planets around M dwarfs remains an open question, the low insolations of M dwarf planets on short periods creates opportunities for statistically studying the presence and evolution of planetary atmospheres.

The first year of *TESS* yielded several small exoplanets orbiting M dwarfs such as LHS 3844b (Vanderspek et al., 2019), the L 98-59 system (Kostov et al., 2019; Cloutier et al., 2019), the TOI 270 system (Günther et al., 2019), the Gl 357 system (Luque et al., 2019), LTT 1445Ab (Winters et al., 2019), the LP 791-18 system (Crossfield et al., 2019), and L 168-9b (Astudillo-Defru et al., 2020). The two planets we present in this paper are challenging for precise RV mass measurements, but both are smaller than 3 R_E and their low insolations and short periods (see Fig. 2.1) position them as interesting candidates for atmospheric follow-up. They may have retained their atmospheres despite being too hot to be considered habitable and may help us understand atmospheric evolution and the diversity of atmospheres of small planets.

The rest of the paper is organized as follows. In §2 we describe the *TESS* observations, the photometric and spectroscopic follow-up data we gathered, and arguments against these planets being false positives. In §3 we describe the results of stellar parameter estimation and transit light curve fitting, and in §4 we discuss the results and their implications for future work.

2.3 Data

2.3.1 TESS Photometry

TESS has four 24×24 degree field of view cameras, each with four $2k \times 2k$ CCDs. The *TESS* bandpass is 600-1000 nm, and the pixel scale is 21 arcseconds (Ricker et al., 2015). For our analysis of the *TESS* light curves (Fig. 2.2), we accessed the *TESS* data using `lightkurve` (Lightkurve Collaboration et al., 2018) and downloaded the Science Processing Operations Center (SPOC,

Date	Observatory	Filter	t_{exp}(s)	R_{Aperture}(”)	T_0 (BJD TDB)
TOI 122b					
2018-09-18	SSO iTelescope	Clear	120	4.8	(Egress Only)
2018-09-18	LCO SSO (1m)	r’	180	4.28	2458379.9015 ± 0.0012
	LCO SSO (1m)	i’	30	3.89	
2018-10-18	LCO SAAO (1m)	I	42	5.45	(Too Noisy)
2018-11-02	TRAPPIST South (0.6m)	I+z’	60	5.2	2458425.6026 ± 0.0006
	LCO CTIO (1m)	I	42	4.67	
2019-07-10	LCO SAAO (1m)	I	50	5.06	2458674.4275 ± 0.0012
2019-07-15	LCO SAAO (1m)	I	50	3.50	(Too Noisy)
2019-07-25	LCO CTIO (1m)	g’	240	4.67	2458689.6577 ± 0.0012
	LCO CTIO (1m)	g’	240	3.89	
2019-08-04	LCO CTIO (1m)	V	240	5.45	2458699.8177 ± 0.0020
TOI 237b					
2018-12-16	LCO SAAO (1m)	i’	65	4.67	(Bad Ephemeris)
2019-05-07	LCO SAAO (1m)	i’	100	3.89	(Bad Ephemeris)
2019-06-02	TRAPPIST South (0.6m)	I+z’	60	5.2	$2458637.9225^{+0.0014}_{-0.0014}$
2019-06-14	LCO CTIO (1m)	I	60	6.22	$2458648.7971^{+0.0019}_{-0.0017}$
2019-06-19	LCO CTIO (1m)	I	60	8.56	(Too Noisy)
2019-08-02	LCO CTIO (1m)	I	75	5.45	2458697.7198 ± 0.0008
	LCO CTIO (1m)	g’	300	4.67	
2019-08-13	LCO SAAO (1m)	I	70	4.67	$2458708.5923^{+0.0015}_{-0.0012}$
2019-09-03	LCO SAAO (1m)	I	70	5.06	$2458730.3419^{+0.0011}_{-0.0016}$

Table 2.1: Ground-based follow-up observations of the two planets, with mid-transit times (if a transit is detected), exposure times, and filters. For data sets in which a transit is not detected, this could be due to the transit being missed entirely, or the transit being obscured by noise. LCO is the Las Cumbres Observatory which includes SAAO, the South African Astronomical Observatory, CTIO, the Cerro-Telolo Interamerican Observatory, and SSO, the telescopes at the Siding Spring Observatory. SSO iTelescope is the Siding Spring Observatory iTelescope, which is not part of the LCO network. Observations from this site unfortunately missed most of the transit so we do not include these data in our analysis. We report mid-transit times based on the joint modeling described in the text.

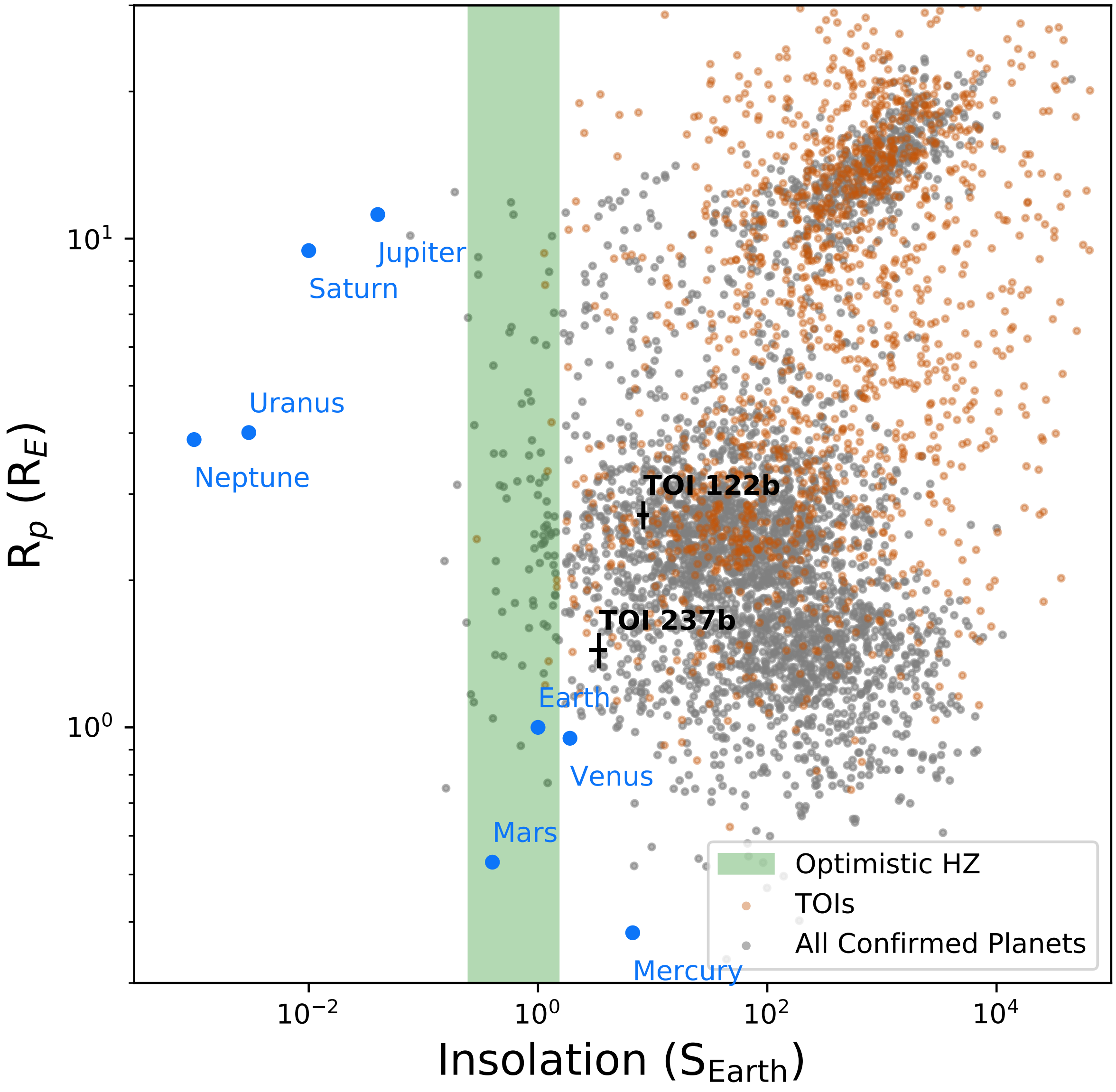

Figure 2.1: All confirmed exoplanets and current *TESS* Objects of Interest (TOIs) (as of February 2020) with current values for R_p (R_E) and S (S_E). Orange points are the TOIs (validated and unvalidated), while the gray points are all confirmed exoplanets (as of March 2020). Highlighted in green is the "recent Venus-early Mars" habitable zone covering 0.25-1.5 S_E (e.g., Kopparapu et al., 2019), in which a few systems fall. This optimistic habitable zone is likely shifted to lower insolations for M dwarfs given more recent studies of energy budgets and albedos for M dwarf planets (Shields et al., 2019).

Jenkins et al., 2016a) Presearch Data Conditioning Simple Aperture Photometry (PDCSAP) flux light curves (Stumpe et al., 2012; Smith et al., 2012; Stumpe et al., 2014). The light curves shown in Figure 2.2 are 2-minute cadence data phase-folded to the orbital periods we refined in this work.

***TESS* Object of Interest (TOI) 122b** (TIC 231702397) was observed in Sector 1 of *TESS* from 2018 July 25 to 2018 August 22 with CCD 1 of Camera 2. Four transits were observed with a 5.1 day period and a 6 ppt depth. The SPOC (Jenkins et al., 2016b) pipeline flagged the light curve as a planet candidate and it was submitted to the MIT TOI alerts page[1] (Guerrero et al., submitted), where we accessed the preliminary SPOC data validation transit parameters (Twicken et al., 2018; Li et al., 2019) and scheduled follow-up observations with ground based observatories. Preliminary parameters indicated that the stellar host was an M dwarf, implying the orbiter was super-Earth or sub-Neptune in size.

TOI 237b (TIC 305048087) was observed in Sector 2 of *TESS* from 2018 August 22 to 2018 September 20 with CCD 1 of Camera 1. Five transits were observed with a 5.4 day period and a 6 ppt depth. The SPOC pipeline flagged the light curve as a planet candidate and it was submitted to the MIT TOI alerts page, where we accessed the preliminary transit parameters and scheduled follow-up observations with ground based observatories. Preliminary parameters indicated that the stellar host was an M dwarf, implying the orbiter was also super-Earth in size.

2.3.2 Ground-Based Photometry

The follow-up observations are summarized in Table 2.1. Both systems were observed extensively as part of the *TESS* Follow-up Observing Program Sub-Group 1 (TFOP SG1) photometric campaign. Ground-based observations span several months for both targets, from observatories around the globe. For both TOI 122 and TOI 237, we used the TESS Transit Finder tool, which is a customized version of the Tapir software package (Jensen, 2013), to schedule the photometric time-series observations. Ground-based light curves used in the analysis are shown in Figures 2.3 and 2.4.

LCO Photometry

Most photometric data were taken at Las Cumbres Observatory sites via the Las Cumbres

---

[1] https://tess.mit.edu/toi-releases/

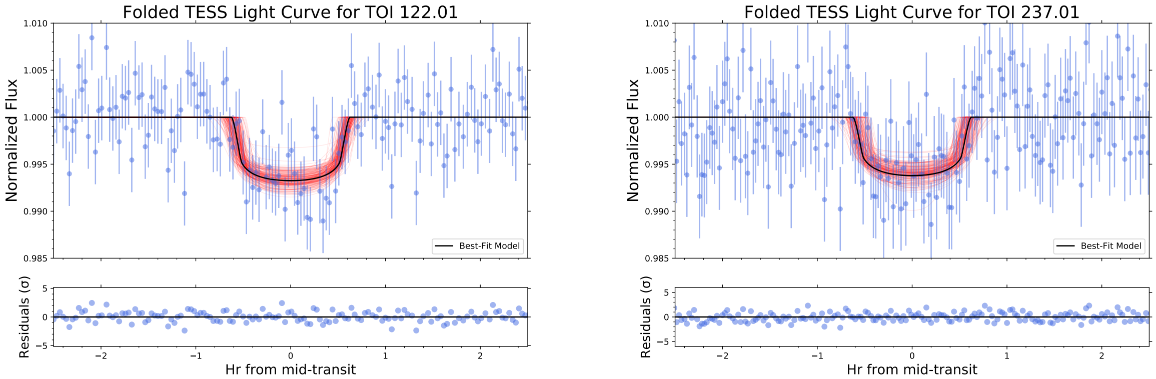

Figure 2.2: *TESS* light curves, phase-folded across a full 27-day sector to the periods refined in this work. We model these light curves with a 3-parameter MCMC that explores values for transit depth, inclination, and the scaled semi-major axis. The best fit model (50^{th} percentile values) is the black line, and red lines are random samples drawn from the posterior distributions. The posteriors from the *TESS* light curves are consistent with the posteriors for the follow-up observations, with larger uncertainties. The follow-up observations have allowed us to constrain the transit parameters effectively.

Observatory Global Telescope (LCOGT) network (Brown et al., 2013). These observations were done with 1-m telescopes equipped with *Sinistro* cameras which have a plate scale of 0.389 arcseconds and a FOV of $26.4' \times 26.4'$. Filters and photometric aperture radii vary between observations and are provided in Table 2.1. Additional information and the full datasets can be found on ExoFOP-TESS[2] .

LCOGT data are reduced via a standard reduction pipeline ("BANZAI", McCully et al., 2018) which performs bias and dark subtractions, flat field correction, bad pixel masking, astrometric calibration, and source extraction[3] . We scheduled most observations in red bandpasses (I, i', z) where the S/N is highest for M dwarfs. Observing windows were chosen to include the full transit along with 1-3 hours of pre- and post-transit baseline. Many of our observations were defocused, to allow longer integration times for brighter stars and to smear the PSF over more pixels, reducing any error introduced by uncertainties in the flat-field.

We performed differential aperture photometry on the data using the AstroImageJ tool

---

[2] https://exofop.ipac.caltech.edu/tess/

[3] https://lco.global/documentation/data/BANZAIpipeline/

(Collins et al., 2017). Using a finder chart, we drew apertures of varying radii (see Table 2.1) around the target star, 2-6 bright comparison stars, and any stars of similar brightness within 2.5'. Light curves of the nearby stars were examined for evidence of being eclipsing binaries, variable stars, or the true source of the transit signal in *TESS*' large pixels. For both of these systems, the transit was found around the target star, and no evidence of nearby eclipsing binaries or periodic stellar variation was found within 2.5' that could have given rise to the transit signal.

TRAPPIST-South Photometry

TRAPPIST-South at ESO-La Silla Observatory in Chile is a 60 cm Ritchey-Chretien telescope, which has a thermoelectrically cooled 2k×2k FLI Proline CCD camera with a field of view of $22' \times 22'$ and pixel-scale of 0.65"/px (Jehin et al., 2011; Gillon et al., 2013). We carried out a full-transit observation of TOI 122 on 2019 November 02 with $I + z$ filter with an exposure time of 60 s. We took 222 images and made use of AstroImageJ to perform aperture photometry, using an aperture radius of 8 pixels (5.2") given the target PSF of 3.7". We confirmed the event on the target star on time and we cleared all the stars of eclipsing binaries within the 2.5' around the target star. For TOI 237 the observations were carried out on 2019 June 02 with $I + z$ filter and exposure time of 60 s. We took 207 images and used AstroImageJ to perform the aperture photometry, using an aperture radius of 8 pixels (5.2") given the target PSF of 4.3".

2.3.3 SOAR Speckle Imaging

High-angular resolution imaging is needed to search for nearby sources not resolved in the seeing-limited ground-based photometry. Nearby sources can contaminate the TESS photometry, resulting in a diluted transit and an underestimated planetary radius. We searched for nearby sources to TOI 122 with SOAR speckle imaging (Tokovinin, 2018) on 2018 December 21 in I-band, a similar visible bandpass as TESS. Further details of observations from the SOAR TESS survey are available in Ziegler et al. (2020). We detected no nearby stars within 3" of TOI 122 within the 5σ detection sensitivity of the observation, which is plotted along with the speckle auto-correlation function in Figure 2.5. Companions within 2.5 magnitudes of the target (which could dilute transit

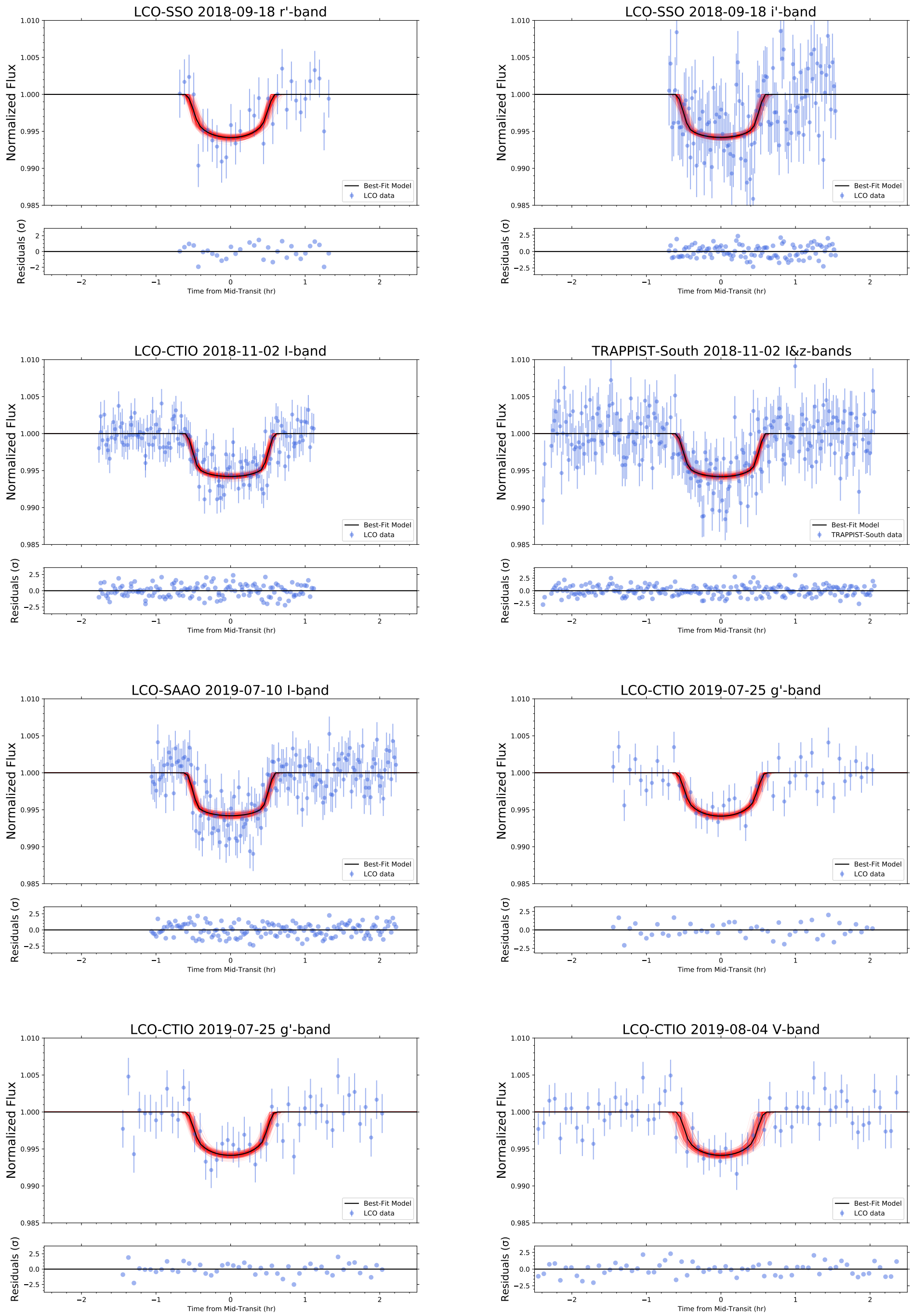

LCO-SSO 2018-09-18 r'-band

LCO-SSO 2018-09-18 i'-band

LCO-CTIO 2018-11-02 I-band

TRAPPIST-South 2018-11-02 I&z-bands

LCO-SAAO 2019-07-10 I-band

LCO-CTIO 2019-07-25 g'-band

LCO-CTIO 2019-07-25 g'-band

LCO-CTIO 2019-08-04 V-band

Figure 2.3: Light curves for all eight of the viable follow-up transits of TOI 122b. Best fit MCMC models are in black with 200 random samples plotted in red. Requiring that the transit depth, semi-major axis, and inclination were identical between visits led to a consistent model that fit all the transits.

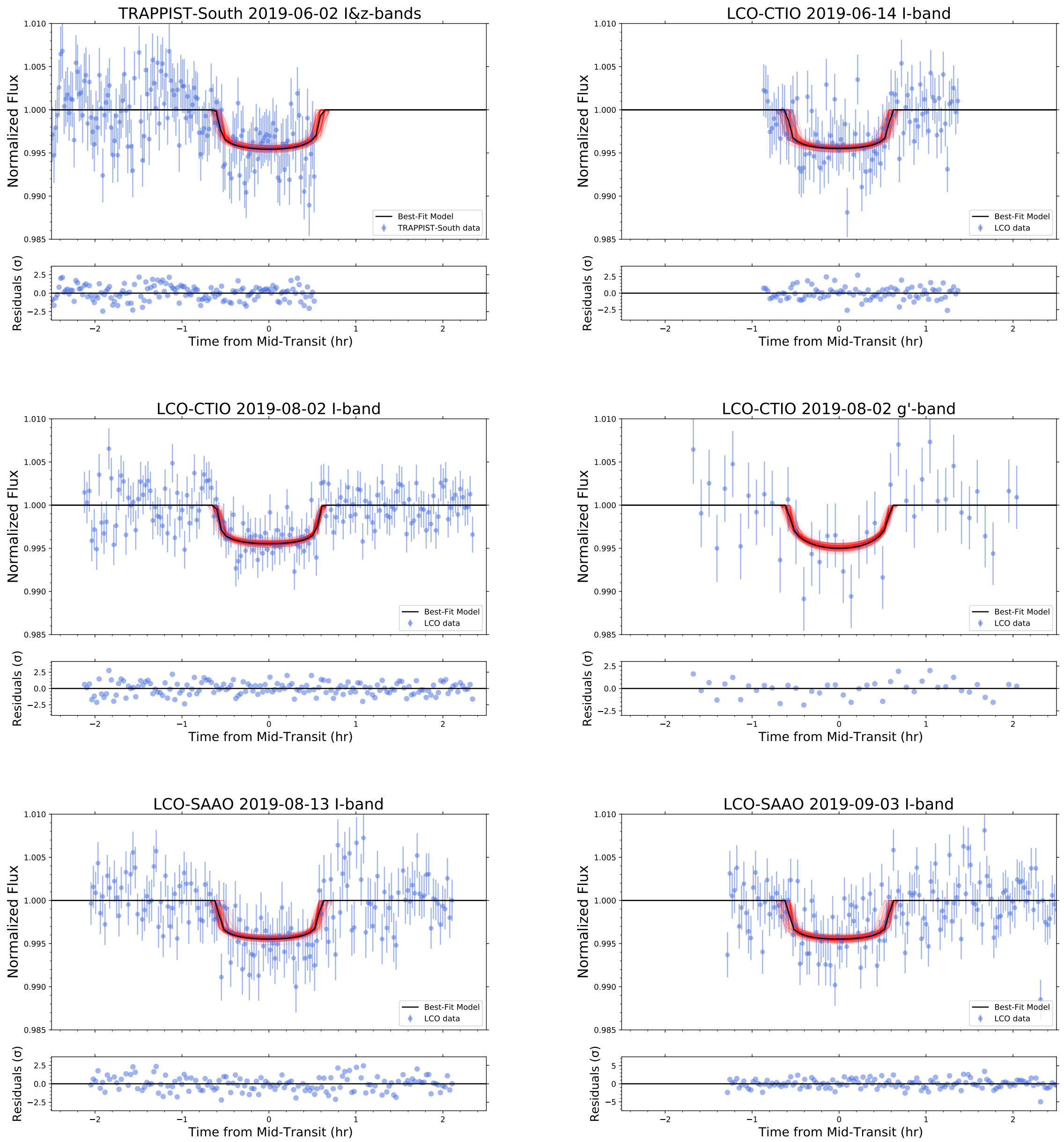
TRAPPIST-South 2019-06-02 I&z-bands

LCO-CTIO 2019-06-14 I-band

LCO-CTIO 2019-08-02 I-band

LCO-CTIO 2019-08-02 g'-band

LCO-SAAO 2019-08-13 I-band

LCO-SAAO 2019-09-03 I-band

Figure 2.4: Light curves for ground-based follow-up transits of TOI 237b. Best fit MCMC models are in black with 200 random samples plotted in red. Requiring that the transit depth, semi-major axis, and inclination were consistent between visits led to a final model that fit all the transits.

depths by 10%) are excluded down to separations of about 0.3”.

2.3.4 Stellar Spectra

Magellan Spectra

We obtained near-IR spectra of TOI 122 and TOI 237 on 2018 December 22 with the Folded-port InfraRed Echellete (FIRE) spectrograph (Simcoe et al., 2008). FIRE is hosted on the 6.5 Baade Magellan telescope at Las Campanas Observatory. It covers the 0.8-2.5 micron band with a spectral resolving power of R = 6000. Both targets were observed in the ABBA nod patterns using the 0.6" slit. TOI 122 was observed three times and TOI 237 was observed twice, both at 160s integration time. A nearby A0V standard was taken for both targets in order to aid with telluric corrections. The reduction of the spectra were completed using the FIREhose IDL package[4] .

SALT–HRS Spectra

We obtained optical echelle spectra for each system using the High-Resolution Spectrograph (HRS; Crause et al., 2014) on the Southern African Large Telescope (SALT; Buckley et al., 2006). Two observations were made for each system (TOI 122 on 2019 August 09, 10; TOI 237 on 2019 August 10, 12), with each epoch consisting of 3 consecutive integrations in the high-resolution mode ($R \sim 46{,}000$). The spectra were reduced using a HRS-tailored reduction pipeline (Kniazev et al., 2016; Kniazev et al., 2017)[5] , which performed flat fielding and wavelength calibration. Due to the faint apparent magnitudes of these systems, we focused our analysis on wavelengths greater than 5000 Å, where the spectra had signal-to-noise > 10.

To determine systemic radial velocities for both systems and to search for spatially-unresolved stellar companions, we computed spectral-line broadening functions (BFs) for each observation. The BF is computed via a linear inversion of the observed spectrum with a narrow-lined template, and represents a reconstruction of the average photospheric absorption-line profile (Rucinski, 1992; Tofflemire et al., 2019). For both systems, the BF is very clearly single peaked, indicating a contribution from only one star. Figure 2.6 presents a region of the SALT–HRS spectrum for each system with its corresponding template and broadening function.

For each spectrum, the BFs computed for each echelle order were combined and fit with a Gaussian profile to determine the system's radial velocity. Uncertainties on these measurements

---

[4] http://web.mit.edu/rsimcoe/www/FIRE/

[5] http://www.saao.ac.za/∼akniazev/pub/HRS_MIDAS/

were derived from the standard deviation of the line fits for BFs combined from three independent subsets of the echelle orders. The radial velocity for each epoch was then calculated as the error-weighted mean of the three consecutive measurements from each night. More detail on this process can be found in Tofflemire et al. (2019). From the two epochs spaced one to two days apart, we found no evidence for radial-velocity variability. The mean and standard error of the RV measurements are provided in Tables 2.2 and 2.3.

2.4 False Positive Vetting

Instrumental effects or statistical false positive

From the SPOC data validation reports, the *TESS* detections are significant with a S/N of 8.0 for TOI 122b and 9.8 for TOI 237b. These are both near the 7-σ detection significance cutoff (Jenkins, 2002), which means these planets were found near *TESS*' observational limits of discovery. However, given that we redetected transits of both planets from the ground, with consistent depths and timing, we are confident these detections are in fact robust.

Nearby transit or eclipsing binary

For both of these planets, we searched all nearby (< 2.5' radius) stars in the seeing-limited LCO data that were bright enough to have caused the detected transits if blended in the *TESS* photometry. We found no evidence of sources that were variable or eclipsing on the time scale of these planets' orbital periods. Both of these stars have high proper motions, and examination of archival images indicated that there are no bright stars at the targets' locations (see Fig. 2.7). In addition, we positively detected a transit in the aperture placed around the target star, so we believe these detections are not due to any physically-unbound nearby stars.

Contaminated apertures

The photometric apertures we used for the ground-based observations were typically <6" (see Table 2.1), so we can rule out contaminating sources outside that approximate radius from our target stars. In the *TESS* data, the PDCSAP light curves have already been corrected for contamination of nearby sources present in the TIC, and our higher-resolution ground-based observations

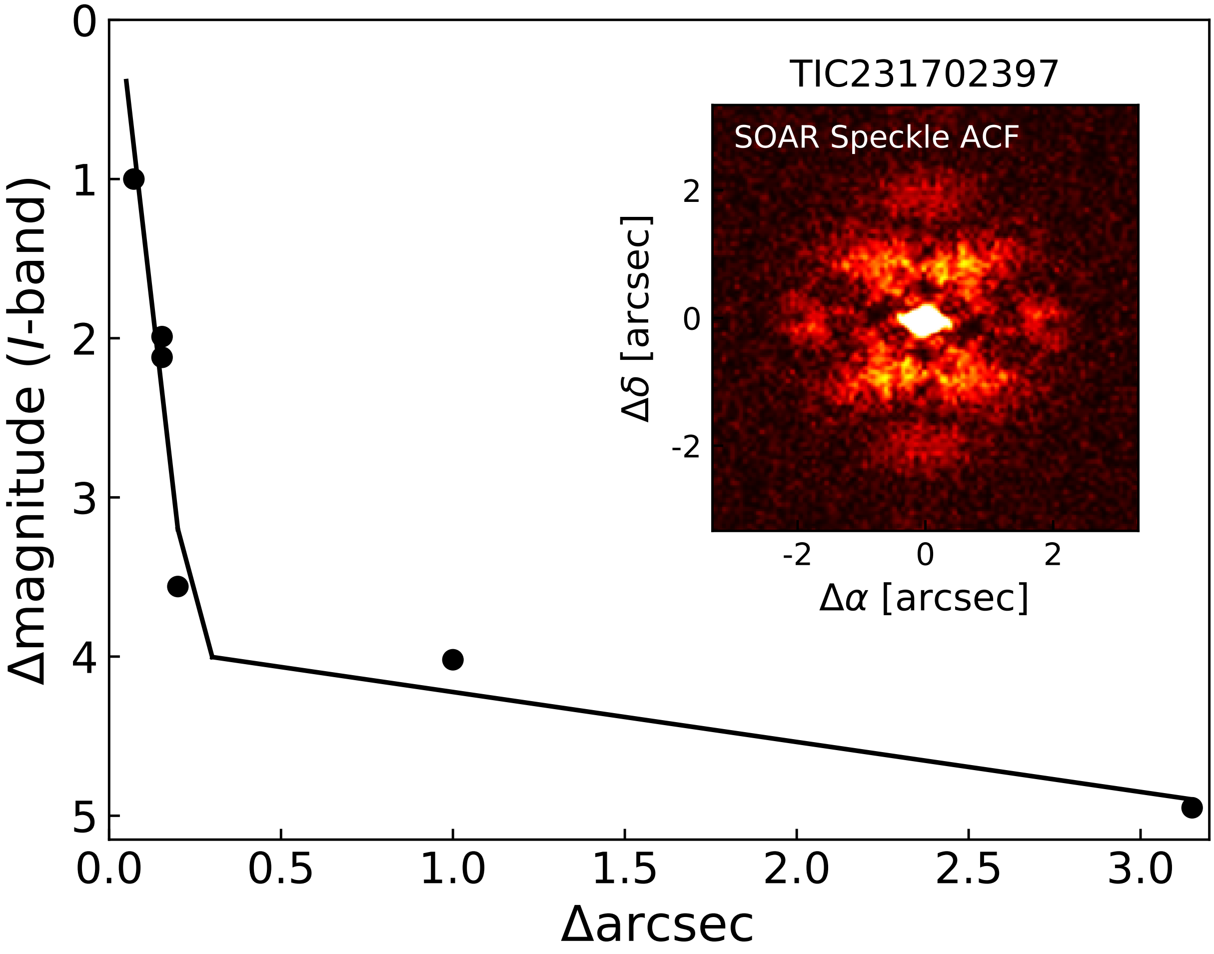

Figure 2.5: 5σ detection limits of SOAR Speckle imaging for TOI 122. The inset shows that no companions were detected down to a limit of 3".

show depths consistent with the *TESS* light curves. SALT spectra show both sources to be single-lined, indicating a lack of evidence for unresolved luminous companions (see Fig. 2.6). We also obtained SOAR speckle imaging of TOI 122 which indicated there was not a nearby companion down to a separation of 0.3" which could contaminate the aperture (see Fig. 2.5).

Non-planet transiting object

Based on the measured transit depths and inferred stellar parameters, we can constrain both planets to R_p <0.8 R_J, which makes them small enough to be in the planet regime (Burrows et al., 2011). We also estimate upper-limit masses from the SALT radial velocity data. Using the two RV

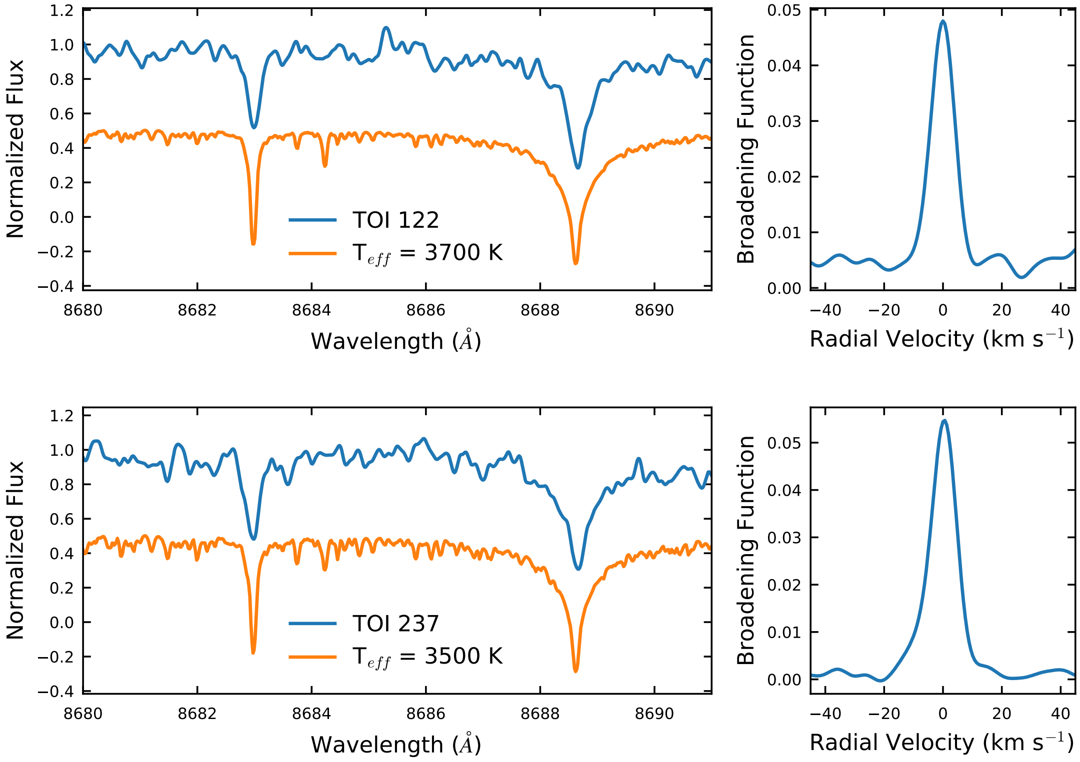

Figure 2.6: **Left:** Region of a SALT–HRS spectrum (**blue**) with the corresponding synthetic template (**orange**), where we have offset the flux slightly for clarity. **Right:** The broadening function computed from this spectral region. Inspection of the broadening function and individual spectral lines indicates each system is single-lined, and does not host a short-period stellar companion. Note that the model temperatures cited on the figure are higher than the values we report for these two stars; this is discussed in Section 2.5.2

.

data points for each system, we model a range of masses consistent with these values to estimate the upper limit planet masses. These models were done using a 100k step MCMC (20k step burn-in) with the baseline and planet mass as free parameters, the assumption of circular orbits, and the only constraining prior that the planet mass is non-negative. We find the upper limit (95th percentile) masses for both of these planets to be in the planetary regime: $\mathrm{M_p} \leq 6.7\ \mathrm{M_J}$ for TOI 122b and 2.1 $\mathrm{M_J}$ for TOI 237b (see Fig. 2.8). Lastly, we have transit data in multiple bands for both objects, with consistent depths. This achromaticity suggests that these are non-luminous objects such as planets (see Parviainen et al., 2019).

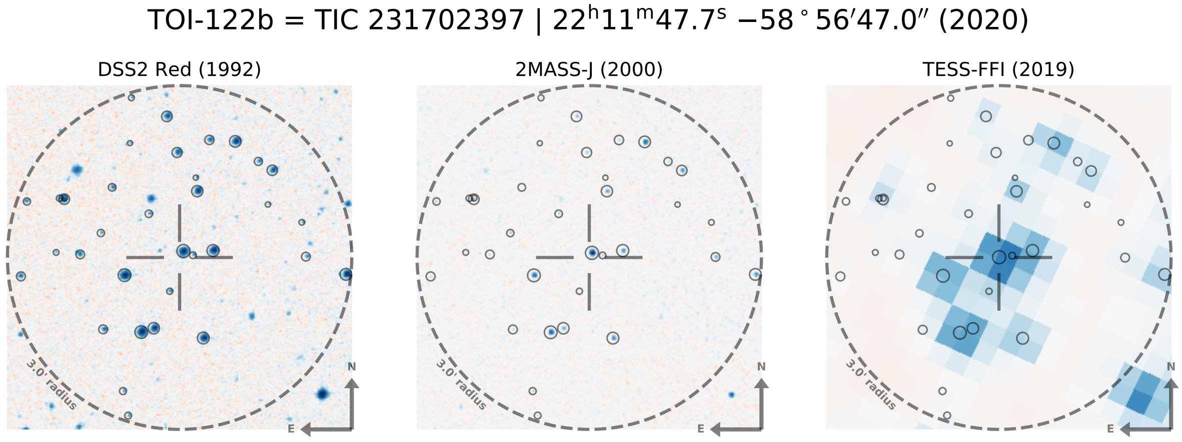

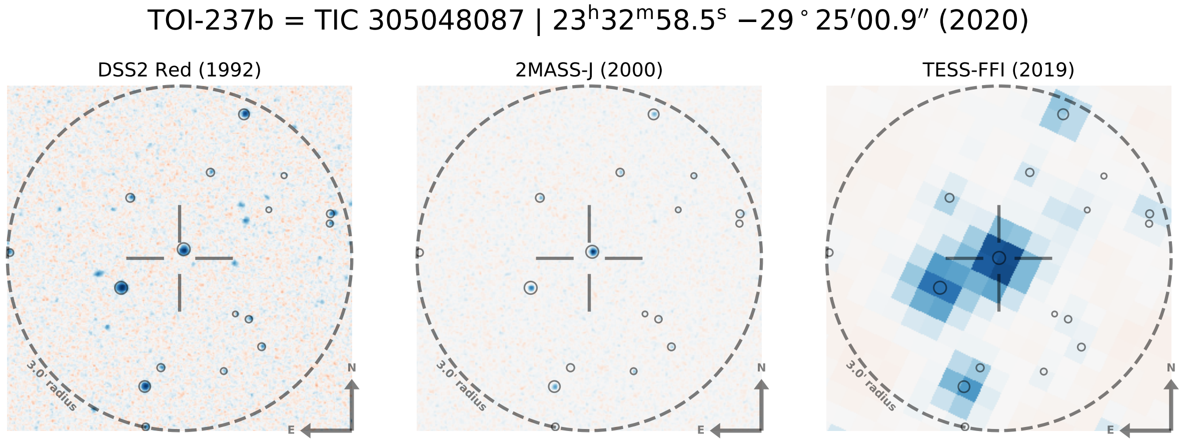

Figure 2.7: Finder charts for TOI 122 (**top**) and TOI 237 (**bottom**), including scanned red-sensitive photograph plates from the Digitized Sky Survey (**left**), 2MASS (**middle**), and the *TESS* full-frame images (**right**). Circles indicate stars from Gaia DR2, with areas logarithmically expressing apparent brightness. Crosshairs indicate targets' position in the year 2019, near the time of the *TESS* imaging.

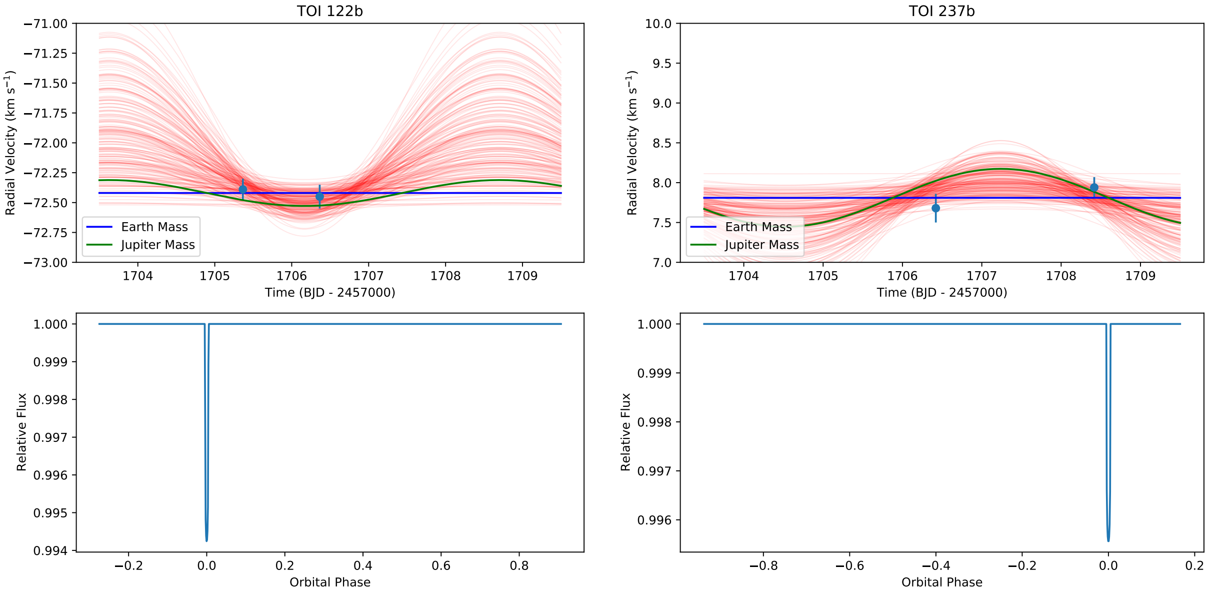

Figure 2.8: Reconnaissance radial velocity observations from SALT–HRS for both systems, including model orbits for different planet masses (**top**) plotted with the corresponding transit light curves (**bottom**). Theoretical RV curves for Earth (**blue**) and Jupiter (**green**) masses are shown, as well as 200 random samples from the posterior distributions (**red**). While we cannot obtain precise planetary masses from these spectra, we are able to rule out super-planetary mass companions by calculating the maximum mass consistent with these measurements. These upper-limit masses based on the 95^{th} percentile samples are 6.7 M_J for TOI 122b, and 2.1 M_J for TOI 237b.

2.5 Results

2.5.1 Light Curve Analysis

For both systems, we omitted 2 observations of TOI 122 and 1 observation of TOI 237 where the transit is completely obscured by the noise. This corresponds to a photometric RMS such that the transit signal-to-noise is ~ 1, which we argue is justified given the large number of observations which clearly show a transit (see Table 2.1). We also omitted observations that did not capture the mid-transit, to prevent the MCMC walkers from running away with obviously incorrect mid-transit times and semi-major axes. We modeled all ground-based light curves simultaneously by requiring the inclination, $a/R_\star$, and $R_p/R_\star$ to be the same value across all transits, but allowing T_0 to vary for transits at different epochs. T_0 is fixed between transits that occurred at the same epoch (where we have observations from multiple telescopes, for example). To fit the baseline flux alongside the light curve parameters, We implemented a linear 2-parameter airmass model of the form $(C_1 + C_2 a)B$ where a is the airmass at each exposure and B is the `BATMAN` light curve model. This added up to 24 modeled parameters for TOI 122b and 20 parameters for TOI 237b, the difference being due to a different number of observations for both systems. After analyzing the follow-up lightcurves and refining the orbital periods, we modeled the phase-folded *TESS* light curves to examine how well the systems' properties were improved. For a discussion on period refinement, see §2.5.5.

The models are created using `BATMAN` (Kreidberg, 2015), which is based on the analytic transit model from Mandel & Agol (2002). Stellar limb darkening coefficients were calculated for each separate bandpass with `LDTk`, the stellar Limb Darkening Toolkit (Parviainen & Aigrain, 2015), and these coefficients are listed in Table 2.4. Figures 2.2, 2.3, and 2.4 show all transit light curves with models.

We found posterior distributions through Bayesian analysis using `emcee` (Foreman-Mackey et al., 2013). We ran the MCMC with 150 walkers and 200k steps, discarding the first 40k steps (20%) and using uniform priors for all parameters. We chose the number of steps based on when each chain converged, using the integrated autocorrelation time heuristic built into `emcee`. With our 160k steps (post-burn-in), all chains reached >100 independent samples, suggesting adequate convergence (for a discussion of MCMC convergence, see Hogg & Foreman-Mackey, 2018). The priors are set so that the planet does not have a negative radius ($0 \leq \mathrm{R_p/R_\star} \leq 1$), the mid-transit time is within the range of the data, the eccentricity is 0, the semi-major axis is physically reasonable ($2 \leq \mathrm{a/R_\star} \leq 200$), and the inclination is geometrically limited to be i $\leq$ 90$oavoidduplicatesolutionsofi$¿90

The results cited in Tables 2.2 and 2.3 are the 50^{th} percentile values with 1-σ uncertainties based on the central 68% confidence intervals of the ground-based MCMC samples which have had the burn-in removed. In Figure 2.9, we show the posterior distributions from fitting only the folded *TESS* light curves as well as posterior distributions for only the follow-up transits, for both systems. Results from modeling the follow-up transits are consistent with the *TESS* fits, but the ground-based follow-up provides much tighter constraints due to the improved signal-to-noise we get with the larger-aperture LCO 1-m telescopes and from having additional independent transits.

2.5.2 Stellar Parameters

Mass and Radius: We first used the emprical relations in Mann et al. (2019) to calculate stellar masses from Gaia parallaxes and 2MASS K-band magnitudes. From Gaia DR2 (Gaia Collaboration et al., 2018), the distance to TOI 122 is 62.23±0.21 pc and the distance to TOI 237 is 38.11±0.23 pc. Using the Mann et al. (2019) relations, we get $M_\star = 0.312 \pm 0.007\ M_\odot$ for TOI 122 and $M_\star = 0.179 \pm 0.004\ M_\odot$ for TOI 237. Using the analogous Mann et al. (2015) absolute M_K relation for stellar radii, we found $R_\star = 0.334 \pm 0.010\ R_\odot$ and $0.211 \pm 0.006\ R_\odot$ for TOI 122 and 237, respectively. As a verification, we compared the stellar densities from the empirical masses and radii to the stellar densities calculated directly from the light curves:

$$\rho_\star = \frac{3\pi}{GP^2}\left(\frac{a}{R_\star}\right)^3, \tag{2.1}$$

where $\rho_\star$ is the stellar density, P is the orbital period of the planet, $a/R_\star$ is the normalized semi-major axis, and we have assumed circular orbits (Seager & Mallén-Ornelas, 2003b; Sozzetti et al., 2007). The densities derived from the light curves are $12.8^{+9.5}_{-4.2}$ g cm^{-3} for TOI 122 and $25.6^{+4.3}_{-8.7}$ g cm^{-3} for TOI 237, which agree well with the densities from our empirically derived masses and radii (11.8±2.0 g cm^{-3} and 27.0±4.0 g cm^{-3} for TOI 122 and 237, respectively). Similarly, we calculated the semi-major axes of these systems from the stellar mass predictions and measured periods, and convert them to $a/R_\star$ using the Mann et al. (2015) empirically predicted radii. These calculated semi-major axes give us $a/R_\star$ of 25.2±1.5 (compared to $25.9^{+5.3}_{-3.2}$ from the light curves) and 34.7±2.9 (compared to $34.2^{+1.9}_{-4.6}$ from the light curves) for TOI 122b and 237b.

Effective Temperature ($T_{\rm eff}$) and Luminosity: For both stars,we calculated $T_{\rm eff}$ using six of the different empirical color magnitude relations (equations 1-3 and 11-13 of Table 2) in Mann et al. (2015). Taking the weighted average of the six temperatures, we get $T_{\rm eff} = 3403 \pm 100$ K for TOI 122 and 3212±100 K for TOI 237. For both sets of calculations, the standard deviation of the six temperatures was ~ 55 K.

For stellar luminosities, we calculate the V-band bolometric correction based on the V-J empirical relation in Mann et al. (2015). This gives luminosities of 0.0140±0.0003 $L_\odot$ and 0.0041±0.0001 $L_\odot$ for TOI 122 and 237, respectively. We then compared these luminosities to the luminosities calculated from the Mann et al. (2015) radii and effective temperatures (described above):

$$\frac{L}{L_\odot} = \left(\frac{R}{R_\odot}\right)^2 \left(\frac{T_{\rm eff}}{T_\odot}\right)^4, \tag{2.2}$$

where we use $T_\odot$ = 5772 K (Prša et al., 2016). This resulted in L=0.013±0.003 $L_\odot$ for TOI 122 and L=0.0042±0.0007 $L_\odot$ for TOI 237, in good agreement with the bolometric-correction luminosities. Given the collective agreement between light curve densities, bolometric luminosities, and empirical estimates for radii, masses, and effective temperatures, we adopt the Mann et al. (2015, 2019)-derived stellar parameters and corresponding uncertainties for these two stars.

We chose to calculate our stellar parameters based on empirical models rather than adopting values from our spectral observations because of some inconsistencies in the spectra. The method we used to analyze RV signals from SALT spectra is optimized to detect precise RVs but not to accurately calculate stellar temperature. Therefore, the temperature that corresponds to the best fit RV model is not necessarily an accurate estimate of stellar temperature. This aspect of the modeling does not affect the *vsini* values presented in this paper. The FIRE spectra indicate TOI 122 is a significantly larger and hotter M dwarf, opposing other estimates of its size and temperature. We attribute this to the observing conditions and telluric contamination of the Magellan FIRE spectra, and we therefore do not use the effective temperatures and radii we derive from these spectra.

2.5.3 Assumption of Circular Orbits

All of the analysis was done under the assumption of circular orbits for these two systems. To justify this, we calculate the tidal circularization timescales following Goldreich & Soter (1966):

$$\tau_{circ} = \frac{2PQ'}{63\pi}\left(\frac{M_p}{M_\star}\right)\left(\frac{a}{R_p}\right)^5, \tag{2.3}$$

Parameter	Value	Source
TOI 122		
TIC ID	231702397	TICv8
RA (J2000)	22:11:47.300	TICv8
Dec (J2000)	-58:56:42.25	TICv8
TESS Magnitude	13.048 ± 0.007	TICv8
Apparent V Magnitude	15.526 ± 0.026	TICv8
Apparent J Magnitude	11.531 ± 0.024	TICv8
Apparent H Magnitude	11.020 ± 0.022	TICv8
Apparent K Magnitude	10.771 ± 0.021	TICv8
Gaia DR2 ID	6411096106487783296	Gaia DR2
Distance [pc]	62.23 ± 0.21	Gaia DR2
Proper Motion RA [mas yr^{-1}]	138.138 ± 0.089	Gaia DR2
Proper Motion DEC [mas yr^{-1}]	-235.81 ± 0.076	Gaia DR2
Gaia G mag	14.3357	Gaia DR2
Gaia RP mag	13.1523	Gaia DR2
Gaia BP mag	15.7971	Gaia DR2
Stellar Mass [$M_\odot$]	0.312 ± 0.007	†
Stellar Radius [$R_\odot$]	0.334 ± 0.010	†
$T_{\rm eff}$ [K]	3403 ± 100	†
Luminosity [$L_\odot$]	0.0140 ± 0.0003	†
Stellar log g	4.88 ± 0.05	This Work
Radial Velocity [km s^{-1}]	-72.4 ± 1.0	This Work
Stellar Density [g cm^{-3}]	$12.8^{+9.5}_{-4.2}$	This Work
v sin$i$ [km s^{-1}]	≤ 7.2	This Work
Hα Equivalent Width [Å]	0.09	This Work
TOI 122b		
Period [days]	5.078030 ± 0.000015	This Work
Transit Depth [%]	0.56	This Work
$R_p/R_\star$	0.075 ± 0.003	This Work
Planet Radius [R_E]	2.72 ± 0.18	This Work
Planet Mass [M_E]	$8.8^{+9.0}_{-3.1}$	‡
Planet Type	100% Neptunian	‡
$\frac{a}{R_\star}$	25.2 ± 1.5	This Work
Semi-major Axis [AU]	0.0392 ± 0.0007	This Work
i [degrees]	$88.4^{+0.6}_{-0.4}$	This Work
Impact Parameter (b)	$0.72^{+0.07}_{-0.18}$	This Work
Insolation [S_E]	8.8 ± 1.0	This Work
Equilibrium Temperature, $T_{\rm eq}$ [K]:		
Bond Albedo = 0.75 (Venus-like)	333	This Work
Bond Albedo = 0.3 (Earth-like)	431	
Bond Albedo = 0 (Upper Limit)	471	

Table 2.2: System parameters for TOI 122b. TICv8 information can be found in Stassun et al. (2019). †: derived from Mann et al. (2015), ‡: predicted from Chen & Kipping (2017).

Parameter	Value	Source
TOI 237		
TIC ID	305048087	TICv8
RA (J2000)	23:32:58.270	TICv8
Dec (J2000)	-29:24:54.19	TICv8
TESS Magnitude	13.410 ± 0.007	TICv8
Apparent V Magnitude	16.37 ± 0.20	TICv8
Apparent J Magnitude	11.74 ± 0.02	TICv8
Apparent H Magnitude	11.019 ± 0.022	TICv8
Apparent K Magnitude	10.896 ± 0.025	TICv8
Gaia DR2 ID	2329387852426700800	Gaia DR2
Distance [pc]	38.11±0.23	Gaia DR2
Proper Motion RA [mas yr^{-1}]	151.047±0.108	Gaia DR2
Proper Motion DEC [mas yr^{-1}]	-333.194±0.156	Gaia DR2
Gaia G mag	14.754	Gaia DR2
Gaia RP mag	13.5016	Gaia DR2
Gaia BP mag	16.4447	Gaia DR2
Stellar Mass [M$_\odot$]	0.179±0.004	†
Stellar Radius [R$_\odot$]	0.211±0.006	†
T$_{\mathrm{eff}}$ [K]	3212±100	†
Luminosity [L$_\odot$]	0.0041±0.0001	†
Stellar log g [cgs]	5.04 ± 0.07	This Work
Radial Velocity [km s^{-1}]	7.8±1.0	This Work
Stellar Density [g cm^{-3}]	$25.6^{+4.3}_{-8.7}$	This Work
v sin$i$ [km s^{-1}]	≤ 6.4	This Work
Hα Equivalent Width [Å]	1.74	This Work
TOI 237b		
Period [days]	5.436098±0.000039	This Work
Transit Depth [%]	0.38	This Work
R$_\mathrm{p}$/R$_\star$	0.062±0.002	This Work
Planet Radius [R$_\mathrm{E}$]	1.44±0.12	This Work
Planet Mass [M$_\mathrm{E}$]	$3.0^{+2.0}_{-1.1}$	‡
Planet Type	25% Terran, 75% Neptunian	‡
$\frac{a}{R_\star}$	34.7±2.9	This Work
Semi-major Axis [AU]	0.0341 ± 0.0010	This Work
i [degrees]	$89.5^{+0.4}_{-0.6}$	This Work
Impact Parameter (b)	$0.30^{+0.27}_{-0.21}$	This Work
Insolation [S$_\mathrm{E}$]	3.7±0.5	This Work
Equilibrium Temperature, T$_{\mathrm{eq}}$ [K]:		
Bond Albedo = 0.75 (Venus-like)	274	This Work
Bond Albedo = 0.3 (Earth-like)	355	
Bond Albedo = 0 (Upper Limit)	388	

Table 2.3: System parameters for TOI 237b. †: derived from Mann et al. (2015), ‡: predicted from Chen & Kipping (2017).

Filter	Value $[u_1, u_2]$	Uncertainty $[\sigma_1, \sigma_2]$
	TOI 122	
V	[0.5266, 0.2934]	[0.0151, 0.0240]
g’	[0.5161, 0.2998]	[0.0124, 0.0200]
r’	[0.5209, 0.2644]	[0.0149, 0.0234]
i’	[0.3050, 0.2898]	[0.0069, 0.0139]
I	[0.2558, 0.2566]	[0.0046, 0.0098]
I&z’	[0.2768, 0.2918]	[0.0067, 0.0140]
	TOI 237	
g’	[0.5720, 0.2925]	[0.0191, 0.0296]
I	[0.2657, 0.2911]	[0.0100, 0.0205]
I&z’	[0.2967, 0.3343]	[0.0138, 0.0260]

Table 2.4: Quadratic limb darkening parameters $[u_1, u_2]$ and associated uncertainties $[\sigma_1, \sigma_2]$, calculated using `LDTk` using the stellar parameters listed in Tables 2.2 and 2.3.

where P is the planet's orbital period and Q' quantifies how well the planet dissipates energy under deformation. Rocky planets tend to have lower Q' values while gaseous planets have larger Q' values. We adopt $Q' = 1 \times 10^4$ for TOI 122b and $Q' = 500$ for TOI 237b. These values are based on Q' values derived for the solar system planets, where Earth has Q' ~100 and Neptune has a $Q' \sim 6 \times 10^4$ (Goldreich & Soter, 1966). We do not have measurements of M_p for these planets, but our predicted masses based on the empirical relations in Chen & Kipping (2017) provide a precise enough estimate for this timescale. For TOI 122b and 237b, we calculate $\tau_{\rm circ}$ of 0.59 Gyr and 0.17 Gyr, respectively.

From the SALT spectra, we derived upper limits on $v\sin i$ to be <7.2 km s^{-1} for TOI 122 and <6.4 km s^{-1} for TOI 237, which allow us to derive lower limits on the rotational periods of both stars under the assumption that the stellar rotation axis is perpendicular to the line of sight. We find those lower limits to be $>$ 2.3 days for TOI 122 and $>$ 1.7 days for TOI 237. In addition, the lack of any significant flaring activity or rotational modulation seen in the *TESS* light curves for these two systems leads us to assume the stellar rotational periods are long, and probably greater than 27 days (the *TESS* observation window for a single sector). While the relation between rotation period and age for M dwarfs is poorly constrained, Newton et al. (2016b) found the rotation rates of field M dwarfs to be between 0.1 and 140 days, with M dwarfs younger than 2 Gyr having rotational periods less than 10 days. We also calculate the Hα equivalent widths (EW) from the SALT spectra, as Hα emission is indicative of the activity level of M dwarfs (see Newton et al., 2017). We find the EWs to be 0.09 Å for TOI 122 and 1.74 Å for TOI 237, placing both of these stars in the canonically inactive regime (EW>-1Å). Newton et al. (2017) provide a more direct way to estimate the rotational periods of inactive M dwarfs based on a polynomial fit with stellar mass. Given our derived masses for these two stars, we predict $P_{122} = 72 \pm 22$ d and $P_{237} = 102 \pm 22$ d from that relation. From the age-inactivity-spectral type relationship for cool stars described in West et al. (2008), we predict that TOI 122 (an M3V) is likely older than 2 Gyr, and TOI 237 (an M4.5V) (spectral types based on Rajpurohit et al., 2013) is likely older than 4.5 Gyr, consistent with our other estimates of their ages.

We can see a picture emerging that these stars are inactive, slowly rotating, and old, in spite of precise stellar ages being difficult to obtain for M dwarfs. Given that $\tau_{\rm circ}$ for both planets is < 1 Gyr, we assume both planets are on circular orbits. Our assumption that eccentricity is ~ 0 is also supported by the agreement between the stellar densities calculated from the light curves and densities based on empirical estimates of mass and radius (see Section 2.5.2).

2.5.4 Insolation and Equilibrium Temperature

In order to form a picture of the thermal environment of these planets, we calculate the insolation these planets receive, relative to the bolometric flux that Earth receives from the Sun. We also calculate equilibrium temperatures under different assumptions for the Bond albedo, $A_{\rm B}$, which is the fraction of incident stellar radiation that is reflected by the planet, integrated over both wavelength and angle.

Under the assumptions of circular orbits, efficient heat redistribution, and planets that are thermal emitters (for a discussion of these assumptions, see Cowan & Agol, 2011), we use the a/R$_\star$ values derived from our orbital periods and stellar masses to calculate planetary equilibrium temperature as:

$$T_{\rm eq} = (1 - A_{\rm B})^{\frac{1}{4}} \left(\frac{2a}{R_\star}\right)^{-\frac{1}{2}} T_{\rm eff}, \tag{2.4}$$

and insolation as:

$$\frac{S}{S_{\rm E}} = \left(\frac{T_{\rm eff}}{T_\odot}\right)^4 \left(\frac{a_{\rm E}/R_\odot}{a/R_\star}\right)^2, \tag{2.5}$$

where S is the bolometric insolation, a is the semi-major axis derived from the stellar masses and orbital periods, $R_\star$ is the inferred stellar radius, and $\rm a_E/R_\odot = 215$. We present $T_{\rm eq}$ (see Tables 2.2 and 2.3) as a range of values assuming an Earth-like $A_{\rm B} = 0.3$, a Venus-like $A_{\rm B} = 0.75$, and $A_{\rm B} = 0$.

2.5.5 Period Refinement and TTVs

For both systems, we fit a linear model to the *TESS* epoch and the follow-up epochs to refine the period, which we cite in Tables 2.2 and 2.3. In doing this, we are also able to examine the difference between the expected and observed mid-transit times to search for evidence of periodic TTVs. The reduced-χ^2 of a linear ephemeris (2.2 and 2.3 for TOI 122b and 237b, respectively) gave marginal hints of variations on the time scale of minutes, but a Lomb-Scargle periodogram (for a discussion of Lomb-Scargle periodograms, see VanderPlas, 2018) applied to the O-C (observed minus calculated) mid-transit times showed no significant periodicity for either system, so we report no significant TTV detection.

2.6 Discussion & Conclusions

These two planets help fill the parameter space for cool worlds near the boundary between rocky and gas-rich compositions. Neither is in the circumstellar habitable zone of its star as both receive more flux than the approximately 0.9 S_E moist greenhouse inner limit calculated by Kopparapu et al. (2013) for stars with these effective temperatures. However, with insolations of 8.8 ± 1.0 and 3.7 ± 0.5 S_E, they are relatively cool among known transiting exoplanets.

2.6.1 Radial Velocity Prospects

We do not have mass-constraining radial velocities for these two stars, so we applied the Chen & Kipping (2017) empirical mass-radius forecaster to predict $M_{122b} = 8.8^{+9.0}_{-3.1}$ M_E and $M_{237b} = 3.0^{+2.0}_{-1.1}$ M_E, based on the planets' radii. The degeneracy between planet radius and bulk composition leads to large uncertainties in these predicted masses. The forecaster results classify TOI 122b as 100% likely Neptunian and TOI 237b as 25% likely to be Terran and 75% likely to be Neptunian, where "Terran" is the term used by Chen & Kipping (2017) to describe worlds similar to the inner terrestrial solar system planets and "Neptunian" is used to describe worlds similar in their basic properties to Neptune and Uranus. The transition between these planet types was found by Chen & Kipping (2017) to be at 2.0 ± 0.7 M_E. We can compare the stellar magnitudes and predicted RV semi-amplitudes to the current and near-future capabilities of RV facilities. Using the periods, stellar masses, and predicted planet masses, we estimate RV semi-amplitudes of 7.1 m s^{-1} and 3.4 m s^{-1} for TOI 122b and 237b, respectively. These semi-amplitudes are above the instrumental noise floors for many RV spectrographs, although the faint magnitudes of these stars implies that mass-constraining RV measurements will be very time-intensive.

The CARMENES (Quirrenbach et al., 2010) instrument would require 460 s exposures to obtain 7.1 m s^{-1} precision for TOI 122 and 2250 s exposures to obtain 3.4 m s^{-1} precision for TOI 237b[6] . The latter is just beyond the 1800s maximum individual exposure time for this instrument, but the former implies the mass of TOI 122b could be within reach of a reasonably ambitious CARMENES observing program. Likewise, the Habitable Zone Planet Finder (HPF) spectrograph (Mahadevan et al., 2012, 2014) could possibly achieve precision as good as 10 m s^{-1} for TOI 122 and 5 m s^{-1} for TOI 237 with 15-minute exposures (see Fig. 2 of Mahadevan et al., 2012). With slightly longer exposure times, this instrument may be able to achieve mass-constraining precision for these two planets. The recent discovery of the G 9-40 system (Stefansson et al., 2020) used HPF to constrain planetary masses, achieving 6.49 m s^{-1} precision with exposure times of 945 s. This star has $\mathrm{K_s} = 9.2$, so scaled to the magnitudes of TOIs 122 and 237, we would need exposure times of ∼4 ks to achieve this precision for the systems presented here. Another instrument, the InfraRed Doppler (IRD) for the *Subaru* telescope (Kotani et al., 2014) also provides some hope. The sensitivity estimator[7] implies that for both of these stars, ∼2 m s^{-1} precision (S/N>100) may be possible with 1 hr exposures.

2.6.2 Atmospheric Characterization Prospects

In order to assess the viability of TOI 122b and TOI 237b for atmospheric studies, we calculated their emission spectroscopy metrics (ESM) following Kempton et al. (2018). This metric represents the S/N of a single secondary eclipse observed by JWST's MIRI LRS instrument. The emission S/N scales directly as the flux of the planet and the square root of the number of detected photons, and inversely to the flux of the star, so hot planets orbiting cool nearby stars will have a larger ESM.

---

[6] https://carmenes.caha.es/ext/instrument/index.html

[7] http://ird.mtk.nao.ac.jp/IRDpub/sensitivity/sensitivity.html

We calculate the ESM assuming that the planet dayside temperatures are equal to $1.1\times T_{eq}$ (following the process outlined in Kempton et al., 2018), and that both have an Earth-like albedo of 0.3. We find ESM to be 2.9 for TOI 122b and 0.6 for TOI 237b. Compared to GJ 1132b (ESM = 7.5) these planets are much less favorable for atmospheric follow-up with JWST. A minimum of 12 eclipses would be necessary to achieve a $S/N > 10$ for TOI 122b and a minimum of 278 eclipses would be needed for TOI 237b, as the S/N scales as $\sqrt{N_{obs}}$. Detecting thermal emission with JWST would be challenging for TOI 122b and impractical for TOI 237b.

We also calculate the transmission spectroscopy metric (TSM) from Kempton et al. (2018). This metric corresponds to the expected S/N of transmission features for a cloud-free atmosphere, over 10 hours of observation (5 hours in-transit). Our predicted TSMs are 54 for TOI 122b and 7 for TOI 237b, which imply these planets could both be amenable to transmission spectroscopy with JWST's NIRISS instrument, although planetary mass measurements would be necessary to make precise inferences from their transmission spectra (Batalha et al., 2019).

2.6.3 Volatile Evolution

These two planets span an interesting range of radii and insolations, making them exciting cases that may help us learn more about the diversity of atmospheres possessed by small planets orbiting M dwarfs. Figure 2.10 shows the Jeans escape parameter (e.g., Ingersoll, 2013, Box 2.2) for these systems as well as Solar System bodies and all confirmed exoplanets for which this parameter could be calculated. This ratio of gravitational-to-thermal energy is an extremely approximate tracer of atmospheric escape, but it can help us qualitatively understand the relative susceptibility of different planets to atmospheric loss. With only loose predictions for the masses of TOI 122b and TOI 237b, their position on this plot leaves us with an ambiguous picture of whether they have atmospheres and what their compositions could be. They may even represent the transition between worlds that have lost almost all of their H/He (such as Earth and Venus) and worlds that have retained those lighter elements (such as Neptune or Uranus). Though we cannot determine any strong constraints with this Jeans approximation alone, these two planets are not in a regime where they would have obviously lost their atmospheres, as Mercury and Mars have. A more detailed investigation into the current and past XUV irradiation, which is a main driver of atmospheric loss, would be necessary to more cleanly place these planets in context (Zahnle & Catling, 2017).

TOI 122b is a sub-Neptune-sized planet orbiting an M dwarf that is 33% the radius of our Sun. It likely has a thick atmosphere but on a 5.1 day orbit, it is far interior to the habitable zone of its star and irradiated at over 8× the flux of the Earth. It is dim enough to present a challenge for most existing radial velocity instruments, but mass measurements might be possible with a sufficient investment of time on IR spectrographs. Its atmosphere is on the edge of detectability in both emission and transmission with JWST. With a relatively low equilibrium temperature, there could be very interesting atmospheric chemistry in this planet's atmosphere that might be observable with sufficiently ambitious observing programs.

TOI 237b is a super-Earth-sized planet orbiting a M dwarf that is 21% the radius of our Sun and only 3200 K. With its 5.4 day orbit, it receives nearly 4× Earth insolation from its host star. Given the size of this planet and dimness of the star, mass measurements are likely very difficult to achieve, and we may not know its mass for some time. Even cooler than TOI 122b, this planet cannot be studied with emission spectroscopy, but transmission spectroscopy is possible and we may be able to learn about this planet's atmosphere, if it has retained one.

We are left with the following pictures of these systems: TOI 122b and TOI 237b are two worlds that span planetary radii not seen in our own solar system and are interesting laboratories to study planet formation, dynamics, and composition. Their long periods leave them too cool for emission spectroscopy but as a result, they occupy a very interesting space of relatively cool, though still uninhabitably warm, planets. Thus, they may give us insight to an as-yet poorly understood type of planetary atmosphere. While more targeted atmospheric or radial velocity studies would require a significant investment of time for these two systems, they are valuable additions to the statistical distribution of known planets.

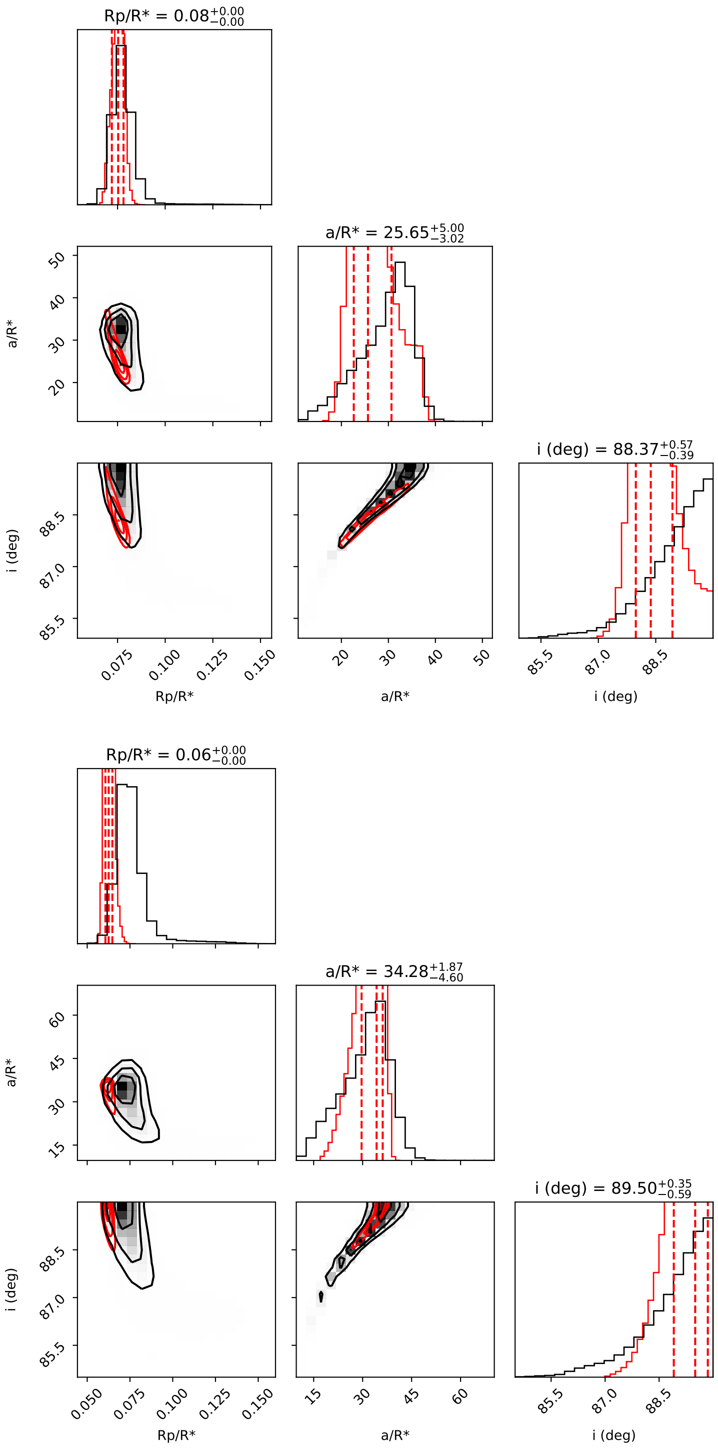

Figure 2.9: Corner plots (Foreman-Mackey, 2016) for the MCMC posteriors of all fits for TOI 122b (top) and TOI 237b (bottom). The posteriors from modeling only the phase-folded *TESS* light curves (**gray**) agree with those from modeling only the ground-based follow-up light curves (**black**), with the constraints from ground-based telescopes being more precise due to their larger apertures. Labels on top of the posteriors are from the ground-based results.

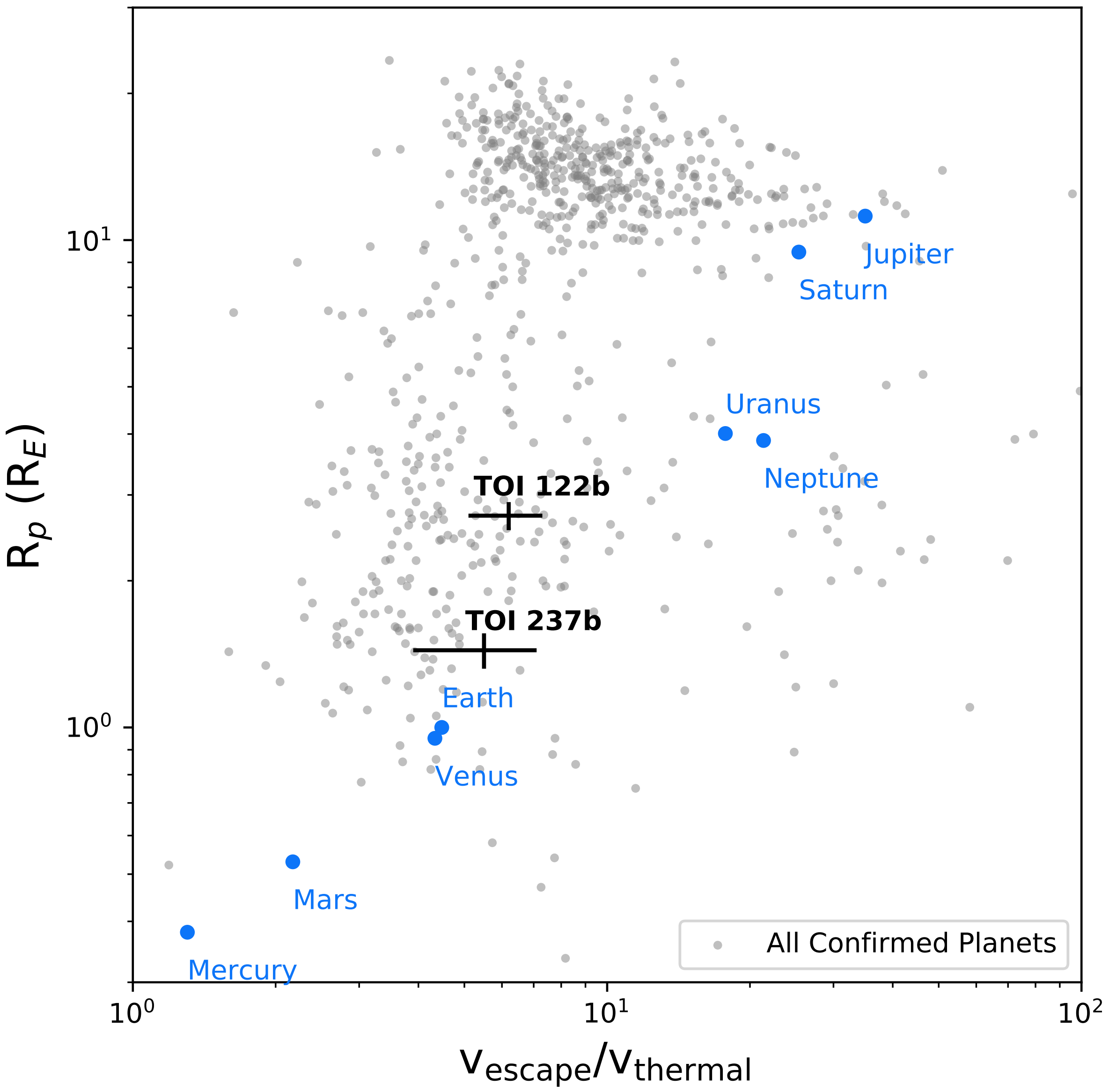

Figure 2.10: The ratio of planetary escape velocity to the thermal energy of an H atom at the planetary equilibrium temperature (the "escape parameter"; Jeans, 1905), for known transiting and Solar System planets. TOI 122b and TOI 237b are included, using predicted masses from Chen & Kipping (2017) to calculate their gravity. This extremely rough proxy for susceptibility to atmospheric escape indicates these planets may be broadly similar to Earth and Venus, in terms of ongoing mass loss from their atmospheres. This qualitative comparison does not account for the important XUV radiation illuminating the planets, either now or in the past. We estimate the uncertainties for TOI 122b and 237b by propagating our uncertainties from the planet parameters, which are dominated by large uncertainties on predicted masses.

Chapter 3

Lyman-alpha in the GJ 1132 System: Stellar Emission and Planetary Atmospheric Evolution

This chapter has been published in the Astronomical Journal as: W. C. Waalkes, Z. K. Berta-Thompson, V. Bourrier, E. Newton, D. Ehrenreich, E. M.-R. Kempton, D. Charbonneau, J. Irwin, J. Dittmann,*Lyman-α in the GJ 1132 System: Stellar Emission and Planetary Atmospheric Evolution*, The Astronomical Journal, 2019, 158, 50.

Specific contributions include: W. C. Waalkes led the data analysis and model fitting, Z. K. Berta-Thompson PI'd the HST observing proposal, and V. Bourrier provided detailed analysis of the escaping exosphere (Figures 3.8 and 3.9).

3.1 Preface

GJ 1132b, which orbits an M dwarf, is one of the few known Earth-sized planets, and at 12 pc away it is one of the closest known transiting planets. Receiving roughly 19x Earth's insolation, this planet is too hot to be habitable but can inform us about the volatile content of rocky planet atmospheres around cool stars. Using Hubble STIS spectra, we search for a transit in the Lyman-α line of neutral hydrogen (Lyα). If we were to observe a deep Lyα absorption signature, that would indicate the presence of a neutral hydrogen envelope flowing from GJ 1132b. On the other hand, ruling out deep absorption from neutral hydrogen may indicate that this planet does not have a detectable amount of hydrogen loss, is not losing hydrogen, or lost hydrogen and other volatiles early in the star's life. We do not detect a transit and determine a 2-σ upper limit on the effective envelope radius of 0.36 R_* in the red wing of the Lyα line, which is the only portion of the spectrum we detect after absorption by the ISM. We analyze the Lyα spectrum and stellar variability of GJ1132, which is a slowly-rotating 0.18 solar mass M dwarf with previously uncharacterized UV activity. Our data show stellar variabilities of 5-22%, which is consistent with the M dwarf UV variabilities of up to 41% found by Loyd & France (2014). Understanding the role that UV variability plays in planetary atmospheres is crucial to assess atmospheric evolution and the habitability of cooler rocky exoplanets.

3.2 Introduction

The recent discoveries of terrestrial planets orbiting nearby M dwarfs (Gillon et al., 2017; Berta-Thompson et al., 2015; Dittmann et al., 2017; Bonfils et al., 2018; Ment et al., 2019) provide us with the first opportunity to study small terrestrial planets outside our solar system, and observatories such as the Hubble Space Telescope allow us to analyze the atmospheres of these rocky exoplanets. Additionally, it is important that we learn as much as we can about these planets as we prepare for atmospheric characterization with the James Webb Space Telescope (Deming et al., 2009; Morley et al., 2017). JWST will provide unique characterization advantages due to its collecting area, spectral range, and array of instruments that allow for both transmission and emission spectroscopy (Beichman et al., 2014).

M dwarfs have been preferred targets for studying Earth-like planets due to their size and temperature which allow for easier detection and characterization of terrestrial exoplanets. However, the variability and high UV-to-bolometric flux ratio of these stars makes habitability a point of contention (e.g., Shields et al., 2016; Tilley et al., 2017). It is currently unknown whether rocky planets around M dwarfs can retain atmospheres and liquid surface water or if UV irradiation and frequent flaring render these planets uninhabitable (e.g., Scalo et al., 2007; Hawley et al., 2014; Luger & Barnes, 2015; Bourrier et al., 2017a). On the contrary, UV irradiation may boost the photochemical synthesis of the building blocks of life (e.g., Rimmer et al., 2018). We must study the UV irradiation environments of these planets, especially given that individual M stars with the

Parameter	Value	Source
GJ 1132		
Mass [$M_\odot$]	0.181 ± 0.019	Berta-Thompson et al. (2015)
Radius [$R_\odot$]	$0.2105^{+0.0102}_{-0.0085}$	Dittmann et al. (2017)
Distance [pc]	12.04 ± 0.24	Berta-Thompson et al. (2015)
Radial Velocity [km s^{-1}]	35.1 ± 0.8	Bonfils et al. (2018)
GJ 1132b		
Mass [M_E]	1.66 ± 0.23	Bonfils et al. (2018)
Radius [R_E]	1.13 ± 0.02	Dittmann et al. (2017)
Semi-major Axis, a [AU]	0.0153 ± 0.0005	Bonfils et al. (2018)
Period [days]	1.628931 ± 0.000027	Bonfils et al. (2018)
Epoch [BJD TDB]	$2457184.55786 \pm 0.00032$	Berta-Thompson et al. (2015)
$\frac{a}{R_*}$	$16.54^{+0.63}_{-0.71}$	Dittmann et al. (2017)
i (degrees)	$88.68^{+0.40}_{-0.33}$	Dittmann et al. (2017)
Surface Gravity [m s^{-2}]	12.9 ± 2.2	Bonfils et al. (2018)
Equilibrium Temperature, T_{eq} [K]:		
Bond Albedo = 0.3 (Earth-like)	529 ± 9	Bonfils et al. (2018)
Bond Albedo = 0.75 (Venus-like)	409 ± 7	Bonfils et al. (2018)

Table 3.1: GJ 1132 system parameters.

same spectral type can exhibit very different UV properties (e.g., Youngblood et al., 2017), and a lifetime of UV flux from the host star can have profound impacts on the composition and evolution of their planetary atmospheres.

One aspect of terrestrial planet habitability is volatile retention, including that of water in the planet's atmosphere. One possible pathway of evolution for water on M dwarf terrestrial worlds is the evaporation of surface water and subsequent photolytic destruction of H_2O into H and O species (e.g., Bourrier et al., 2017a; Jura, 2004). The atmosphere then loses the neutral hydrogen while the oxygen is combined into O_2/O_3 and/or resorbed into surface sinks (e.g., Wordsworth & Pierrehumbert, 2013; Tian & Ida, 2015; Luger & Barnes, 2015; Shields et al., 2016; Ingersoll, 1969). In this way, large amounts of neutral H can be generated and subsequently lost from planetary atmospheres. Studies have shown O_2 and O_3 alone to be unreliable biosignatures for M dwarf planets because they possess abiotic formation mechanisms (Tian et al., 2014), though they are still important indicators when used with other biomarkers (see Meadows et al., 2018). Understanding atmospheric photochemistry for terrestrial worlds orbiting M dwarfs is critical to our search for life.

3.2.1 Prior Work

Kulow et al. (2014) and Ehrenreich et al. (2015) discovered that Gliese 436b, a warm Neptune orbiting an M dwarf, has a 56.3±3.5% transit depth in the blue-shifted wing of the stellar Lyα line. Lavie et al. (2017) further studied this system to solidify the previous results and verify the predictions made for the structure of the outflowing gas made by Bourrier et al. (2016). For planets of this size and insolation, atmospheric escape can happen as a result of the warming of the upper layers of the atmosphere, which expand and will evaporate if particles begin reaching escape velocity (e.g., Vidal-Madjar et al., 2003; Lammer et al., 2003; Murray-Clay et al., 2009).

Miguel et al. (2015) find that the source of this outflowing hydrogen is from the H_2-dominated atmosphere of Gl 436b, with reactions fueled by OH^-. Lyα photons from the M dwarf host star dissociate atmospheric H_2O into OH and H, which destroy H_2. HI at high altitudes where escape is occurring is formed primarily through dissociation of H_2 with contributions from the photolyzed H_2O.

Modeling of Gl 436b (Bourrier et al., 2015, 2016) demonstrates that the combination of low radiation pressure, low photo-ionization, and charge-exchange with the stellar wind can determine the structure of the outflowing hydrogen, which manifests as a difference in whether the light curve shows a transit in the blue-shifted region of Lyα or the red-shifted region and imprints a specific spectro-temporal signature to the blue-shifted absorption. Lavie et al. (2017) used new observations to confirm the Bourrier et al. (2016) predictive simulations that this exosphere is shaped by charge-exchange and radiative braking.

As giant hydrogen clouds have thus been detected around warm Neptunes (see also the case of GJ 3470b; Bourrier et al., 2018b), it opens the possibility for the atmospheric characterization of smaller, terrestrial planets. Miguel et al. (2015) also find that photolysis of H_2O also increases CO_2 concentrations. For Earth-like planets orbiting M dwarfs, understanding the photochemical interaction of Lyα photons with water is very important for the evolution and habitability of a planet's atmosphere.

3.2.2 GJ 1132b

GJ 1132b is a small terrestrial planet discovered through the MEarth project (Berta-Thompson et al., 2015). It orbits a 0.181 $M_\odot$ M dwarf located 12 parsecs away with an orbital period of 1.6 days (Dittmann et al., 2017). Table 3.1 summarizes its basic properties. This is one of the nearest known transiting rocky exoplanets and therefore provides us with a unique opportunity to study terrestrial atmospheric evolution and composition.

While GJ 1132b is too hot to have liquid surface water, it is important to establish whether

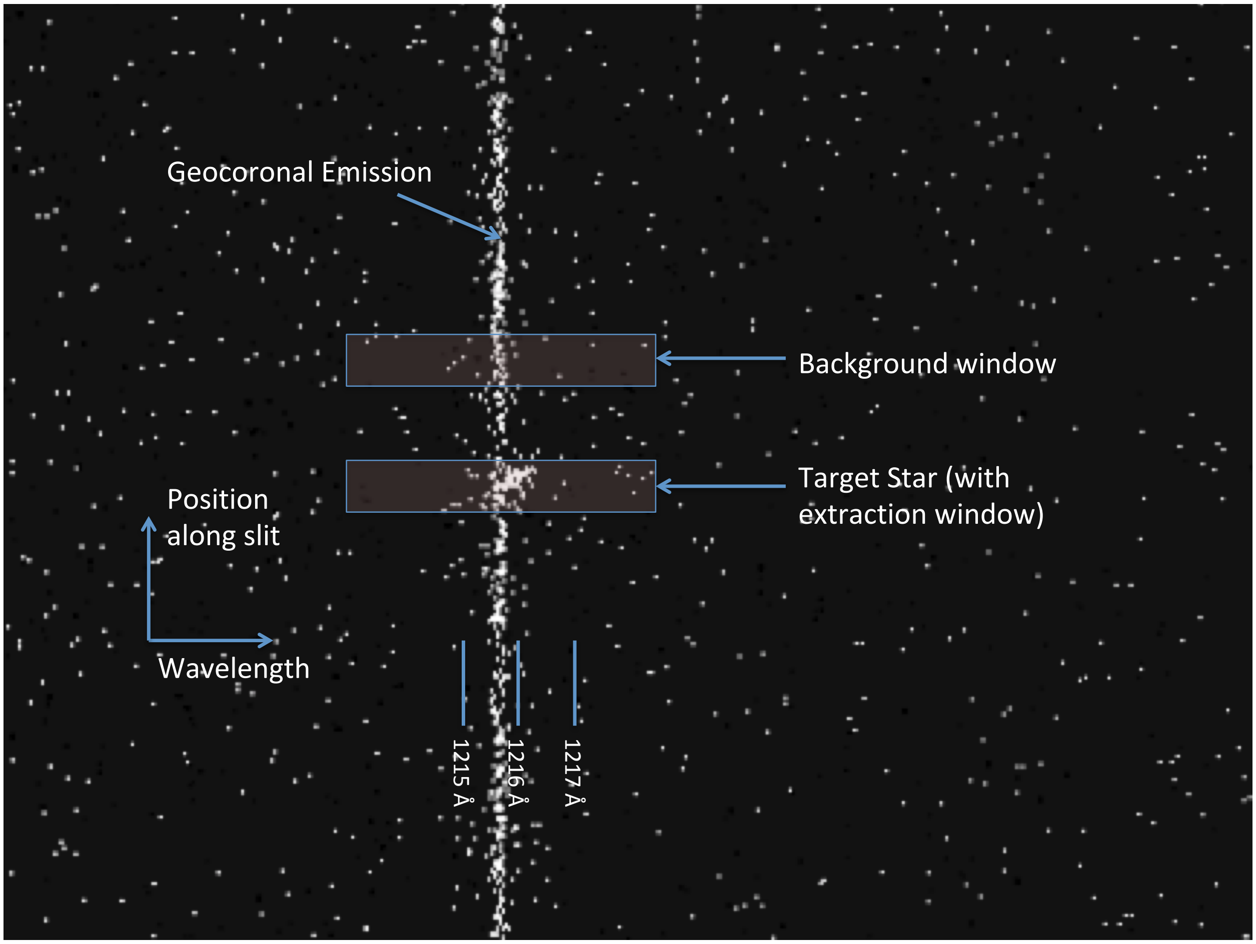

Figure 3.1: Image of a STIS x2d spectrum. Geocoronal Lyα is shown as a long vertical line while the GJ 1132 Lyα emission is shown in the center.

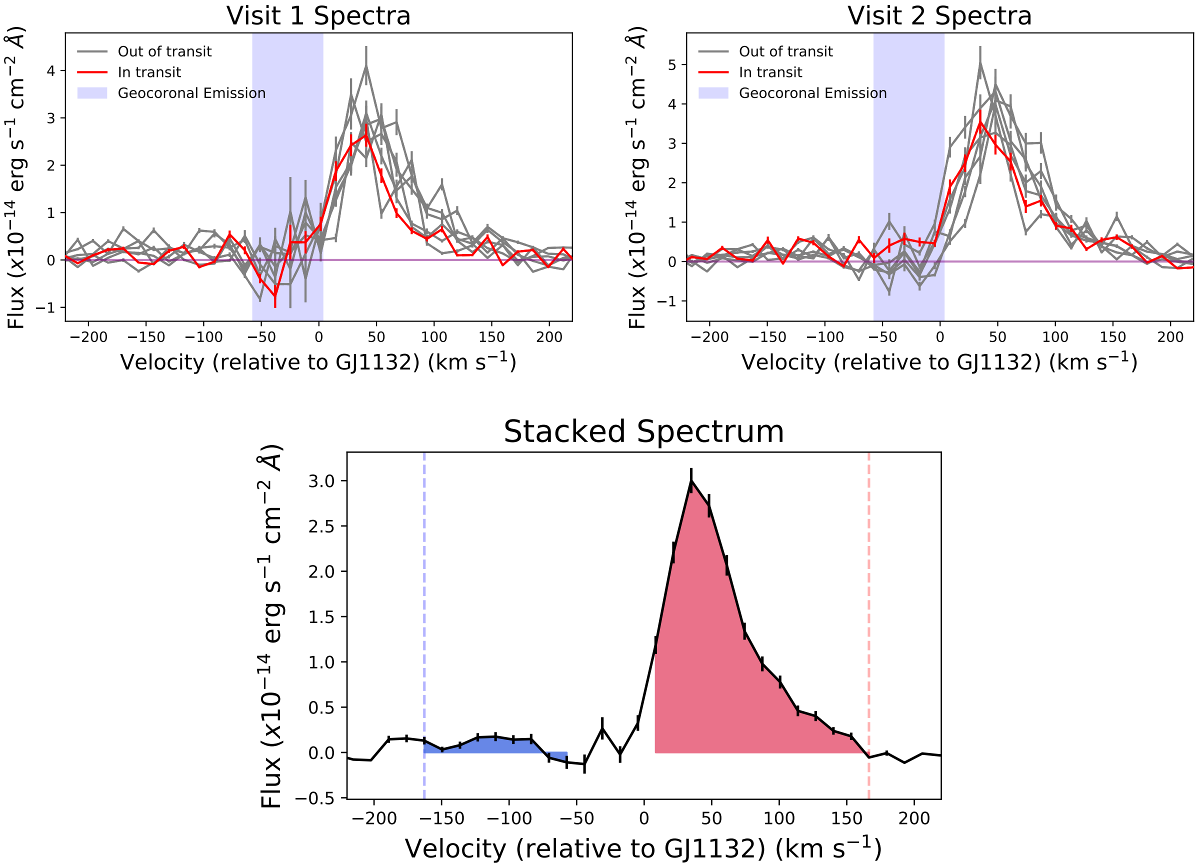

Figure 3.2: All 14 STIS Lyα spectra in visits 1 (a) and 2 (b) and the averaged stacked spectrum (c). The shape of the stellar Lyα line is a Voigt profile which has been reshaped by convolution with the STIS line spread function and ISM absorption by neutral atomic hydrogen and deuterium. The integration regions for summing up the total Lyα flux are the shaded blue and red areas in (b), with a region in the middle that we omit due to the geocoronal emission. It is apparent that the blue-shifted region of the spectrum is at the noise level, and therefore unlikely to give us any viable information. We set the reference velocity for the spectral profiles at 35 km s^{-1}, as this is the cited system velocity (Berta-Thompson et al., 2015).

this planet and others like it retain substantial atmospheres under the intense UV irradiation of their M dwarf host stars. Knowing whether warm super-Earths such as GJ 1132b regularly retain volatiles such as water in their atmospheres constrains parameter space for our understanding of atmospheric survivability and habitability.

Diamond-Lowe et al. (2018) rule out a low mean-molecular weight atmosphere for this planet by analyzing ground-based transmission spectra at 700-1040 nm. By fitting transmission models for atmospheric pressures of 1-1000 mbar and varying atmospheric composition, they find that all low mean-molecular weight atmospheres are a poor fit to the data, which is better described as a flat transmission spectrum that could be due to a >10x solar metallicity or >10% water abundance. Whether these results imply GJ 1132b has a high mean molecular weight atmosphere or no atmosphere at all remains to be seen. If we detect a Lyα transit then this implies UV photolysis of H_2O into neutral H and O, leading to outflowing neutral H. The oxygen could recombine into O_2 and O_3, resulting in a high mean-molecular weight atmosphere, and wholesale oxidation of the surface.

This work serves as the first characterization of whether there is a neutral hydrogen envelope outflowing from GJ 1132b as well as an opportunity to characterize the deepest (longest integration) Lyα spectrum of any quiet M dwarf of this mass.

3.2.3 Solar System Analogs

The atmospheric evolution and photochemistry we evaluate here is similar to what we have seen in Mars and Venus. Much of Mars' volatile history has been studied in the context of Lyα observations of a neutral H corona that surrounds present-day Mars. Chaffin et al. (2015) use Lyα observations to constrain Martian neutral H loss coronal structure, similar to what we attempt in this work. Indeed, Mars has historically lost H_2O via photochemical destruction and escape of neutral H (Nair et al., 1994; Zahnle et al., 2008), though the solar wind-driven escape mechanisms for Mars are not necessarily the same as what we propose for GJ 1132b in this work.

Venus has long been the example for what happens when a terrestrial planet is irradiated beyond the point of habitability, as is more than likely the case with GJ 1132b. Venus experienced a runaway greenhouse effect which caused volatile loss and destruction of H_2O. Kasting & Pollack (1983) study the effects of solar UV radiation on an early Venus atmosphere. They find that within a billion years, Venus could have lost most of a terrestrial ocean of water through hydrodynamic escape of neutral H, after photochemical destruction of H_2O. GJ 1132b has a higher surface gravity

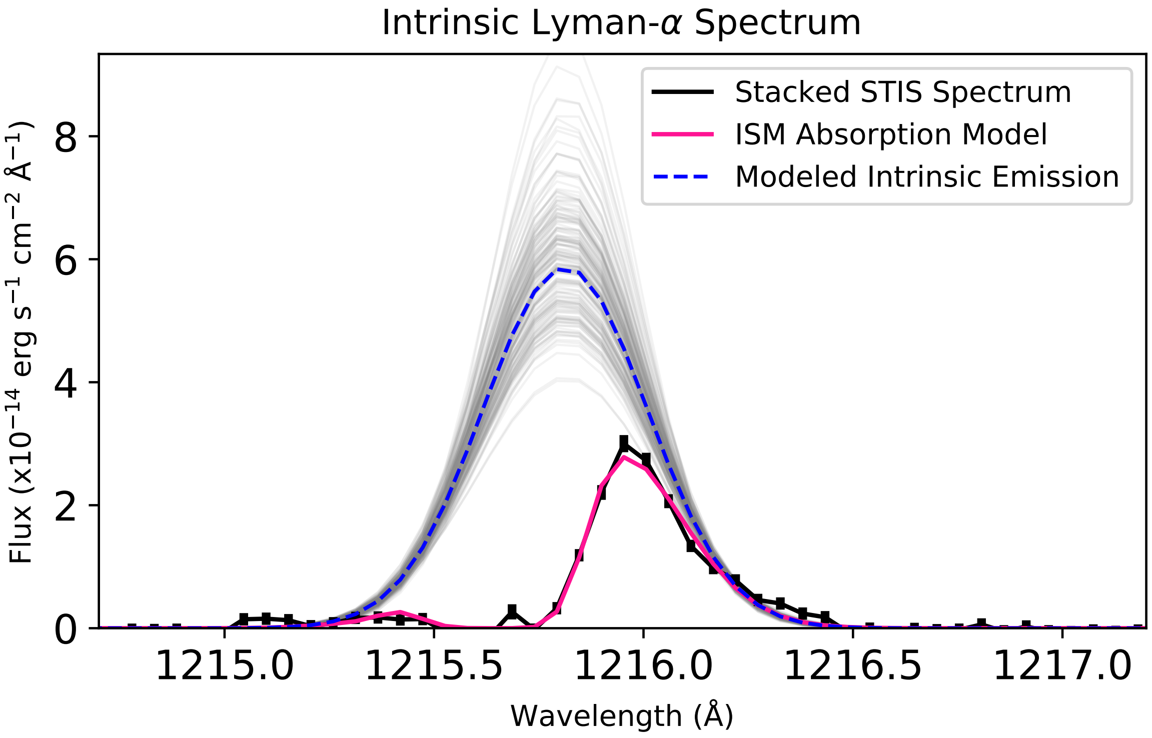

Figure 3.3: Intrinsic Lyα profile for GJ 1132b, with 200 random MCMC samples in gray. The absorption and intrinsic emission models were modeled with the `Lyapy` software which assumes a Voigt profile for the emission and parameterizes the ISM absorption into velocity, line width, and column density. Here, the line center is in the system's rest frame.

than Venus, which would extend this time scale of hydrogen loss, but it also has a much higher insolation which would reduce the hydrogen loss timescale. Later in this work, we will estimate the expected maximum mass loss rate for GJ 1132b based on the stellar Lyα profile.

The rest of the paper will be as follows. In §2 we describe the methods of analyzing the STIS data, reconstructing the stellar spectrum, and analyzing the light curves. In §3 we describe the transit fit and intrinsic spectrum results. We discuss the results and their implications in §4, including estimates of the mass loss rate from this planet's atmosphere. In §5 we describe what pictures of GJ 1132b's atmosphere we are left with.

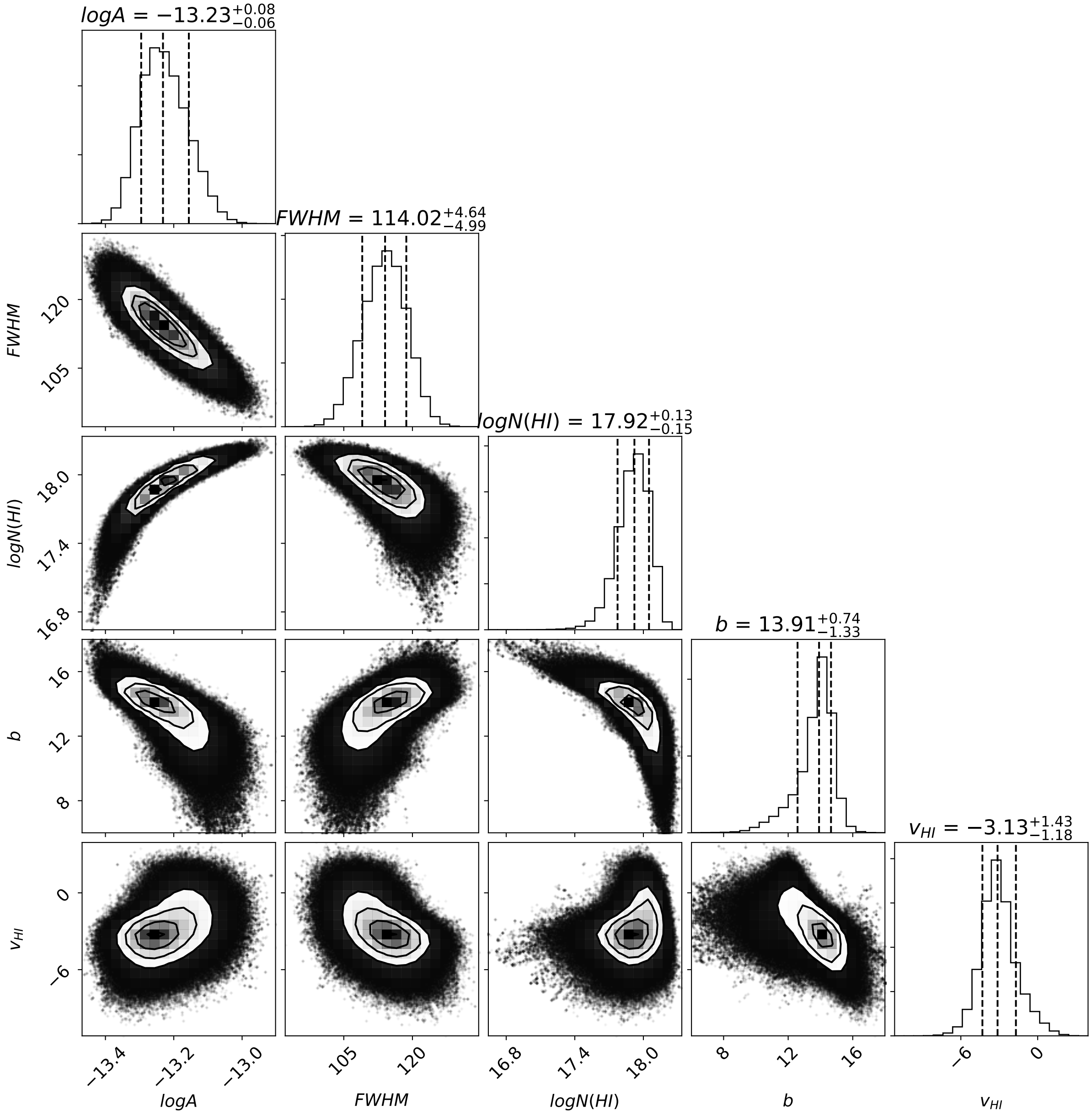

Figure 3.4: Corner plot showing the samples used in recreating the intrinsic emission profile. We omitted the stellar radial velocity samples because the prior was well constrained by independent radial velocity measurements. In this plot, log(A) is the log of the emission amplitude (which has units of erg s^{-1} cm^{-2} $Å^{-1}$), FWHM is the emission Full Width Half Maximum in km s^{-1}, logN(HI) is the log of the column density of neutral ISM hydrogen (which has units of cm^{-2}), b is the ISM Doppler parameter in km s^{-1}, and v_{HI} is the ISM cloud velocity in km s^{-1}.

3.3 Methods

3.3.1 Hubble STIS Observations

To study the potential existence of a neutral hydrogen envelope around this planet, we scheduled 2 transit observations of 7 orbits each (2 observations several hours from mid-transit for an out of transit measurement and 5 observations spanning the transit) with the Space Telescope Imaging Spectrograph (STIS) on the Hubble Space Telescope (HST)[1] . We used the G140M grating with the 52"x0.05" slit, collecting data in TIME-TAG mode with the FUV-MAMA photon-counting detector. This resulted in 14 spectra containing the Lyα emission line (1216 Å), which show a broad profile that has been centrally absorbed by neutral ISM atomic hydrogen.

We re-extracted the spectra and corrected for geocoronal emission using the `calstis` pipeline (Hodge & Baum, 1995). The STIS spectrum extraction involved background subtraction which accounts for geocoronal emission (see Fig. 3.1), leaving us only with the need to model the stellar emission and ISM absorption. We omit data points from both visits that fall within the geocoronal emission signal, wavelengths from both visits that overlapped with strong geocoronal emission and therefore had high photon noise. We thus define our blue-shifted region to be <-60 km s^{-1} and our red-shifted region to be >10 km s^{-1} relative to the star. One potential source of variability is where the target star falls on the slit. If it fell directly on the slit, then the observed flux will be more than if the star was partially off the slit. To account for this, we scheduled ACQ/PEAK observations at the start of each HST orbit to center the star on the slit and minimize this variability.

In order to analyze the light curves with higher temporal resolution, we used the STIS time-tag mode to split each of the 14 2 ks exposures into 4 separate 0.5 ks sub-exposures. This detector records the arrival time of every single photon, which is what allows us to create sub-exposures in time-tag mode. Each 2D spectrum sub-exposure was then converted into a 1D spectrum. To do this, we first defined an extraction window around the target spectrum (see Fig. 3.1) and summed up all the flux in that window along the spatial axis. Extraction windows were also defined on

---

[1] Cycle 24 GO proposal 14757, PI: Z Berta-Thompson

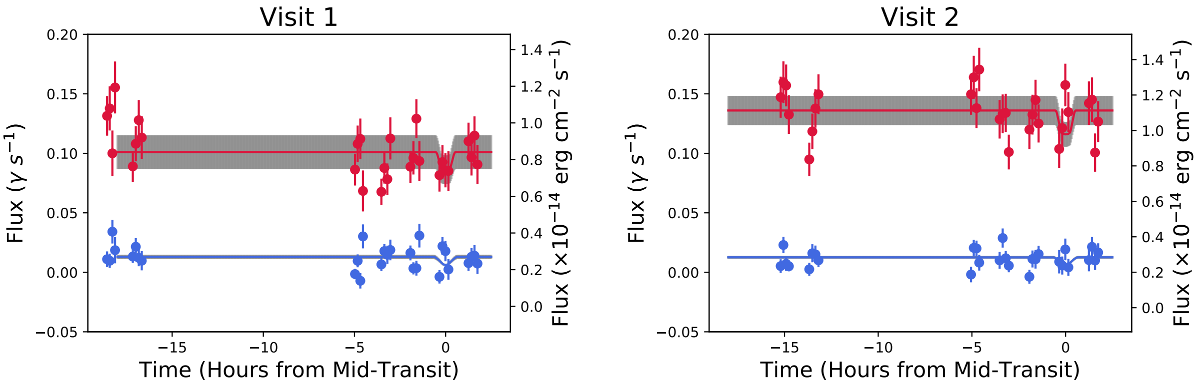

Figure 3.5: Modeled light curves from both visits. In addition to the calibrated flux values, we display the flux in photons s^{-1} because the SNR is very low at Lyα and this motivated us to use a Poisson likelihood in our analysis of the light curves. Some data points fall to negative values, which can happen when the data point has effectively no flux and then data reduction processes (such as background subtraction) subtract a slightly higher amount of flux. The gray bars indicate what we calculate as a 15% "stellar variability" fudge factor - acquired by calculating what size of error bars would be necessary to result in a χ^2 value of 1 for our best fit models. The blue wing light curves don't provide much information due to their extremely low flux but we can see from the red wing fits that there is an upper limit on the transit depth.

either side of the target in order to estimate the background and subtract that from the target window. This results in a noisy line core but eliminates the geocoronal emission signature (Fig. 3.2a & 3.2b). These steps were all performed with `calstis`.

3.3.2 Stellar Spectrum Reconstruction

With the same spectra used for light curve analysis, we created a single weighted average spectrum, representing 29.3 ks (8.1 hrs) of integration at Lyα across 14 exposures (Fig. 3.2c). This stacked spectrum was used with `LyaPy` modeling program (Youngblood et al., 2016) that uses a 9-dimensional MCMC to reconstruct the intrinsic stellar spectrum assuming a Voigt profile. Modeling observed Lyα spectra is tricky because of the neutral ISM hydrogen found between us and GJ 1132. This ISM hydrogen has its own column density, velocity, and line width which creates a characteristic absorption profile within our Lyα emission line.

This model takes 3 ISM absorption parameters (column density, cloud velocity, Doppler parameter) and models the line core absorption while simultaneously modeling the intrinsic emission which would give us the resulting observations. Turbulent velocity of the ISM is assumed to be negligible, with the line width dominated by thermal broadening. A fixed deuterium-to-hydrogen ratio of 1.56×10^{-5} (Wood et al., 2004) is also applied to account for the deuterium absorption and emission near Lyα. Modeling the ISM parameters required us to approximate the local interstellar medium as a single cloud with uniform velocity, column density, and Doppler parameter. While the local ISM is more complex than this single component and contains two clouds (G, Cet) in the line of sight toward GJ 1132 (based on the model described in Redfield & Linsky, 2000), our MCMC results strongly favored the velocity of the G cloud, so we defined the ISM priors based on this cloud (Redfield & Linsky, 2000, 2008).

We use uniform priors for the emission amplitude and FWHM, and Gaussian priors for the HI column density, stellar velocity, HI Doppler width, and HI ISM velocity. The HI column density and Doppler width parameter spaces were both truncated in order to prevent the model from exploring physically unrealistic values. For N_{HI}, we restrict the parameter space to 10^{16}-10^{20} cm^{-2}, based on the stellar distance (12.04 pc) and typical n_{HI} values of $0.01 - 0.1$ cm^{-3} (Redfield & Linsky, 2000; Wood et al., 2005). We limit the Doppler width to 6-18 km s^{-1}, based on estimates of the Local Interstellar Cloud (LIC) ISM temperatures (Redfield & Linsky, 2000).

3.3.3 Light Curve Analysis

The extracted 1D spectra were then split into a blue-shifted regime and red-shifted regime, on either side of the Lyα core (Fig. 3.2c) so that we could integrate the total blue-shifted and red-shifted flux and create 4 total light curves from the 2 visits (Fig. 3.5). Each of these light curves was fitted with a `BATMAN` (Kreidberg, 2015) light curve using a 2-parameter MCMC with the `emcee` package (Foreman-Mackey et al., 2013). The `BATMAN` models assume that the transiting object is an opaque disk, which is usually appropriate for modeling planetary sizes. However, we are modeling a possible hydrogen exosphere which may or may not be disk-like, and which would have varying opacity with radius. For this work, we use the `BATMAN` modeling software with the

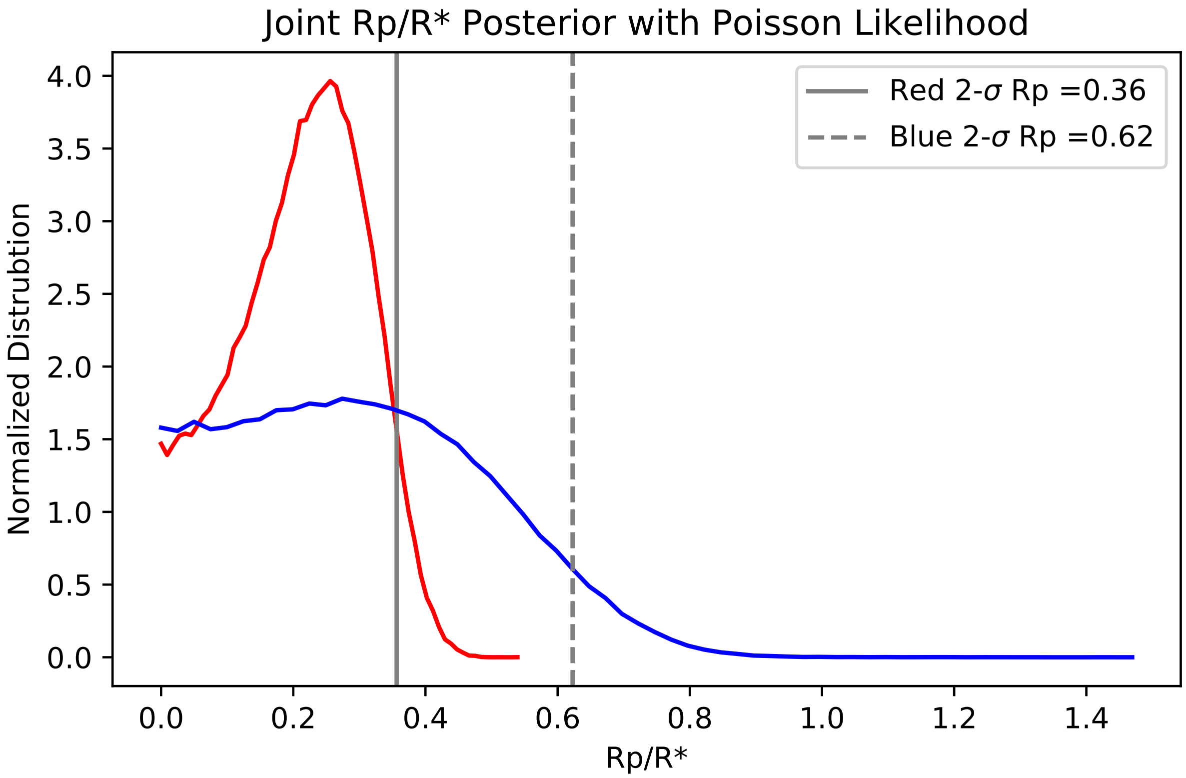

Figure 3.6: Joint posterior distribution for the R_p/R_* distributions for both visits. Poisson likelihoods were used due to the low photon count regime of these spectra.

understanding that our results tell us the effective radius of a cartoon hydrogen exosphere, with an assumed spherical geometry.

We fit for R_p/R_* and the baseline flux using a Poisson likelihood for each visit. We use a Poisson distribution because at Lyα, the STIS detector is receiving very few photons. Our log(likelihood) function is:

$$\ln(likelihood) = \sum_i [d_i \ln(m_i) - m_i - \ln(d_i!)]$$

where d_i is the total (*gross*) number of photons detected and m_i is the modeled number of photons detected. The photon model is acquired by taking a `BATMAN` model of in-transit photons and adding the *sky* photons, which is data provided through the `calstis` reduction pipeline. Uniform priors are assumed for both R_p/R_* and the baseline flux. We restrict our parameter space to explore only effective cloud radii > 0, representing physically plausible clouds that block light during transit. By taking simple averages of the light curve fluxes, we find the ratio of the in-transit flux compared with out-of-transit flux to be 1.01 ± 0.16 for the visit 1 red-wing flux and 0.97 ± 0.13 for the visit 2 red-wing. As both are consistent with no detectable transit, the constraints we obtain from the fitting procedure will represent upper limits on the effective size of any hypothetical cloud.

3.4 Results

3.4.1 Spectrum Reconstruction

Figure 3.3 shows the best fit emission model with 1-sigma models and a corner plot to display the most crucial modeling parameters, with MCMC results shown in Table 3.2 and Figure 3.4. This result gives us the total Lyα flux for this M dwarf.

The results of the stellar spectrum reconstruction indicate that there is one component of Lyα flux, though that is potentially a result of the low SNR regime of these observations. Additionally, our fit indicates that there is one dominant source of ISM absorption between us and GJ 1132 - a single cloud with velocity -3.1 km s^{-1}, HI column density $10^{17.9}$ cm^{-2} and Doppler parameter 13.9 km s^{-1}. Our current understanding of LIC (Redfield & Linsky, 2000, 2008) indicates that there should be 2 clouds, *G* and *Cet* in the line of sight of GJ 1132, but our derived v_{HI} is consistent with the velocity of *G*, which is reported as -2.73 ± 0.94 km s^{-1}. We take this to mean that the *G* cloud is the dominant source of absorption and that we can subsequently reconstruct this spectrum under a single-cloud assumption.

By integrating the reconstructed emission profile, we find a Lyα flux of $2.88^{+0.42}_{-0.31}$x10^{-14} erg s^{-1} cm^{-2} which gives f[Lyα]/f[bol] = 2.9$\pm$0.4x10^{-5}, where we have calculated the bolometric luminosity of GJ 1132b as:

$$f_{\mathrm{bol}} = \sigma T_{\mathrm{eff}}^4 \left(\frac{R_*}{\mathrm{distance}}\right)^2, \tag{3.1}$$

Where values for the T_{eff} and R_* were taken from Bonfils et al. (2018) and the distance to the star

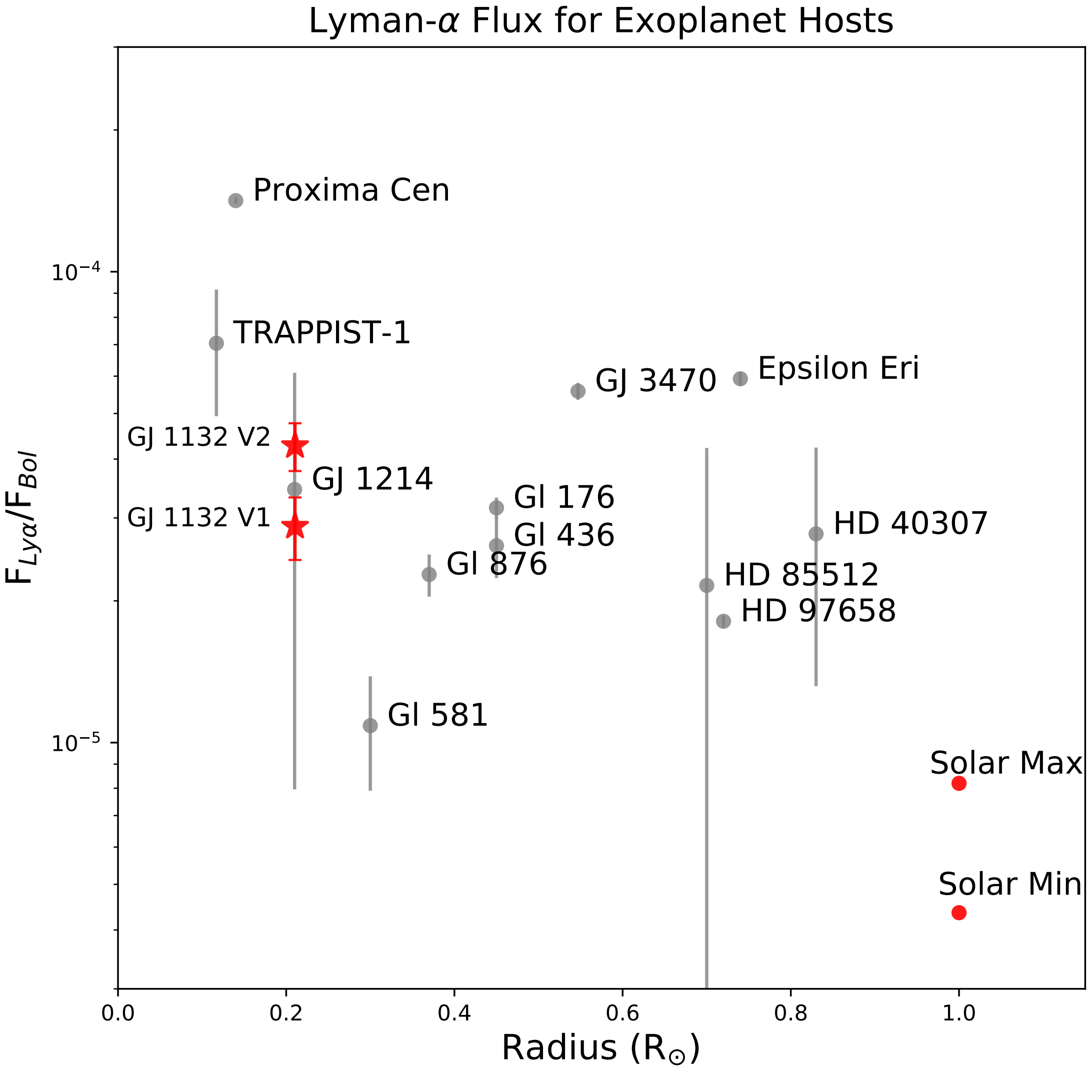

Figure 3.7: Comparison of F[Lyα]/F[bol] for GJ 1132 compared with stars in the MUSCLES Treasury Survey (Youngblood et al., 2016, 2017), TRAPPIST-1 (Bourrier et al., 2017a), HD 97658 (Bourrier et al., 2017b), GJ 436 (Bourrier et al., 2015), GJ 3470 (Bourrier et al., 2018a), as well as the Sun (Linsky et al., 2013). The stars shown here are all M and K dwarfs that are known exoplanet hosts. The error bars on GJ 1132 are statistical errors based on our modeling, so we have included the flux ratios from both visits (9 months apart) to display the variability we see in the data, labeled V1 and V2.

is taken from Dittmann et al. (2017). Compared with the Sun which has f[Lyα]/f[bol] = 4.6x10^{-6} (Linsky et al., 2013), we can see that this M dwarf emits fractionally 6x more of its radiation in the ultraviolet.

Given the intra-visit stellar variability, we also modeled the average Lyα spectra for visits 1 and 2 separately. All modeled parameters (see Fig. 3.4) were consistent between visits except the FWHM, which were different by 3-σ, and the total integrated fluxes which differed by 2-σ ($2.90^{+0.47}_{-0.41}$x10^{-14} erg s^{-1} cm^{-2} for visit 1 and $4.30^{+0.52}_{-0.43}$x10^{-14} erg s^{-1} cm^{-2} for visit 2). For the calculation of mass loss rates in section §4.1, we use the integrated flux of the combined reconstructed spectrum (Fig. 3.3).

3.4.2 Light Curve Modeling

The light curves for both visits are shown in Figure 3.5. MCMC modeling of these light curves resulted in best fit parameters shown in Table 3.3. We report no statistically significant transits, but we can use the modeling results to calculate limits on the hydrogen cloud parameters. To ensure that we were not biasing our results by converting from the measured flux counts to photons s^{-1}, we also analyzed the flux-calibrated light curves with Gaussian likelihoods based on pipeline errors and found the results did not significantly differ from what we present here.

3.4.2.1 The STIS Breathing Effect

There is a well-known intra-orbit systematic which shows up in Hubble STIS observations known as the *breathing effect* which can result in a change of amplitude of about 0.1% over the course of an HST orbit. (e.g., Brown et al., 2001; Sing et al., 2008; Bourrier et al., 2017a). This effect is small compared to the photon uncertainty in these observations, but to examine this STIS systematic, we perform our light curve analysis on the non-time-tagged data. We find that the results are consistent with our time-tagged analysis, so we posit that this effect does not significantly alter our conclusions.

3.4.3 Stellar Variability

The red wing of our spectral data show a highly variable stellar Lyα flux over the course of these HST visits and we quantify this variability as a Gaussian uncertainty,

$$\sigma_x^2 = \sigma_{\text{measured}}^2 - \sigma_{\text{photometric}}^2, \tag{3.2}$$

where σ_{measured} is our RMS noise and $\sigma_{\text{photometric}}$ is the `calstis`-generated error propagated through our spectral integration. Within one 90-minute HST orbit, we see flux variabilities (σ_x) of 5-16% for visit 1 and 7-18% for visit 2. Among one entire 18-hour visit, variability is 20% for visit 1 and 14% for visit 2 while in the 9 months between the two visits, there is a 22% offset. These results are consistent with the 1-41% M dwarf UV variability found by Loyd & France (2014).

3.5 Discussion

With 14 STIS exposures, we have characterized a long-integration Lyα spectrum and furthered our understanding of the intensity of UV flux from this M dwarf. France et al. (2012) find that as much as half of the UV flux of quiescent M dwarfs is emitted at Lyα, so knowing the total amount of flux at this wavelength serves as a proxy for the total amount of UV flux for this type of star. Our measurement of this Lyα flux provides a useful input for photochemical models of haze, atmospheric escape, and molecular abundances in this planet's atmosphere.

From the red-shifted light curves, we can calculate a 2-σ upper limit on the radius of this potential hydrogen cloud outflowing from GJ 1132b. We calculate this upper limit (see Fig. 3.6) by taking the joint (visit 1 & visit 2) posterior distributions that resulted from MCMC modeling of these light curves and integrating the CDF to the 95% confidence interval and examining the corresponding R_p/R_*. The 2-σ upper limit from the red-shifted Lyα spectra gives us an R_p/R_* of 0.36. The upper limit R_p/R_* from the blue-shifted light curves is 0.62 but given the very low SNR of that data, this is not a meaningful constraint. The red-shifted result is an upper limit on the effective radius of a hydrogen coma, and the real coma could be much more diffuse and asymmetric.

Line Velocity [km s^{-1}]	$35.23^{+0.99}_{-0.98}$
log(Amplitude) [erg s^{-1} cm^{-2} $Å^{-1}$]	$-13.23^{+0.08}_{-0.06}$
FWHM [km s^{-1}]	$114.02^{+4.64}_{-4.99}$
log(HI Column Density) [cm^{-2}]	$17.92^{+0.13}_{-0.15}$
Doppler Parameter (b) [km s^{-1}]	$13.91^{+0.74}_{-1.33}$
HI Velocity [km s^{-1}]	$-3.13^{+1.43}_{-1.18}$
Total Flux [erg s^{-1} cm^{-2}]	$2.9 \times 10^{-14}{}^{+4\times10^{-15}}_{-3\times10^{-15}}$
Total Flux (1 Au) [erg s^{-1} cm^{-2}]	$0.18^{+0.03}_{-0.02}$

Table 3.2: Intrinsic emission line model parameters taken from MCMC samples, with 1-σ error bars. *Total Flux (1 Au)* is the flux if it were measured 1 Au from the star, whereas the *Total Flux* is the flux as measured at HST.

3.5.1 GJ 1132b Atmospheric Loss

In order to connect our results to an upper limit on the possible mass loss rate of neutral H from this planet's atmosphere, we follow the procedure outlined in Kulow et al. (2014).

Assuming a spherically symmetric outflowing cloud of neutral H, the equation for mass loss is

$$\dot{M}_{HI} = 4\pi r^2 v(r) n_{HI}(r) \tag{3.3}$$

Where $v(r)$ is the outflowing particle velocity and $n_{HI}(r)$ is the number density of HI at a given radius, r. For this calculation, we will be examining our 2-σ upper limit radius at which the cloud becomes optically thick, where $(\mathrm{R}_p/\mathrm{R}_*)^2 = \delta = 0.13$. We assume a v range of $10-100$ km s^{-1}, which is the range of the planet's escape velocity (10 km s^{-1}) and the stellar escape velocity (100 km s^{-1}).

Kulow et al. (2014) reduce Equation (3) to

$$\dot{M}_{HI} = \frac{2\delta R_* m v}{\sigma_0} \tag{3.4}$$

with a Lyα absorption cross-section σ_0 defined as

$$\sigma_0 = \frac{\sqrt{\pi} e^2}{m_e c \Delta\nu_D} f \tag{3.5}$$

where e is the electron charge, m_e is the electron mass, c is the speed of light, f is the particle oscillator strength (taken to be 0.4161 for HI) and $\Delta\nu_D$ is the Doppler width, b/λ_0, where we use 100 km s^{-1} for b, as was done in Kulow et al. (2014).

This gives us an upper limit mass loss rate of $\dot{M}_{HI} < 0.86 \times 10^9$ g s^{-1} for neutral hydrogen, corresponding to 15.4×10^9 g s^{-1} of water decomposition, assuming all escaping neutral H comes from H_2O. If this upper-limit mass loss rate was sustained, GJ 1132b would lose an Earth ocean in approximately 6 Myr. If we had actually detected mass loss at this high rate, it would likely indicate that there had been recent delivery or outgassing of water on GJ 1132b, because primordial atmospheric water would have been lost on time scales much shorter than the present age of the system.

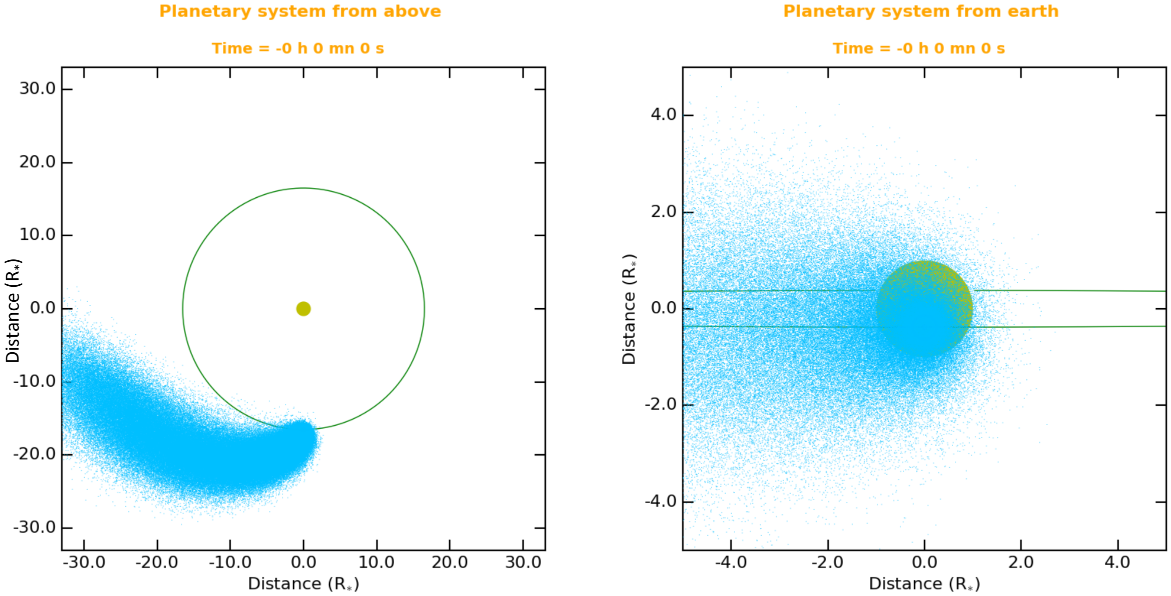

Figure 3.8: Simulations of the GJ1132 system showing the dynamics of a hypothetical outflowing hydrogen cloud. The left panel shows a top-down view of the system, as a hydrogen tail extends in a trailing orbit. The right panel shows the view from an Earth line of sight, at mid-transit.

We can also calculate the energy limited mass loss rate, corresponding to the the ratio of the incoming XUV energy to the work required to lift the particles out of the atmosphere:

$$\dot{M} = \frac{F_{XUV} \pi R_p^2}{G M_p \ R_p^{-1}} = \frac{F_{XUV} \pi R_p^3}{G M_p}. \tag{3.6}$$

The total $\mathrm{F_{XUV}}$ is the flux value at the orbit of GJ 1132b. Using our derived Lyα flux, the `Lyapy` package calculates stellar EUV spectrum and luminosity from 100-1171 Å based on Linsky et al. (2014). From that EUV spectrum, we then calculate the 5-100 Å XUV flux based on relations described in King et al. (2018).

Assuming 100% efficiency, we obtain an energy-limited neutral hydrogen mass loss rate of 3.0×10^9 g s^{-1} estimated from the stellar spectrum reconstruction. This energy-limited escape rate is commensurate with the upper-limit we calculate based on the transit depth and stellar properties in the previous section. If we assume a heating efficiency of 1% (based on similar simulations done in Bourrier et al., 2016), then we arrive at a low expected neutral hydrogen loss rate of 3.0×10^7 g s^{-1}, below the level of detectability with these data.

3.5.2 Simulating HI Outflow from GJ 1132b

Figure 3.8 shows simulation results for neutral hydrogen outflowing from GJ 1132b from the EVaporating Exoplanet code (`EVE`) (Bourrier et al., 2013, 2016). This code performs a 3D numerical

MCMC Results	Visit 1	Visit 2	Joint
$\mathrm{R}_p/\mathrm{R}_*$ (R)	$0.34^{+0.11}_{-0.15}$	$0.15^{+0.12}_{-0.10}$	$0.22^{+0.09}_{-0.12}$
$\mathrm{R}_p/\mathrm{R}_*$ (B)	$0.29^{+0.24}_{-0.20}$	$0.46^{+0.30}_{-0.30}$	$0.30^{+0.21}_{-0.21}$
Baseline (γ s^{-1}) (R)	$0.102^{+0.003}_{-0.003}$	$0.136^{+0.003}_{-0.004}$	$0.101^{+0.003}_{-0.003}$ $0.136^{+0.003}_{-0.003}$
Baseline (γ s^{-1}) (B)	$0.013^{+0.001}_{-0.001}$	$0.013^{+0.001}_{-0.002}$	$0.013^{+0.001}_{-0.001}$ $0.013^{+0.001}_{-0.002}$

Table 3.3: Light curve fit results for MCMC sampling where Poisson likelihoods were used.

particle simulation given stellar input parameters and atmospheric composition assumptions. These simulations were performed using the Lyα spectrum derived in this work, where the full XUV spectrum has been found as described in the previous section. This spectrum is used directly in `EVE` to calculate the photoionization of the neutral H atoms and calculate theoretical Lyα spectra during the transit of the planet as they would be observed with HST/STIS. In addition, our Lyα spectrum is used to calculate the radiation pressure felt by the escaping neutral hydrogen, which informs the dynamics of the expanding cloud.

`EVE` simulations were created with the following assumptions: The outflowing neutral hydrogen atoms escape from the Roche lobe altitude ($\sim 5\ R_p$) at a rate of 1×10^7 g s^{-1}, modeled as a Maxwellian velocity distribution with upward bulk velocity of 5 km s^{-1} and temperature of 7000 K, resulting in a cloud which could absorb upwards of 80% of the flux in the blue wing. However, GJ 1132 has a positive radial velocity, so blue-shifted flux falls into the regime of ISM absorption and the signal is lost. Simulations of the in-transit and out-of-transit absorption spectra as they would be observed at infinite resolution by HST are shown in Figure 3.9. However, the simulations don't rule out that some thermospheric neutral H may absorb some extra flux in the red wing (see Salz et al., 2016, for a justification of simulation parameters). We note that for planets around M dwarfs, the upward velocity may have a strong influence on the extension of the hydrogen coma. The thermosphere is simulated as a 3D grid within the Roche Lobe, defined by a hydrostatic density profile, and the temperature and upward velocity from above. The exosphere is collisionless with its dynamics dominated by radiation pressure.

There might be other processes shaping the exosphere of GJ 1132b (magnetic field, collisions with the stellar wind, the escaping outflow remaining collisional at larger altitudes than the Roche lobe), but for these simulations we take the simplest possible approach based on what we actually know of the system. Finally, we do not include self-shielding effects of HI atoms within the exosphere, as we do not expect the exosphere is dense enough for self-shielding to significantly alter the results.

The integrated Lyα spectrum corresponds with a maximum ratio of stellar radiation pressure

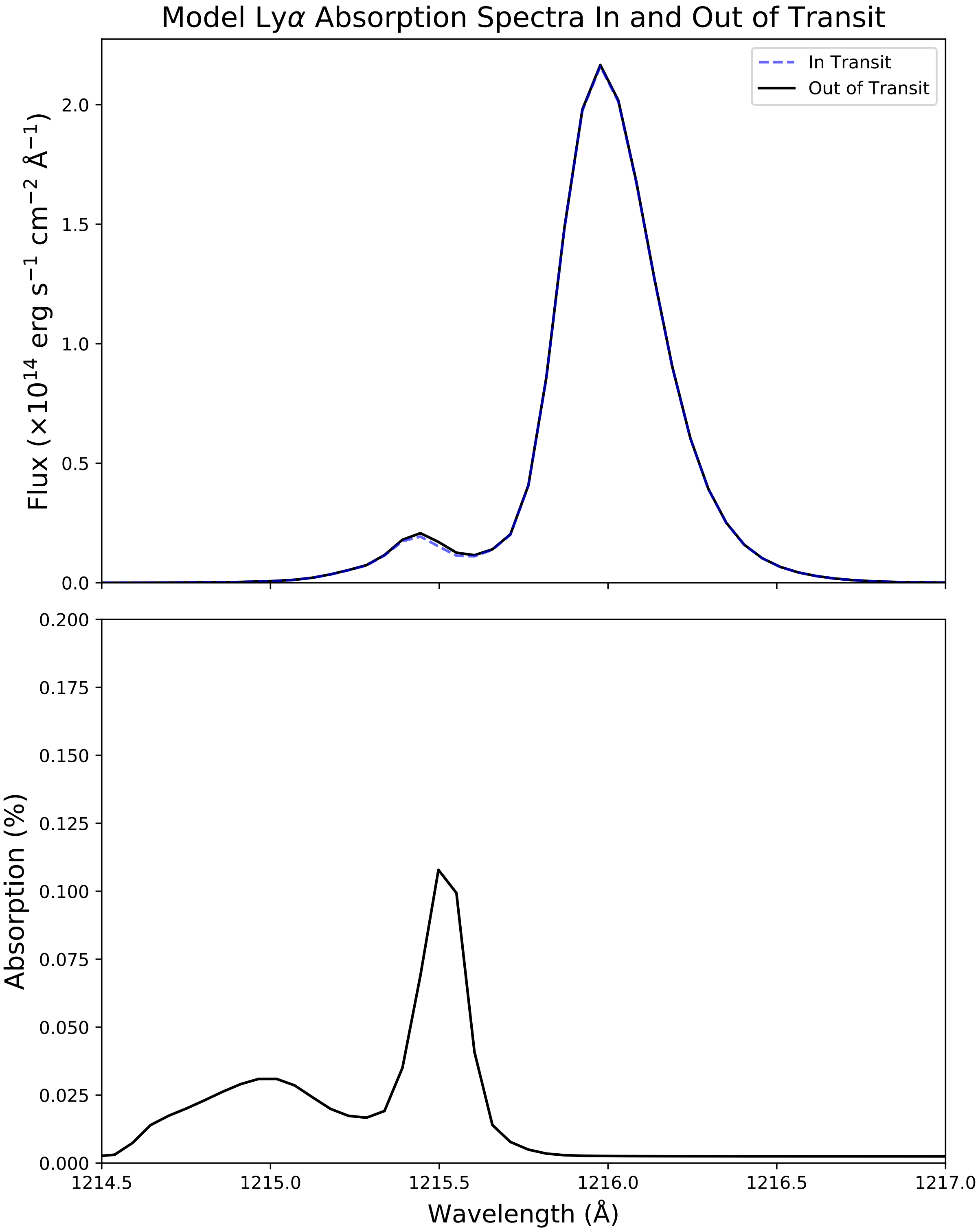

Figure 3.9: `EVE` simulated absorption spectra in-transit and 4 hours pre-transit. We can see that the only region of significant absorption is at 1215.5 Å, where absorption peaks at about 12% as seen in the bottom panel. While there is a larger expected flux decrease in the blue wing, the signal is largely in the region that the ISM absorbs and our data are too noisy in the blue wing to detect the possible absorption signal seen in the models. The mass loss rate corresponding to the above model is $1{\times}10^7$g s^{-1}.

to stellar gravity of 0.4, which puts this system in the regime of radiative breaking (Bourrier et al., 2015), which has a slight effect of pushing neutral hydrogen to a larger orbit. However, the gas is not blown away so the size of the hydrogen cloud will increase if we increase the outward particle velocity. Since the exosphere is not accelerated, most of its absorption is close to 0 km s^{-1} in the stellar reference frame, with some blue-shifted absorption because atoms in the tail move to a slightly larger orbit than the planet. This indicates that the lack of blue-shifted flux in our observations, due to ISM absorption, is a hindrance to fully understanding the possible hydrogen cloud around this planet. The upper limit cloud size that we quote is based on the observed red-shifted flux in a system which is moving away from us at 35 km s^{-1}, so any cloud absorption of flux closer to the line center is outside of the scope of what we can detect.

3.6 Conclusions

In this work we make the first characterization of the exosphere of GJ 1132b. Until a telescope like LUVOIR (Roberge & Moustakas, 2018), these observations will likely be the deepest possible characterization for Lyα transits of this system. If this planet has a cloud of neutral hydrogen escaping from its upper atmosphere, the effective size of that cloud must be less than 0.36 R_* (7.3 R_p) in the red-shifted wing. The blue wing indicates an upper limit of 0.62 R_* (12.6 R_p), though this is a very weak constraint. In addition, we were able to model the intrinsic Lyα spectrum of this star.

This Lyα transit's upper limit R_p/R_* implies a maximum hydrogen escape rate of $0.08-0.8\times 10^9$ g s^{-1}. If this is the case, GJ 1132b loses an Earth ocean of water between $6-60$ Myr. Since the mass loss rate scales linearly with F_{XUV}, we estimate that if this planet were in the habitable zone of its star, about 5x further than its current orbit (based on HZ estimates in Shields et al., 2016), the planet would lose an Earth ocean of water in as little as 0.15-1.5 Gyr. However, these values are based on 2-σ upper limits and theoretical calculations suggest mass loss rates lower than these values, so further Lyα observations are needed to better constrain this mass loss. In addition, these estimates are based on the current calculated UV flux of GJ 1132, which likely decreases over the star's lifetime (e.g., Stelzer et al., 2013) and this results in an underestimate of the mass loss.

The relative Lyα/Bolometric flux is roughly 1 order of magnitude higher for this M dwarf than it is for the Sun, which has grave implications for photolytic destruction of molecules in planets around M dwarfs of this mass. Even when considering the EUV spectrum of GJ 1132 (calculated with methods described in Youngblood et al., 2016) and the EUV flux of the Sun (Zhitnitsky, 2018), we find that GJ 1132 emits 6x as much EUV flux (relative to F_{bol}) as the Sun.

This work leaves us with several possible pictures of the atmosphere of GJ 1132b:

- The real atmospheric loss rates may be comparable to these upper limits, or they may be much less, which leaves us with an open question about the atmosphere and volatile content of GJ 1132b. There could be some loss, but below the detection limit of our instruments.
- If there is a neutral hydrogen envelope around GJ 1132b, then this super-Earth is actively losing water driven by photochemical destruction and hydrodynamic escape of H. The remaining atmosphere will then be rich in oxygen species such as O_2 and the greenhouse gas CO_2.
- GJ 1132b could be Mars-like or Venus-like, having lost its H_2O long ago, with a thick CO_2 and O_2 atmosphere remaining, or no atmosphere at all. We posit that this is the most likely scenario, and thermal emission observations with JWST (Morley et al., 2017) would give further insight to the atmospheric composition of GJ 1132b.
- There might be a giant cloud of neutral hydrogen around GJ1132b based on the `EVE` simulations, which is undetectable because of ISM absorption. However, if there are other volatiles in the atmosphere we could detect this cloud using other tracers such as carbon or oxygen with HST in the FUV, or helium (Spake et al., 2018) with ground-based high-resolution infrared spectrographs (see Allart et al., 2018; Nortmann et al., 2018) or with JWST.

GJ 1132b presents one of our first opportunities to study terrestrial exoplanet atmospheres and their evolution. While future space observatories will allow us to probe longer wavelength atmospheric signatures, these observations are our current best tool for understanding the hydrogen content and possible volatile content loss of this warm rocky exoplanet.

Chapter 4

Quantifying the Transit Light Source Effect: Measurements of Spot Temperature and Coverage on the Photosphere of AU Microscopii with High-Resolution Spectroscopy and Multi-Color Photometry

This chapter has been resubmitted to AAS Journals after being recommended for publication with minor revision, under the following title: W. C. Waalkes, Z. K. Berta-Thompson, E. Newton, A. Mann, P. Gao, H. Wakeford, L. Alderson, P. Plavchan, *Quantifying the Transit Light Source Effect: Measurements of Spot Temperature and Coverage on the Photosphere of AU Microscopii with High-Resolution Spectroscopy and Multi-Color Photometry.*

Specific contributions include: W. C. Waalkes led the data analysis and model fitting, Z. K. Berta-Thompson and E. Newton PI'd some of the observing proposals which provided data for this paper.

4.1 Abstract

AU Mic is an active 24±3 Myr pre-main sequence M dwarf in the stellar neighborhood (d=9.7 pc) with a rotation period of 4.86 days. The two transiting planets orbiting AU Mic, AU Mic b and c, are warm sub-Neptunes on 8.5 and 18.9-day periods and are targets of interest for atmospheric observations of young planets. Here we study AU Mic's unocculted starspots using ground-based photometry and spectra in order to complement current and future transmission spectroscopy of its planets. We gathered multi-color LCO 0.4m SBIG photometry to study the star's rotational modulations and LCO NRES high-resolution spectra to measure the different spectral

components within the integrated spectrum of the star, parameterized by 3 spectral components and their coverage fractions. We find AU Mic's surface has at least 2 spectral components, a $T_{\mathrm{amb}}=4003^{+15}_{-14}\tilde{K}$ ambient photosphere with cool spots that have a temperature of $T_{\mathrm{spot}}=3003^{+63}_{-71}\tilde{K}$ covering a globally-averaged area of $39 \pm 4\%$ which increases and decreases by $5.1 \pm 0.3\%$ from the average throughout a rotation. We also detect a third flux component with a filling factor less than 0.5% and a largely uncertain temperature between 8500-10000K that we attribute to flare flux not entirely omitted when time-averaging the spectra. We include measurements of spot characteristics using a 2-temperature model, which we find agree strongly with the 3-temperature results. Our expanded use of various techniques to study starspots will help us better understand this system and may have applications for interpreting the transmission spectra for exoplanets transiting stars of a wide range of activity levels.

4.2 Introduction

Observations from JWST are now revealing exoplanet atmospheres in more detail than ever before (Ahrer et al., 2023; Alderson et al., 2023; Feinstein et al., 2023; Rustamkulov et al., 2023; Fu et al., 2022) using an observational technique called transmission spectroscopy (Seager & Sasselov, 2000a; Brown et al., 2001; Pont et al., 2007; Berta et al., 2012; Sing et al., 2011). Transmission spectroscopy is done by measuring the transit depth (which is a proxy for the planet's radius) of an exoplanet as a function of wavelength and inferring atmospheric absorption (e.g., Seager & Sasselov, 2000a) and/or scattering (e.g., Robinson et al., 2014; Sing et al., 2016) at wavelengths where the planet's transit is deeper. The stellar photons that are absorbed by the planet and its atmosphere originate specifically from the transit chord, the swathe of stellar surface occulted by the planet which in general is indistinguishable from the surrounding photosphere except in compact systems which exhibit transits at multiple latitudes. Stellar surfaces can be homogeneous (i.e., spatially "smooth" aside from granulation and limb-darkening effects), in which case the chord spectrum is the same as the disk-integrated spectrum, or they can be heterogeneous (containing active regions), in which case the transit chord is not necessarily representative of the disk-integrated stellar spectrum.

A homogeneous stellar background surface has typically been adopted in transmission studies. While this assumption holds true in some cases, most stars do not have smooth, single-temperature surfaces but are instead spotted with activity-induced heterogeneities. Spots are created where magnetic field lines pass through the photosphere and the magnetic pressure overwhelms the local gas pressure, suspending convection and causing the region within the intersecting field to cool. Faculae arise from weaker concentrations of field lines where this pressure isn't enough to suspend convection but is enough to reduce the local opacity and increase the flux emanating from deeper in the photosphere, creating a brightening effect (Basri, 2021).

A non-axisymmetric distribution of spots and faculae creates time- and wavelength-dependent changes in the stellar surface flux, which has been observed in high-resolution stellar spectra (Wing et al., 1967; Afram & Berdyugina, 2015), color-magnitude relations (Vogt, 1979; Olah et al., 1997), stellar rotational modulation (Vogt, 1979; Pass et al., 2023), and more recently in exoplanet transits (Brown et al., 2001; Pont et al., 2008; Sing et al., 2011; Sanchis-Ojeda & Winn, 2011). When spots or faculae lie on the transit chord and are occulted by transiting planets, they create bumps or dips in the transit light curve that can bias the exoplanet radius measurement. Occulted active regions, provided they occupy discrete regions of the transit chord and their flux contrast appears above the noise, show up directly in transit light curves and can be identified and removed from the measured transmission spectrum. Unocculted active regions, however, alter the disk-averaged spectrum such that it is no longer representative of the true source spectrum of photons entering the planetary atmosphere. This in turn creates spurious λ-dependent changes to the exoplanet transit depth in what is now known as the transit light source effect (TLSE, Rackham et al., 2018, 2019).

On cool stellar surfaces (below about 4000 K), molecular absorption lines (like H_2O, VO, and TiO, Jones et al., 1995; Allard et al., 2012) begin to appear in the stellar spectrum and become entangled with molecular absorption signals in planetary atmospheres. Cool unocculted spots with different or deeper molecular absorption lines than the surrounding photosphere will appear to add molecular absorption at those wavelengths in planetary transmission spectra and lead to mischaracterization of exoplanets and their atmospheres. Additionally, unocculted spots give rise to an increasing transit depth toward bluer wavelengths as their contrast against the surrounding photosphere increases, which can be mistakenly identified as Rayleigh scattering in a transiting exoplanet's atmosphere (e.g., Robinson et al., 2014). Until we can precisely and reliably determine spot characteristics on our host stars, the signature of exoplanet atmospheres will be very challenging or impossible to disentangle from spot contamination for nearly all transmission observations of exoplanets M and K dwarfs. This degeneracy, exemplified in recent transmission observations of sub-Neptune exoplanets TOI 270d (Mikal-Evans et al., 2023), Gl 486b (Moran et al., 2023), K2-33b (Thao et al., 2023), L 98-59 c (Barclay et al., 2023), and temperate terrestrial exoplanet TRAPPIST-1b (Lim et al., 2023) is what we aim to mitigate for transmission observations of AU Mic b by precisely measuring spot characteristics for its host star in this work.

Quantity	**Value**
AU Mic	
D [pc]	9.714 ± 0.002^{a}
$T_{\rm eff}$ [K]	3665 ± 31^{b}
M_* [$M_\odot$]	0.60 ± 0.03^{c}
R_* [$R_\odot$]	0.82 ± 0.05^{c}
$P_{\rm rot}$ [days]	$4.86 \pm 0.005^{c,d}$
Metallicity [dex]	0.12 ± 0.10^{c}
$\log g$ [$\log_{10}$(cm/s^2)]	4.52 ± 0.05^{c}
AU Mic b	
P [days]	8.4631427^{e}
R_p/R_*	0.0433 ± 0.0017^{e}

Table 4.1: System parameters relevant to this study. a: Gaia Collaboration et al. (2023), b: Cristofari et al. (2023), c: Donati et al. (2023), d: Martioli et al. (2021), e: Szabó et al. (2022).

AU Microscopii AU Mic (Torres & Ferraz Mello, 1973) is a nearby (9.7 pc; Gaia Collaboration et al., 2023), young (24 ± 3 Myr; Mamajek & Bell, 2014), rapidly rotating ($P_{\rm rot} = 4.86$ d; Plavchan et al., 2020; Donati et al., 2023) pre-main sequence M dwarf with a debris disk (Kalas et al., 2004; Chen et al., 2005; MacGregor et al., 2013). This star has an inflated radius as it settles onto the main sequence, with M= 0.60 $M_\odot$ and R= 0.82 $R_\odot$ (Donati et al., 2023) and an effective temperature of 3600-3700K (e.g., Afram & Berdyugina, 2019; Plavchan et al., 2020; Cristofari et al., 2023) There are two transiting warm Neptunes on 8.46 and 18.86-day periods (Hirano et al., 2020; Plavchan et al., 2020; Martioli et al., 2021; Gilbert et al., 2022; Zicher et al., 2022) and 2 unconfirmed candidate non-transiting planets on 12.74 and 33.39-day periods recently discovered through transit timing variations and radial velocity analysis (Wittrock et al., 2022, 2023; Donati et al., 2023). The existence of an observable debris disk with interior transiting planets is a rare and exciting architecture that holds vast scientific potential.

Furthermore, this system is one of the best cases we have for studying star-planet interactions and the effects of young M dwarf activity on planetary atmospheres, an issue of great interest and concern in the search for terrestrial atmospheres and potentially habitable planets orbiting M dwarf stars (e.g., Shields et al., 2016; Louca et al., 2023). This star's frequent high-energy flaring that may eventually lead to photo-evaporation of the atmospheres of AU Mic b and c (Feinstein et al., 2022) and even in the case where atmospheres are preserved, the long term implications of young M dwarf activity on planetary habitability are ominous. By continuing to study AU Mic and its planets, we can build an internally consistent understanding of a nearby multi-planet system in the early stages of formation with a stellar surface evolving on months-long timescales (e.g., Donati et al., 2023). System parameters are summarized in Table 4.1 and a thorough review of AU Mic's stellar and planetary characteristics can be found in Donati et al. (2023).

Transmission Observations of AU Mic b The observations we present in this work are part of a companion study alongside HST/WFC3 transmission spectra of AU Mic b; the first on 2021 Aug 30 (BJD 2459455.98) and the second on 2022 Apr 14 (BJD 2459684.40). Because AU Mic's spots evolve noticeably over time (e.g., Szabó et al., 2021, 2022; Gilbert et al., 2022), we have collected photometric and spectroscopic observations contemporaneous with the WFC3 observations to provide constraints on spot contamination at the time of both transmission visits. This transmission spectrum will be analyzed in the context of our results and presented in a subsequent paper.

Objectives and Layout In order to characterize AU Mic's spots and forward-model the spot contamination level in AU Mic b's transmission spectrum, we assembled a self-consistent statistical framework that combines multi-color time-series photometry with contemporaneous high-resolution spectroscopy. This method allows us to break observational degeneracies between spot coverage and spot contrast and better understand the *bulk* characteristics of AU Mic's spots. We use *bulk* to mean the spatially-unresolved flux-weighted characteristics based on the treatment of spots as discrete regions without complex temperature profiles, ignoring for example the distinction between umbra and penumbra. These are heavy assumptions, but we argue that our models are appropriate for the quality of our data and the information we hope to obtain.

This paper is laid out as follows: in Section 4.3 we describe the types of observations used in spot analysis and the specific observations we acquired, along with the data reduction and processing. In Section 4.4 we describe our methods of analyzing AU Mic's rotational modulations (4.4.1), assembling the self-consistent statistical framework for modeling spot filling factor and temperature (4.4.2), and forward-modeling the spot contamination in AU Mic b's transmission spectrum (4.4.3). In Section 4.5 we report the results of our spot model and in Section 4.6 we discuss the physical implications of our results, how they compare to previous studies, and the limitations of our approach.

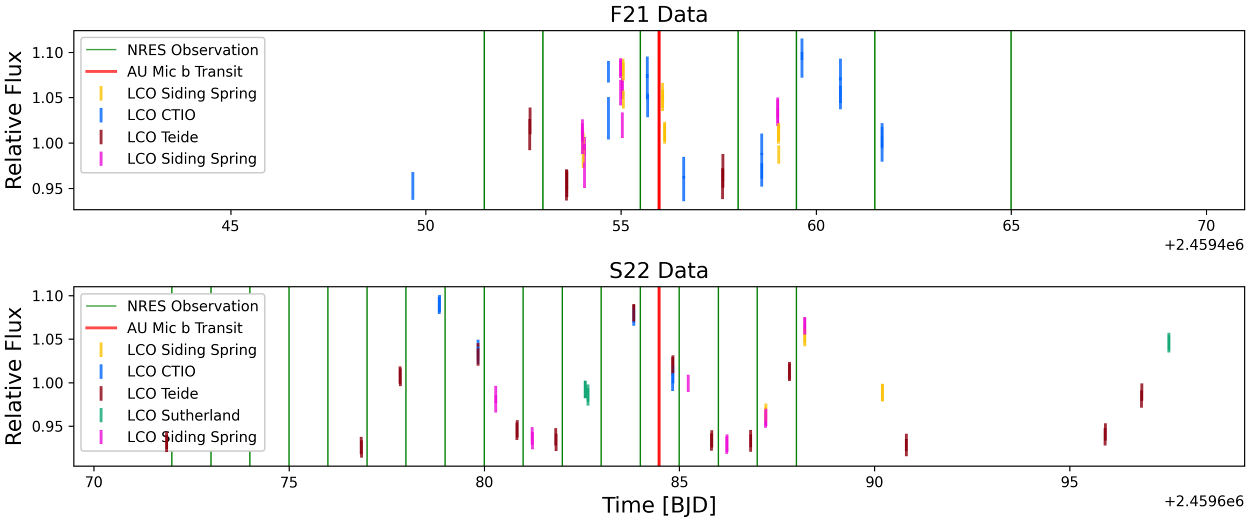

Figure 4.1: Processed and baseline-corrected photometry data for all filters in visits F21 (top) and S22 (bottom) with vertical markers showing the temporal distribution of WFC3 (red) and NRES (green) observations. The color of each photometric data point is based on the LCO site where that data was observed. The time between transit observations is 229 days.

4.3 Observations and Data Reduction

Observing Spots Starspot characteristics are difficult to disentangle in practice as there is a degeneracy between spot coverage and temperature contrast that creates similar observational effects within a single waveband. In addition, the physics and structure of stellar surfaces is poorly understood for all but the most heavily studied stars. Stars of different type, rotation rate, and magnetic field strength exhibit differing forms of surface phenomena which are or will eventually be relevant to understand for the future of exoplanet discovery and characterization.

Breaking spot degeneracies can be done by combining observations across optical and infrared wavelengths. Short-wavelength broadband photometry allows us to probe starspots where they stand out the most against the stellar background (higher flux contrast toward the Wien limit), while long-wavelength observations are useful for identifying molecular characteristics of starspots where they overlap with planetary atmospheric absorption. Broadband photometric variability measurements help us probe different temperature components on rotating stars, but generally only provides a lower limit on total spot coverage due to unknown axisymmetries in spot distribution (Apai et al., 2018). Photometric variability amplitudes decrease with wavelength as the two flux components approach the Rayleigh-Jeans limit, so measuring rotational variability across the optical to the infrared provides strong constraints on the spot-to-photosphere temperature contrast (e.g., Strassmeier & Olah, 1992).

High-resolution, time-series spectra have been used to study the relationships between stellar activity tracers and spot coverage (e.g., Schöfer et al., 2019; Medina et al., 2022). For spectroscopic studies, stellar spectra are modeled as a combination of two or more temperature components (often referred to as *spectral decomposition*, e.g., Gully-Santiago et al., 2017; Zhang et al., 2018; Wakeford et al., 2019). Specific molecular lines are often used as spot tracers including TiO (Wing et al., 1967; Vogt, 1979), CaH, MgH, FeH, and CrH (e.g., Neff et al., 1995; Afram & Berdyugina, 2019). We recommend Berdyugina (2005); Apai et al. (2018); Rackham et al. (2018) for a more thorough review of starspots and the techniques used to study them.

4.3.1 Data

We acquired Las Cumbres Observatory (LCO) 0.4m g'-, r'-, and i'-band[1] SBIG photometry and Network of Robotic Echelle Spectrographs (NRES) high-resolution echelle spectra on two separate visits spanning 2-3 weeks around their respective transmission observations (occurring in Fall 2021 and Spring 2022, hereafter F21 and S22). These data were acquired contemporaneously with observations of AU Mic b's HST/WFC3 transmission spectrum (see Figure 4.1) with the hope of precisely constraining the magnitude of spot contamination at the appropriate stellar epoch and phase.

4.3.1.1 SBIG Imaging

Photometry was acquired between 2021 Aug 12-2021 Sept 03 (F21) and 2022 Apr 01-2022 Apr 27 (S22) using 5 separate telescopes automatically scheduled depending on weather, telescope availability, and target observability. Typical exposure times were 20s in g', 10s in r', and 6s in i'. Photometric data were automatically reduced into calibrated images by the BANZAI pipeline (McCully et al., 2022) and downloaded from the LCO Science Archive[2] . We performed aperture photometry with AstroImageJ's multi-aperture photometry tool (Collins et al., 2017). For each filter, the same 3 comparison stars are used to account for local atmospheric effects throughout the night and measure the target star's relative flux. The fact that AU Mic is far brighter than its nearby comparison stars (g', r', and i' magnitudes of 9.579±0.05, 8.636±0.09, and 7.355±0.14, respectively Zacharias et al., 2012) means that the photon noise in the photometry is set by the comparison star brightness, rather than by AU Mic itself. Scintillation also contributes significantly to the photometric noise budget, particularly in the i' photometry where exposure times are very short to avoid AU Mic saturating. After performing aperture photometry, S/N per exposure was 300-600 in F21 g' and r', 200-300 in F21 i', and 500-1000 in S22 g' and r'. For the first visit (F21), we have 450 exposures in SDSS g', 1036 exposures in r', and 1175 in i'. For the second visit (S22)

---

[1] `https://lco.global/observatory/instruments/filters/`

[2] `https://archive.lco.global/`

Order	λ (μm)	**Note**
53*	0.873-0.888	TiO line [8860 Å]
54	0.858-0.872	
55	0.842-0.857	Excluded - Telluric Contamination
56	0.826-0.841	Excluded - Telluric Contamination
57	0.810-0.826	Excluded - Telluric Contamination
58	0.798-0.812	Excluded - Telluric Contamination
59*	0.784-0.798	
60	0.771-0.784	Excluded - Poor Fit
61*	0.759-0.772	TiO line [7600 Å]
62	0.746-0.760	Excluded - Poor Fit
63	0.734-0.748	Excluded - Telluric Contamination
64	0.723-0.736	Excluded - Telluric Contamination
65	0.712-0.724	Excluded - Telluric Contamination — TiO line [7150 Å]
66	0.701-0.713	Excluded - Telluric Contamination — TiO line [7050 Å]
67	0.690-0.702	Excluded - Telluric Contamination
68	0.680-0.692	Excluded - Telluric Contamination
69*	0.671-0.682	
70	0.661-0.672	Excluded - Poor Fit
71*	0.652-0.663	H-α band
72*	0.642-0.653	
73*	0.634-0.645	Excluded - Poor Fit
74	0.625-0.636	Excluded - Telluric Contamination
75*	0.617-0.627	
76*	0.609-0.619	
77	0.601-0.611	Excluded - Poor Fit
78	0.593-0.603	Excluded - Telluric Contamination
79	0.586-0.596	Excluded - Telluric Contamination
80	0.578-0.588	Excluded - Poor Fit
81*	0.571-0.581	
82*	0.564-0.574	
83*	0.558-0.567	

Table 4.2: Details on the NRES Echelle spectra acquired for this study. The full spectrum spans 0.39-0.91 μm (orders 119-52) but we truncate the table and the analysis at orders 53 and 83 to focus on orders which are not dominated by noise. Orders that we omit from the final analysis are noted with a brief explanation, and further discussion of modeling specific orders is provided in the Appendix. Most omitted orders were heavily contaminated by telluric absorption, whereas the orders labeled “Poor Fit” typically exhibit extremely cold spots, at the limit of the spectral library. Note that wavelength decreases with order.

we have 328 in g' and 330 in r'.

For each night of observations, we stitch together all data in a single filter and take the median in order to minimize the effect of flares. We use `scipy.optimize` to fit an initial sinusoid model for sigma-clipping. We clip $10-\sigma$ outliers from the initial model to account for flux variations outside of the rotational modulation (i.e., flares), generate an optimized fit with `scipy.optimize.minimize`, clip $5-\sigma$ outliers from that model, re-optimize a final time, and normalize uncertainties based on the reduced χ^2 statistic from this final optimized fit. The first cutoff is set at $10-\sigma$ because after median binning, the uncertainties were underestimated and a slightly wrong initial model could easily exclude otherwise useful data. The second cutoff is set at $5-\sigma$ to account for any extreme outliers still remaining without being too restrictive, accounting for known uncertainties in the chosen model. After processing, the typical per-night S/N was 70-100 for g' and r' and 30-50 in i', with a total of 19 data points for F21 g', 18 for r', 17 for F21 i', 28 data points for S22 g', and 30 for S22 r'. The per-night S/N only reaches to 100 because we set a minimum uncertainty of 1% on the post-processing photometry based on the per-night spread in flux.

4.3.1.2 NRES Spectra

AU Mic's spectrum was observed in the $0.39-0.91\mu$m NRES bandpass with 600s exposure times resulting in a total of 38 observations from 2021 August 24-2021 September 09 (F21) and 48 observations from 2022 April 02-2022 April 18 (S22). The R=53,000 NRES spectra were reduced by the BANZAI-NRES pipeline (McCully et al., 2022) and downloaded from the LCO Science Archive. Spectra from individual observations show typical peak S/N of 35 where the star is brightest (around order 60) and drops off to below 10 in order 52 and beyond order 83, so we omit orders outside of this range from our analysis. We processed the spectra with the `chromatic`[3] tool, first correcting for the velocity shift in each order's spectra from the movement of the Earth in different positions of its orbit. This was -9.5km/s in F21 and 33.0 km/s in S22 derived from a χ^2 grid search using a single-temperature optimized model spectrum and `scipy.optimize.minimize`.

---

[3] `https://github.com/zkbt/chromatic`

We median-combine spectra in time to one averaged spectrum per night resulting in 7 spectra in F21 and 17 spectra in S22. We also bin each spectrum to 0.05 nm (roughly R=11000-18000); this is greater than the Doppler broadening width of 0.015-0.024 nm that we estimate for the NRES bandpass based on AU Mic's vsini of $8 - 9$ km/s (e.g., Donati et al., 2023). Zeeman broadening is an additional effect which alters line profiles in magnetically active stars (e.g., Gray, 1984), but we calculate the Zeeman broadening (Reiners et al., 2013) to be less than rotational broadening at these wavelengths and accounted for within our chosen bin size. Many of our spectral orders overlap with absorption bands in Earth's atmosphere so we trim out any wavelengths where the molecular line transmission fraction of the atmosphere is < 0.995 (i.e., any wavelength at which $\geq$0.5% of the photons are absorbed) based on time-averaged telluric data from Skycalc (Noll et al., 2012; Jones et al., 2013). We run a σ-clipping routine that first calculates an optimized single-temperature PHOENIX model (Husser et al., 2013) for each spectrum, and second clips emission lines, defined as points $> 3 - \sigma$ *above* the optimized model. Uncertainties on the time-averaged spectra are inflated to give a reduced χ^2 of 1 when fit against a 3650K template. This is an increase in uncertainty of 7-55x depending on the order, resulting in typical per-order S/N of 10-40.

After processing, we omitted two-thirds of the spectral orders from the final analysis based on their level of telluric overlap or in some cases because the ambient or spotted component was very poorly constrained, possibly due to the spectral model fidelity problem (Iyer & Line, 2020; Rackham & de Wit, 2023). The orders we include in the final analysis are 53, 54, 59, 61, 69, 71, 72, 75, 76, 81, 82, and 83, with details in Table 4.2. In F21, there are total of 1831 spectral data points, with 1828 in S22, for a total of 3659 spectral data points. Discussion on the choice of orders to include and spectral model results for each individual order are in the Appendix.

4.4 Methods

Our analysis is ordered in three steps:

(1) Measuring the stellar rotation signal, where photometric data is modeled as a sine wave to

infer the semi-amplitude of stellar variability.

(2) Modeling spot characteristics, where we infer spot characteristics based on AU Mic's $T_{\rm eff}$, measured photometric variabilities, and the time-averaged spectra. This is the primary focus of our analysis.

(3) Forward modeling the TLSE, where we take the posterior samples from our modeling to calculate the range of spectral contamination we can expect in the HST/WFC3 transmission data for AU Mic b.

Figure 4.2 shows the cartoon stellar surface we model as a combination of ambient photosphere with a characteristic spectrum $S(\lambda, T_{\rm amb})$ and spots with characteristic spectra $S(\lambda, T_{\rm spot})$ covering a globe-averaged $f_{\rm spot}$ which deviates from the average coverage by $\pm\Delta f_{\rm spot}$ throughout the stellar rotation. We include a third flux component (not shown on the figure) and label this component "hot" (with attributes $f_{\rm hot}$ and $T_{\rm hot}$) as we are uncertain about the physical source of the measured hot component, if it exists. The primary results we report in section 4.5 come from this 3-temperature modeling, but we also test a 2-temperature model and discuss its results and implications in section 4.6. The two visits are modeled with the same set of parameters (implying no change to the surface components between visits), an assumption we test and discuss later in the paper.

4.4.1 Measuring Photometric Variability

Once the photometry data were processed as described in Section 4.3, we measure the rotational variability with a sinusoidal model with the following form:

$$F(t) = A\ \sin(2\pi t/P) + B\cos(2\pi t/P) + C_k, \tag{4.1}$$

where t is the time of an individual data point, P is the stellar rotation period which we keep fixed at 4.86 days, A and B are amplitude parameters, and $C_{\rm k}$ is the offset parameter unique to each camera in each visit. We fit each camera's data separately as we expect different cameras to have slightly different responses and should be normalized to their separate average fluxes. While AU Mic has a notably asymmetric light curve (e.g., the TESS light curves shown in Martioli et al., 2021) and Angus et al. (2018) caution against using simple sinusoidal models to fit stellar rotation curves, our goal here is not to infer a precise rotation curve morphology and spot distribution but to measure the relative amplitude of flux variability between separate bandpasses.

Using `emcee` (Foreman-Mackey et al., 2013), we ran a Markov Chain Monte Carlo (MCMC) with 100 walkers, 1000 steps, and 25% burn-in. We used the auto-correlation time to judge when the sampler had converged for each parameter (e.g., Hogg et al., 2010). Median-value parameters and their 1-σ uncertainties calculated from the sample distributions are propagated through to the following reformulation of Equation 4.1:

$$F(t) = X\sin(2\pi t/P + \theta) + C_k, \tag{4.2}$$

where $X = \sqrt{A^2 + B^2}$ and $\theta = \arccos(A/X)$. X is the photometric semi-amplitude of variability (or $\frac{\Delta \mathrm{S}}{\mathrm{S_{avg}}}$) for a given photometric bandpass, which we use as inputs for the spot characteristics model described below. We inflate the uncertainty on each variability measurement by 25% to account for the assumptions of a simple rotation curve and negligible facular contribution.

Quantity	**Prior**
$\mathrm{T_{eff}}$ [K]	3650 ± 100
$\mathrm{T_{hot}}$[K]	$\mathcal{U}[\mathrm{T_{amb}}, 12000]$
$\mathrm{T_{spot}}$ [K]	$\mathcal{U}[2300, \mathrm{T_{amb}}]$
$\mathrm{T_{amb}}$ [K]	$\mathcal{U}[\mathrm{T_{spot}}, \mathrm{T_{hot}}]$
f_{hot}	$\mathcal{U}[0,0.5]$
f_{spot}	$\mathcal{U}[0,(1.0\text{-}f_{\mathrm{hot}})]$
Δf_{spot}	$\mathcal{U}[0, f_{\mathrm{spot}}]$

Table 4.3: Priors placed on our model parameters in the spot characteristics Monte Carlo simulation.

4.4.2 Spot Characteristics Model

To draw inferences about AU Mic's spot and facula characteristics, we assembled a model for 3 data components: The effective temperature, $\mathrm{T_{eff}}$, the photometric semi-amplitude of variability,

$\frac{\Delta S}{S_{\rm avg}}$, and the time-averaged stellar spectrum, $S_{\rm avg}$. Each of these components is modeled as a function of some combination of $f_{\rm hot}$, $f_{\rm spot}$, $T_{\rm hot}$, $T_{\rm spot}$, and $T_{\rm amb}$, with model priors described in Table 4.3.

Modeling photometric variability requires one additional parameter, the |peak-average| amplitude of the change in spot coverage throughout a rotation, $\Delta f_{\rm spot}$. This parameter represents a change in spot coverage relative to the average coverage in a way that is not relevant to our models of the time-averaged spectral data or $T_{\rm eff}$. It can range from 0, where the surface is homogeneous or the surface features are distributed symmetrically around the rotation axis, to $\Delta f_{\rm spot}$=$f_{\rm spot}$, where the total spot coverage is clustered on the surface such that it rotates entirely in and out of view. While photometric variabilities only provide a lower limit on the *average* spot coverage fraction, the magnitude of variability depends strongly on this change in spot coverage throughout a rotation and can be precisely constrained with sufficient evidence of the spectral contrast between the ambient and spotted photosphere.

Effective Temperature Similar to Libby-Roberts et al. (2022), we treat $T_{\rm eff}$ in the following form:

$$T_{\rm eff}{}^4 = f_{\rm spot} T_{\rm spot}{}^4 + f_{\rm hot} T_{\rm hot}{}^4 + f_{\rm amb} T_{\rm amb}{}^4, \tag{4.3}$$

where $f_{\rm spot}$ is the globally-averaged spot coverage fraction with temperature $T_{\rm spot}$, $f_{\rm hot}$is the average coverage of any potential third component (which may be faculae, flares, or something else) with temperature $T_{\rm hot}$, and $f_{\rm amb}$ is the coverage of the ambient photosphere which has temperature $T_{\rm amb}$. The ambient coverage is not a unique parameter in the model but is calculated as $f_{\rm amb} = 1 - (f_{\rm spot} + f_{\rm hot})$. This constraint effectively ensures that whatever combination of spectral components is being modeled accurately reproduces the known surface-averaged bolometric flux emitted from the stellar surface.

Photometric Variability Following the formalism in Libby-Roberts et al. (2022), we can calculate the semi-amplitude of variability due to spots as the following:

$$\frac{\Delta S(\lambda)}{S_{\rm avg}(\lambda)} = -\Delta f_{\rm spot} \left(\frac{1 - \frac{S(\lambda, T_{\rm spot})}{S(\lambda, T_{\rm amb})}}{1 - f_{\rm spot}[1 - \frac{S(\lambda, T_{\rm spot})}{S(\lambda, T_{\rm amb})}]} \right). \tag{4.4}$$

The expression above, the only calculation in our model which depends on Δf_{spot}, is integrated across the filter bandpasses to generate a single variability datum for each filter. We account for the filter response curves by normalizing our variability integral by the filter response function:

$$\frac{\Delta S}{S_{\mathrm{avg}}} = \frac{\int_{\lambda_1}^{\lambda_2} \frac{\Delta S(\lambda)}{S_{\mathrm{avg}(\lambda)}} W(\lambda) S(\lambda, \mathrm{T_{eff}}) \mathrm{d}\lambda}{\int_{\lambda_1}^{\lambda_2} W(\lambda) S(\lambda, \mathrm{T_{eff}}) \mathrm{d}\lambda}, \tag{4.5}$$

where the SDSS filter response functions (W_{λ}) are acquired through `Speclite`[4] . The stellar spectrum term ($S(\lambda, \mathrm{T_{eff}})$, calculated at $\mathrm{T_{eff}} = 3650K$) accounts for the non-uniform distribution of stellar flux emitted across bandpasses. These bandpass-integrated model variabilities are then fit to the broadband variability measurements extracted from the stellar rotation curve models (section 4.4.1).

We ignore a facular contribution to the rotational variability because magnetically active stars are expected have photometric variabilities dominated by spots (Shapiro et al., 2016), an assumption we argue is valid considering the low filling factor of this component we measure, discussed in the results. It does factor into the calculation of $\mathrm{T_{eff}}$ however, and therefore indirectly affects the model results when we examine the variability separate from the spectra. The variability light curve is also highly under-sampled, so adding another component for this stage would be over-fitting the very few (5) photometric variability data points we have.

Average Spectrum From the NRES Echelle spectra, we calculate a time-averaged spectrum which we model as a combination of a spotted spectrum and an ambient spectrum weighted by their globally-averaged coverage:

$$\mathrm{S_{avg}} = f_{\mathrm{spot}} S(\lambda, \mathrm{T_{spot}}) + f_{\mathrm{hot}} S(\lambda, \mathrm{T_{hot}}) + f_{\mathrm{amb}} S(\lambda, \mathrm{T_{amb}}). \tag{4.6}$$

Older studies of starspots have been limited in this approach due to the computation time required to model thousands of spectral lines and as a result they typically probed specific regions and rotational or vibrational temperatures which may not be indicative of the bulk spot properties. Here we modeled as many possible regions of the spectrum as possible, including orders which have

---

[4] `https://speclite.readthedocs.io/en/latest/filters.html`

weak or non-existent spot signatures as well as those with strong signatures indicative of very cool regions, to understand the most complete picture of the star provided by the spectral data.

4.4.3 Spot Contamination Model

Atmospheric absorption will induce a wavelength-dependent change in the transit depth ($\Delta \mathrm{D}(\lambda)$) of the planet, expressed as

$$\Delta \mathrm{D}(\lambda) = \left(\frac{\mathrm{R_p}}{\mathrm{R_*}}\right)^2 + \Delta \mathrm{D}(\lambda)_{\mathrm{atm}} + \Delta \mathrm{D}(\lambda)_{\mathrm{spot}}, \tag{4.7}$$

with $\Delta \mathrm{D}(\lambda)_{\mathrm{atm}}$ is defined as:

$$\Delta \mathrm{D}(\lambda)_{\mathrm{atm}} = \frac{2\mathrm{R_p}}{\mathrm{R_*^2}} \mathrm{H} \times \mathrm{n}(\lambda), \tag{4.8}$$

where H is the scale height and $n(\lambda)$ is the number of opaque scale heights at each wavelength, which typically varies between 0-5 for cloud-free atmospheres (Seager & Sasselov, 2000b).

Following the derivations in Rackham et al. (2018); Zhang et al. (2018); Libby-Roberts et al. (2022), we can express $\Delta \mathrm{D}(\lambda)_{\mathrm{spot}}$ as:

$$\Delta \mathrm{D}(\lambda)_{\mathrm{spot}} = \left(\frac{\mathrm{R_p}}{\mathrm{R_*}}\right)^2 \left[\frac{(1 - f_{\mathrm{spot,tra}}) + f_{\mathrm{spot,tra}} \frac{\mathrm{S}(\lambda, \mathrm{T_{spot}})}{\mathrm{S}(\lambda, \mathrm{T_{amb}})}}{(1 - f_{\mathrm{spot}}) + f_{\mathrm{spot}} \frac{\mathrm{S}(\lambda, \mathrm{T_{spot}})}{\mathrm{S}(\lambda, \mathrm{T_{amb}})}} - 1\right]. \tag{4.9}$$

This expression can similarly be used to calculate facular depth contribution but we assume this contribution is negligible on AU Mic. Equation 4.9 does not explicitly rely on Δf_{spot}, but the value we derive for Δf_{spot} can be used to project the spot coverage at a given time or phase, which is needed to account for spot contamination at the time of transit. In this work we assume f_{tra} to be zero for both spots and faculae, which implies that the contamination calculated for a given set of parameters represents an upper limit relative to a spotted transit chord. Samples for f_{spot}, f_{hot}, $\mathrm{T_{spot}}$, $\mathrm{T_{hot}}$, and $\mathrm{T_{amb}}$ are injected into this model to generate a posterior distribution of $\Delta \mathrm{D}(\lambda)_{\mathrm{spot}}$.

4.4.4 Experimental Design

We run several different iterations of the spot characteristics model in order to examine the information and constraints provided by each component of the data: we model the photometric measurements separate from the spectra, the spectra without photometric models, and the ensemble model which includes both data types. The model is set up as a Monte-Carlo simulation using the `emcee` sampler (Foreman-Mackey et al., 2013), run with 100 walkers and 2000 steps with a 25% burn-in. Models ran past convergence in accordance with the auto-correlation time of the sampler chains (for a discussion of convergence and autocorrelation, see Foreman-Mackey et al., 2013). This framework maintains a distinction between the temperatures of the different spectral surface components ($T_{\rm spot} \leq T_{\rm amb} \leq T_{\rm hot}$) while allowing $f_{\rm spot}$ and $f_{\rm hot}$ to vary, enabling models to arrive at solutions where the the surface is ≥50% covered in spots. Technically $f_{\rm hot}$ is allowed to vary as high as 50% but in practice the models almost never preferred values of $f_{\rm hot}$ greater than a few percent. Time-domain analysis of the 7 NRES spectra from F21 and 17 spectra from S22 should contain information about the change in spot coverage with stellar phase but no periodic signal could be found so we do not include a time-domain spectral model in the analysis. Independent modeling of the separate visits returned strongly consistent measurements for $f_{\rm spot}$, $f_{\rm hot}$, and $\Delta f_{\rm spot}$ which could be be a robust finding, considering the time between visits is 2× the 120-150 day activity evolution timescale (which we can approximate to be a spot decay timescale) measured by Donati et al. (2023).

4.5 Results

4.5.1 Variability Amplitude Results

For the F21 visit, we measure variability semi-amplitudes, $\Delta S/S$, in g', r', and i' of 0.075±0.006, 0.071±0.006, and 0.041±0.007, and for the S22 visit we measure $\Delta S/S$ of 0.075±0.003 in g' and 0.075±0.003 in r', shown in Figure 4.3 and summarized in Table 4.4.

Measuring the signal for i' was slightly challenging because, as the reddest bandpass, this filter showed the weakest variability signal and therefore smallest signal-to-noise. Moreover, AU Mic is much brighter than the nearby comparison stars and exposure times are short, scintillation noise is prevalent. To account for poorly constrained measurements in i' and improve the internal

Filter	**Amplitude**	**phase**
First Visit (F21)		
g'	0.075±0.006	1.89 ± 0.05
r'	0.071±0.006	1.93 ± 0.05
i '	0.041±0.007	2.00 ± 0.04
Second Visit (S22)		
g'	0.075±0.003	2.02 ± 0.04
r'	0.075±0.003	2.03 ± 0.04

Table 4.4: Parameters from the MCMC fits of the photometry. Period was kept fixed at the literature period of 4.86d while the phase and amplitude were modeled as a combination of sine and cosine terms.

consistency of our multi-color variability measurements, we impose a prior on the phase (θ) for *i*'. The independently-modeled g' and r' rotation curves agree within their 1-σ uncertainties in phase, so we use the average of their phases (1.91+/-0.04) as a prior when modeling *i*', resulting in a modeled phase in agreement with *g*' and *r*'. This is a reasonable approach to improving our i' results because we would expect the phase of 3 separate but contemporaneous data sets to be equal, so forcing the i' phase to be consistent with g' and r' increases the consistency between the three measurements and lends confidence to the relative amplitudes our signal measurements. The phase is not used further in this work but will be useful for the analysis of AU Mic b's atmospheric transmission spectrum when we need to estimate the spot coverage at the time of transit.

4.5.2 Spot Characteristics Model

We examine the spot characteristics results when we model only the stellar effective temperature and photometric variability data (excluding NRES spectral models) and similarly when we model only the NRES spectra with stellar effective temperature (excluding the multi-color photometric variability data). Finally, we examine the results of modeling the stellar T_{eff}, photometric variabilities, and NRES spectra together in an "ensemble" model which models the 12 spectral orders and multi-color variabilities for both visits, from which we report the final results.

4.5.2.1 Photometric Variability

Figure 4.4 shows our measured photometric variability semi-amplitudes with random samples drawn from the photometry-only posterior distributions, with statistical results in Figure 4.6. The photometric variabilities, along with AU Mic' $T_{\rm eff}$, show evidence for essentially any spot coverage between 10-90% with temperature 3141^{+266}_{-389} K, changing throughout an orbit by $6 \pm 3\%$. Solutions for ambient temperature are 3719^{+302}_{-502} K, with an upper limit of 40% coverage of a hot component with temperature 4873^{+1922}_{-727}K. The hot component is only relevant to the effective temperature calculation in the variability-only modeling, so it is acting more as an extra free parameter to improve the fit than it is related to anything physical. The measurement of $T_{\rm spot}$ is surprisingly accurate compared to the other measurements in this paper and others.

2-Temperature Models of the variabilities return tighter constraints on the *ratio* of $T_{\rm spot}$ to $T_{\rm amb}$ and their individual measurements, but the measurement of $T_{\rm spot}$ is significantly warmer ($T_{\rm spot}$=3454^{+155}_{-208} K) than virtually every other measurement of $T_{\rm spot}$ we present in this paper. Measurements of $f_{\rm spot}$ and $\Delta f_{\rm spot}$ are consistent with the 3-temperature fits. Results for two-temperature modeling are in Table 4.6.

4.5.2.2 Spectral Decomposition Results

When modeling the 12 spectral orders (Figure 4.5) simultaneously and without photometric variability, we find more precisely constrained temperatures and coverages of all three components. The change in spot coverage, $\Delta f_{\rm spot}$ is unconstrained by these models because we are modeling time-averaged spectra. The stellar spectra indicate a large fraction ($f_{\rm spot}$=0.39 ± 0.04) of cool spots with temperature 2974^{+72}_{-71} K, a dominant "ambient" (warmer) photosphere with temperature 4002^{+14}_{-15} K, and a very tenuous detection of a hot component with temperature 8681^{+868}_{-629} K covering less than 0.5% of the surface.

2-Temperature Models of the spectra result in fully consistent measurements of each parameter. The spot component measured to cover $41 \pm 3\%$ of AU Mic with temperature 3083^{+31}_{-45}

K, and the ambient photosphere temperature is measured to be 3998^{9}_{11} K.

4.5.2.3 Ensemble Model

Results from our ensemble model, where all 5 photometric variability measurements are jointly modeled with the spectra of both visits, are shown in Figures 4.6, 4.7, and 4.8, along with Table 4.5. This model finds well-constrained spot characteristics of f_{spot}=0.39±0.04, $\Delta f_{\text{spot}}=0.05^{+0.004}_{-0.003}$, and $\text{T}_{\text{spot}}=3003^{+63}_{-71}$ K, with $\text{T}_{\text{amb}}=4003^{+15}_{-14}$ K.

Some degenerate solutions can be seen which prefer what looks like a fourth flux component between 3600-3900 K with a coverage fraction of 6-10%. This could be very weak evidence of either the spot penumbra or faculae, but attempts to extract that component were unsuccessful and can be pursued more in future work.

We can see that this ensemble model exhibits characteristics of both the photometry-only and spectra-only models. The photometric variabilities strongly constrain Δf_{spot} and the temperature ratio but provide poor constraints on the quantity of spots. Variability measurements in multiple wavebands across the optical-NIR constrain temperature contrast because the relative change in variability with wavelength is set by the ratio of spectral temperature components. Further into the red, the spectral components are more similar and variability decreases. At bluer wavelengths, variability reaches a maximum as the difference in spectra is greatest.

The spectral decomposition returns a precise estimate of f_{spot}, which is further constrained with the inclusion of photometric modeling. The cold spot preference of the spectral models is balanced by the photometric limits on how cool the spots can be, given the contrast at longer wavelengths. The spot coverage fraction is unconstrained when modeling the photometry due to degenerate observational effects between f_{spot} and T_{spot} but is precisely constrained when spectral modeling is included. The ensemble model results are primarily driven by the spectra, with the photometry being most important for the measurement of Δf_{spot}.

We argue that the consistency between measurements of the separate components based on different data-model combinations indicates that the results we report from the ensemble model

Parameter	Photometry Model	Spectral Model	**Ensemble Model**
$T_{\rm spot}$ (K)	3141^{+266}_{-389}	2974^{+72}_{-71}	3003^{+63}_{-71}
$f_{\rm spot}$	$0.57^{+0.22}_{-0.28}$	0.39 ± 0.04	0.39 ± 0.04
$\Delta f_{\rm spot}$	0.06 ± 0.03	< 0.40	$0.05^{+0.004}_{-0.003}$
$f_{\rm hot}$	< 0.40	< 0.01	< 0.005
$T_{\rm hot}$ (K)	4873^{+1922}_{-727}	8681^{+868}_{-629}	8671^{+890}_{-629}
$T_{\rm amb}$ (K)	3719^{+302}_{-502}	4002^{+14}_{-15}	4003^{+15}_{-14}
$T_{\rm eff}$ (K)	3664 ± 101	3783 ± 37	3789 ± 35
χ^2	2.59 (2.59)	2124 (0.581)	2136 (0.584)

Table 4.5: Parameters from fitting the different data combinations with a 3-temperature model. The photometry model uses the 5 photometric variability measurements, the spectral model uses 12 spectral orders from both visits. The ensemble model is applied to all the photometric and spectroscopic data. Results are broadly consistent with the 2-T model, most importantly recovering an approximately 3000K spot in either case. The results we recommend citing for AU Mic's surface components are the Ensemble Model results in the rightmost column of this table.

are physically realistic.

2-Temperature Models agree with the 3-temperature results remarkably well, showing spot coverage of $41 \pm 3\%$ that changes throughout a rotation by $5.1 \pm 0.3\%$, with $T_{\rm spot}=3093^{+29}_{-41}$ and $T_{\rm amb}=3998^{+10}_{-12}$.

4.5.3 Spot Contamination

We forward-modeled spot contamination (Equation 4.9) under the assumption of 0% spot coverage on the transit chord using ensemble model posteriors generated in the previous step, shown in Figure 4.9. At short wavelengths like the TESS bandpass (0.6-1μm), contamination ranges from 550-1400 ppm. In the WFC3 bandpass, contamination is between 500-750ppm, and decreases to 250-500ppm at longer wavelengths. The transit depth of AU Mic b reported in Szabó et al. (2022) calculated from TESS and CHEOPS (0.33-1.1μm) transits translates to about 1875 ppm, so the spot contamination is 25-75% of that signal if $f_{\rm tra} = 0$. This means that without accounting for spot contamination, AU Mic b's true radius (3.46 R_E if the Szabó et al. (2022) value is uncontaminated) may be overestimated by as much as 0.5-1.7 Earth radii. For AU Mic c, the Szabó et al. (2022) depth is about 980 ppm, with contamination calculated to be between 400-750 ppm. This translates to an over-estimated planetary radius of between 0.6-1.3 Earth radii.

Parameter	Photometry Model	Spectral Model	Ensemble Model
$T_{\rm spot}$ (K)	3454^{+155}_{-208}	3083^{+31}_{-45}	3093^{+29}_{-41}
$f_{\rm spot}$	$0.61^{+0.22}_{-0.27}$	0.41 ± 0.03	0.41 ± 0.03
$\Delta f_{\rm spot}$	$0.08^{+0.06}_{-0.04}$	< 0.4	0.05 ± 0.003
$T_{\rm amb}$ (K)	3876^{+234}_{-157}	3998^{9}_{11}	3998^{+10}_{-12}
$T_{\rm eff}$ (K)	3649 ± 98	3704 ± 24	3707 ± 24
χ^2	1.9 (1.9)	3060 (0.837)	3058 (0.836)

Table 4.6: Parameters from fitting the different data combinations with a 2-temperature model. The photometry model uses the 5 photometric variability measurements, the spectral model uses 12 spectral orders from both visits. The ensemble model is applied to all the photometric and spectroscopic data. The primary difference compared to 3-T results can be seen in the temperatures measured for $T_{\rm spot}$ and $T_{\rm amb}$.

The magnitude of this shorter-wavelength contamination may be much different at different points in AU Mic's activity cycle and long term magnetic evolution, so these are rough estimates and contemporaneous measurements of transit depths across the optical to infrared would shed more light on the true radius of AU Mic b.

4.6 Discussion

In this work, we present an analysis of broadband photometry and high-resolution spectroscopy to constrain the spot coverage fraction and temperature contrast on AU Mic. This is crucial for addressing the spot contamination in the transmission spectrum of AU Mic b and therefore understanding its atmosphere. With observational data of stellar effective temperature, multi-color time-series photometry, and high resolution stellar spectra, we parameterized the spectroscopic and photometric effects of starspots into spot coverage and temperature, with a well-constrained ambient temperature and tentative measurement of a hot component.

4.6.1 The Photometric Variability Spectrum

Photometric variability has wavelength-dependent characteristic which can be used to constrain the primary flux components. Amplitudes increase to some maximum at blue wavelengths as the flux contrast increases to 1, and decreases at redder wavelengths toward the Rayleigh-Jeans limit. The shape and extent of the amplitude of rotational variability as a function of wavelength provides an important constraint on spot temperatures. Because our measured variability amplitude is significantly less in i' than g' or r', the spot temperature contrast is very sensitive to the magnitude and uncertainty of i'. The i' variability measurement thus carries more weight than any other single data point in this study, as it strongly constrains spot contrast and limits how cool the spots can be. If the i' measurement showed greater variability, this would allow spot temperature solutions to be cooler, as the contrast would be greater into the red. The variability must instead decrease in this bandpass, which forces the range of solutions to be narrower and the spot contrast to be within a certain range. The importance of this i' measurement indicates that further photometric studies of spotted stars must be sure to include multiple bandpasses in the optical-to-infrared in order to precisely determine the wavelength regime where variability decrease or *"turn-off"* happens. The wavelengths where this turn-off is observed are highly descriptive of the stars spot spectra.

4.6.2 Two Flux Components or Three?

The primary results in this work are reported from the 3-temperature modeling, but we examine how those results changed when modeled with only two temperatures, finding it returns tightly constrained and consistent measurements for f_{spot}, Δf_{spot}, T_{spot}, and T_{amb}. When we allow a third component, it finds a poorly constrained temperature between 7000-10000 K, with a small number of solutions closer to the ambient photosphere, around 4000-5000 K. If the 7000-10000 K component is physical, it may be due to flares which are persistent enough to leave their flux in the median-averaged spectra.

Faculae on M dwarfs may be up to a few hundred K above the ambient photosphere (e.g., Norris et al., 2023) and a small cluster of solutions in this temperature range stand apart from the primary results (seen in Figures 4.6 and 4.7). This could be indicative of faculae but we did not recover that component in concerted attempts and its filling factor must be even less than the filling factor measured for the hotter temperature, detected at less than 0.5%.

There is one key difference in outcome between 2- and 3-temperature models. When modeling only T_{eff} and photometric variabilities, the 2-temperature model returns a significantly warmer T_{spot} and a tighter ratio of T_{spot} to T_{amb} compared with the 3-temperature model. A third temperature, which only factors into the calculation of T_{eff}, brings spot temperature solutions into agreement with the other measurements we report, with larger uncertainties and a weaker (though still noticeable) relationship between spotted and unspotted temperatures.

Further investigation into multi-component rotation models and independent measurements of spot temperatures will be needed to help clarify when 2- or 3-temperature rotation models are most appropriate, and what cautions to impose on interpreting spot characteristics from photometric variabilities alone.

4.6.3 Physical Interpretation of AU Mic's Spot Characteristics

Much work has been done to measure and theoretically determine spot temperatures, distributions, and filling factors as a function of stellar type. Still, observational evidence of consistent spot temperatures and precise filling factors for AU Mic is tenuous. Spot characteristics are notoriously difficult to determine and different approaches can lead to inconsistent results. Here we will discuss the results, limitations of this approach, and physical interpretation of AU Mic's starspots.

Spot Temperature We report a characteristic spot temperature for AU Mic of $T_{\text{spot}} = 3003^{+63}_{-71}$ K. A study of diatomic molecular lines in AU Mic's spot spectra found in Berdyugina et al. (2011) implies a ΔT (T_{eff}-T_{spot}) of 500-700 K, which would translate to spot temperatures of 3000-3200 K for a star with T_{eff} of 3700 K. More recently, Ikuta et al. (2023) calculate $T_{\text{spot}} = 3140 \pm 64$K for AU Mic based on Equation 4 of Herbst et al. (2021), which is based on the work done by Berdyugina (2005). Rackham et al. (2018) suggest that for cool stars, T_{spot} can be estimated as $0.86 \times T_{\text{phot}}$ (which we have labeled T_{amb} in this work). Given our modeled T_{amb} of 4003^{+15}_{-14}, the estimated spot temperature would be roughly 3300-3400K, which is over 200K warmer than our spectral and ensemble results but in agreement with our photometry-only model results. Recent work by Flagg et al. (2022) found evidence of a cold H_2 layer in AU Mic's photosphere with 1000K $<$T$_{\text{spot}}<$ 2400K. Afram & Berdyugina (2019) use molecular lines to measure spot temperatures and find that M0 stars may have spot temperatures $\sim$2200K less than the stellar effective temperature, implying spots on AU Mic may have T$_{\text{spot}}$ $\lesssim$ 1500 K and T$_{\text{spot}}$-to-T$_{\text{eff}}$ ratios $\sim\leq$ 0.4.

Placed in context, the spot temperatures we measure in this work are much cooler than the $\Delta T = 400$K or T$_{\text{spot}}$=0.86T$_{\text{amb}}$ estimates for low mass stars and slightly cooler than (but consistent with) the Ikuta et al. (2023) and Berdyugina et al. (2011) estimates for AU Mic, warmer than some of the molecular and vibrational estimates for spots, but consistent with older measurements of spot temperatures on young active stars similar to AU Mic (e.g., Ramsey & Nations, 1980; Vogt, 1981). The range of temperatures measured using different methods may be indicative that our assumption of spots as a feature with a single descriptive bulk temperature is breaking down, and we need to further develop our theoretical spot models to account for a temperature gradient. If the spots on AU Mic have complex temperature profiles and extensive penumbrae, then the f_{spot}recovered in these models may be an overestimate of the true spot umbra and an under-estimate of the spot umbra + penumbra.

Spot Filling Factor Our models indicate that the surface of AU Mic is f_{spot}= 0.39 ± 0.04 covered in cool spots, with a change in spot coverage throughout a stellar rotation of Δf_{spot}= $0.05^{+0.004}_{-0.003}$. This estimate is within the very broad and uncertain range of possible spot coverage fractions measured for sun-like and cooler stars and indicates a heavily spotted stellar surface. Yamashita et al. (2022) estimate f_{spot} of between 1-21% for Zero Age Main Sequence stars using a fixed starspot temperature variability model, but such models are typically underestimates on f_{spot} (Rackham et al., 2018; Apai et al., 2018). Cao et al. (2022) use APOGEE H-band spectra to measure average spot filling factors to be 0.248±0.005 for active stars in the Pleiades cluster and 0.03±0.008 for main sequence G and K stars in M67. Other estimates of f_{spot} for low mass stars range from $<$ 1% to 50% (see Table 3 in Rackham et al., 2018). Our results are consistent with the range of expected coverage fractions, and our derived Δf_{spot} is consistent with values modeled by Libby-Roberts et al. (2022) of $\Delta f_{\text{spot}}\leq$ 0.1, though this is a much older and slowly rotating star.

4.6.4 Caveats

Here we will briefly describe some of the limitations of this work and possible directions for future spot studies.

- We use a simple sinusoidal rotation model, which is not necessarily the best choice for complex rotation curves like AU Mic's, but the photometry is not densely sampled and individual measurements have large uncertainties, so for the primary purpose of measuring the *relative* amplitude of variability between filters we argue this is an appropriate model.
- AU Mic is a bright star, so ground-based differential photometry is difficult with LCO's field of view. Without similarly bright field stars, our photometry is very noisy, limiting the precision with which we can measure variability signals, especially in redder bandpasses.
- Our spot contamination forward-models assume that $f_{\mathrm{tra}} = 0$, which means our contamination results are upper-limit cases for different sets of spot parameters. In reality, there may be some non-zero fraction of spot coverage on the transit chord, which will lower the contamination level in the transmission spectrum.
- It is unclear what the source of the hot component is or whether it is truly a real signal, and the choice to include a third component affects the measurement of spot temperature from photometric variability models.
- Our understanding of M star photosphere spectra is limited with the current generation of high-resolution synthetic spectral libraries like the Husser et al. (2013) PHOENIX models, described in detail by Iyer & Line (2020) and Rackham & de Wit (2023). Choosing the best spectral template is a problem for cool stars generally, but describing AU Mic with these models is further complicated by its pre-main sequence age, a specific environment for which no truly appropriate model spectra yet exist. Alternative spectral models for M dwarfs exist, such as BT-SETTL (Allard et al., 2011; Allard, 2014) or SPHINX (Iyer et al., 2023), but those are low- to mid- resolution libraries whereas the Husser et al. (2013)

library has a resolution of R=100000-500000 and is more appropriate for the R=53000 echelle spectra we acquired.

4.7 Conclusions

In this work, we have demonstrated the use in acquiring broadband photometry and high-resolution spectroscopy of only the star (without data acquired during transit) for the purpose of studying starspots and estimating their effect on transmission spectra. The results of our modeling lead us to the following conclusions:

- At the time of these observations, AU Mic may have been $f_{\rm spot}$=39±4% covered in spots with a change of $\Delta f_{\rm spot}$=6±1% throughout a rotation. The spots have a bulk (flux-weighted, not distinguishing umbra from penumbra) temperature of $\rm T_{spot}=3003^{+63}_{-71}$ K surrounded by a $\rm T_{amb}=4003^{+15}_{-14}$ K photosphere. We found very weak evidence for facular coverage, and tentatively detect evidence of flux from flares with characteristic temperature 8671^{+890}_{-629} K. The fractional uncertainties measured on our final results for $\rm T_{amb}$ and $\rm T_{spot}$ come out to 0.25% and 2%, respectively. Berardo et al. (2023) report theoretical precision limits on stellar spectral models with current instruments and spectral libraries, finding we can constrain photospheric spectra to $\geq 0.2\%$ and spot spectra down to $1-5\%$, which translate to temperature uncertainties of $\leq$ 0.05% on $\rm T_{amb}$ and $0.25-1.25\%$ on $\rm T_{spot}$. If our results are physically accurate, we have measured the temperature of AU Mic's spots with a precision near but slightly worse than the Berardo et al. (2023) theoretical precision limit, and AU Mic's ambient photosphere temperature down to near its limit.
- Spot contamination in transmission spectra for AU Mic b will be significant, adding between $250-1200$ppm contamination across the 0.5-5μm range, overlapping with wavelengths where we measure planetary absorption features. This contamination is based on zero spot coverage on the transit chord, which could likely be an incorrect assumption if the large spot coverage fraction we measure is accurate. Nevertheless, spot contamination may be

causing us to significantly overestimate the radii of AU Mic b and c. Determining the true planetary radii may require further acquisition and study of contemporaneous multi-color transit observations.

- From these measurements we calculate T_{amb}-$T_{\text{spot}} = 1000$ K and $T_{\text{spot}}/T_{\text{amb}} = 0.75$. Spots this cool should show up noticeably if occulted in transit if our measurements and interpretation of AU Mic's photosphere are correct, but none have yet been confirmed. With AU Mic's short period and large radius, it is possible that spots exist primarily or only at high latitudes, in which case spot crossings would be rarely or never observed.

- For stellar surfaces dominated by a single heterogeneity like spots (*or* faculae, but the picture becomes more complicated with significant filling factors of both), multi-color photometric variabilities provide significant constraints on the ratio of $T_{\text{spot}}/T_{\text{amb}}$(or $T_{\text{fac}}/T_{\text{amb}}$) and potentially accurate measurements of T_{spot}. Sampling the sensitive regions of a star's *variability spectrum*, even with broad photometric bandpasses, is useful for roughly estimating the temperatures of different spectral components.

- Modeling the data with either 2-T or 3-T spectral decomposition did not significantly change measurements of T_{spot}, T_{amb}, or Δf_{spot}, which indicates that these measurements are robust. As we are uncertain of the nature and significance of the hot component we detect, further investigation of the phase-resolved stellar spectrum may help distinguish the nature of the different flux components.

- Modeling only the variabilities provides a less accurate result for the coverage fraction or when only 2 temperatures are included, even though this only affects the calculation of T_{eff}. The 3-T T_{eff} and variability model returns an accurate (but highly uncertain) spot temperature while the 2-T T_{eff} and variability model prefers spots of nearly half the temperature. We recommend further investigation into the accuracy of measuring spot and/or facula temperatures with multi-color rotation modulations using both 2- and 3-

temperature modeling.

- Improving measurements of spot characteristics on exoplanet host stars and understanding spot contamination is challenging but tractable with a multi-modal approach that covers a broad range of the visible-IR electromagnetic spectrum. As spot models and synthetic spectra improve, spot characteristics on our host stars will become much clearer.

4.8 Appendix

We include this appendix to show visit-specific models of the photometric variabilities (Figure 4.10), and order-specific modeling of the NRES spectra (Figure 4.11). Comparing F21 and S22 variability models demonstrates how important the i' measurement is and the relative constraints provided with or without it. The order-specific spectral models show agreement in many ways, as well as some poorly constrained orders which are likely due to telluric contamination.

4.8.1 Visit-Specific Variability Measurements

While the magnitude of stellar variability in any given waveband is related to degeneracies between spot temperature and spot coverage, the relative variability between photometric bandpasses and the wavelengths where the variability begins to decrease contain a lot of information about the spectral temperatures on the surface of the star. If the bulk spot temperatures are very cold relative to the photosphere, the variability will remain high at redder wavelengths. Similarly, if spot temperatures are closer to the ambient photosphere temperature, then the variability will decrease within optical and bluer wavelengths. The right panel in Figure 4.10 shows the greater spread in models at redder wavelengths resulting from the absence of an i' measurement, allowing the spot temperatures can be much cooler and much further from the ambient photosphere. The different model solutions possible are strongly constrained by this i' variability, and we extend that observation to say that multi-color photometric variabilities covering the optical-NIR provide very strong constraints on the temperature contrast for spotted stars.

4.8.2 Spectral Decomposition by Order

In the ensemble model described in the main text, we fit spotted spectral models to 18 orders simultaneously, but here we examine the results from modeling each order individually to check for consistency between orders and which orders might be the most informative. In this part of the modeling, we model the data from both F21 and S22 with the same set of parameters, under the assumption that AU Mic's spot characteristics have not changed measurably between visits. Examining the results (Figure 4.11), we cut orders from the analysis if their solutions are poorly constrained and they satisfy any of the following criteria: there is telluric contamination, unconstrained ambient characteristics (which should be the dominant signal), or extremely cold spot temperatures (which is often coincident with heavy telluric contamination). Spectral orders that satisfy these conditions are excluded if we suspect useful information cannot be gained from the spectral order, most frequently due to telluric contamination. Many orders also exhibit what appears to be a hot component a few hundred Kelvin hotter than the ambient component, which could be evidence of a facular flux component. Attempts to recover this component were unsuccessful, but perhaps worth future investigation.

The ambient photosphere has a characteristic spectrum, $S(\lambda, T_{amb})$, and covers a total fractional area $(1-f)$.

Spots have a characteristic spectrum, $S(\lambda, T_{spot})$, and cover a total fractional area f

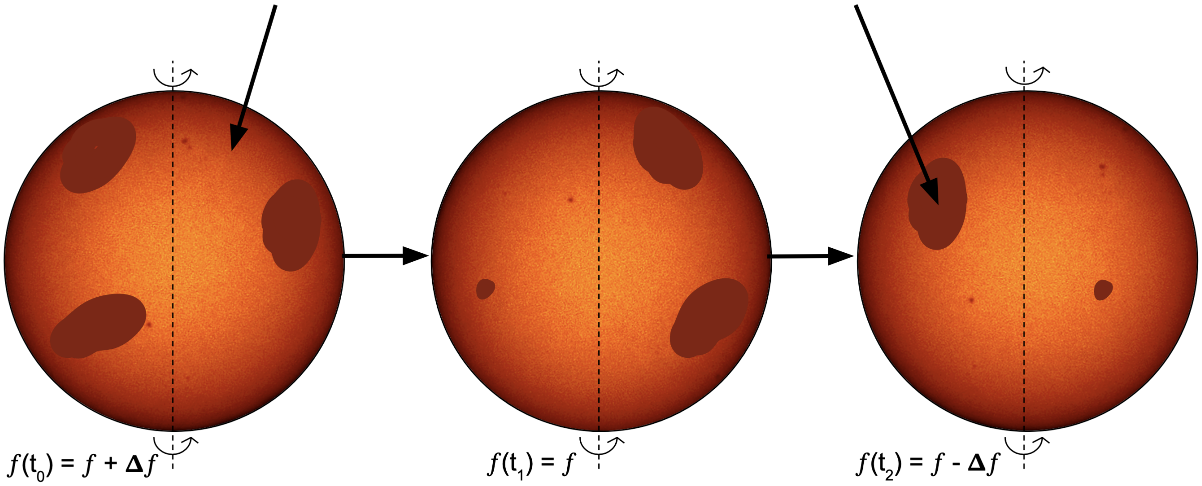

Throughout the star's rotation, spot coverage on the observable stellar face increases and decreases from an average f to f +/- Δf

Figure 4.2: Cartoon of a spotted star showing the parameters used in this study.

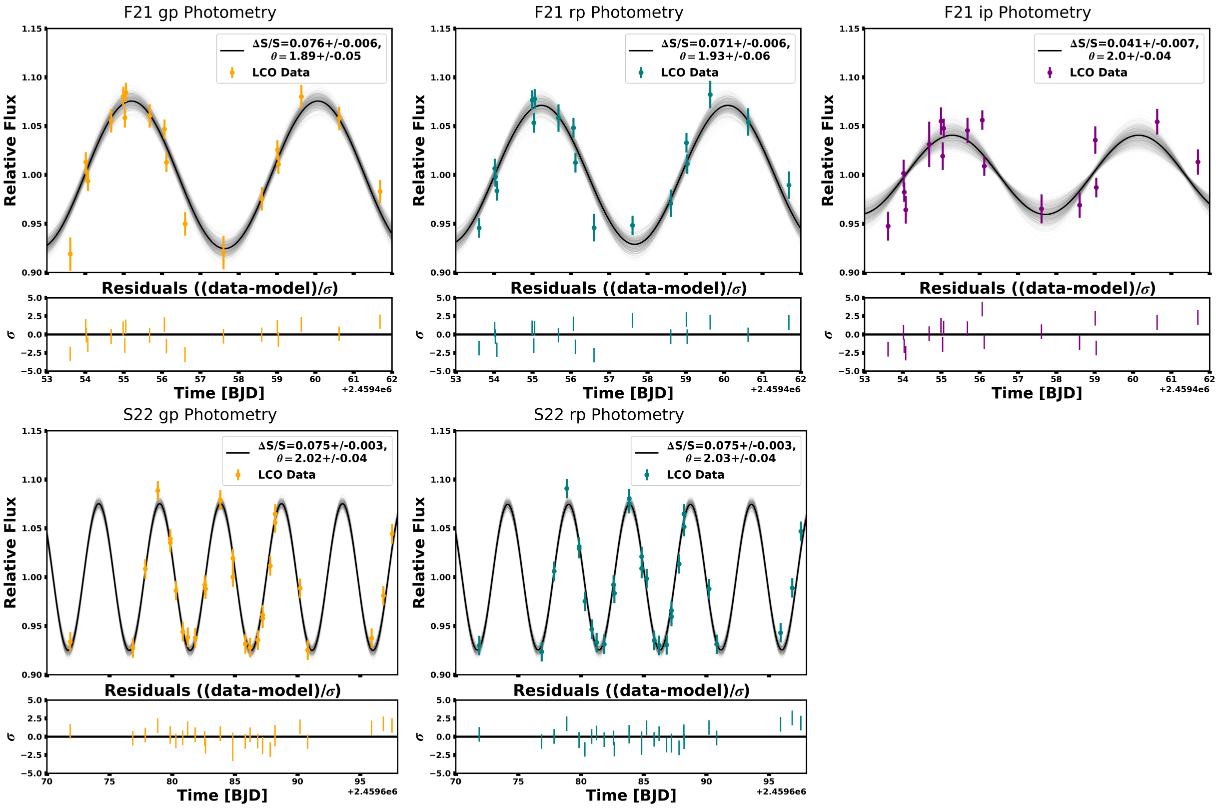

Figure 4.3: LCO 0.4m photometry of AU Mic in the g', r', and i' filters with the rotation model fits described in section 4.3. Variability decreases with wavelength, exhibiting a significant decrease between r' and i' measurements. The shaded regions are randomly sampled models showing the distribution we quote as uncertainty on the amplitude, and the color of each data set corresponds to the filter response curves in Figure 4.10. Model results are provided in Table 4.4.

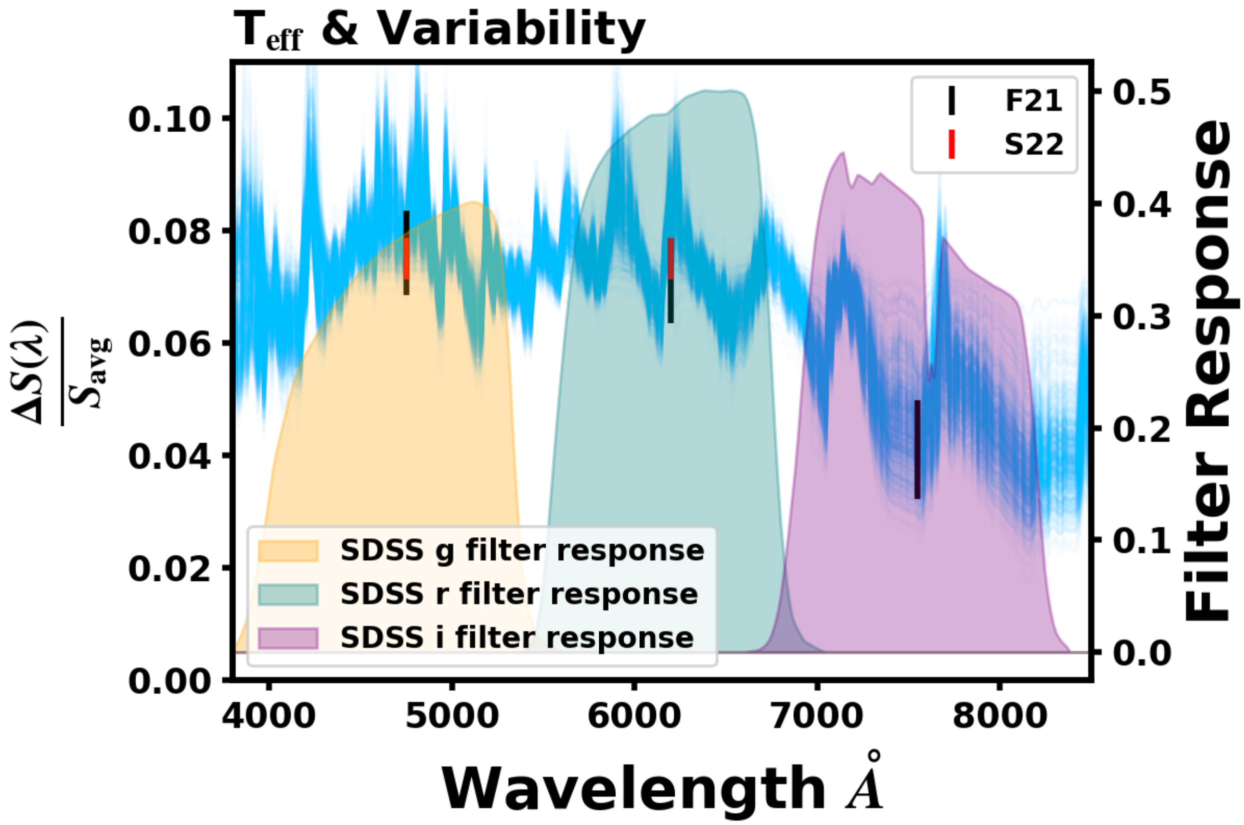

Figure 4.4: All 5 measured rotational variabilities with random models (blue) drawn from the variability model samples. Shaded regions in the background are the filter response curves for our observations. We fit both visits together because the photometric and spectroscopic data are consistent despite the 6 months between visits (e.g., Robertson et al., 2020). Variability decreases with wavelength as the spot-to-photosphere flux contrast decreases, and when modeling the visits separately we find that our solutions were very sensitive to the magnitude and uncertainty of the i' measurement. We have photometry for all 3 filters in F21 but only g' and r' in S22.

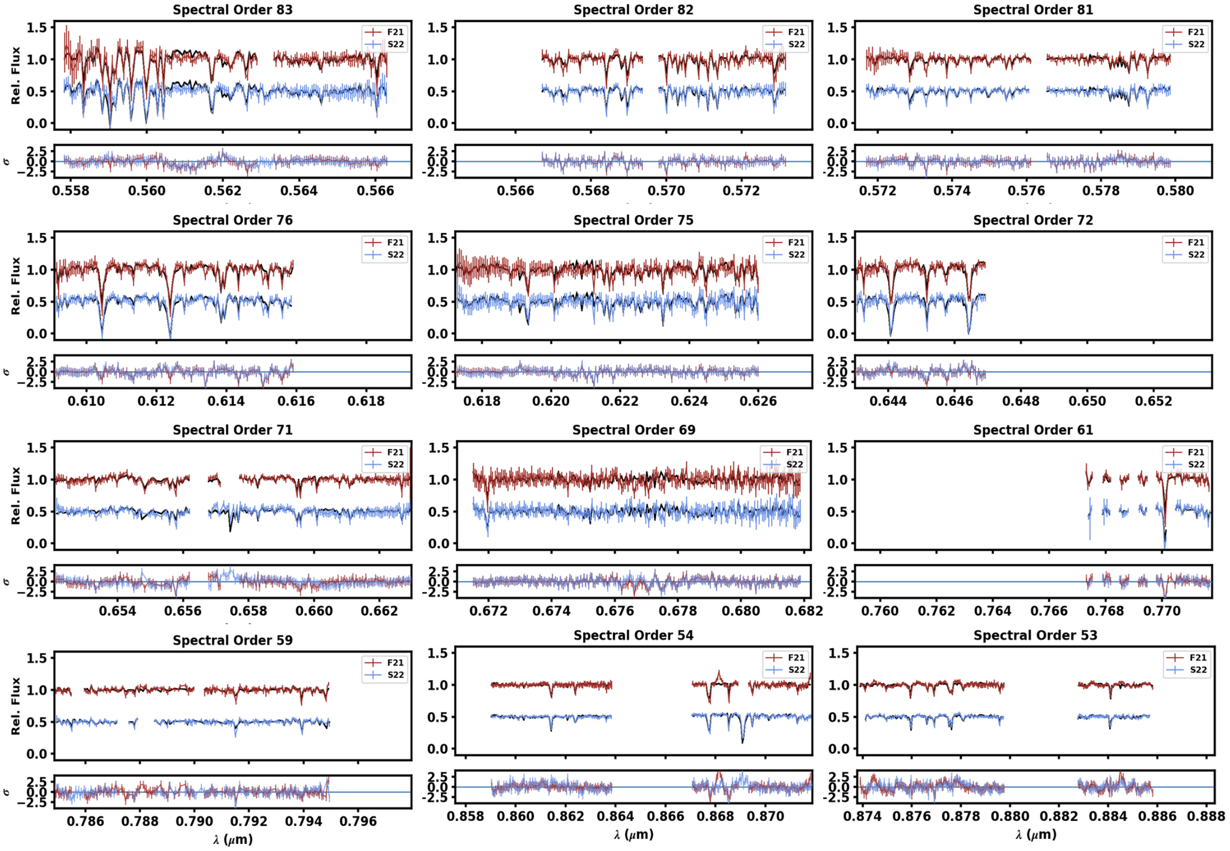

Figure 4.5: Spectra used in this analysis. The red and blue data points (F21 and S22, respectively) are median-averaged in time and have had their uncertainties normalized so a 3650 K template model has a reduced χ^2 of 1. 100 randomly sampled models are plotted in black, which in most cases is a tight spread and difficult to notice in these plots. Despite some poorly fit line depths, there is a tight constraint on spot temperatures and filling factor from the spectra with or without photometric variabilities.

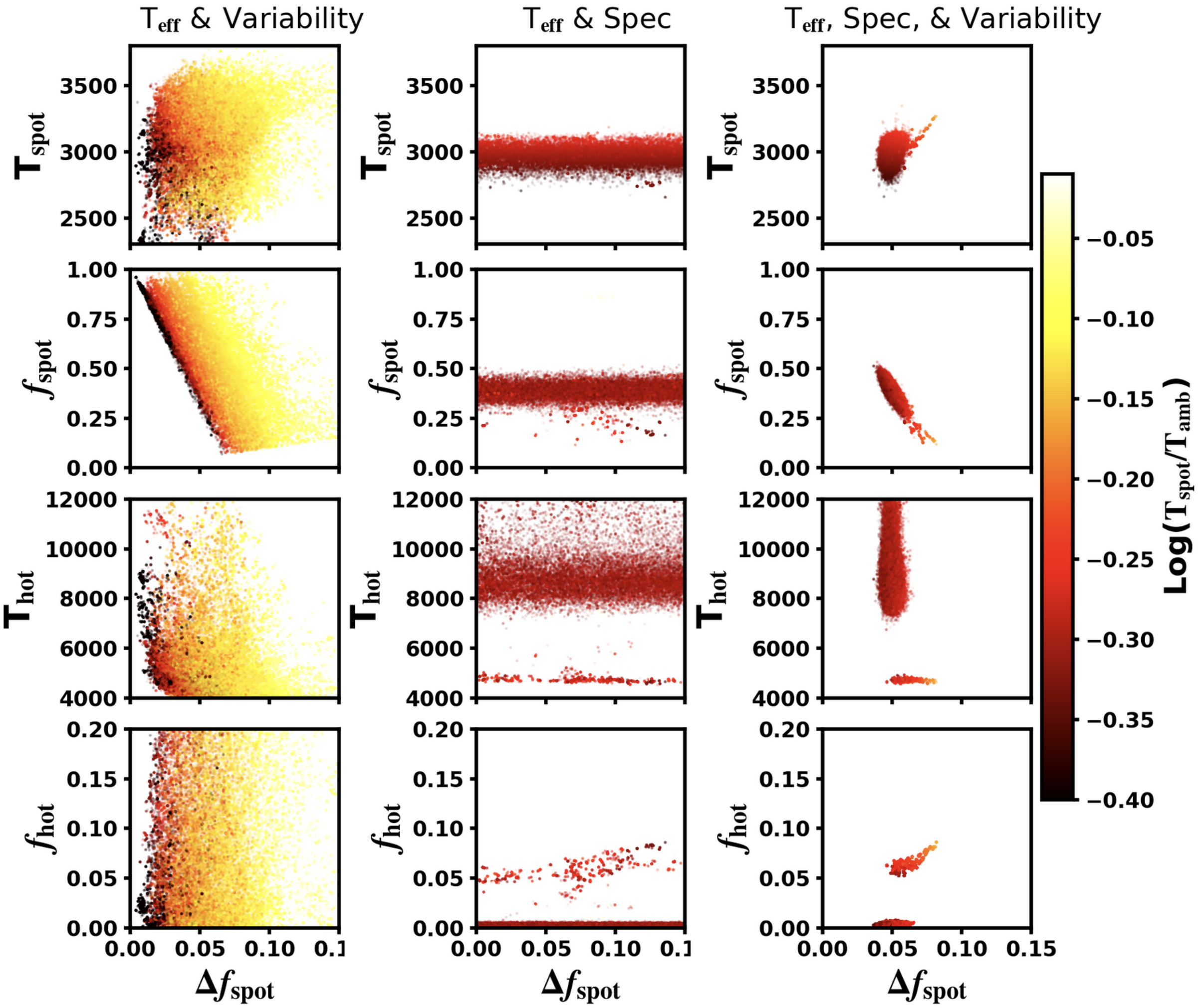

Figure 4.6: Posterior samples for the variability model (left), spectral model (middle) and the ensemble model (right), which retains characteristics of the separate model results. The spectra constrain how hot spot temperatures can be while the photometry constrains how cool they can be. Limits on spot coverage fraction are mostly provided by the spectral modeling, with the variability providing constraints on Δf_{spot}. The color of each point corresponds to the log of the temperature ratio ($T_{\text{spot}}/T_{\text{amb}}$), with redder points being spots that are further from the ambient temperature.

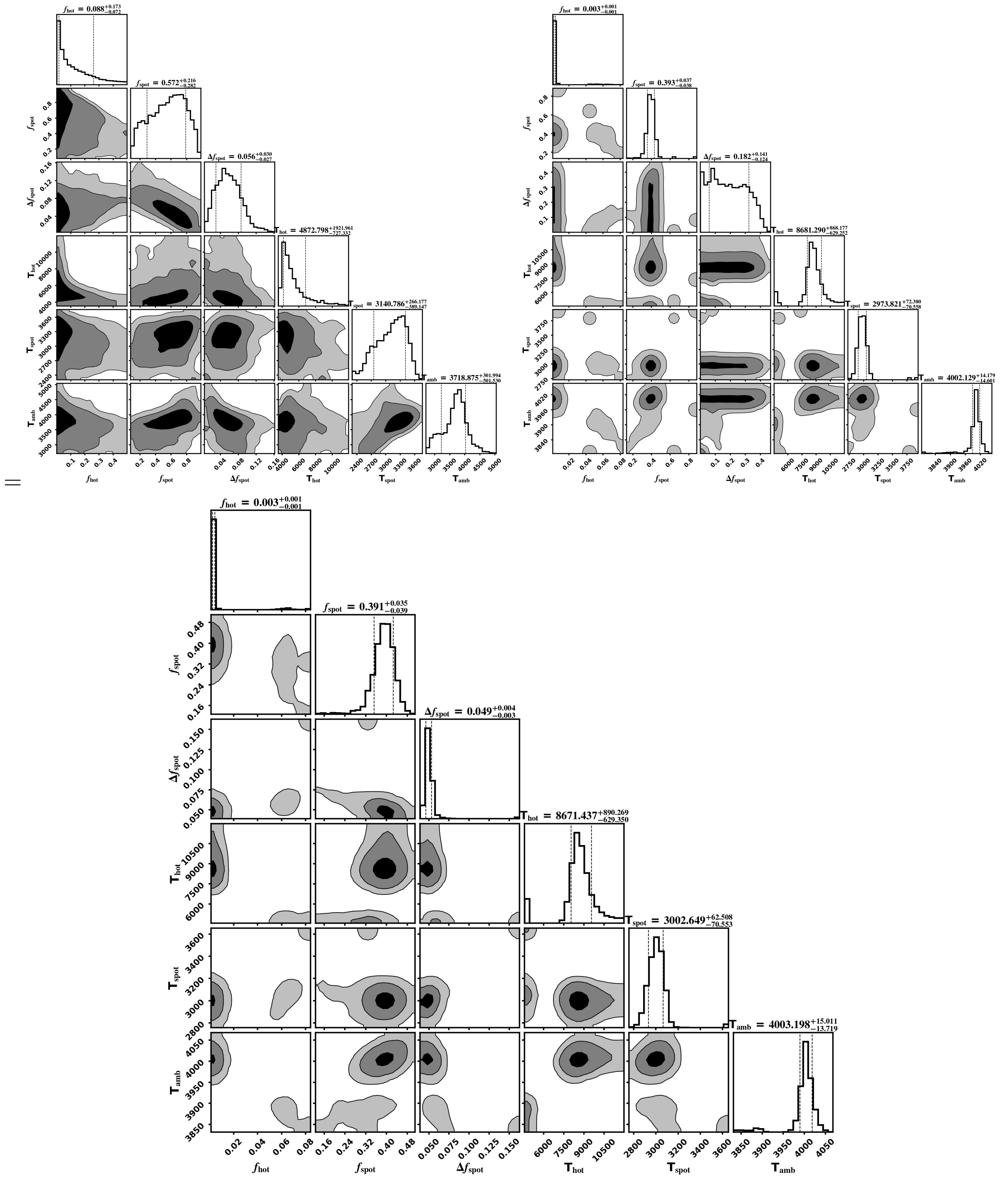

Figure 4.7: Posterior histograms for the variability (top left) and spectral models (top right), with the ensemble results (bottom) exhibiting what looks like the separate-model posteriors multiplied together.

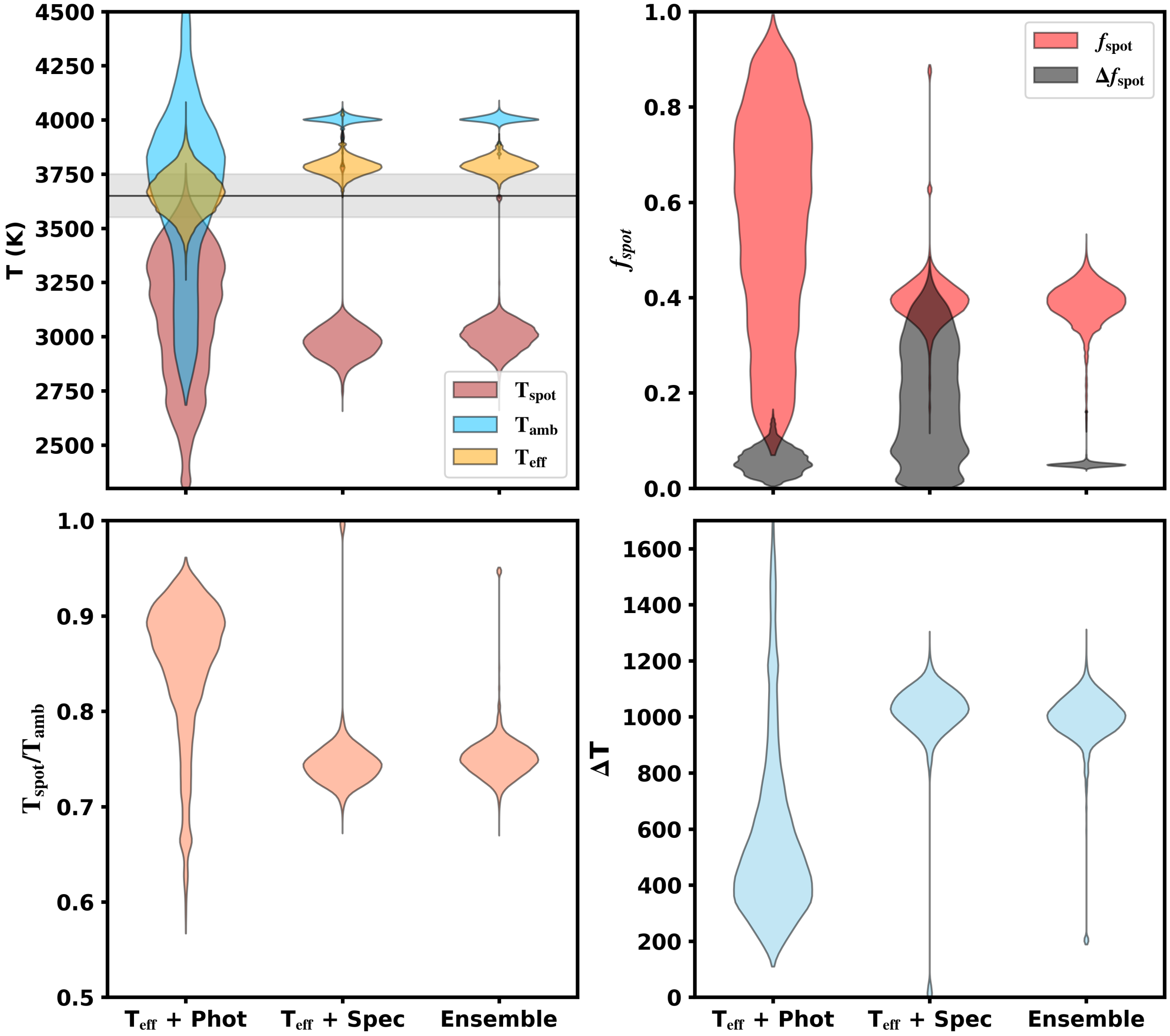

Figure 4.8: Violin plot posteriors for the variability modeling (left distribution on each panel), spectral modeling (middle distribution), and the ensemble model (right distribution). Top left: temperature posteriors showing T_{spot}, T_{amb}, and T_{eff}. Top right: $f_{spot}$and Δf_{spot} posteriors. Bottom left: temperature ratio, T_{spot}/T_{amb}, and bottom right: ΔT, the difference between the spotted and ambient temperatures. The ensemble results exhibit a narrower parameter space for spot characteristics which is effectively the product of the variability and spectral posteriors.

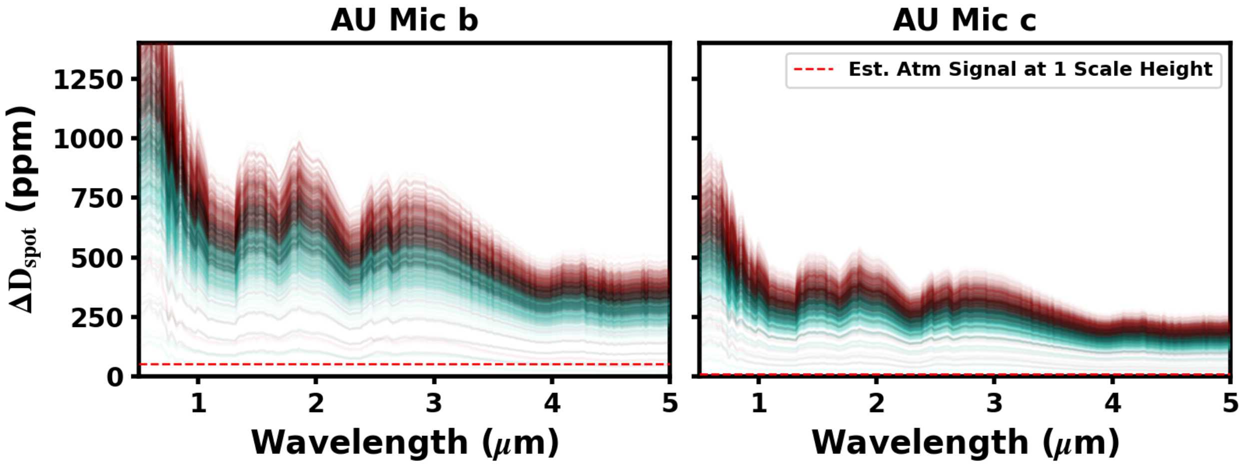

Figure 4.9: Forward-modeled spot contamination in the transmission spectrum of AU Mic b (left) and AU Mic c (right) with models calculated using sampled parameters from the ensemble model posterior. Red corresponds to models with $f = f_{\text{spot}} + \Delta f_{\text{spot}}$ (The point of maximum spot coverage and minimum flux throughout AU Mic's rotation), black to $f = f_{\text{spot}}$ and turquoise to models with $f = f_{\text{spot}} - \Delta f_{\text{spot}}$. Atmospheric depth estimates come from Equation 4.8 and are calculated to be 52 ppm for AU Mic b and 10ppm for AU Mic c at one scale height. For an optimistic case where we can measure 5 scale heights of a cloud-free atmosphere, AU Mic b's atmospheric features will be comparable to lower estimates of spot contamination, while AU Mic c's atmospheric features will still be a factor of a few below the lowest contamination scenarios.

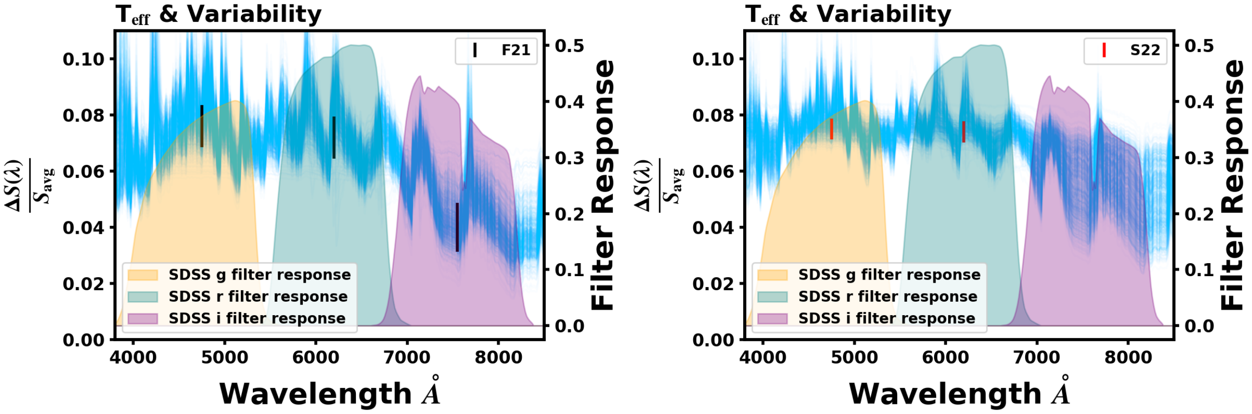

Figure 4.10: F21 (left) and S22 (right) sampled variability models (without spectral fits). The tighter model constraints imposed by an i' measurement can be seen in the spread of model solutions in the red when comparing visits. The presence or absence of i' is strongly constraining and further work should emphasize multi-band measurements to better constrain the spectral temperature contrast.

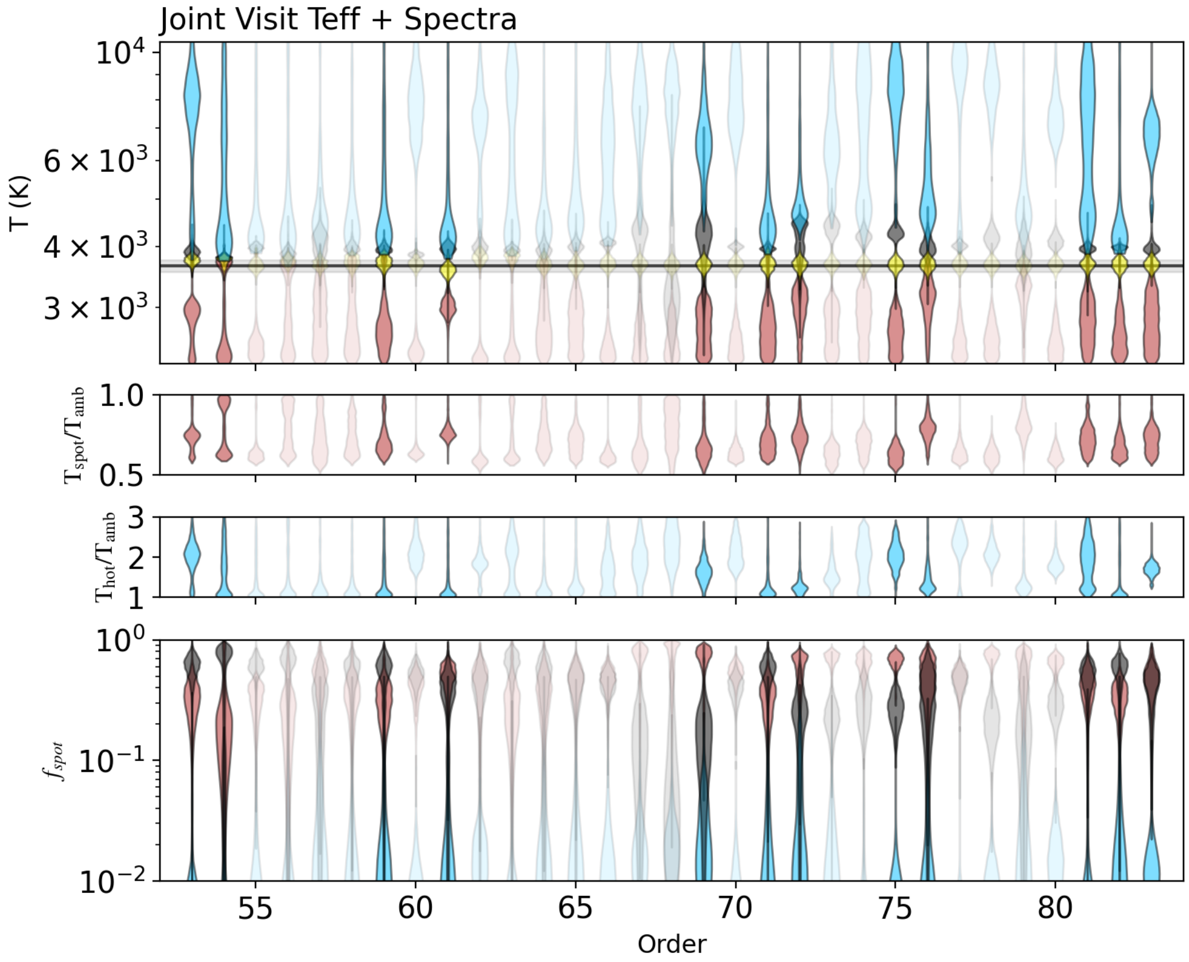

Figure 4.11: Combined-visit model violin plots showing the posterior distributions when modeling only the spectra and T_{eff}. Spectral orders shown in this plot span 0.557-0.888 μm, with wavelength decreasing to the right. Top: Temperature components for the hot (blue), middle (black) and spot (red) components. In yellow is the corresponding T_{eff}. Most orders exhibit a hot component between 7000-10000 K, consistent with the temperature of flares in this wavelength range. Spot temperatures are generally poorly constrained, with the 3000K spot seemingly detected in a handful of orders (53, 61, 72, 76, 79). Middle: the temperature ratio, T_{spot}/T_{amb}. The 5 orders showing a spot solution tend to show a temperature ratio of between 0.7-0.8. Bottom: coverage fractions for the spotted (red), ambient (black), and hot (blue) components. The hot component is very small, less than 3%. There is no clear agreement with spot coverage between orders, with the largest component being the ambient photosphere in the early orders while the later orders show more spot-dominated photospheres. Orders with very poor constraints tend to overlap with orders that are contaminated by tellurics. Orders omitted from the analysis are grayed out.

Chapter 5

Thesis Summary and Potential Future Projects

My thesis work addressed the challenge of observing and characterizing sub-Neptune exoplanet atmospheres with a combination of space- and ground-based observations of M dwarfs with transiting planets. I helped find new planets for atmospheric study, attempted to observe an escaping atmosphere, characterized stellar variability, and developed our capabilities to detect and disentangle atmospheric absorption from complex stellar photospheres. In this conclusion, Section 5.1 summarizes my work and contributions to the field, and Section 5.2 discusses some possible directions for future work.

5.1 Thesis Summary

In this thesis we studied sub-Neptune exoplanets orbiting M dwarf stars. We contributed to the detection of new planets, characterized stellar variability, and studied the impact of stellar activity on exoplanet atmospheres. A substantial fraction of my work has involved using ground-based observatories to verify the planetary nature of TESS Objects of Interest (TOIs). As a contributing member of the TESS Follow-up Observing Program (TFOP), I focused on chasing down exciting new sub-Neptune planets orbiting M dwarfs discovered by TESS and validating systems which may be viable targets for atmospheric transmission observations. In 2020 I led a TESS discovery paper which involved synthesizing a wide variety of ground-based data, from photometric observations at LCO to SOAR speckle imaging, Magellan spectra, and SALT HRS spectra in order to characterize TOIs 122b and 237b and their host stars (Chapter 2). We found these to be two of the cooler planets found in the first few years of TESS, both orbiting nearby low-activity M dwarfs and receiving $< 10\times$ the insolation of Earth. These planets are viable targets for RV and transmission studies for near-future spectrographs or heavy investment with current RV instruments and large ground-based observatories.

One way to study atmospheres is to search for outflowing gas around highly irradiated exoplanets as evidence of atmospheric escape due to photochemical breakdown. Using HST STIS UV spectra, I searched for a Lyman-α absorption signature in and around the transit of exoplanet GJ 1132b which, if detected, would have indicated an extended cloud of neutral H outflowing from the planet (Chapter 3). This involved re-extracting spectra when the automatic pipeline failed to extract the faint UV spectrum for GJ 1132. We did not detect a transit at Lyman-α but were able to place an upper limit on the escape rate of hydrogen from the atmosphere of GJ 1132b and reconstruct the Lyman-α profile of the star.

In Chapter 4 I used ground-based multi color photometry and high resolution spectroscopy to characterize starspots on the surface of nearby transiting exoplanet host AU Mic to complement HST/WFC3 transmission observations of AU Mic b. I was able to precisely measure the bulk temperature of AU Mic's spots to be 3000-3100 K covering $40\pm4\%$ of the stellar photosphere. These measurements translate to contamination as high as 1200 ppm at wavelengths shorter than 1 micron, and between 250-600 ppm in the HST/WFC3 bandpass which is used to search for exoplanetary water absorption. The followup to this project, my eventual next publication, applies these spot measurements to a joint spot & atmospheric model of AU Mic b's WFC3 transmission spectrum. This work is in the early stages of analysis, but we hope the measured spot characteristics are precise enough to allow us to disentangle spot contamination from atmospheric absorption in this system and return the first confidently decontaminated transmission spectrum of an M dwarf exoplanet atmosphere. My investigation into AU Mic's spots has inspired the following future projects, which seek to strengthen the connection between stellar theory and exoplanet characterization.

Name	R_p/R_*	P_{orb}(d)	$P_{rot,star}$(d)	Distance (pc)	Vmag	Spectral Type
LHS 6343C	0.221	12.71	13.13	50.1	13.4	M2.5
TOI 2119 B	0.218	7.20	13.20	31.4	12.7	M0
TOI 1278 B	0.191	14.48		75.5	13.5	M0
AD 3116 B	0.328	1.98	2.30	182.8	17.5	M3.9
LP 261-75B	0.322	1.88	1.11	33.9	15.4	M4.5
NGTS-7Ab	0.233	0.68	0.68	152.7	15.5	M3
TOI-263b	0.245	0.56	0.56	277.4	19.0	M3.5
ZTF J2020+5033	0.560	0.08		136.0	19.0	M6

Table 5.1: Target list of transiting brown dwarfs around M stars, excluding those with highly uncertain periods and/or radii. The high occurrence of close-in 1:1 spin-orbit resonances in these systems implies strong magnetic interactions and heavy spot coverage, which may be observable in multi-wavelength variability and transit measurements.

5.2 Potential Future Project Ideas

The old assumption of immaculate photospheres behind our transiting planets is proving hazardous. Spot contamination has recently been recognized in HST and JWST transmission observations of M dwarf sub-Neptunes TOI 270d (Mikal-Evans et al., 2023), K2-33b (Thao et al., 2023), Gl 486b (Moran et al., 2023), L 98-59c (Barclay et al., 2023), and the TRAPPIST-1 system (e.g., Zhang et al., 2018; Wakeford et al., 2019; Lim et al., 2023) - all nearby planets on temperate orbits that are promising targets for atmospheric study. Transmission observations of these planets show features consistent with spot contamination and/or atmospheric absorption, with signals entangled until we have a detailed understanding of the stellar surface of each of those stars at the time of transit. As JWST kicks off a new era of exoplanet characterization, it is important to devote time and resources to studying the surfaces and magnetic properties of low-mass host stars, observing their spots, and mitigating spot contamination in exoplanet observations. In thinking about how to address spot contamination, I have developed several project ideas which take a holistic approach to spots which includes developing and refining observational techniques, ruling out contamination scenarios with transit observations, and modeling fully convective stellar dynamos to build the connection between spots and stellar magnetism.

- **Directly Measuring the TLSE.** One way to study stellar contamination in isolation is

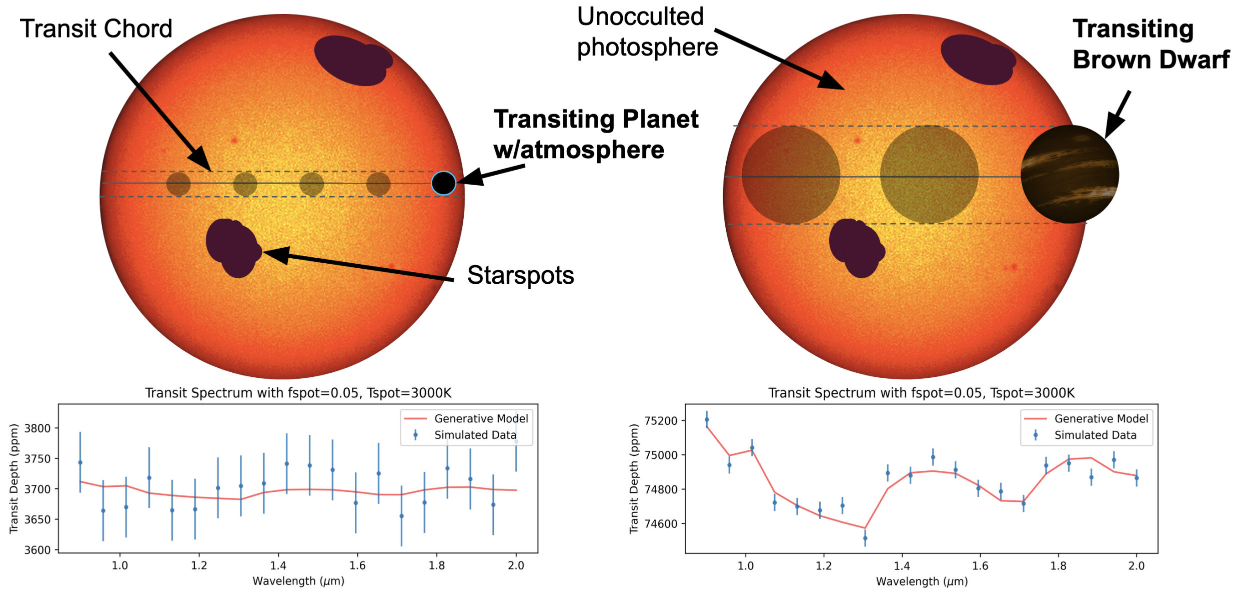

Figure 5.1: Cartoon transiting systems with simulated spot contamination spectra showing the enhanced observability of transiting brown dwarf systems (right) compared to transiting sub-Neptune worlds (left) for constraining the TLSE. Bottom panels: simulated spot-contaminated transmission spectra for a sub-Neptune exoplanet versus a brown dwarf in a wavelength regime relevant to molecular absorption wavelengths and transmission observations with HST and JWST. Uncertainties are only first order estimates set at 50 ppm across all wavelengths to allow a simple comparison between scenarios.

by observing transiting objects that have a negligible atmospheric scale height (no atmosphere, high mean molecular weight atmosphere, or high surface gravity), allowing the spot contamination to be measured directly from any significant deviation from a flat transit spectrum (Figure 5.1). Brown dwarfs (BDs) orbiting M stars exhibit a deep transit signature but due to their high surface gravity, atmospheric absorption features fall within the noise limit of most observations (< 100 ppm). In these systems, the contamination signal is likely thousands of ppm, depending on the spot coverage and spectrum of each host star. This will be an observational survey of BD - M dwarf binaries which will provide the first direct observations of spot contamination in transmission spectra. There are 10 such known systems, 8 of which have periods short enough for viable study on a postdoc timeline. Details summarized in Table 5.1. Spots are ubiquitous on stars with convective envelopes, which includes nearly every exoplanet host and every single M star, making each of these 8 targets a viable candidate for observing spot contamination. A multi-wavelength transit survey of these systems covering the optical-IR would yield limits on the contamination present in each of their transit spectra, providing us with the first confirmed spot contamination in transmission, in a very high S/N regime with stellar types representative of many of the host stars with transiting targets we study. Given the small sample size and the fact that almost every single pair is either in or very close to a 1:1 spin-orbit resonance, the spot characteristics on these M stars and the inferences we are able to make about them may be fairly unique to these systems, but the sample can be scaled in future work to include transiting BDs around more massive stars which are not synchronously rotating. These systems are further complicated by the self-luminosity of BDs. In the context of the proposed observations of these systems, BD emission will be a relatively constant factor that can be accounted for. This study will require new transmission-like observations from space and/or ground observatories. While some molecules like water cannot be observed from the ground and require a space telescope, any set of multi-color transit measurements between 0.1-10 microns is useful to place limits on spot contamination. I will request observations to study contamination (with an emphasis on H_2O bands) with HST/WFC3 and JWST/NIRSpec and Magellan/IMACS, Magellan/LDSS3, APO/KOSMOS, NEID, and others depending on institution-specific resources. The timeline of this first project is highly uncertain because observations must be proposed for and acquired on schedules unique to each observatory, but in most of these cases archival transit observations of some form will be available (i.e., TESS observations), which will be useful as a starting point. This project can be expanded in future work with photometric and spectroscopic monitoring of these systems to observe spot evolution over many rotations.

- **SODA, the Spot Occultation Detections Archive.** Spot occultations occur when some or all of a spot lies on the transit chord, creating a bump in the transit light curve and providing a direct measurement of the spot's flux contrast in the observed waveband (Figure 5.2). When spot occultations are measured in multiple wavebands, spectral information emerges (e.g., Schutte et al., 2023). The flux contrast between spotted and ambient photosphere varies as a function of wavelength, reaching a maximum in the Wien limit and approaching a minimum contrast in the Rayleigh-Jeans limit where their spectra converge. Spot occultations measured in any given waveband provides first-order information about spot contrast, morphology, and location. In multiple wavebands, the spot contrast becomes a low resolution spot spectrum and with high enough photometric precision, the multi-color morphology of spot crossings may allow us to distinguish between spot umbrae and penumbrae and better understand spot spectra. This independent measure of spot contrast can also be used to validate other estimates of spot temperature like the multi-color rotational variability model described in Chapter 4. A systematic study of spot occultations in the literature has not yet been done, and this will provide insight into spot characteristics across stellar type and allow more in-depth characterization of spots and contamination for a statistical sample of exoplanet host stars. The sample for this study will be assembled starting with a list of ground-based observations assembled by the NASA Exoplanet Exploration

Study Analysis Group 21 report (Rackham et al., 2023) and will include those systems which have occultations in archival space telescope data (Kepler, TESS, HST, and JWST) along with additional crossing events that have since been published. The (unpublished) SODA catalog I have compiled so far contains 17 systems with ground-based and with 16 space-based observations of spot crossings, with 4 of those systems having both space and ground observations. This project will develop our understanding of the sources of stellar variability and stellar surface magnetism while enabling more robust science with future atmospheric transmission observations. As transit studies and spot detections will continue indefinitely, this work is intended to be built upon in future work by myself and others, with results eventually accessible through a public database. A team at MIT is beginning a re-analysis of all HST transit data sets, to be available on MAST in roughly 1 year (HST AR 17551) which will be a very useful publicly available tool for this project.

- **Investigating the connection between the fully convective stellar dynamo and starspots.** Stellar dynamo processes (a combination of rotation and convection) and the magnetic fields they create have a very important role in the structure and evolution of exoplanet atmospheres but are poorly understood for almost all stars. Magnetic fields on the stellar surface create active regions but we do not yet understand how those fields themselves are created or evolve let alone for stars of different type and activity level. Below a certain mass limit (roughly 0.35 M_{sun} or spectral type M4), M dwarfs have fully convective interiors. Unlike other stars, these have a much simpler interior structure that can be modeled as a Lane-Emden polytrope. These stars are the most numerous in the galaxy, ubiquitously have compact multi-planet systems (e.g., Dressing & Charbonneau, 2015), and have magnetic or magnetically-induced interactions with their planets that influence the composition, evolution, and habitability of those planets' atmospheres. Brown et al. (2020) recently demonstrated models of a fully-convective slowly rotating star and found single-hemisphere global magnetic fields. This result raises some interesting questions: Is it a robust finding? If it is robust, can it help us understand the connection between rotation, global magnetic field topology, and the emergence of starspots? Does this illuminate the relationship between magnetic properties and spot properties like location, temperature, morphology, and/or evolution? Using the Dedalus package (Burns et al., 2020), I will run a set of Magneto-hydrodynamic (MHD) simulations of slowly rotating fully convective M stars to test the Brown et al. (2020) results in different rotation regimes, focusing initially on stars with Rossby number (the ratio of a star's rotation period to convective turnover timescale) between 0.1-5, a regime the includes the transition region from fully saturated activity to decreasing activity identified by Newton et al. (2016a). This is a pilot study from which I hope to ultimately develop testable predictions for spot location (using spot occultations among other methods) and temperature (using the relation in Kopp & Rabin, 1992) as a function of magnetic field strength and stellar rotation. The yield of this project could have significant implications for our understanding of star-planet interactions and exoplanet habitability around slowly-rotating late M stars, the most common exoplanet host in the galaxy.

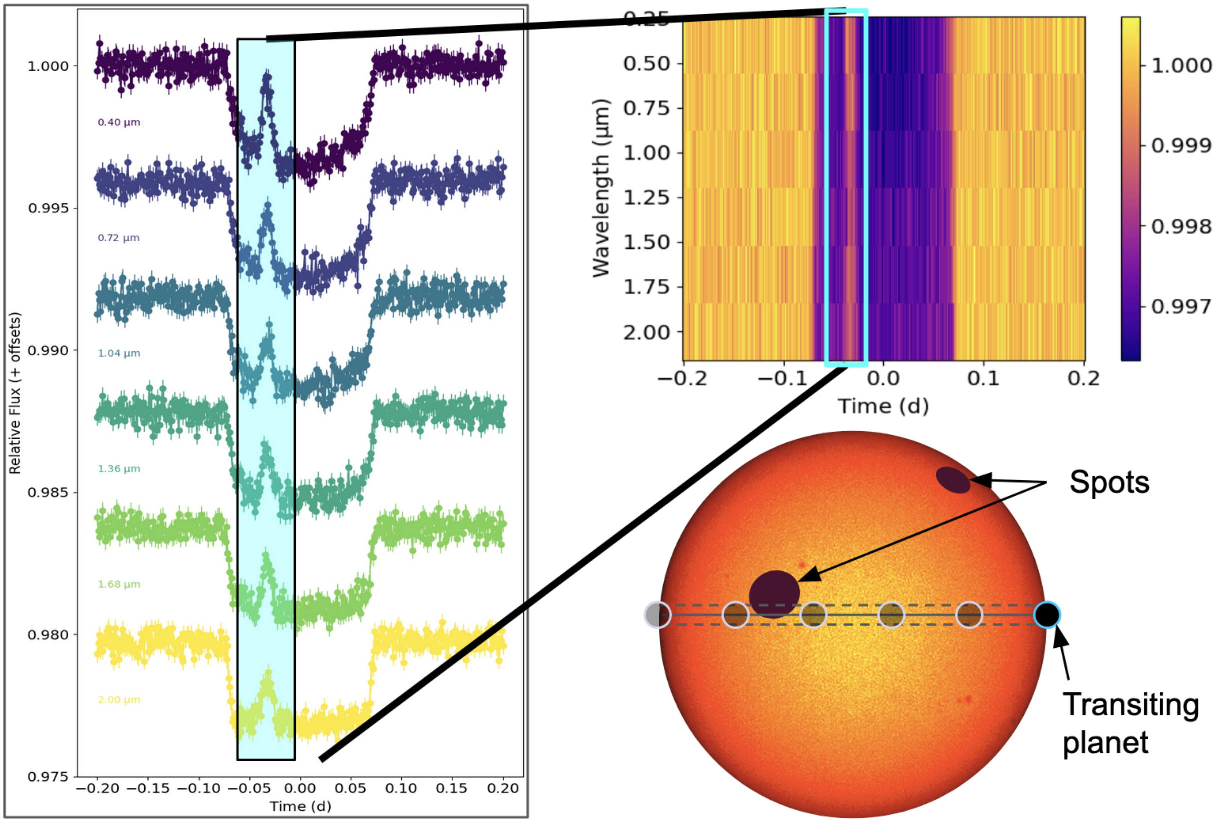

Figure 5.2: This spot crossing simulation for a 3000 K spot on a 3700 K star from 0.4-2 μm shows how spot contrasts measured from transit light curves can be used to infer spot spectra.

Bibliography

Afram, N. & Berdyugina, S. V., 2015, Molecules as magnetic probes of starspots, *A&A*, 576, A34.

Afram, N. & Berdyugina, S. V., 2019, Complexity of magnetic fields on red dwarfs, *A&A*, 629, A83.

Ahrer, E.-M., Stevenson, K. B., Mansfield, M., Moran, S. E., Brande, J., Morello, G., Murray, C. A., Nikolov, N. K., Petit dit de la Roche, D. J. M., Schlawin, E., Wheatley, P. J., Zieba, S., Batalha, N. E., Damiano, M., Goyal, J. M., Lendl, M., Lothringer, J. D., Mukherjee, S., Ohno, K., Batalha, N. M., Battley, M. P., Bean, J. L., Beatty, T. G., Benneke, B., Berta-Thompson, Z. K., Carter, A. L., Cubillos, P. E., Daylan, T., Espinoza, N., Gao, P., Gibson, N. P., Gill, S., Harrington, J., Hu, R., Kreidberg, L., Lewis, N. K., Line, M. R., López-Morales, M., Parmentier, V., Powell, D. K., Sing, D. K., Tsai, S.-M., Wakeford, H. R., Welbanks, L., Alam, M. K., Alderson, L., Allen, N. H., Anderson, D. R., Barstow, J. K., Bayliss, D., Bell, T. J., Blecic, J., Bryant, E. M., Burleigh, M. R., Carone, L., Casewell, S. L., Changeat, Q., Chubb, K. L., Crossfield, I. J. M., Crouzet, N., Decin, L., Désert, J.-M., Feinstein, A. D., Flagg, L., Fortney, J. J., Gizis, J. E., Heng, K., Iro, N., Kempton, E. M. R., Kendrew, S., Kirk, J., Knutson, H. A., Komacek, T. D., Lagage, P.-O., Leconte, J., Lustig-Yaeger, J., MacDonald, R. J., Mancini, L., May, E. M., Mayne, N. J., Miguel, Y., Mikal-Evans, T., Molaverdikhani, K., Palle, E., Piaulet, C., Rackham, B. V., Redfield, S., Rogers, L. K., Roy, P.-A., Rustamkulov, Z., Shkolnik, E. L., Sotzen, K. S., Taylor, J., Tremblin, P., Tucker, G. S., Turner, J. D., de Val-Borro, M., Venot, O., & Zhang, X., 2023, Early Release Science of the exoplanet WASP-39b with JWST NIRCam, *Nature*, 614(7949), 653–658.

Alderson, L., Wakeford, H. R., Alam, M. K., Batalha, N. E., Lothringer, J. D., Adams Redai, J., Barat, S., Brande, J., Damiano, M., Daylan, T., Espinoza, N., Flagg, L., Goyal, J. M., Grant, D., Hu, R., Inglis, J., Lee, E. K. H., Mikal-Evans, T., Ramos-Rosado, L., Roy, P.-A., Wallack, N. L., Batalha, N. M., Bean, J. L., Benneke, B., Berta-Thompson, Z. K., Carter, A. L., Changeat, Q., Colón, K. D., Crossfield, I. J. M., Désert, J.-M., Foreman-Mackey, D., Gibson, N. P., Kreidberg, L., Line, M. R., López-Morales, M., Molaverdikhani, K., Moran, S. E., Morello, G., Moses, J. I., Mukherjee, S., Schlawin, E., Sing, D. K., Stevenson, K. B., Taylor, J., Aggarwal, K., Ahrer, E.-M., Allen, N. H., Barstow, J. K., Bell, T. J., Blecic, J., Casewell, S. L., Chubb, K. L., Crouzet, N., Cubillos, P. E., Decin, L., Feinstein, A. D., Fortney, J. J., Harrington, J., Heng, K., Iro, N., Kempton, E. M. R., Kirk, J., Knutson, H. A., Krick, J., Leconte, J., Lendl, M., MacDonald, R. J., Mancini, L., Mansfield, M., May, E. M., Mayne, N. J., Miguel, Y., Nikolov, N. K., Ohno, K., Palle, E., Parmentier, V., Petit dit de la Roche, D. J. M., Piaulet, C., Powell, D., Rackham, B. V., Redfield, S., Rogers, L. K., Rustamkulov, Z., Tan, X., Tremblin, P., Tsai, S.-M., Turner, J. D., de Val-Borro, M., Venot, O., Welbanks, L., Wheatley, P. J., & Zhang, X., 2023, Early Release Science of the exoplanet WASP-39b with JWST NIRSpec G395H, *Nature*, 614(7949), 664–669.

Allard, F., 2014, The BT-Settl Model Atmospheres for Stars, Brown Dwarfs and Planets, *in* Booth, M., Matthews, B. C., & Graham, J. R. (eds), *Exploring the Formation and Evolution of Planetary Systems*, Vol. 299, pp. 271–272.

Allard, F., Homeier, D., & Freytag, B., 2011, Model Atmospheres From Very Low Mass Stars to Brown Dwarfs, *in* Johns-Krull, C., Browning, M. K., & West, A. A. (eds), *16th Cambridge Workshop on Cool Stars, Stellar Systems, and the Sun*, Vol. 448 of *Astronomical Society of the Pacific Conference Series*, p. 91.

Allard, F., Homeier, D., Freytag, B., & Sharp, C. M., 2012, Atmospheres From Very Low-Mass Stars to Extrasolar Planets, *in* Reylé, C., Charbonnel, C., & Schultheis, M. (eds), *EAS Publications Series*, Vol. 57 of *EAS Publications Series*, pp. 3–43.

Allart, R., Bourrier, V., Lovis, C., Ehrenreich, D., Spake, J. J., Wyttenbach, A., Pino, L., Pepe, F., Sing, D. K., & Lecavelier des Etangs, A., 2018, Spectrally resolved helium absorption from the extended atmosphere of a warm Neptune-mass exoplanet, *Science*, 362, 1384–1387.

Angus, R., Morton, T., Aigrain, S., Foreman-Mackey, D., & Rajpaul, V., 2018, Inferring probabilistic stellar rotation periods using Gaussian processes, *MNRAS*, 474(2), 2094–2108.

Apai, D., Rackham, B. V., Giampapa, M. S., Angerhausen, D., Teske, J., Barstow, J., Carone, L., Cegla, H., Domagal-Goldman, S. D., Espinoza, N., Giles, H., Gully-Santiago, M., Haywood, R., Hu, R., Jordan, A., Kreidberg, L., Line, M., Llama, J., López-Morales, M., Marley, M. S., & de Wit, J., 2018, Understanding Stellar Contamination in Exoplanet Transmission Spectra as an Essential Step in Small Planet Characterization, *arXiv e-prints*, p. arXiv:1803.08708.

Araújo, A. & Valio, A., 2023, The connection between starspots and superflares: a case study of two stars, *MNRAS*, 522(1), L16–L20.

Astudillo-Defru, N., Cloutier, R., Wang, S. X., Teske, J., Brahm, R., Hellier, C., Ricker, G., Vand erspek, R., Latham, D., Seager, S., Winn, J. N., Jenkins, J. M., Collins, K. A., Stassun, K. G., Ziegler, C., Almenara, J. M., Anderson, D. R., Artigau, E., Bonfils, X., Bouchy, F., Briceño, C., Butler, R. P., Charbonneau, D., Conti, D. M., Crane, J., Crossfield, I. J. M., Davies, M., Delfosse, X., Díaz, R. F., Doyon, R., Dragomir, D., Eastman, J. D., Espinoza, N., Essack, Z., Feng, F., Figueira, P., Forveille, T., Gan, T., Glidden, A., Guerrero, N., Hart, R., Henning, T., Horch, E. P., Isopi, G., Jenkins, J. S., Jordán, A., Kielkopf, J. F., Law, N., Lovis, C., Mallia, F., Mann, A. W., de Medeiros, J. R., Melo, C., Mennickent, R. E., Mignon, L., Murgas, F., Nusdeo, D. A., Pepe, F., Relles, H. M., Rose, M., Santos, N. C., Ségransan, D., Shectman, S., Shporer, A., Smith, J. C., Torres, P., Udry, S., Villasenor, J., Winters, J. G., & Zhou, G., 2020, A hot terrestrial planet orbiting the bright M dwarf L 168-9 unveiled by TESS, *A&A*, 636, A58.

Atri, D. & Mogan, S. R. C., 2021, Stellar flares versus luminosity: XUV-induced atmospheric escape and planetary habitability, *MNRAS*, 500(1), L1–L5.

Ballard, S., 2019, Predicted Number, Multiplicity, and Orbital Dynamics of TESS M-dwarf Exoplanets, *AJ*, 157(3), 113.

Ballard, S., Fabrycky, D., Fressin, F., Charbonneau, D., Desert, J.-M., Torres, G., Marcy, G., Burke, C. J., Isaacson, H., Henze, C., Steffen, J. H., Ciardi, D. R., Howell, S. B., Cochran, W. D., Endl, M., Bryson, S. T., Rowe, J. F., Holman, M. J., Lissauer, J. J., Jenkins, J. M., Still, M., Ford, E. B., Christiansen, J. L., Middour, C. K., Haas, M. R., Li, J., Hall, J. R., McCauliff, S., Batalha, N. M., Koch, D. G., & Borucki, W. J., 2011, The Kepler-19 System: A Transiting 2.2 R $_\oplus$ Planet and a Second Planet Detected via Transit Timing Variations, *ApJ*, 743(2), 200.

Ballerini, P., Micela, G., Lanza, A. F., & Pagano, I., 2012, Multiwavelength flux variations induced by stellar magnetic activity: effects on planetary transits, *A&A*, 539, A140.

Barclay, T., Pepper, J., & Quintana, E. V., 2018, A Revised Exoplanet Yield from the Transiting Exoplanet Survey Satellite (TESS), , .
URL: *http://arxiv.org/abs/1804.05050*

Barclay, T., Sheppard, K. B., Latouf, N., Mandell, A. M., Quintana, E. V., Gilbert, E. A., Liuzzi, G., Villanueva, G. L., Arney, G., Brande, J., Colón, K. D., Covone, G., Crossfield, I. J. M., Damiano, M., Domagal-Goldman, S. D., Fauchez, T. J., Fiscale, S., Gallo, F., Hedges, C. L., Hu, R., Kite, E. S., Koll, D., Kopparapu, R. K., Kostov, V. B., Kreidberg, L., Lopez, E. D., Mang, J., Morley, C. V., Mullally, F., Mullally, S. E., Pidhorodetska, D., Schlieder, J. E., Vega, L. D., Youngblood, A., & Zieba, S., 2023, The transmission spectrum of the potentially rocky planet L 98-59 c, *arXiv e-prints*, p. arXiv:2301.10866.

Basri, G., 2021, *An Introduction to Stellar Magnetic Activity*.

Basri, G., Walkowicz, L. M., & Reiners, A., 2013, Comparison of Kepler Photometric Variability with the Sun on Different Timescales, *ApJ*, 769(1), 37.

Batalha, N. E., Lewis, T., Fortney, J. J., Batalha, N. M., Kempton, E., Lewis, N. K., & Line, M. R., 2019, The Precision of Mass Measurements Required for Robust Atmospheric Characterization of Transiting Exoplanets, *ApJ*, 885(1), L25.

Beichman, C., Benneke, B., Knutson, H., Smith, R., Lagage, P.-O., Dressing, C., Latham, D., Lunine, J., Birkmann, S., Ferruit, P., Giardino, G., Kempton, E., Carey, S., Krick, J., Deroo, P. D., Mandell, A., Ressler, M. E., Shporer, A., Swain, M., Vasisht, G., Ricker, G., Bouwman, J., Crossfield, I., Greene, T., Howell, S., Christiansen, J., Ciardi, D., Clampin, M., Greenhouse, M., Sozzetti, A., Goudfrooij, P., Hines, D., Keyes, T., Lee, J., McCullough, P., Robberto, M., Stansberry, J., Valenti, J., Rieke, M., Rieke, G., Fortney, J., Bean, J., Kreidberg, L., Ehrenreich, D., Deming, D., Albert, L., Doyon, R., & Sing, D., 2014, Observations of Transiting Exoplanets with the James Webb Space Telescope (<i>JWST</i>), *Publications of the Astronomical Society of the Pacific*, 126(946), 1134–1173.
URL: *http://iopscience.iop.org/article/10.1086/679566*

Berardo, D., de Wit, J., & Rackham, B. V., 2023, Empirically Constraining the Spectra of a Stars Heterogeneities From Its Rotation Lightcurve, *arXiv e-prints*, p. arXiv:2307.04785.

Berdyugina, S. V., 2005, Starspots: A Key to the Stellar Dynamo, *Living Reviews in Solar Physics*, 2(1), 8.

Berdyugina, S. V., Berdyugin, A. V., Fluri, D. M., & Piirola, V., 2011, Polarized Reflected Light from the Exoplanet HD189733b: First Multicolor Observations and Confirmation of Detection, *ApJ*, 728(1), L6.

Berta-Thompson, Z. K., Irwin, J., Charbonneau, D., Newton, E. R., Dittmann, J. A., Astudillo-Defru, N., Bonfils, X., Gillon, M., Jehin, E., Stark, A. A., Stalder, B., Bouchy, F., Delfosse, X., Forveille, T., Lovis, C., Mayor, M., Neves, V., Pepe, F., Santos, N. C., Udry, S., & Wünsche, A., 2015, A rocky planet transiting a nearby low-mass star, *Nature*, 527(7577), 204–207.
URL: *http://www.nature.com/doifinder/10.1038/nature15762*

Berta, Z. K., Irwin, J., Charbonneau, D., Burke, C. J., & Falco, E. E., 2012, Transit Detection in the MEarth Survey of Nearby M Dwarfs: Bridging the Clean-first, Search-later Divide, *AJ*, 144(5), 145.

Blake, C. H., Bloom, J. S., Latham, D. W., Szentgyorgyi, A. H., Skrutskie, M. F., Falco, E. E., & Starr, D. S., 2008, Near-Infrared Monitoring of Ultracool Dwarfs: Prospects for Searching for Transiting Companions, *PASP*, 120(870), 860.

Bochanski, J. J., Hawley, S. L., Covey, K. R., West, A. A., Reid, I. N., Golimowski, D. A., & Ivezić, Ž., 2010, The Luminosity and Mass Functions of Low-mass Stars in the Galactic Disk. II. The Field, *AJ*, 139(6), 2679–2699.

Bonfils, X., Almenara, J.-M., Cloutier, R., Wünsche, A., Astudillo-Defru, N., Berta-Thompson, Z., Bouchy, F., Charbonneau, D., Delfosse, X., Díaz, R. F., Dittmann, J., Doyon, R., Forveille, T., Irwin, J., Lovis, C., Mayor, M., Menou, K., Murgas, F., Newton, E., Pepe, F., Santos, N. C., & Udry, S., 2018, Radial velocity follow-up of GJ1132 with HARPS A precise mass for planet 'b' and the discovery of a second planet, , .
URL: *https://arxiv.org/pdf/1806.03870.pdf*

Borucki, W. J., Koch, D., Basri, G., Batalha, N., Brown, T., Caldwell, D., Caldwell, J., Christensen-Dalsgaard, J., Cochran, W. D., DeVore, E., Dunham, E. W., Dupree, A. K., Gautier, T. N., Geary, J. C., Gilliland, R., Gould, A., Howell, S. B., Jenkins, J. M., Kondo, Y., Latham, D. W., Marcy, G. W., Meibom, S., Kjeldsen, H., Lissauer, J. J., Monet, D. G., Morrison, D., Sasselov, D., Tarter, J., Boss, A., Brownlee, D., Owen, T., Buzasi, D., Charbonneau, D., Doyle, L., Fortney, J., Ford, E. B., Holman, M. J., Seager, S., Steffen, J. H., Welsh, W. F., Rowe, J., Anderson, H., Buchhave, L., Ciardi, D., Walkowicz, L., Sherry, W., Horch, E., Isaacson, H., Everett, M. E., Fischer, D., Torres, G., Johnson, J. A., Endl, M., MacQueen, P., Bryson, S. T., Dotson, J., Haas, M., Kolodziejczak, J., Van Cleve, J., Chandrasekaran, H., Twicken, J. D., Quintana, E. V., Clarke, B. D., Allen, C., Li, J., Wu, H., Tenenbaum, P., Verner, E., Bruhweiler, F., Barnes, J., & Prsa, A., 2010, Kepler Planet-Detection Mission: Introduction and First Results, *Science*, 327(5968), 977.

Borucki, W. J., Koch, D. G., Lissauer, J. J., Basri, G. B., Caldwell, J. F., Cochran, W. D., Dunham, E. W., Geary, J. C., Latham, D. W., Gilliland, R. L., Caldwell, D. A., Jenkins, J. M., & Kondo, Y., 2003, The Kepler mission: a wide-field-of-view photometer designed to determine the frequency of Earth-size planets around solar-like stars, *in* Blades, J. C. & Siegmund, O. H. W. (eds), *Future EUV/UV and Visible Space Astrophysics Missions and Instrumentation.*, Vol. 4854 of *Society of Photo-Optical Instrumentation Engineers (SPIE) Conference Series*, pp. 129–140.

Bourrier, V., de Wit, J., Bolmont, E., Stamenković, V., Wheatley, P. J., Burgasser, A. J., Delrez, L., Demory, B. O., Ehrenreich, D., Gillon, M., Jehin, E., Leconte, J., Lederer, S. M., Lewis, N., Triaud, A. H. M. J., & Van Grootel, V., 2017a, Temporal Evolution of the High-energy Irradiation and Water Content of TRAPPIST-1 Exoplanets, *AJ*, 154(3), 121.

Bourrier, V., dos Santos, L. A., Sanz-Forcada, J., García Muñoz, A., Henry, G. W., Lavvas, P., Lecavelier, A., López-Morales, M., Mikal-Evans, T., Sing, D. K., Wakeford, H. R., & Ehrenreich, D., 2021, The Hubble PanCET program: long-term chromospheric evolution and flaring activity of the M dwarf host GJ 3470, *A&A*, 650, A73.

Bourrier, V., Ehrenreich, D., & des Etangs, A. L., 2015, Radiative braking in the extended exosphere of GJ436b, , 65, 1–9.
URL: *http://arxiv.org/abs/1508.06634%0Ahttp://dx.doi.org/10.1051/0004-6361/201526894*

Bourrier, V., Ehrenreich, D., King, G., Lecavelier des Etangs, A., Wheatley, P. J., Vidal-Madjar, A., Pepe, F., & Udry, S., 2017b, No hydrogen exosphere detected around the super-Earth HD 97658 b, *A&A*, 597, A26.

Bourrier, V., Ehrenreich, D., Wheatley, P. J., Bolmont, E., Gillon, M., de Wit, J., Burgasser, A. J., Jehin, E., Queloz, D., & Triaud, A. H. M. J., 2017c, Reconnaissance of the TRAPPIST-1 exoplanet system in the Lyman-α line, *A&A*, 599, L3.

Bourrier, V., Lecavelier des Etangs, A., Dupuy, H., Ehrenreich, D., Vidal-Madjar, A., Hébrard, G., Ballester, G. E., Désert, J.-M., Ferlet, R., Sing, D. K., & Wheatley, P. J., 2013, Atmospheric escape from HD 189733b observed in H I Lyman- α : detailed analysis of HST/STIS September 2011 observations, *Astronomy & Astrophysics*, 551, A63.
URL: *https://arxiv.org/pdf/1301.6030.pdf http://www.aanda.org/10.1051/0004-6361/201220533*

Bourrier, V., Lecavelier des Etangs, A., Ehrenreich, D., Sanz-Forcada, J., Allart, R., Ballester, G. E., Buchhave, L. A., Cohen, O., Deming, D., Evans, T. M., García Muñoz, A., Henry, G. W., Kataria, T., Lavvas, P., Lewis, N., López-Morales, M., Marley, M., Sing, D. K., & Wakeford, H. R., 2018a, Hubble PanCET: an extended upper atmosphere of neutral hydrogen around the warm Neptune GJ 3470b, *A&A*, 620, A147.

Bourrier, V., Lecavelier des Etangs, A., Ehrenreich, D., Sanz-Forcada, J., Allart, R., Ballester, G. E., Buchhave, L. A., Cohen, O., Deming, D., Evans, T. M., García Muñoz, A., Henry, G. W., Kataria, T., Lavvas, P., Lewis, N., López-Morales, M., Marley, M., Sing, D. K., & Wakeford, H. R., 2018b, Hubble PanCET: an extended upper atmosphere of neutral hydrogen around the warm Neptune GJ 3470b, *A&A*, 620, A147.

Bourrier, V., Lecavelier des Etangs, A., Ehrenreich, D., Tanaka, Y. A., & Vidotto, A. A., 2016, An evaporating planet in the wind: stellar wind interactions with the radiatively braked exosphere of GJ 436 b, *Astronomy & Astrophysics*, 591, A121.
URL: *http://www.aanda.org/10.1051/0004-6361/201628362*

Bowler, B. P., Liu, M. C., Shkolnik, E. L., & Tamura, M., 2015, Planets around Low-mass Stars (PALMS). IV. The Outer Architecture of M Dwarf Planetary Systems, *ApJS*, 216, 7.

Brown, B. P., Oishi, J. S., Vasil, G. M., Lecoanet, D., & Burns, K. J., 2020, Single-hemisphere Dynamos in M-dwarf Stars, *ApJ*, 902(1), L3.

Brown, T. M., Baliber, N., Bianco, F. B., Bowman, M., Burleson, B., Conway, P., Crellin, M., Depagne, É., De Vera, J., Dilday, B., Dragomir, D., Dubberley, M., Eastman, J. D., Elphick, M., Falarski, M., Foale, S., Ford, M., Fulton, B. J., Garza, J., Gomez, E. L., Graham, M., Greene, R., Haldeman, B., Hawkins, E., Haworth, B., Haynes, R., Hidas, M., Hjelstrom, A. E., Howell, D. A., Hygelund, J., Lister, T. A., Lobdill, R., Martinez, J., Mullins, D. S., Norbury, M., Parrent, J., Paulson, R., Petry, D. L., Pickles, A., Posner, V., Rosing, W. E., Ross, R., Sand, D. J., Saunders, E. S., Shobbrook, J., Shporer, A., Street, R. A., Thomas, D., Tsapras, Y., Tufts, J. R., Valenti, S., Vander Horst, K., Walker, Z., White, G., & Willis, M., 2013, Las Cumbres Observatory Global Telescope Network, *PASP*, 125, 1031.

Brown, T. M., Charbonneau, D., Gilliland, R. L., Noyes, R. W., & Burrows, A., 2001, Hubble Space Telescope Time-Series Photometry of the Transiting Planet of HD 209458, *ApJ*, 552(2), 699–709.

Buckley, D. A. H., Swart, G. P., & Meiring, J. G., 2006, Completion and commissioning of the Southern African Large Telescope, *Society of Photo-Optical Instrumentation Engineers (SPIE) Conference Series*, Vol. 6267 of *Proc. SPIE*, p. 62670Z.

Budding, E., 1977, The Interpretation of Cyclical Photometric Variations in Certain Dwarf ME-Type Stars, *Ap&SS*, 48(1), 207–223.

Budding, E. & Zeilik, M., 1987, An Analysis of the Light Curves of Short-Period RS Canum Venaticorum Stars: Starspots and Fundamental Properties, *ApJ*, 319, 827.

Burns, K. J., Vasil, G. M., Oishi, J. S., Lecoanet, D., & Brown, B. P., 2020, Dedalus: A flexible framework for numerical simulations with spectral methods, *Physical Review Research*, 2(2), 023068.

Burrows, A., Heng, K., & Nampaisarn, T., 2011, The Dependence of Brown Dwarf Radii on Atmospheric Metallicity and Clouds: Theory and Comparison with Observations, *ApJ*, 736, 47.

Cao, L., Pinsonneault, M. H., Hillenbrand, L. A., & Kuhn, M. A., 2022, Age Spreads and Systematics in λ Orionis with Gaia DR2 and the SPOTS Tracks, *ApJ*, 924(2), 84.

Chabrier, G. & Baraffe, I., 2000, Theory of Low-Mass Stars and Substellar Objects, *ARA&A*, 38, 337–377.

Chadney, J. M., Koskinen, T. T., Galand, M., Unruh, Y. C., & Sanz-Forcada, J., 2017, Effect of stellar flares on the upper atmospheres of HD 189733b and HD 209458b, *A&A*, 608, A75.

Chaffin, M. S., Chaufray, J. Y., Deighan, J., Schneider, N. M., McClintock, W. E., Stewart, A. I. F., Thiemann, E., Clarke, J. T., Holsclaw, G. M., Jain, S. K., Crismani, M. M. J., Stiepen, A., Montmessin, F., Eparvier, F. G., Chamberlain, P. C., & Jakosky, B. M., 2015, Three-dimensional structure in the Mars H corona revealed by IUVS on MAVEN, *Geophysical Research Letters*, 42(21), 9001–9008.
URL: *http://doi.wiley.com/10.1002/2015GL065287*

Charbonneau, D., Brown, T. M., Latham, D. W., & Mayor, M., 2000, Detection of Planetary Transits Across a Sun-like Star, *The Astrophysical Journal*, 529(1), L45–L48.
URL: *http://stacks.iop.org/1538-4357/529/i=1/a=L45*

Charbonneau, D., Brown, T. M., Noyes, R. W., & Gilliland, R. L., 2002, Detection of an Extrasolar Planet Atmosphere, *ApJ*, 568(1), 377–384.

Chen, C. H., Patten, B. M., Werner, M. W., Dowell, C. D., Stapelfeldt, K. R., Song, I., Stauffer, J. R., Blaylock, M., Gordon, K. D., & Krause, V., 2005, A Spitzer Study of Dusty Disks around Nearby, Young Stars, *ApJ*, 634(2), 1372–1384.

Chen, J. & Kipping, D., 2017, Probabilistic Forecasting of the Masses and Radii of Other Worlds, *ApJ*, 834(1), 17.

Cloutier, R., Astudillo-Defru, N., Bonfils, X., Jenkins, J. S., Berdiñas, Z., Ricker, G., Vand erspek, R., Latham, D. W., Seager, S., Winn, J., Jenkins, J. M., Almenara, J. M., Bouchy, F., Delfosse, X., Díaz, M. R., Díaz, R. F., Doyon, R., Figueira, P., Forveille, T., Kurtovic, N. T., Lovis, C., Mayor, M., Menou, K., Morgan, E., Morris, R., Muirhead, P., Murgas, F., Pepe, F., Santos, N. C., Ségransan, D., Smith, J. C., Tenenbaum, P., Torres, G., Udry, S., Vezie, M., & Villasenor, J., 2019, Characterization of the L 98-59 multi-planetary system with HARPS. Mass characterization of a hot super-Earth, a sub-Neptune, and a mass upper limit on the third planet, *A&A*, 629, A111.

Cointepas, M., Almenara, J. M., Bonfils, X., Bouchy, F., Astudillo-Defru, N., Murgas, F., Otegi, J. F., Wyttenbach, A., Anderson, D. R., Artigau, É., Canto Martins, B. L., Charbonneau, D., Collins, K. A., Collins, K. I., Correia, J. J., Curaba, S., Delboulbé, A., Delfosse, X., Díaz, R. F., Dorn, C., Doyon, R., Feautrier, P., Figueira, P., Forveille, T., Gaisne, G., Gan, T., Gluck, L., Helled, R., Hellier, C., Jocou, L., Kern, P., Lafrasse, S., Law, N., Leão, I. C., Lovis, C., Magnard, Y., Mann, A. W., Maurel, D., de Medeiros, J. R., Melo, C., Moulin, T., Pepe, F., Rabou, P., Rochat, S., Rodriguez, D. R., Roux, A., Santos, N. C., Ségransan, D., Stadler, E., Ting, E. B., Twicken, J. D., Udry, S., Waalkes, W. C., West, R. G., Wünsche, A., Ziegler, C., Ricker, G., Vanderspek, R., Latham, D. W., Seager, S., Winn, J., & Jenkins, J. M., 2021, TOI-269 b: an eccentric sub-Neptune transiting a M2 dwarf revisited with ExTrA, *A&A*, 650, A145.

Collins, K. A., Kielkopf, J. F., Stassun, K. G., & Hessman, F. V., 2017, AstroImageJ: Image Processing and Photometric Extraction for Ultra-precise Astronomical Light Curves, *AJ*, 153(2), 77.

Cowan, N. B. & Agol, E., 2011, The Statistics of Albedo and Heat Recirculation on Hot Exoplanets, *ApJ*, 729(1), 54.

Crause, L. A., Sharples, R. M., Bramall, D. G., Schmoll, J., Clark, P., Younger, E. J., Tyas, L. M. G., Ryan, S. G., Brink, J. D., Strydom, O. J., Buckley, D. A. H., Wilkinson, M., Crawford, S. M., & Depagne, E., 2014, Performance of the Southern African Large Telescope (SALT) High Resolution Spectrograph (HRS), *Ground-based and Airborne Instrumentation for Astronomy V*, 9147, 91476T.

Cristofari, P. I., Donati, J. F., Folsom, C. P., Masseron, T., Fouqué, P., Moutou, C., Artigau, E., Carmona, A., Petit, P., Delfosse, X., Martioli, E., & the SLS consortium, 2023, Constraining atmospheric parameters and surface magnetic fields with ZeeTurbo: an application to SPIRou spectra, *MNRAS*, 522(1), 1342–1357.

Crossfield, I. J. M., Waalkes, W., Newton, E. R., Narita, N., Muirhead, P., Ment, K., Matthews, E., Kraus, A., Kostov, V., Kosiarek, M. R., Kane, S. R., Isaacson, H., Halverson, S., Gonzales, E., Everett, M., Dragomir, D., Collins, K. A., Chontos, A., Berardo, D., Winters, J. G., Winn, J. N., Scott, N. J., Rojas-Ayala, B., Rizzuto, A. C., Petigura, E. A., Peterson, M., Mocnik, T., Mikal-Evans, T., Mehrle, N., Matson, R., Kuzuhara, M., Irwin, J., Huber, D., Huang, C., Howell, S., Howard, A. W., Hirano, T., Fulton, B. J., Dupuy, T., Dressing, C. D., Dalba, P. A., Charbonneau, D., Burt, J., Berta-Thompson, Z., Benneke, B., Watanabe, N., Twicken, J. D., Tamura, M., Schlieder, J., Seager, S., Rose, M. E., Ricker, G., Quintana, E., Lépine, S., Latham, D. W., Kotani, T., Jenkins, J. M., Hori, Y., Colon, K., & Caldwell, D. A., 2019, A Super-Earth and Sub-Neptune Transiting the Late-type M Dwarf LP 791-18, *ApJ*, 883(1), L16.

Czesla, S., Huber, K. F., Wolter, U., Schröter, S., & Schmitt, J. H. M. M., 2009, How stellar activity affects the size estimates of extrasolar planets, *A&A*, 505(3), 1277–1282.

Deming, D. & Sheppard, K., 2017, Spectral Resolution-linked Bias in Transit Spectroscopy of Extrasolar Planets, *ApJ*, 841(1), L3.

Deming, D., Seager, S., Winn, J., Miller-Ricci, E., Clampin, M., Lindler, D., Greene, T., Charbonneau, D., Laughlin, G., Ricker, G., Latham, D., & Ennico, K., 2009, Discovery and Characterization of Transiting Super Earths Using an All-Sky Transit Survey and Follow-up by the <i>James Webb Space Telescope</i>, *Publications of the Astronomical Society of the Pacific*, 121(883), 952–967.
URL: *http://iopscience.iop.org/article/10.1086/605913*

Diamond-Lowe, H., Berta-Thompson, Z., Charbonneau, D., & Kempton, E. M.-R., 2018, Ground-based Optical Transmission Spectroscopy of the Small, Rocky Exoplanet GJ 1132b, *AJ*, 156, 42.

Dittmann, J. A., Irwin, J. M., Charbonneau, D., Bonfils, X., Astudillo-Defru, N., Haywood, R. D., Berta-Thompson, Z. K., Newton, E. R., Rodriguez, J. E., Winters, J. G., Tan, T.-G., Almenara, J.-M., Bouchy, F., Delfosse, X., Forveille, T., Lovis, C., Murgas, F., Pepe, F., Santos, N. C., Udry, S., Wünsche, A., Esquerdo, G. A., Latham, D. W., & Dressing, C. D., 2017, A temperate rocky super-Earth transiting a nearby cool star, , .
URL: *http://arxiv.org/abs/1704.05556 http://dx.doi.org/10.1038/nature22055*

Donati, J. F., Cristofari, P. I., Finociety, B., Klein, B., Moutou, C., Gaidos, E., Cadieux, C., Artigau, E., Correia, A. C. M., Boué, G., Cook, N. J., Carmona, A., Lehmann, L. T., Bouvier, J., Martioli, E., Morin, J., Fouqué, P., Delfosse, X., Doyon, R., Hébrard, G., Alencar, S. H. P., Laskar, J., Arnold, L., Petit, P., Kóspál, Á., Vidotto, A., Folsom, C. P., & collaboration, t. S. L. S., 2023, The magnetic field and multiple planets of the young dwarf AU Mic, *MNRAS*, 525(1), 455–475.

Dressing, C. D. & Charbonneau, D., 2015, The Occurrence of Potentially Habitable Planets Orbiting M Dwarfs Estimated from the Full Kepler Dataset and an Empirical Measurement of the Detection Sensitivity, *ApJ*, 807(1), 45.

Ehrenreich, D., Bourrier, V., Wheatley, P. J., des Etangs, A. L., Hébrard, G., Udry, S., Bonfils, X., Delfosse, X., Désert, J.-M., Sing, D. K., & Vidal-Madjar, A., 2015, A giant comet-like cloud of hydrogen escaping the warm Neptune-mass exoplanet GJ 436b, *Nature*, 522(7557), 459–461.
URL: *http://www.nature.com/doifinder/10.1038/nature14501*

Ehrenreich, D., Lecavelier Des Etangs, A., Hébrard, G., Désert, J. M., Vidal-Madjar, A., McConnell, J. C., Parkinson, C. D., Ballester, G. E., & Ferlet, R., 2008, New observations of the extended hydrogen exosphere of the extrasolar planet HD 209458b, *A&A*, 483(3), 933–937.

Evans, T. M., Aigrain, S., Gibson, N., Barstow, J. K., Amundsen, D. S., Tremblin, P., & Mourier, P., 2015, A uniform analysis of HD 209458b Spitzer/IRAC light curves with Gaussian process models, *MNRAS*, 451(1), 680–694.

Feinstein, A. D., France, K., Youngblood, A., Duvvuri, G. M., Teal, D. J., Cauley, P. W., Seligman, D. Z., Gaidos, E., Kempton, E. M. R., Bean, J. L., Diamond-Lowe, H., Newton, E., Ginzburg, S., Plavchan, P., Gao, P., & Schlichting, H., 2022, AU Microscopii in the Far-UV: Observations in Quiescence, during Flares, and Implications for AU Mic b and c, *AJ*, 164(3), 110.

Feinstein, A. D., Radica, M., Welbanks, L., Murray, C. A., Ohno, K., Coulombe, L.-P., Espinoza, N., Bean, J. L., Teske, J. K., Benneke, B., Line, M. R., Rustamkulov, Z., Saba, A., Tsiaras, A., Barstow, J. K., Fortney, J. J., Gao, P., Knutson, H. A., MacDonald, R. J., Mikal-Evans, T., Rackham, B. V., Taylor, J., Parmentier, V., Batalha, N. M., Berta-Thompson, Z. K., Carter, A. L., Changeat, Q., dos Santos, L. A., Gibson, N. P., Goyal, J. M., Kreidberg, L., López-Morales, M., Lothringer, J. D., Miguel, Y., Molaverdikhani, K., Moran, S. E., Morello, G., Mukherjee, S., Sing, D. K., Stevenson, K. B., Wakeford, H. R., Ahrer, E.-M., Alam, M. K., Alderson, L., Allen, N. H., Batalha, N. E., Bell, T. J., Blecic, J., Brande, J., Caceres, C., Casewell, S. L., Chubb, K. L., Crossfield, I. J. M., Crouzet, N., Cubillos, P. E., Decin, L., Désert, J.-M., Harrington, J., Heng, K., Henning, T., Iro, N., Kempton, E. M. R., Kendrew, S., Kirk, J., Krick, J., Lagage, P.-O., Lendl, M., Mancini, L., Mansfield, M., May, E. M., Mayne, N. J., Nikolov, N. K., Palle, E., Petit dit de la Roche, D. J. M., Piaulet, C., Powell, D., Redfield, S., Rogers, L. K., Roman, M. T., Roy, P.-A., Nixon, M. C., Schlawin, E., Tan, X., Tremblin, P., Turner, J. D., Venot, O., Waalkes, W. C., Wheatley, P. J., & Zhang, X., 2023, Early Release Science of the exoplanet WASP-39b with JWST NIRISS, *Nature*, 614(7949), 670–675.

Flagg, L., Johns-Krull, C. M., France, K., Herczeg, G., Najita, J., Youngblood, A., Carvalho, A., Carptenter, J., Kenyon, S. J., Newton, E., & Rockcliffe, K., 2022, The Mysterious Affair of the H_2 in AU Mic, *ApJ*, 934(1), 8.

Foreman-Mackey, D., 2016, corner.py: Scatterplot matrices in python, *The Journal of Open Source Software*, 1(2), 24.
URL: *https://doi.org/10.21105/joss.00024*

Foreman-Mackey, D., Hogg, D. W., Lang, D., & Goodman, J., 2013, emcee: The MCMC Hammer, *PASP*, 125, 306.

France, K., Froning, C. S., Linsky, J. L., Roberge, A., Stocke, J. T., Tian, F., Bushinsky, R., Désert, J.-M., Mauas, P., Vieytes, M., & Walkowicz, L. M., 2013, The Ultraviolet Radiation Environment around M dwarf Exoplanet Host Stars, *ApJ*, 763(2), 149.

France, K., Linsky, J. L., Tian, F., Froning, C. S., & Roberge, A., 2012, Time-resolved Ultraviolet Spectroscopy of the M-dwarf GJ 876 Exoplanetary System, *ApJ*, 750(2), L32.

Fu, G., Espinoza, N., Sing, D. K., Lothringer, J. D., Dos Santos, L. A., Rustamkulov, Z., Deming, D., Kempton, E. M. R., Komacek, T. D., Knutson, H. A., Albert, L., Pontoppidan, K., Volk, K., & Filippazzo, J., 2022, Water and an Escaping Helium Tail Detected in the Hazy and Methane-depleted Atmosphere of HAT-P-18b from JWST NIRISS/SOSS, *ApJ*, 940(2), L35.

Gaia Collaboration, G., Brown, A. G. A., Vallenari, A., Prusti, T., de Bruijne, J. H. J., Babusiaux, C., & Bailer-Jones, C. A. L., 2018, Gaia Data Release 2. Summary of the contents and survey properties, , .
URL: *http://arxiv.org/abs/1804.09365*

Gaia Collaboration, Vallenari, A., Brown, A. G. A., Prusti, T., de Bruijne, J. H. J., Arenou, F., Babusiaux, C., Biermann, M., Creevey, O. L., Ducourant, C., Evans, D. W., Eyer, L., Guerra, R., Hutton, A., Jordi, C., Klioner, S. A., Lammers, U. L., Lindegren, L., Luri, X., Mignard, F., Panem, C., Pourbaix, D., Randich, S., Sartoretti, P., Soubiran, C., Tanga, P., Walton, N. A., Bailer-Jones, C. A. L., Bastian, U., Drimmel, R., Jansen, F., Katz, D., Lattanzi, M. G., van Leeuwen, F., Bakker, J., Cacciari, C., Castañeda, J., De Angeli, F., Fabricius, C., Fouesneau, M., Frémat, Y., Galluccio, L., Guerrier, A., Heiter, U., Masana, E., Messineo, R., Mowlavi, N., Nicolas, C., Nienartowicz, K., Pailler, F., Panuzzo, P., Riclet, F., Roux, W., Seabroke, G. M., Sordo, R., Thévenin, F., Gracia-Abril, G., Portell, J., Teyssier, D., Altmann, M., Andrae, R., Audard, M., Bellas-Velidis, I., Benson, K., Berthier, J., Blomme, R., Burgess, P. W., Busonero, D., Busso, G., Cánovas, H., Carry, B., Cellino, A., Cheek, N., Clementini, G., Damerdji, Y., Davidson, M., de Teodoro, P., Nuñez Campos, M., Delchambre, L., Dell'Oro, A., Esquej, P., Fernández-Hernández, J., Fraile, E., Garabato, D., García-Lario, P., Gosset, E., Haigron, R., Halbwachs, J. L., Hambly, N. C., Harrison, D. L., Hernández, J., Hestroffer, D., Hodgkin, S. T., Holl, B., Janßen, K., Jevardat de Fombelle, G., Jordan, S., Krone-Martins, A., Lanzafame, A. C., Löffler, W., Marchal, O., Marrese, P. M., Moitinho, A., Muinonen, K., Osborne, P., Pancino, E., Pauwels, T., Recio-Blanco, A., Reylé, C., Riello, M., Rimoldini, L., Roegiers, T., Rybizki, J., Sarro, L. M., Siopis, C., Smith, M., Sozzetti, A., Utrilla, E., van Leeuwen, M., Abbas, U., Ábrahám, P., Abreu Aramburu, A., Aerts, C., Aguado, J. J., Ajaj, M., Aldea-Montero, F., Altavilla, G., Álvarez, M. A., Alves, J., Anders, F., Anderson, R. I., Anglada Varela, E., Antoja, T., Baines, D., Baker, S. G., Balaguer-Núñez, L., Balbinot, E., Balog, Z., Barache, C., Barbato, D., Barros, M., Barstow, M. A., Bartolomé, S., Bassilana, J. L., Bauchet, N., Becciani, U., Bellazzini, M., Berihuete, A., Bernet, M., Bertone, S., Bianchi, L., Binnenfeld, A., Blanco-Cuaresma, S., Blazere, A., Boch, T., Bombrun, A., Bossini, D., Bouquillon, S., Bragaglia, A., Bramante, L., Breedt, E., Bressan, A., Brouillet, N., Brugaletta, E., Bucciarelli, B., Burlacu, A., Butkevich, A. G., Buzzi, R., Caffau, E., Cancelliere, R., Cantat-Gaudin, T., Carballo, R., Carlucci, T., Carnerero, M. I., Carrasco, J. M., Casamiquela, L., Castellani, M., Castro-Ginard, A., Chaoul, L., Charlot, P., Chemin, L., Chiaramida, V., Chiavassa, A., Chornay, N., Comoretto, G., Contursi, G., Cooper, W. J., Cornez, T., Cowell, S., Crifo, F., Cropper, M., Crosta, M., Crowley, C., Dafonte, C., Dapergolas, A., David, M., David, P., de Laverny, P., De Luise, F., De March, R., De Ridder, J., de Souza, R., de Torres, A., del Peloso, E. F., del Pozo, E., Delbo, M., Delgado, A., Delisle, J. B., Demouchy, C., Dharmawardena, T. E., Di Matteo, P., Diakite, S., Diener, C., Distefano, E., Dolding, C., Edvardsson, B., Enke, H., Fabre, C., Fabrizio, M., Faigler, S., Fedorets, G., Fernique, P., Fienga, A., Figueras, F., Fournier, Y., Fouron, C., Fragkoudi, F., Gai, M., Garcia-Gutierrez, A., Garcia-Reinaldos, M., García-Torres, M., Garofalo, A., Gavel, A., Gavras, P., Gerlach, E., Geyer, R., Giacobbe, P., Gilmore, G., Girona, S., Giuffrida, G., Gomel, R., Gomez, A., González-Núñez, J., González-Santamaría, I., González-Vidal, J. J., Granvik, M., Guillout, P., Guiraud, J., Gutiérrez-Sánchez, R., Guy, L. P., Hatzidimitriou, D., Hauser, M., Haywood, M., Helmer, A., Helmi, A., Sarmiento, M. H., Hidalgo, S. L., Hilger, T., Hładczuk, N., Hobbs, D., Holland, G., Huckle, H. E., Jardine, K., Jasniewicz, G., Jean-Antoine Piccolo, A., Jiménez-Arranz, Ó., Jorissen, A., Juaristi Campillo, J., Julbe, F., Karbevska, L., Kervella, P., Khanna, S., Kontizas, M., Kordopatis, G., Korn, A. J., Kóspál, Á., Kostrzewa-Rutkowska, Z., Kruszyńska, K., Kun, M., Laizeau, P., Lambert, S., Lanza, A. F., Lasne, Y., Le Campion, J. F., Lebreton, Y., Lebzelter, T., Leccia, S., Leclerc, N., Lecoeur-Taibi, I., Liao, S., Licata, E. L., Lindstrøm, H. E. P., Lister, T. A., Livanou, E., Lobel, A., Lorca, A., Loup, C., Madrero Pardo, P., Magdaleno Romeo, A., Managau, S., Mann, R. G., Manteiga, M., Marchant, J. M., Marconi, M., Marcos, J., Marcos Santos, M. M. S., Marín Pina, D., Marinoni, S., Marocco, F., Marshall,

D. J., Martin Polo, L., Martín-Fleitas, J. M., Marton, G., Mary, N., Masip, A., Massari, D., Mastrobuono-Battisti, A., Mazeh, T., McMillan, P. J., Messina, S., Michalik, D., Millar, N. R., Mints, A., Molina, D., Molinaro, R., Molnár, L., Monari, G., Monguió, M., Montegriffo, P., Montero, A., Mor, R., Mora, A., Morbidelli, R., Morel, T., Morris, D., Muraveva, T., Murphy, C. P., Musella, I., Nagy, Z., Noval, L., Ocaña, F., Ogden, A., Ordenovic, C., Osinde, J. O., Pagani, C., Pagano, I., Palaversa, L., Palicio, P. A., Pallas-Quintela, L., Panahi, A., Payne-Wardenaar, S., Peñalosa Esteller, X., Penttilä, A., Pichon, B., Piersimoni, A. M., Pineau, F. X., Plachy, E., Plum, G., Poggio, E., Prša, A., Pulone, L., Racero, E., Ragaini, S., Rainer, M., Raiteri, C. M., Rambaux, N., Ramos, P., Ramos-Lerate, M., Re Fiorentin, P., Regibo, S., Richards, P. J., Rios Diaz, C., Ripepi, V., Riva, A., Rix, H. W., Rixon, G., Robichon, N., Robin, A. C., Robin, C., Roelens, M., Rogues, H. R. O., Rohrbasser, L., Romero-Gómez, M., Rowell, N., Royer, F., Ruz Mieres, D., Rybicki, K. A., Sadowski, G., Sáez Núñez, A., Sagristà Sellés, A., Sahlmann, J., Salguero, E., Samaras, N., Sanchez Gimenez, V., Sanna, N., Santoveña, R., Sarasso, M., Schultheis, M., Sciacca, E., Segol, M., Segovia, J. C., Ségransan, D., Semeux, D., Shahaf, S., Siddiqui, H. I., Siebert, A., Siltala, L., Silvelo, A., Slezak, E., Slezak, I., Smart, R. L., Snaith, O. N., Solano, E., Solitro, F., Souami, D., Souchay, J., Spagna, A., Spina, L., Spoto, F., Steele, I. A., Steidelmüller, H., Stephenson, C. A., Süveges, M., Surdej, J., Szabados, L., Szegedi-Elek, E., Taris, F., Taylor, M. B., Teixeira, R., Tolomei, L., Tonello, N., Torra, F., Torra, J., Torralba Elipe, G., Trabucchi, M., Tsounis, A. T., Turon, C., Ulla, A., Unger, N., Vaillant, M. V., van Dillen, E., van Reeven, W., Vanel, O., Vecchiato, A., Viala, Y., Vicente, D., Voutsinas, S., Weiler, M., Wevers, T., Wyrzykowski, Ł., Yoldas, A., Yvard, P., Zhao, H., Zorec, J., Zucker, S., & Zwitter, T., 2023, Gaia Data Release 3. Summary of the content and survey properties, *A&A*, 674, A1.

Gaudi, B. S., Seager, S., Mennesson, B., Kiessling, A., Warfield, K., Cahoy, K., Clarke, J. T., Domagal-Goldman, S., Feinberg, L., Guyon, O., Kasdin, J., Mawet, D., Plavchan, P., Robinson, T., Rogers, L., Scowen, P., Somerville, R., Stapelfeldt, K., Stark, C., Stern, D., Turnbull, M., Amini, R., Kuan, G., Martin, S., Morgan, R., Redding, D., Stahl, H. P., Webb, R., Alvarez-Salazar, O., Arnold, W. L., Arya, M., Balasubramanian, B., Baysinger, M., Bell, R., Below, C., Benson, J., Blais, L., Booth, J., Bourgeois, R., Bradford, C., Brewer, A., Brooks, T., Cady, E., Caldwell, M., Calvet, R., Carr, S., Chan, D., Cormarkovic, V., Coste, K., Cox, C., Danner, R., Davis, J., Dewell, L., Dorsett, L., Dunn, D., East, M., Effinger, M., Eng, R., Freebury, G., Garcia, J., Gaskin, J., Greene, S., Hennessy, J., Hilgemann, E., Hood, B., Holota, W., Howe, S., Huang, P., Hull, T., Hunt, R., Hurd, K., Johnson, S., Kissil, A., Knight, B., Kolenz, D., Kraus, O., Krist, J., Li, M., Lisman, D., Mandic, M., Mann, J., Marchen, L., Marrese-Reading, C., McCready, J., McGown, J., Missun, J., Miyaguchi, A., Moore, B., Nemati, B., Nikzad, S., Nissen, J., Novicki, M., Perrine, T., Pineda, C., Polanco, O., Putnam, D., Qureshi, A., Richards, M., Eldorado Riggs, A. J., Rodgers, M., Rud, M., Saini, N., Scalisi, D., Scharf, D., Schulz, K., Serabyn, G., Sigrist, N., Sikkia, G., Singleton, A., Shaklan, S., Smith, S., Southerd, B., Stahl, M., Steeves, J., Sturges, B., Sullivan, C., Tang, H., Taras, N., Tesch, J., Therrell, M., Tseng, H., Valente, M., Van Buren, D., Villalvazo, J., Warwick, S., Webb, D., Westerhoff, T., Wofford, R., Wu, G., Woo, J., Wood, M., Ziemer, J., Arney, G., Anderson, J., Maíz-Apellániz, J., Bartlett, J., Belikov, R., Bendek, E., Cenko, B., Douglas, E., Dulz, S., Evans, C., Faramaz, V., Feng, Y. K., Ferguson, H., Follette, K., Ford, S., García, M., Geha, M., Gelino, D., Götberg, Y., Hildebrandt, S., Hu, R., Jahnke, K., Kennedy, G., Kreidberg, L., Isella, A., Lopez, E., Marchis, F., Macri, L., Marley, M., Matzko, W., Mazoyer, J., McCandliss, S., Meshkat, T., Mordasini, C., Morris, P., Nielsen, E., Newman, P., Petigura, E., Postman, M., Reines, A., Roberge, A., Roederer, I., Ruane, G., Schwieterman, E., Sirbu, D., Spalding, C., Teplitz, H., Tumlinson, J., Turner, N., Werk, J., Wofford, A., Wyatt, M., Young, A., & Zellem, R., 2020, The Habitable Exoplanet Observatory (HabEx) Mission Concept Study Final Report, *arXiv e-prints*, p. arXiv:2001.06683.

Gilbert, E. A., Barclay, T., Quintana, E. V., Walkowicz, L. M., Vega, L. D., Schlieder, J. E., Monsue, T., Cale, B. L., Collins, K. I., Gaidos, E., El Mufti, M., Reefe, M. A., Plavchan, P., Tanner, A., Wittenmyer, R. A., Wittrock, J. M., Jenkins, J. M., Latham, D. W., Ricker, G. R., Rose, M. E., Seager, S., Vanderspek, R. K., & Winn, J. N., 2022, Flares, Rotation, and Planets of the AU Mic System from TESS Observations, *AJ*, 163(4), 147.

Gillon, M., Jehin, E., Fumel, A., Magain, P., & Queloz, D., 2013, TRAPPIST-UCDTS: A prototype search for habitable planets transiting ultra-cool stars, *European Physical Journal Web of Conferences*, Vol. 47 of *European Physical Journal Web of Conferences*, p. 03001.

Gillon, M., Triaud, A. H. M. J., Demory, B.-O., Jehin, E., Agol, E., Deck, K. M., Lederer, S. M., de Wit, J., Burdanov, A., Ingalls, J. G., Bolmont, E., Leconte, J., Raymond, S. N., Selsis, F., Turbet, M., Barkaoui, K., Burgasser, A., Burleigh, M. R., Carey, S. J., Chaushev, A., Copperwheat, C. M., Delrez, L., Fernandes, C. S., Holdsworth, D. L., Kotze, E. J., Van Grootel, V., Almleaky, Y., Benkhaldoun, Z., Magain, P., & Queloz, D., 2017, Seven temperate terrestrial planets around the nearby ultracool dwarf star TRAPPIST-1, *Nature*, 542(7642), 456–460.
URL: *http://www.nature.com/articles/nature21360*

Goldreich, P. & Soter, S., 1966, Q in the Solar System, *Icarus*, 5, 375–389.

Gray, D. F., 1984, Measurements of Zeeman broadening in F, G, and K dwarfs., *ApJ*, 277, 640–647.

Gully-Santiago, M. A., Herczeg, G. J., Czekala, I., Somers, G., Grankin, K., Covey, K. R., Donati, J. F., Alencar, S. H. P., Hussain, G. A. J., Shappee, B. J., Mace, G. N., Lee, J.-J., Holoien, T. W. S., Jose, J., & Liu, C.-F., 2017, Placing the Spotted T Tauri Star LkCa 4 on an HR Diagram, *ApJ*, 836(2), 200.

Günther, M. N., Pozuelos, F. J., Dittmann, J. A., Dragomir, D., Kane, S. R., Daylan, T., Feinstein, A. D., Huang, C. X., Morton, T. D., Bonfanti, A., Bouma, L. G., Burt, J., Collins, K. A., Lissauer, J. J., Matthews, E., Montet, B. T., Vand erburg, A., Wang, S., Winters, J. G., Ricker, G. R., Vanderspek, R. K., Latham, D. W., Seager, S., Winn, J. N., Jenkins, J. M., Armstrong, J. D., Barkaoui, K., Batalha, N., Bean, J. L., Caldwell, D. A., Ciardi, D. R., Collins, K. I., Crossfield, I., Fausnaugh, M., Furesz, G., Gan, T., Gillon, M., Guerrero, N., Horne, K., Howell, S. B., Ireland , M., Isopi, G., Jehin, E., Kielkopf, J. F., Lepine, S., Mallia, F., Matson, R. A., Myers, G., Palle, E., Quinn, S. N., Relles, H. M., Rojas-Ayala, B., Schlieder, J., Sefako, R., Shporer, A., Suárez, J. C., Tan, T.-G., Ting, E. B., Twicken, J. D., & Waite, I. A., 2019, A super-Earth and two sub-Neptunes transiting the nearby and quiet M dwarf TOI-270, *Nature Astronomy*, p. 420.

Hardegree-Ullman, K. K., Cushing, M. C., Muirhead, P. S., & Christiansen, J. L., 2019, Kepler Planet Occurrence Rates for Mid-type M Dwarfs as a Function of Spectral Type, *AJ*, 158(2), 75.

Hawley, S. L., Davenport, J. R. A., Kowalski, A. F., Wisniewski, J. P., Hebb, L., Deitrick, R., & Hilton, E. J., 2014, KEPLER FLARES. I. ACTIVE AND INACTIVE M DWARFS, *The Astrophysical Journal*, 797(15pp), 121.
URL: *http://iopscience.iop.org/article/10.1088/0004-637X/797/2/121/pdf*

Hebb, L., Petro, L., Ford, H. C., Ardila, D. R., Toledo, I., Minniti, D., Golimowski, D. A., & Clampin, M., 2007, A search for planets transiting the M-dwarf debris disc host, AU Microscopii, *MNRAS*, 379(1), 63–72.

Herbst, K., Papaioannou, A., Airapetian, V. S., & Atri, D., 2021, From Starspots to Stellar Coronal Mass Ejections—Revisiting Empirical Stellar Relations, *ApJ*, 907(2), 89.

Hirano, T., Krishnamurthy, V., Gaidos, E., Flewelling, H., Mann, A. W., Narita, N., Plavchan, P., Kotani, T., Tamura, M., Harakawa, H., Hodapp, K., Ishizuka, M., Jacobson, S., Konishi, M., Kudo, T., Kurokawa, T., Kuzuhara, M., Nishikawa, J., Omiya, M., Serizawa, T., Ueda, A., & Vievard, S., 2020, Limits on the Spin-Orbit Angle and Atmospheric Escape for the 22 Myr Old Planet AU Mic b, *ApJ*, 899(1), L13.

Hodge, P. & Baum, S., 1995, Plans for the STScI STIS Pipeline II: Calstis-1, Two-dimensional Image Reduction, *STIS Instrument Science Report 95-007, 14 pages*, .
URL: *http://adsabs.harvard.edu/abs/1995stis.rept....7B*

Hogg, D. W. & Foreman-Mackey, D., 2018, Data Analysis Recipes: Using Markov Chain Monte Carlo, *ApJS*, 236(1), 11.

Hogg, D. W., Bovy, J., & Lang, D., 2010, Data analysis recipes: Fitting a model to data, , .
URL: *http://arxiv.org/abs/1008.4686*

Howell, S. B., Sobeck, C., Haas, M., Still, M., Barclay, T., Mullally, F., Troeltzsch, J., Aigrain, S., Bryson, S. T., Caldwell, D., Chaplin, W. J., Cochran, W. D., Huber, D., Marcy, G. W., Miglio, A., Najita, J. R., Smith, M., Twicken, J. D., & Fortney, J. J., 2014, The K2 Mission: Characterization and Early Results, *PASP*, 126(938), 398.

Husser, T.-O., Wende-von Berg, S., Dreizler, S., Homeier, D., Reiners, A., Barman, T., & Hauschildt, P. H., 2013, A new extensive library of PHOENIX stellar atmospheres and synthetic spectra, *A&A*, 553, A6.

Ikuta, K., Namekata, K., Notsu, Y., Maehara, H., Okamoto, S., Honda, S., Nogami, D., & Shibata, K., 2023, Starspot mapping with adaptive parallel tempering. II. Application to TESS data for M-dwarf flare stars, AU Microscopii, YZ Canis Minoris, and EV Lacertae, *arXiv e-prints*, p. arXiv:2302.09249.

Ingersoll, A. P., 1969, The Runaway Greenhouse: A History of Water on Venus., *Journal of the Atmospheric Sciences*, 26(6), 1191–1198.

Ingersoll, A. P., 2013, *Planetary Climates*, Princeton University Press.

Irwin, J., Charbonneau, D., Berta, Z. K., Quinn, S. N., Latham, D. W., Torres, G., Blake, C. H., Burke, C. J., Esquerdo, G. A., Fűrész, G., Mink, D. J., Nutzman, P., Szentgyorgyi, A. H., Calkins, M. L., Falco, E. E., Bloom, J. S., & Starr, D. L., 2009, GJ 3236: A New Bright, Very Low Mass Eclipsing Binary System Discovered by the MEARTH Observatory, *ApJ*, 701(2), 1436–1449.

Iyer, A. R. & Line, M. R., 2020, The Influence of Stellar Contamination on the Interpretation of Near-infrared Transmission Spectra of Sub-Neptune Worlds around M-dwarfs, *ApJ*, 889(2), 78.

Iyer, A. R., Line, M. R., Muirhead, P. S., Fortney, J. J., & Gharib-Nezhad, E., 2023, The SPHINX M-dwarf Spectral Grid. I. Benchmarking New Model Atmospheres to Derive Fundamental M-dwarf Properties, *ApJ*, 944(1), 41.

Jeans, J. H., 1905, The Dynamical Theory of Gases, *Nature*, 71(1852), 607.

Jehin, E., Gillon, M., Queloz, D., Magain, P., Manfroid, J., Chantry, V., Lendl, M., Hutsemékers, D., & Udry, S., 2011, TRAPPIST: TRAnsiting Planets and PlanetesImals Small Telescope, *The Messenger*, 145, 2–6.

Jenkins, J. M., 2002, The Impact of Solar-like Variability on the Detectability of Transiting Terrestrial Planets, *ApJ*, 575(1), 493–505.

Jenkins, J. M., Twicken, J. D., McCauliff, S., Campbell, J., Sanderfer, D., Lung, D., Mansouri-Samani, M., Girouard, F., Tenenbaum, P., Klaus, T., Smith, J. C., Caldwell, D. A., Chacon, A. D., Henze, C., Heiges, C., Latham, D. W., Morgan, E., Swade, D., Rinehart, S., & Vanderspek, R., 2016a, The TESS science processing operations center, *Software and Cyberinfrastructure for Astronomy IV*, Vol. 9913 of *Proc. SPIE*, p. 99133E.

Jenkins, J. M., Twicken, J. D., McCauliff, S., Campbell, J., Sanderfer, D., Lung, D., Mansouri-Samani, M., Girouard, F., Tenenbaum, P., Klaus, T., Smith, J. C., Caldwell, D. A., Chacon, A. D., Henze, C., Heiges, C., Latham, D. W., Morgan, E., Swade, D., Rinehart, S., & Vanderspek, R., 2016b, The TESS science processing operations center, *Software and Cyberinfrastructure for Astronomy IV*, Vol. 9913 of *Proc. SPIE*, p. 99133E.

Jensen, E., 2013, Tapir: A web interface for transit/eclipse observability.

Jones, A., Noll, S., Kausch, W., Szyszka, C., & Kimeswenger, S., 2013, An advanced scattered moonlight model for Cerro Paranal, *A&A*, 560, A91.

Jones, H. R. A., Longmore, A. J., Allard, F., Hauschildt, P. H., Miller, S., & Tennyson, J., 1995, Water vapour in cool dwarf stars, *MNRAS*, 277(3), 767–776.

Jura, M., 2004, An Observational Signature of Evolved Oceans on Extrasolar Terrestrial Planets, *The Astrophysical Journal*, 605(1), L65–L68.
URL: *http://stacks.iop.org/1538-4357/605/i=1/a=L65*

Kalas, P., Liu, M. C., & Matthews, B. C., 2004, Discovery of a Large Dust Disk Around the Nearby Star AU Microscopii, *Science*, 303(5666), 1990–1992.

Kasting, J. F. & Pollack, J. B., 1983, Loss of water from Venus. I. Hydrodynamic escape of hydrogen, *Icarus*, 53(3), 479–508.
URL: *https://www.sciencedirect.com/science/article/pii/0019103583902129?via%3Dihub*

Kempton, E. M. R., Bean, J. L., Louie, D. R., Deming, D., Koll, D. D. B., Mansfield, M., Christiansen, J. L., Lopez-Morales, M., Swain, M. R., Zellem, R. T., Ballard, S., Barclay, T., Barstow, J. K., Batalha, N. E., Beatty, T. G., Berta-Thompson, Z., Birkby, J., Buchhave, L. A., Charbonneau, D., Cowan, N. B., Crossfield, I., de Val-Borro, M., Doyon, R., Dragomir, D., Gaidos, E., Heng, K., Hu, R., Kane, S. R., Kreidberg, L., Mallonn, M., Morley, C. V., Narita, N., Nascimbeni, V., Palle, E., Quintana, E. V., Rauscher, E., Seager, S., Shkolnik, E. L., Sing, D. K., Sozzetti, A., Stassun, K. G., Valenti, J. A., & von Essen, C., 2018, A Framework for Prioritizing

the TESS Planetary Candidates Most Amenable to Atmospheric Characterization, , .
URL: *http://arxiv.org/abs/1805.03671*

King, P. K., Fissel, L. M., Chen, C.-Y., & Li, Z.-Y., 2018, Modelling dust polarization observations of molecular clouds through MHD simulations, *Monthly Notices of the Royal Astronomical Society*, 474(4), 5122–5142.
URL: *https://academic.oup.com/mnras/article/474/4/5122/4683257*

Kniazev, A. Y., Gvaramadze, V. V., & Berdnikov, L. N., 2016, MN48: A new Galactic bona fide luminous blue variable revealed by Spitzer and SALT, *Monthly Notices of the Royal Astronomical Society*, 459, 3068–3077.

Kniazev, A. Y., Gvaramadze, V. V., & Berdnikov, L. N., 2017, SALT Spectroscopy of Evolved Massive Stars, *in* Balega, Y. Y., Kudryavtsev, D. O., Romanyuk, I. I., & Yakunin, I. A. (eds), *Stars: From Collapse to Collapse*, Vol. 510 of *Astronomical Society of the Pacific Conference Series*, p. 480.

Kochukhov, O. & Reiners, A., 2020, The Magnetic Field of the Active Planet-hosting M Dwarf AU Mic, *ApJ*, 902(1), 43.

Kopp, G. & Rabin, D., 1992, A Relation Between Magnetic Field Strength and Temperature in Sunspots, *Sol. Phys.*, 141(2), 253–265.

Kopparapu, R. K., Ramirez, R., Kasting, J. F., Eymet, V., Robinson, T. D., Mahadevan, S., Terrien, R. C., Domagal-Goldman, S., Meadows, V., & Deshpande, R., 2013, Habitable Zones around Main-sequence Stars: New Estimates, *ApJ*, 765(2), 131.

Kopparapu, R. k., Wolf, E. T., & Meadows, V. S., 2019, Characterizing Exoplanet Habitability, *arXiv e-prints*, p. arXiv:1911.04441.

Kostov, V. B., Schlieder, J. E., Barclay, T., Quintana, E. V., Colón, K. D., Brand e, J., Collins, K. A., Feinstein, A. D., Hadden, S., Kane, S. R., Kreidberg, L., Kruse, E., Lam, C., Matthews, E., Montet, B. T., Pozuelos, F. J., Stassun, K. G., Winters, J. G., Ricker, G., Vanderspek, R., Latham, D., Seager, S., Winn, J., Jenkins, J. M., Afanasev, D., Armstrong, J. J. D., Arney, G., Boyd, P., Barentsen, G., Barkaoui, K., Batalha, N. E., Beichman, C., Bayliss, D., Burke, C., Burdanov, A., Cacciapuoti, L., Carson, A., Charbonneau, D., Christiansen, J., Ciardi, D., Clampin, M., Collins, K. I., Conti, D. M., Coughlin, J., Covone, G., Crossfield, I., Delrez, L., Domagal-Goldman, S., Dressing, C., Ducrot, E., Essack, Z., Everett, M. E., Fauchez, T., Foreman-Mackey, D., Gan, T., Gilbert, E., Gillon, M., Gonzales, E., Hamann, A., Hedges, C., Hocutt, H., Hoffman, K., Horch, E. P., Horne, K., Howell, S., Hynes, S., Ireland , M., Irwin, J. M., Isopi, G., Jensen, E. L. N., Jehin, E., Kaltenegger, L., Kielkopf, J. F., Kopparapu, R., Lewis, N., Lopez, E., Lissauer, J. J., Mann, A. W., Mallia, F., Mandell, A., Matson, R. A., Mazeh, T., Monsue, T., Moran, S. E., Moran, V., Morley, C. V., Morris, B., Muirhead, P., Mukai, K., Mullally, S., Mullally, F., Murray, C., Narita, N., Palle, E., Pidhorodetska, D., Quinn, D., Relles, H., Rinehart, S., Ritsko, M., Rodriguez, J. E., Rowden, P., Rowe, J. F., Sebastian, D., Sefako, R., Shahaf, S., Shporer, A., Tañón Reyes, N., Tenenbaum, P., Ting, E. B., Twicken, J. D., van Belle, G. T., Vega, L., Volosin, J., Walkowicz, L. M., & Youngblood, A., 2019, The L 98-59 System: Three Transiting, Terrestrial-size Planets Orbiting a Nearby M Dwarf, *The Astronomical Journal*, 158(1), 32.

Kotani, T., Tamura, M., Suto, H., Nishikawa, J., Sato, B., Aoki, W., Usuda, T., Kurokawa, T., Kashiwagi, K., Nishiyama, S., Ikeda, Y., Hall, D. B., Hodapp, K. W., Hashimoto, J., Morino, J.-I., Okuyama, Y., Tanaka, Y., Suzuki, S., Inoue, S., Kwon, J., Suenaga, T., Oh, D., Baba, H., Narita, N., Kokubo, E., Hayano, Y., Izumiura, H., Kambe, E., Kudo, T., Kusakabe, N., Ikoma, M., Hori, Y., Omiya, M., Genda, H., Fukui, A., Fujii, Y., Guyon, O., Harakawa, H., Hayashi, M., Hidai, M., Hirano, T., Kuzuhara, M., Machida, M., Matsuo, T., Nagata, T., Onuki, H., Ogihara, M., Takami, H., Takato, N., Takahashi, Y. H., Tachinami, C., Terada, H., Kawahara, H., & Yamamuro, T., 2014, Infrared Doppler instrument (IRD) for the Subaru telescope to search for Earth-like planets around nearby M-dwarfs, *in* Ramsay, S. K., McLean, I. S., & Takami, H. (eds), *Ground-based and Airborne Instrumentation for Astronomy V*, Vol. 9147 of *Society of Photo-Optical Instrumentation Engineers (SPIE) Conference Series*, p. 914714.

Kreidberg, L., 2015, batman : BAsic Transit Model cAlculatioN in Python, *Publications of the Astronomical Society of the Pacific*, 127(957), 1161–1165.
URL: *http://iopscience.iop.org/article/10.1086/683602*

Kulow, J. R., France, K., Linsky, J., & Loyd, R. O. P., 2014, Lyα Transit Spectroscopy and the Neutral Hydrogen Tail of the Hot Neptune GJ 436b, *ApJ*, 786, 132.

Lammer, H., Selsis, F., Ribas, I., Guinan, E. F., Bauer, S. J., & Weiss, W. W., 2003, Atmospheric Loss of Exoplanets Resulting from Stellar X-Ray and Extreme-Ultraviolet Heating, *The Astrophysical Journal*, 598(2), L121–L124.
URL: *http://stacks.iop.org/1538-4357/598/i=2/a=L121*

Lanza, A. F., De Martino, C., & Rodonò, M., 2008, Astrometric effects of solar-like magnetic activity in late-type stars and their relevance for the detection of extrasolar planets, *New A*, 13(2), 77–84.

Laughlin, G., Bodenheimer, P., & Adams, F. C., 1997, The End of the Main Sequence, *ApJ*, 482(1), 420–432.

Lavie, B., Ehrenreich, D., Bourrier, V., Lecavelier des Etangs, A., Vidal-Madjar, A., Delfosse, X., Gracia Berna, A., Heng, K., Thomas, N., Udry, S., & Wheatley, P. J., 2017, The long egress of GJ 436b's giant exosphere, *Astronomy & Astrophysics*, 605, L7.
URL: *http://www.aanda.org/10.1051/0004-6361/201731340*

Li, J., Tenenbaum, P., Twicken, J. D., Burke, C. J., Jenkins, J. M., Quintana, E. V., Rowe, J. F., & Seader, S. E., 2019, Kepler Data Validation II-Transit Model Fitting and Multiple-planet Search, *PASP*, 131(996), 024506.

Libby-Roberts, J. E., Berta-Thompson, Z. K., Diamond-Lowe, H., Gully-Santiago, M. A., Irwin, J. M., Kempton, E. M. R., Rackham, B. V., Charbonneau, D., Désert, J.-M., Dittmann, J. A., Hofmann, R., Morley, C. V., & Newton, E. R., 2022, The Featureless HST/WFC3 Transmission Spectrum of the Rocky Exoplanet GJ 1132b: No Evidence for a Cloud-free Primordial Atmosphere and Constraints on Starspot Contamination, *AJ*, 164(2), 59.

Lightkurve Collaboration, Cardoso, J. V. d. M. a., Hedges, C., Gully-Santiago, M., Saunders, N., Cody, A. M., Barclay, T., Hall, O., Sagear, S., Turtelboom, E., Zhang, J., Tzanidakis, A., Mighell, K., Coughlin, J., Bell, K., Berta-Thompson, Z., Williams, P., Dotson, J., & Barentsen, G., 2018, Lightkurve: Kepler and TESS time series analysis in Python.

Lim, O., Benneke, B., Doyon, R., MacDonald, R. J., Piaulet, C., Artigau, É., Coulombe, L.-P., Radica, M., L'Heureux, A., Albert, L., Rackham, B. V., de Wit, J., Salhi, S., Roy, P.-A., Flagg, L., Fournier-Tondreau, M., Taylor, J., Cook, N. J., Lafrenière, D., Cowan, N. B., Kaltenegger, L., Rowe, J. F., Espinoza, N., Dang, L., & Darveau-Bernier, A., 2023, Atmospheric Reconnaissance of TRAPPIST-1 b with JWST/NIRISS: Evidence for Strong Stellar Contamination in the Transmission Spectra, *arXiv e-prints*, p. arXiv:2309.07047.

Linsky, J. L., Fontenla, J., & France, K., 2014, The Intrinsic Extreme Ultraviolet Fluxes of F5 V TO M5 V Stars, *ApJ*, 780, 61.

Linsky, J. L., France, K., & Ayres, T., 2013, Computing Intrinsic LYα Fluxes of F5 V to M5 V Stars, *ApJ*, 766(2), 69.

Linsky, J. L., Yang, H., France, K., Froning, C. S., Green, J. C., Stocke, J. T., & Osterman, S. N., 2010, OBSERVATIONS OF MASS LOSS FROM THE TRANSITING EXOPLANET HD 209458b, , .
URL: *https://arxiv.org/pdf/1005.1633.pdf*

Lobo, A. H., Shields, A. L., Palubski, I. Z., & Wolf, E., 2023, Terminator Habitability: The Case for Limited Water Availability on M-dwarf Planets, *ApJ*, 945(2), 161.

Louca, A. J., Miguel, Y., Tsai, S.-M., Froning, C. S., Loyd, R. O. P., & France, K., 2023, The impact of time-dependent stellar activity on exoplanet atmospheres, *MNRAS*, 521(3), 3333–3347.

Loyd, R. O. P. & France, K., 2014, FLUCTUATIONS AND FLARES IN THE ULTRAVIOLET LINE EMISSION OF COOL STARS: IMPLICATIONS FOR EXOPLANET TRANSIT OBSERVATIONS, *The Astrophysical Journal Supplement Series*, 211(25pp), 9.
URL: *http://iopscience.iop.org/article/10.1088/0067-0049/211/1/9/pdf*

Luger, R. & Barnes, R., 2015, Extreme Water Loss and Abiotic O2Buildup on Planets Throughout the Habitable Zones of M Dwarfs, *Astrobiology*, 15, 119–143.

Luque, R. & Pallé, E., 2022, Density, not radius, separates rocky and water-rich small planets orbiting M dwarf stars, *Science*, 377(6611), 1211–1214.

Luque, R., Pallé, E., Kossakowski, D., Dreizler, S., Kemmer, J., Espinoza, N., Burt, J., Anglada-Escudé, G., Béjar, V. J. S., Caballero, J. A., Collins, K. A., Collins, K. I., Cortés-Contreras, M., Díez-Alonso, E., Feng, F., Hatzes, A., Hellier, C., Henning, T., Jeffers, S. V., Kaltenegger, L., Kürster, M., Madden, J., Molaverdikhani, K., Montes, D., Narita, N., Nowak, G., Ofir, A., Oshagh, M., Parviainen, H., Quirrenbach, A., Reffert, S., Reiners, A., Rodríguez-López, C., Schlecker, M., Stock, S., Trifonov, T., Winn, J. N., Zapatero Osorio, M. R., Zechmeister, M., Amado, P. J., Anderson, D. R., Batalha, N. E., Bauer, F. F., Bluhm, P., Burke, C. J., Butler, R. P., Caldwell, D. A., Chen, G., Crane, J. D., Dragomir, D., Dressing, C. D., Dynes, S., Jenkins, J. M., Kaminski, A., Klahr, H., Kotani, T., Lafarga, M., Latham, D. W., Lewin, P., McDermott, S., Montañés-Rodríguez, P., Morales, J. C., Murgas, F., Nagel, E., Pedraz, S., Ribas, I., Ricker, G. R., Rowden, P., Seager, S., Shectman, S. A., Tamura, M., Teske, J., Twicken, J. D., Vanderspeck, R., Wang, S. X., & Wohler, B., 2019, Planetary system around the nearby M dwarf GJ 357 including a transiting, hot, Earth-sized planet optimal for atmospheric characterization, *Astronomy and Astrophysics*, 628, A39.

MacGregor, M. A., Wilner, D. J., Rosenfeld, K. A., Andrews, S. M., Matthews, B., Hughes, A. M., Booth, M., Chiang, E., Graham, J. R., Kalas, P., Kennedy, G., & Sibthorpe, B., 2013, Millimeter Emission Structure in the First ALMA Image of the AU Mic Debris Disk, *ApJ*, 762(2), L21.

Mahadevan, S., Ramsey, L., Bender, C., Terrien, R., Wright, J. T., Halverson, S., Hearty, F., Nelson, M., Burton, A., Redman, S., Osterman, S., Diddams, S., Kasting, J., Endl, M., & Deshpande, R., 2012, The habitable-zone planet finder: a stabilized fiber-fed NIR spectrograph for the Hobby-Eberly Telescope, *in* McLean, I. S., Ramsay, S. K., & Takami, H. (eds), *Ground-based and Airborne Instrumentation for Astronomy IV*, Vol. 8446 of *Society of Photo-Optical Instrumentation Engineers (SPIE) Conference Series*, p. 84461S.

Mahadevan, S., Ramsey, L. W., Terrien, R., Halverson, S., Roy, A., Hearty, F., Levi, E., Stefansson, G. K., Robertson, P., Bender, C., Schwab, C., & Nelson, M., 2014, The Habitable-zone Planet Finder: A status update on the development of a stabilized fiber-fed near-infrared spectrograph for the for the Hobby-Eberly telescope, *in* Ramsay, S. K., McLean, I. S., & Takami, H. (eds), *Ground-based and Airborne Instrumentation for Astronomy V*, Vol. 9147 of *Society of Photo-Optical Instrumentation Engineers (SPIE) Conference Series*, p. 91471G.

Mamajek, E. E. & Bell, C. P. M., 2014, On the age of the β Pictoris moving group, *MNRAS*, 445(3), 2169–2180.

Mandel, K. & Agol, E., 2002, Analytic Light Curves for Planetary Transit Searches, *ApJ*, 580, L171–L175.

Mann, A. W., Dupuy, T., Kraus, A. L., Gaidos, E., Ansdell, M., Ireland, M., Rizzuto, A. C., Hung, C.-L., Dittmann, J., Factor, S., Feiden, G., Martinez, R. A., Ruíz-Rodríguez, D., & Thao, P. C., 2019, How to Constrain Your M Dwarf. II. The Mass-Luminosity-Metallicity Relation from 0.075 to 0.70 Solar Masses, *ApJ*, 871, 63.

Mann, A. W., Feiden, G. A., Gaidos, E., Boyajian, T., & von Braun, K., 2015, How to Constrain Your M Dwarf: Measuring Effective Temperature, Bolometric Luminosity, Mass, and Radius, *ApJ*, 804, 64.

Martioli, E., Hébrard, G., Correia, A. C. M., Laskar, J., & Lecavelier des Etangs, A., 2021, New constraints on the planetary system around the young active star AU Mic. Two transiting warm Neptunes near mean-motion resonance, *A&A*, 649, A177.

May, E. M., MacDonald, R. J., Bennett, K. A., Moran, S. E., Wakeford, H. R., Peacock, S., Lustig-Yaeger, J., Highland, A. N., Stevenson, K. B., Sing, D. K., Mayorga, L. C., Batalha, N. E., Kirk, J., Lopez-Morales, M., Valenti, J. A., Alam, M. K., Alderson, L., Fu, G., Gonzalez-Quiles, J., Lothringer, J. D., Rustamkulov, Z., & Sotzen, K. S., 2023, Double Trouble: Two Transits of the Super-Earth GJ 1132 b Observed with JWST NIRSpec G395H, *arXiv e-prints*, p. arXiv:2310.10711.

Mazeh, T., Naef, D., Torres, G., Latham, D. W., Mayor, M., Beuzit, J.-L., Brown, T. M., Buchhave, L., Burnet, M., Carney, B. W., Charbonneau, D., Drukier, G. A., Laird, J. B., Pepe, F., Perrier, C., Queloz, D., Santos, N. C., Sivan, J.-P., Udry, S., & Zucker, S., 2000, The Spectroscopic Orbit of the Planetary Companion Transiting HD 209458, *ApJ*, 532(1), L55–L58.

McCully, C., Turner, M., Collom, D., & Daily, M., 2022, BANZAI: Beautiful Algorithms to Normalize Zillions of Astronomical Images, Astrophysics Source Code Library, record ascl:2207.031.

McCully, C., Turner, M., Volgenau, N., Harbeck, D., Valenti, S., Riba, A., Bachelet, E., Snyder, I. W., Kurczynski, B., Norbury, M., & Street, R., 2018, Lcogt/banzai: Initial release.
URL: *https://doi.org/10.5281/zenodo.1257560*

Meadows, V. S., Reinhard, C. T., Arney, G. N., Parenteau, M. N., Schwieterman, E. W., Domagal-Goldman, S. D., Lincowski, A. P., Stapelfeldt, K. R., Rauer, H., DasSarma, S., Hegde, S., Narita, N., Deitrick, R., Lustig-Yaeger, J., Lyons, T. W., Siegler, N., & Grenfell, J. L., 2018, Exoplanet Biosignatures: Understanding Oxygen as a Biosignature in the Context of Its Environment, *Astrobiology*, 18(6), 630–662.

Medina, A. A., Charbonneau, D., Winters, J. G., Irwin, J., & Mink, J., 2022, Variability Timescales of Hα on Active Mid-to-late M dwarfs, *ApJ*, 928(2), 185.

Ment, K., Dittmann, J. A., Astudillo-Defru, N., Charbonneau, D., Irwin, J., Bonfils, X., Murgas, F., Almenara, J.-M., Forveille, T., Agol, E., Ballard, S., Berta-Thompson, Z. K., Bouchy, F., Cloutier, R., Delfosse, X., Doyon, R., Dressing, C. D., Esquerdo, G. A., Haywood, R. D., Kipping, D. M., Latham, D. W., Lovis, C., Newton, E. R., Pepe, F., Rodriguez, J. E., Santos, N. C., Tan, T.-G., Udry, S., Winters, J. G., & Wünsche, A., 2019, A Second Terrestrial Planet Orbiting the Nearby M Dwarf LHS 1140, *AJ*, 157, 32.

Miguel, Y., Kaltenegger, L., Linsky, J. L., & Rugheimer, S., 2015, The effect of Lyman α radiation on mini-Neptune atmospheres around M stars: application to GJ 436b, *MNRAS*, 446(1), 345–353.

Mikal-Evans, T., Madhusudhan, N., Dittmann, J., Günther, M. N., Welbanks, L., Van Eylen, V., Crossfield, I. J. M., Daylan, T., & Kreidberg, L., 2023, Hubble Space Telescope Transmission Spectroscopy for the Temperate Sub-Neptune TOI-270 d: A Possible Hydrogen-rich Atmosphere Containing Water Vapor, *AJ*, 165(3), 84.

Miyakawa, K., Hirano, T., Sato, B., Okuzumi, S., & Gaidos, E., 2022, Color Dependence of the Transit Detectability of Young Active M Dwarfs, *AJ*, 164(5), 209.

Modi, A., Estrela, R., & Valio, A., 2023, Impact of M-dwarf stellar wind and photoevaporation on the atmospheric evolution of small planets, *MNRAS*, 525(4), 5168–5179.

Moran, S. E., Stevenson, K. B., Sing, D. K., MacDonald, R. J., Kirk, J., Lustig-Yaeger, J., Peacock, S., Mayorga, L. C., Bennett, K. A., López-Morales, M., May, E. M., Rustamkulov, Z., Valenti, J. A., Adams Redai, J. I., Alam, M. K., Batalha, N. E., Fu, G., Gonzalez-Quiles, J., Highland, A. N., Kruse, E., Lothringer, J. D., Ortiz Ceballos, K. N., Sotzen, K. S., & Wakeford, H. R., 2023, High Tide or Riptide on the Cosmic Shoreline? A Water-rich Atmosphere or Stellar Contamination for the Warm Super-Earth GJ 486b from JWST Observations, *ApJ*, 948(1), L11.

Morello, G., Casasayas-Barris, N., Orell-Miquel, J., Pallé, E., Cracchiolo, G., & Micela, G., 2022, The strange case of Na I in the atmosphere of HD 209458 b. Reconciling low- and high-resolution spectroscopic observations, *A&A*, 657, A97.

Morley, C. V., Fortney, J. J., Marley, M. S., Zahnle, K., Line, M., Kempton, E., Lewis, N., & Cahoy, K., 2015, Thermal Emission and Reflected Light Spectra of Super Earths with Flat Transmission Spectra, *ApJ*, 815(2), 110.

Morley, C. V., Kreidberg, L., Rustamkulov, Z., Robinson, T., & Fortney, J. J., 2017, Observing the Atmospheres of Known Temperate Earth-sized Planets with JWST, *ApJ*, 850, 121.

Mugnai, L. V., Modirrousta-Galian, D., Edwards, B., Changeat, Q., Bouwman, J., Morello, G., Al-Refaie, A., Baeyens, R., Bieger, M. F., Blain, D., Gressier, A., Guilluy, G., Jaziri, Y., Kiefer, F., Morvan, M., Pluriel, W., Poveda, M., Skaf, N., Whiteford, N., Wright, S., Yip, K. H., Zingales, T., Charnay, B., Drossart, P., Leconte, J., Venot, O., Waldmann, I., & Beaulieu, J.-P., 2021, ARES. V. No Evidence For Molecular Absorption in the HST WFC3 Spectrum of GJ 1132 b, *AJ*, 161(6), 284.

Mulders, G. D., Pascucci, I., & Apai, D., 2015, AN INCREASE IN THE MASS OF PLANETARY SYSTEMS AROUND LOWER-MASS STARS, *The Astrophysical Journal*, 814, 130.
URL: *http://archive.stsci.edu/kepler/data_search/search.php*

Murray-Clay, R. A., Chiang, E. I., & Murray, N., 2009, ATMOSPHERIC ESCAPE FROM HOT JUPITERS, *The Astrophysical Journal*, 693, 23–42.
URL: *http://iopscience.iop.org/article/10.1088/0004-637X/693/1/23/pdf*

Nair, H., Allen, M., Anbar, A. D., Yung, Y. L., & Clancy, R. T., 1994, A Photochemical Model of the Martian Atmosphere, *Icarus*, 111(1), 124–150.

Neff, J. E., O'Neal, D., & Saar, S. H., 1995, Absolute Measurements of Starspot Area and Temperature: II Pegasi in 1989 October, *ApJ*, 452, 879.

Newton, E. R., Irwin, J., Charbonneau, D., Berlind, P., Calkins, M. L., & Mink, J., 2017, The Hα Emission of Nearby M Dwarfs and its Relation to Stellar Rotation, *ApJ*, 834(1), 85.

Newton, E. R., Irwin, J., Charbonneau, D., Berta-Thompson, Z. K., & Dittmann, J. A., 2016a, The Impact of Stellar Rotation on the Detectability of Habitable Planets around M Dwarfs, *ApJ*, 821(1), L19.

Newton, E. R., Irwin, J., Charbonneau, D., Berta-Thompson, Z. K., Dittmann, J. A., & West, A. A., 2016b, The Rotation and Galactic Kinematics of Mid M Dwarfs in the Solar Neighborhood, *ApJ*, 821(2), 93.

Noll, S., Kausch, W., Barden, M., Jones, A. M., Szyszka, C., Kimeswenger, S., & Vinther, J., 2012, An atmospheric radiation model for Cerro Paranal. I. The optical spectral range, *A&A*, 543, A92.

Norris, C. M., Unruh, Y. C., Witzke, V., Solanki, S. K., Krivova, N. A., Shapiro, A. I., Yeo, K. L., Cameron, R., & Beeck, B., 2023, Spectral variability of photospheric radiation due to faculae - II. Facular contrasts for cool main-sequence stars, *MNRAS*, 524(1), 1139–1155.

Nortmann, L., Pallé, E., Salz, M., Sanz-Forcada, J., Nagel, E., Alonso-Floriano, F. J., Czesla, S., Yan, F., Chen, G., Snellen, I. A. G., Zechmeister, M., Schmitt, J. H. M. M., López-Puertas, M., Casasayas-Barris, N., Bauer, F. F., Amado, P. J., Caballero, J. A., Dreizler, S., Henning, T., Lampón, M., Montes, D., Molaverdikhani, K., Quirrenbach, A., Reiners, A., Ribas, I., Sánchez-López, A., Schneider, P. C., & Zapatero Osorio, M. R., 2018, Ground-based detection of an extended helium atmosphere in the Saturn-mass exoplanet WASP-69b, *Science*, 362, 1388–1391.

Nutzman, P. & Charbonneau, D., 2008, Design Considerations for a Ground-Based Transit Search for Habitable Planets Orbiting M Dwarfs, *PASP*, 120(865), 317.

Olah, K., Kővári, Z., Bartus, J., Strassmeier, K. G., Hall, D. S., & Henry, G. W., 1997, Time-series photometric SPOT modeling. III. Thirty years in the life of HK Lacertae., *A&A*, 321, 811–821.

Oshagh, M., Santos, N. C., Boisse, I., Boué, G., Montalto, M., Dumusque, X., & Haghighipour, N., 2013, Effect of stellar spots on high-precision transit light-curve, *A&A*, 556, A19.

Owen, J. E. & Altaf, N., 2021, A slim disc approach to external photoevaporation of discs, *MNRAS*, 508(2), 2493–2504.

Parviainen, H. & Aigrain, S., 2015, LDTk: Limb Darkening Toolkit, , .
URL: *http://arxiv.org/abs/1508.02634 http://dx.doi.org/10.1093/mnras/stv1857*

Parviainen, H., Tingley, B., Deeg, H. J., Palle, E., Alonso, R., Montanes Rodriguez, P., Murgas, F., Narita, N., Fukui, A., Watanabe, N., Kusakabe, N., Tamura, M., Nishiumi, T., Prieto-Arranz, J., Klagyivik, P., Béjar, V. J. S., Crouzet, N., Mori, M., Hidalgo Soto, D., Casasayas Barris, N., & Luque, R., 2019, Multicolour photometry for exoplanet candidate validation, *A&A*, 630, A89.

Pass, E. K., Winters, J. G., Charbonneau, D., Irwin, J. M., & Medina, A. A., 2023, Active Stars in the Spectroscopic Survey of Mid-to-late M Dwarfs within 15 pc, *AJ*, 166(1), 16.

Penza, V., Berrilli, F., Bertello, L., Cantoresi, M., & Criscuoli, S., 2021, Prediction of Sunspot and Plage Coverage for Solar Cycle 25, *ApJ*, 922(1), L12.

Peterson, M. S., Benneke, B., Collins, K., Piaulet, C., Crossfield, I. J. M., Ali-Dib, M., Christiansen, J. L., Gagné, J., Faherty, J., Kite, E., Dressing, C., Charbonneau, D., Murgas, F., Cointepas, M., Almenara, J. M., Bonfils, X., Kane, S., Werner, M. W., Gorjian, V., Roy, P.-A., Shporer, A., Pozuelos, F. J., Socia, Q. J., Cloutier, R., Dietrich, J., Irwin, J., Weiss, L., Waalkes, W., Berta-Thomson, Z., Evans, T., Apai, D., Parviainen, H., Pallé, E., Narita, N., Howard, A. W., Dragomir, D., Barkaoui, K., Gillon, M., Jehin, E., Ducrot, E., Benkhaldoun, Z., Fukui, A., Mori, M., Nishiumi, T., Kawauchi, K., Ricker, G., Latham, D. W., Winn, J. N., Seager, S., Isaacson, H., Bixel, A., Gibbs, A., Jenkins, J. M., Smith, J. C., Chavez, J. P., Rackham, B. V., Henning, T., Gabor, P., Chen, W.-P., Espinoza, N., Jensen, E. L. N., Collins, K. I., Schwarz, R. P., Conti, D. M., Wang, G., Kielkopf, J. F., Mao, S., Horne, K., Sefako, R., Quinn, S. N., Moldovan, D., Fausnaugh, M., Fżżrész, G., & Barclay, T., 2023, A temperate Earth-sized planet with tidal heating transiting an M6 star, *Nature*, 617(7962), 701–705.

Plavchan, P., Barclay, T., Gagné, J., Gao, P., Cale, B., Matzko, W., Dragomir, D., Quinn, S., Feliz, D., Stassun, K., Crossfield, I. J. M., Berardo, D. A., Latham, D. W., Tieu, B., Anglada-Escudé, G., Ricker, G., Vanderspek, R., Seager, S., Winn, J. N., Jenkins, J. M., Rinehart, S., Krishnamurthy, A., Dynes, S., Doty, J., Adams, F., Afanasev, D. A., Beichman, C., Bottom, M., Bowler, B. P., Brinkworth, C., Brown, C. J., Cancino, A., Ciardi, D. R., Clampin, M., Clark, J. T., Collins, K., Davison, C., Foreman-Mackey, D., Furlan, E., Gaidos, E. J., Geneser, C., Giddens, F., Gilbert, E., Hall, R., Hellier, C., Henry, T., Horner, J., Howard, A. W., Huang, C., Huber, J., Kane, S. R., Kenworthy, M., Kielkopf, J., Kipping, D., Klenke, C., Kruse, E., Latouf, N., Lowrance, P., Mennesson, B., Mengel, M., Mills, S. M., Morton, T., Narita, N., Newton, E., Nishimoto, A., Okumura, J., Palle, E., Pepper, J., Quintana, E. V., Roberge, A., Roccatagliata, V., Schlieder, J. E., Tanner, A., Teske, J., Tinney, C. G., Vanderburg, A., von Braun, K., Walp, B., Wang, J., Wang, S. X., Weigand, D., White, R., Wittenmyer, R. A., Wright, D. J., Youngblood, A., Zhang, H., & Zilberman, P., 2020, A planet within the debris disk around the pre-main-sequence star AU Microscopii, *Nature*, 582(7813), 497–500.

Pont, F., Gilliland, R. L., Moutou, C., Charbonneau, D., Bouchy, F., Brown, T. M., Mayor, M., Queloz, D., Santos, N., & Udry, S., 2007, Hubble Space Telescope time-series photometry of the planetary transit of HD 189733: no moon, no rings, starspots, *A&A*, 476(3), 1347–1355.

Pont, F., Knutson, H., Gilliland, R. L., Moutou, C., & Charbonneau, D., 2008, Detection of atmospheric haze on an extrasolar planet: the 0.55-1.05 μm transmission spectrum of HD 189733b with the HubbleSpaceTelescope, *MNRAS*, 385(1), 109–118.

Price, E. M., Rogers, L. A., Johnson, J. A., & Dawson, R. I., 2015, How Low Can You Go? The Photoeccentric Effect for Planets of Various Sizes, *ApJ*, 799(1), 17.

Prša, A., Harmanec, P., Torres, G., Mamajek, E., Asplund, M., Capitaine, N., Christensen-Dalsgaard, J., Depagne, É., Haberreiter, M., Hekker, S., Hilton, J., Kopp, G., Kostov, V., Kurtz, D. W., Laskar, J., Mason, B. D., Milone, E. F., Montgomery, M., Richards, M., Schmutz, W., Schou, J., & Stewart, S. G., 2016, Nominal Values for Selected Solar and Planetary Quantities: IAU 2015 Resolution B3, *AJ*, 152(2), 41.

Quirrenbach, A., Amado, P. J., Mandel, H., Caballero, J. A., Mundt, R., Ribas, I., Reiners, A., Abril, M., Aceituno, J., Afonso, C., Barrado y Navascues, D., Bean, J. L., Béjar, V. J. S., Becerril, S., Böhm, A., Cárdenas, M. C., Claret, A., Colomé, J., Costillo, L. P., Dreizler, S., Fernández, M., Francisco, X., Galadí, D., Garrido, R., González Hernández, J. I., Guàrdia, J., Guenther, E. W., Gutiérrez-Soto, F., Joergens, V., Hatzes, A. P., Helmling, J., Henning, T., Herrero, E., Kürster, M., Laun, W., Lenzen, R., Mall, U., Martin, E. L., Martín-Ruiz, S., Mirabet, E., Montes, D., Morales, J. C., Morales Muñoz, R., Moya, A., Naranjo, V., Rabaza, O., Ramón, A., Rebolo, R., Reffert, S., Rodler, F., Rodríguez, E., Rodríguez Trinidad, A., Rohloff, R. R., Sánchez Carrasco, M. A., Schmidt, C., Seifert, W., Setiawan, J., Solano, E., Stahl, O., Storz, C., Suárez, J. C., Thiele, U., Wagner, K., Wiedemann, G., Zapatero Osorio, M. R., del Burgo, C., Sánchez-Blanco, E., & Xu, W., 2010, CARMENES: Calar Alto high-resolution search for M dwarfs with exo-earths with a near-infrared Echelle spectrograph, *in* McLean, I. S., Ramsay, S. K., & Takami, H. (eds), *Ground-based and Airborne Instrumentation for Astronomy III*, Vol. 7735 of *Society of Photo-Optical Instrumentation Engineers (SPIE) Conference Series*, p. 773513.

Rackham, B. V. & de Wit, J., 2023, Towards robust corrections for stellar contamination in JWST exoplanet transmission spectra, *arXiv e-prints*, p. arXiv:2303.15418.

Rackham, B. V., Apai, D., & Giampapa, M. S., 2018, The Transit Light Source Effect: False Spectral Features and Incorrect Densities for M-dwarf Transiting Planets, *ApJ*, 853(2), 122.

Rackham, B. V., Apai, D., & Giampapa, M. S., 2019, The Transit Light Source Effect. II. The Impact of Stellar Heterogeneity on Transmission Spectra of Planets Orbiting Broadly Sun-like Stars, *AJ*, 157(3), 96.

Rackham, B. V., Espinoza, N., Berdyugina, S. V., Korhonen, H., MacDonald, R. J., Montet, B. T., Morris, B. M., Oshagh, M., Shapiro, A. I., Unruh, Y. C., Quintana, E. V., Zellem, R. T., Apai, D., Barclay, T., Barstow, J. K., Bruno, G., Carone, L., Casewell, S. L., Cegla, H. M., Criscuoli, S., Fischer, C., Fournier, D., Giampapa, M. S., Giles, H., Iyer, A., Kopp, G., Kostogryz, N. M., Krivova, N., Mallonn, M., McGruder, C., Molaverdikhani, K., Newton, E. R., Panja, M., Peacock, S., Reardon, K., Roettenbacher, R. M., Scandariato, G., Solanki, S., Stassun, K. G., Steiner, O., Stevenson, K. B., Tregloan-Reed, J., Valio, A., Wedemeyer, S., Welbanks, L., Yu, J., Alam, M. K., Davenport, J. R. A., Deming, D., Dong, C., Ducrot, E., Fisher, C., Gilbert, E., Kostov, V., López-Morales, M., Line, M., Močnik, T., Mullally, S., Paudel, R. R., Ribas, I., & Valenti, J. A., 2023, The effect of stellar contamination on low-resolution transmission spectroscopy: needs identified by NASA's Exoplanet Exploration Program Study Analysis Group 21, *RAS Techniques and Instruments*, 2(1), 148–206.

Rajpurohit, A. S., Reylé, C., Allard, F., Homeier, D., Schultheis, M., Bessell, M. S., & Robin, A. C., 2013, The effective temperature scale of M dwarfs, *A&A*, 556, A15.

Ramsey, L. W. & Nations, H. L., 1980, HR 1099 and the starspot hypothesis for RS CVn binaries., *ApJ*, 239, L121–L124.

Redfield, S. & Linsky, J. L., 2000, The Three-dimensional Structure of the Warm Local Interstellar Medium. II. The Colorado Model of the Local Interstellar Cloud, *ApJ*, 534(2), 825–837.

Redfield, S. & Linsky, J. L., 2008, The Structure of the Local Interstellar Medium. IV. Dynamics, Morphology, Physical Properties, and Implications of Cloud-Cloud Interactions, *ApJ*, 673(1), 283–314.

Reiners, A. & Basri, G., 2007, The First Direct Measurements of Surface Magnetic Fields on Very Low Mass Stars, *ApJ*, 656(2), 1121–1135.

Reiners, A., Shulyak, D., Anglada-Escudé, G., Jeffers, S. V., Morin, J., Zechmeister, M., Kochukhov, O., & Piskunov, N., 2013, Radial velocity signatures of Zeeman broadening, *A&A*, 552, A103.

Reiners, A., Yan, F., Ellwarth, M., Ludwig, H. G., & Nortmann, L., 2023, Solar center-to-limb variation in Rossiter-McLaughlin and exoplanet transmission spectroscopy, *A&A*, 673, A71.

Ricker, G. R., Winn, J. N., Vanderspek, R., Latham, D. W., Bakos, G. Á., Bean, J. L., Berta-Thompson, Z. K., Brown, T. M., Buchhave, L., Butler, N. R., Butler, R. P., Chaplin, W. J., Charbonneau, D., Christensen-Dalsgaard, J., Clampin, M., Deming, D., Doty, J., De Lee, N., Dressing, C., Dunham, E. W., Endl, M., Fressin, F., Ge, J., Henning, T., Holman, M. J., Howard, A. W., Ida, S., Jenkins, J. M., Jernigan, G., Johnson, J. A., Kaltenegger, L., Kawai, N., Kjeldsen, H., Laughlin, G., Levine, A. M., Lin, D., Lissauer, J. J., MacQueen, P., Marcy, G., McCullough, P. R., Morton, T. D., Narita, N., Paegert, M., Palle, E., Pepe, F., Pepper, J., Quirrenbach, A., Rinehart, S. A., Sasselov, D., Sato, B., Seager, S., Sozzetti, A., Stassun, K. G., Sullivan, P., Szentgyorgyi, A., Torres, G., Udry, S., & Villasenor, J., 2015, Transiting Exoplanet Survey Satellite (TESS), *Journal of Astronomical Telescopes, Instruments, and Systems*, 1(1), 014003.

Rimmer, P. B., Xu, J., Thompson, S. J., Gillen, E., Sutherland, J. D., & Queloz, D., 2018, The origin of RNA precursors on exoplanets, *Science Advances*, 4, eaar3302.

Roberge, A. & Moustakas, L. A., 2018, The Large Ultraviolet/Optical/Infrared Surveyor, *Nature Astronomy*, 2(8), 605–607.
URL: *http://www.nature.com/articles/s41550-018-0543-8*

Robertson, P., Stefansson, G., Mahadevan, S., Endl, M., Cochran, W. D., Beard, C., Bender, C. F., Diddams, S. A., Duong, N., Ford, E. B., Fredrick, C., Halverson, S., Hearty, F., Holcomb, R., Juan, L., Kanodia, S., Lubin, J., Metcalf, A. J., Monson, A., Ninan, J. P., Palafoutas, J., Ramsey, L. W., Roy, A., Schwab, C., Terrien, R. C., & Wright, J. T., 2020, Persistent Starspot Signals on M Dwarfs: Multiwavelength Doppler Observations with the Habitable-zone Planet Finder and Keck/HIRES, *ApJ*, 897(2), 125.

Robinson, T. D., Maltagliati, L., Marley, M. S., & Fortney, J. J., 2014, Titan solar occultation observations reveal transit spectra of a hazy world, *Proceedings of the National Academy of Science*, 111(25), 9042–9047.

Rockcliffe, K. E., Newton, E. R., Youngblood, A., Duvvuri, G. M., Plavchan, P., Gao, P., Mann, A. W., & Lowrance, P. J., 2023, The Variable Detection of Atmospheric Escape around the Young, Hot Neptune AU Mic b, *AJ*, 166(2), 77.

Rucinski, S. M., 1992, Spectral-line broadening functions of WUMa-type binaries. I - AW UMa, *AJ*, 104, 1968–1981.

Rustamkulov, Z., Sing, D. K., Mukherjee, S., May, E. M., Kirk, J., Schlawin, E., Line, M. R., Piaulet, C., Carter, A. L., Batalha, N. E., Goyal, J. M., López-Morales, M., Lothringer, J. D., MacDonald, R. J., Moran, S. E., Stevenson, K. B., Wakeford, H. R., Espinoza, N., Bean, J. L., Batalha, N. M., Benneke, B., Berta-Thompson, Z. K., Crossfield, I. J. M., Gao, P., Kreidberg, L., Powell, D. K., Cubillos, P. E., Gibson, N. P., Leconte, J., Molaverdikhani, K., Nikolov, N. K., Parmentier, V., Roy, P., Taylor, J., Turner, J. D., Wheatley, P. J., Aggarwal, K., Ahrer, E., Alam, M. K., Alderson, L., Allen, N. H., Banerjee, A., Barat, S., Barrado, D., Barstow, J. K., Bell, T. J., Blecic, J., Brande, J., Casewell, S., Changeat, Q., Chubb, K. L., Crouzet, N., Daylan, T., Decin, L., Désert, J., Mikal-Evans, T., Feinstein, A. D., Flagg, L., Fortney, J. J., Harrington, J., Heng, K., Hong, Y., Hu, R., Iro, N., Kataria, T., Kempton, E. M. R., Krick, J., Lendl, M., Lillo-Box, J., Louca, A., Lustig-Yaeger, J., Mancini, L., Mansfield, M., Mayne, N. J., Miguel, Y., Morello, G., Ohno, K., Palle, E., Petit dit de la Roche, D. J. M., Rackham, B. V., Radica, M., Ramos-Rosado, L., Redfield, S., Rogers, L. K., Shkolnik, E. L., Southworth, J., Teske, J., Tremblin, P., Tucker, G. S., Venot, O., Waalkes, W. C., Welbanks, L., Zhang, X., & Zieba, S., 2023, Early Release Science of the exoplanet WASP-39b with JWST NIRSpec PRISM, *Nature*, 614(7949), 659–663.

Salz, M., Czesla, S., Schneider, P. C., & Schmitt, J. H. M. M., 2016, Simulating the escaping atmospheres of hot gas planets in the solar neighborhood, *A&A*, 586, A75.

Sánchez-López, A., Alonso-Floriano, F. J., López-Puertas, M., Snellen, I. A. G., Funke, B., Nagel, E., Bauer, F. F., Amado, P. J., Caballero, J. A., Czesla, S., Nortmann, L., Pallé, E., Salz, M., Reiners, A., Ribas, I., Quirrenbach, A., Anglada-Escudé, G., Béjar, V. J. S., Casasayas-Barris, N., Galadí-Enríquez, D., Guenther, E. W., Henning, T., Kaminski, A., Kürster, M., Lampón, M., Lara, L. M., Montes, D., Morales, J. C., Stangret, M., Tal-Or, L., Sanz-Forcada, J., Schmitt, J. H. M. M., Zapatero Osorio, M. R., & Zechmeister, M., 2019, Water vapor detection in the transmission spectra of HD 209458 b with the CARMENES NIR channel, *A&A*, 630, A53.

Sanchis-Ojeda, R. & Winn, J. N., 2011, Starspots, Spin-Orbit Misalignment, and Active Latitudes in the HAT-P-11 Exoplanetary System, *ApJ*, 743(1), 61.

Scalo, J., Kaltenegger, L., Segura, A., Fridlund, M., Ribas, I., Kulikov, Y. N., Grenfell, J. L., Rauer, H., Odert, P., Leitzinger, M., Selsis, F., Khodachenko, M. L., Eiroa, C., Kasting, J., & Lammer, H., 2007, M Stars as Targets for Terrestrial Exoplanet Searches And Biosignature Detection, *Astrobiology*, 7(1), 85–166.
URL: *http://www.liebertonline.com/doi/abs/10.1089/ast.2006.0125*

Schaefer, L., Wordsworth, R. D., Berta-Thompson, Z., & Sasselov, D., 2016, PREDICTIONS OF THE ATMOSPHERIC COMPOSITION OF GJ 1132b, *The Astrophysical Journal*, 829.
URL: *http://iopscience.iop.org/article/10.3847/0004-637X/829/2/63/pdf*

Schöfer, P., Jeffers, S. V., Reiners, A., Shulyak, D., Fuhrmeister, B., Johnson, E. N., Zechmeister, M., Ribas, I., Quirrenbach, A., Amado, P. J., Caballero, J. A., Anglada-Escudé, G., Bauer, F. F., Béjar, V. J. S., Cortés-Contreras, M., Dreizler, S., Guenther, E. W., Kaminski, A., Kürster, M., Lafarga, M., Montes, D., Morales, J. C., Pedraz, S., & Tal-Or, L., 2019, The CARMENES search for exoplanets around M dwarfs. Activity indicators at visible and near-infrared wavelengths, *A&A*, 623, A44.

Schutte, M. C., Hebb, L., Wisniewski, J. P., Cañas, C. I., Libby-Roberts, J. E., Lin, A. S. J., Robertson, P., & Stefánsson, G., 2023, Measuring the Temperature of Starspots from Multi-filter Photometry, *AJ*, 166(3), 92.

Schwarz, H., Brogi, M., de Kok, R., Birkby, J., & Snellen, I., 2015, Evidence against a strong thermal inversion in HD 209458b from high-dispersion spectroscopy, *A&A*, 576, A111.

Seager, S. & Mallén-Ornelas, G., 2003a, A Unique Solution of Planet and Star Parameters from an Extrasolar Planet Transit Light Curve, *ApJ*, 585(2), 1038–1055.

Seager, S. & Mallén-Ornelas, G., 2003b, A Unique Solution of Planet and Star Parameters from an Extrasolar Planet Transit Light Curve, *ApJ*, 585, 1038–1055.

Seager, S. & Sasselov, D. D., 2000a, Theoretical Transmission Spectra during Extrasolar Giant Planet Transits, *ApJ*, 537(2), 916–921.

Seager, S. & Sasselov, D. D., 2000b, Theoretical Transmission Spectra during Extrasolar Giant Planet Transits, *ApJ*, 537(2), 916–921.

Shapiro, A. I., Solanki, S. K., Krivova, N. A., Yeo, K. L., & Schmutz, W. K., 2016, Are solar brightness variations faculae- or spot-dominated?, *A&A*, 589, A46.

Shields, A. L., Ballard, S., & Johnson, J. A., 2016, The habitability of planets orbiting M-dwarf stars, *Physics Reports*, 663, 1–38.

Shields, A. L., Bitz, C. M., & Palubski, I., 2019, Energy Budgets for Terrestrial Extrasolar Planets, *ApJ*, 884(1), L2.

Silva-Valio, A., 2008, Estimating Stellar Rotation from Starspot Detection during Planetary Transits, *ApJ*, 683(2), L179.

Simcoe, R. A., Burgasser, A. J., Bernstein, R. A., Bigelow, B. C., Fishner, J., Forrest, W. J., McMurtry, C., Pipher, J. L., Schechter, P. L., & Smith, M., 2008, FIRE: a near-infrared cross-dispersed echellette spectrometer for the Magellan telescopes, *Proc. SPIE*, Vol. 7014 of *Society of Photo-Optical Instrumentation Engineers (SPIE) Conference Series*, p. 70140U.

Sing, D. K., Fortney, J. J., Nikolov, N., Wakeford, H. R., Kataria, T., Evans, T. M., Aigrain, S., Ballester, G. E., Burrows, A. S., Deming, D., Désert, J.-M., Gibson, N. P., Henry, G. W., Huitson, C. M., Knutson, H. A., Lecavelier Des Etangs, A., Pont, F., Showman, A. P., Vidal-Madjar, A., Williamson, M. H., & Wilson, P. A., 2016, A continuum from clear to cloudy hot-Jupiter exoplanets without primordial water depletion, *Nature*, 529(7584), 59–62.

Sing, D. K., Pont, F., Aigrain, S., Charbonneau, D., Désert, J. M., Gibson, N., Gilliland, R., Hayek, W., Henry, G., Knutson, H., Lecavelier Des Etangs, A., Mazeh, T., & Shporer, A., 2011, Hubble Space Telescope transmission spectroscopy of the exoplanet HD 189733b: high-altitude atmospheric haze in the optical and near-ultraviolet with STIS, *MNRAS*, 416(2), 1443–1455.

Sing, D. K., Vidal-Madjar, A., Désert, J.-M., Lecavelier des Etangs, A., & Ballester, G., 2008, Hubble Space Telescope STIS Optical Transit Transmission Spectra of the Hot Jupiter HD 209458b, *ApJ*, 686, 658–666.

Smith, J. C., Stumpe, M. C., Van Cleve, J. E., Jenkins, J. M., Barclay, T. S., Fanelli, M. N., Girouard, F. R., Kolodziejczak, J. J., McCauliff, S. D., Morris, R. L., & Twicken, J. D., 2012, Kepler Presearch Data Conditioning II - A Bayesian Approach to Systematic Error Correction, *PASP*, 124, 1000.

Snellen, I. A. G., de Kok, R. J., de Mooij, E. J. W., & Albrecht, S., 2010, The orbital motion, absolute mass and high-altitude winds of exoplanet HD209458b, *Nature*, 465(7301), 1049–1051.

Southworth, J., Mancini, L., Madhusudhan, N., Mollière, P., Ciceri, S., & Henning, T., 2017, Detection of the Atmosphere of the 1.6 $M_\oplus$ Exoplanet GJ 1132 b, *AJ*, 153(4), 191.

Sozzetti, A., Torres, G., Charbonneau, D., Latham, D. W., Holman, M. J., Winn, J. N., Laird, J. B., & O'Donovan, F. T., 2007, Improving Stellar and Planetary Parameters of Transiting Planet Systems: The Case of TrES-2, *ApJ*, 664, 1190–1198.

Spake, J. J., Sing, D. K., Evans, T. M., Oklopčić, A., Bourrier, V., Kreidberg, L., Rackham, B. V., Irwin, J., Ehrenreich, D., Wyttenbach, A., Wakeford, H. R., Zhou, Y., Chubb, K. L., Nikolov, N., Goyal, J. M., Henry, G. W., Williamson, M. H., Blumenthal, S., Anderson, D. R., Hellier, C., Charbonneau, D., Udry, S., & Madhusudhan, N., 2018, Helium in the eroding atmosphere of an exoplanet, *Nature*, 557, 68–70.

Spruit, H. C., 1982, Effect of spots on a star's radius and luminosity, *A&A*, 108(2), 348–355.

Stassun, K. G., Oelkers, R. J., Paegert, M., Torres, G., Pepper, J., De Lee, N., Collins, K., Latham, D. W., Muirhead, P. S., Chittidi, J., Rojas-Ayala, B., Fleming, S. W., Rose, M. E., Tenenbaum, P., Ting, E. B., Kane, S. R., Barclay, T., Bean, J. L., Brassuer, C. E., Charbonneau, D., Ge, J., Lissauer, J. J., Mann, A. W., McLean, B., Mullally, S., Narita, N., Plavchan, P., Ricker, G. R., Sasselov, D., Seager, S., Sharma, S., Shiao, B., Sozzetti, A., Stello, D., Vanderspek, R., Wallace, G., & Winn, J. N., 2019, The Revised TESS Input Catalog and Candidate Target List, *AJ*, 158(4), 138.

Stefansson, G., Cañas, C., Wisniewski, J., Robertson, P., Mahadevan, S., Maney, M., Kanodia, S., Beard, C., Bender, C. F., Brunt, P., Clemens, J. C., Cochran, W., Diddams, S. A., Endl, M., Ford, E. B., Fredrick, C., Halverson, S., Hearty, F., Hebb, L., Huehnerhoff, J., Jennings, J., Kaplan, K., Levi, E., Lubar, E., Metcalf, A. J., Monson, A., Morris, B., Ninan, J. P., Nitroy, C., Ramsey, L., Roy, A., Schwab, C., Sigurdsson, S., Terrien, R., & Wright, J. T., 2020, A Sub-Neptune-sized Planet Transiting the M2.5 Dwarf G 9-40: Validation with the Habitable-zone Planet Finder, *AJ*, 159(3), 100.

Stelzer, B., Marino, A., Micela, G., López-Santiago, J., & Liefke, C., 2013, The UV and X-ray activity of the M dwarfs within 10 pc of the Sun, *MNRAS*, 431, 2063–2079.

Strassmeier, K. G. & Olah, K., 1992, On the starspot temperature of HD 12545., *A&A*, 259, 595–599.

Stumpe, M. C., Smith, J. C., Catanzarite, J. H., Van Cleve, J. E., Jenkins, J. M., Twicken, J. D., & Girouard, F. R., 2014, Multiscale Systematic Error Correction via Wavelet-Based Bandsplitting in Kepler Data, *PASP*, 126, 100.

Stumpe, M. C., Smith, J. C., Van Cleve, J. E., Twicken, J. D., Barclay, T. S., Fanelli, M. N., Girouard, F. R., Jenkins, J. M., Kolodziejczak, J. J., McCauliff, S. D., & Morris, R. L., 2012, Kepler Presearch Data Conditioning I—Architecture and Algorithms for Error Correction in Kepler Light Curves, *PASP*, 124(919), 985.

Sullivan, P. W., Winn, J. N., Berta-Thompson, Z. K., Charbonneau, D., Deming, D., Dressing, C. D., Latham, D. W., Levine, A. M., McCullough, P. R., Morton, T., Ricker, G. R., Vanderspek, R., & Woods, D., 2015, The Transiting Exoplanet Survey Satellite: Simulations of Planet Detections and Astrophysical False Positives, *ApJ*, 809(1), 77.

Swain, M. R., Estrela, R., Roudier, G. M., Sotin, C., Rimmer, P. B., Valio, A., West, R., Pearson, K., Huber-Feely, N., & Zellem, R. T., 2021, Detection of an Atmosphere on a Rocky Exoplanet, *AJ*, 161(5), 213.

Szabó, G. M., Gandolfi, D., Brandeker, A., Csizmadia, S., Garai, Z., Billot, N., Broeg, C., Ehrenreich, D., Fortier, A., Fossati, L., Hoyer, S., Kiss, L., Lecavelier des Etangs, A., Maxted, P. F. L., Ribas, I., Alibert, Y., Alonso, R., Anglada Escudé, G., Bárczy, T., Barros, S. C. C., Barrado, D., Baumjohann, W., Beck, M., Beck, T., Bekkelien, A., Bonfils, X., Benz, W., Borsato, L., Busch, M. D., Cabrera, J., Charnoz, S., Collier Cameron, A., Van Damme, C. C., Davies, M. B., Delrez, L., Deleuil, M., Demangeon, O. D. S., Demory, B. O., Erikson, A., Fridlund, M., Futyan, D., García Muñoz, A., Gillon, M., Guedel, M., Guterman, P., Heng, K., Isaak, K. G., Lacedelli, G., Laskar, J., Lendl, M., Lovis, C., Luntzer, A., Magrin, D., Nascimbeni, V., Olofsson, G., Osborn, H. P., Ottensamer, R., Pagano, I., Pallé, E., Peter, G., Piazza, D., Piotto, G., Pollacco, D., Queloz, D., Ragazzoni, R., Rando, N., Rauer, H., Santos, N. C., Scandariato, G., Ségransan, D., Serrano, L. M., Sicilia, D., Simon, A. E., Smith, A. M. S., Sousa, S. G., Steller, M., Thomas, N., Udry, S., Van Grootel, V., Walton, N. A., & Wilson, T. G., 2021, The changing face of AU Mic b: stellar spots, spin-orbit commensurability, and transit timing variations as seen by CHEOPS and TESS, *A&A*, 654, A159.

Szabó, G. M., Garai, Z., Brandeker, A., Gandolfi, D., Wilson, T. G., Deline, A., Olofsson, G., Fortier, A., Queloz, D., Borsato, L., Kiefer, F., Lecavelier des Etangs, A., Lendl, M., Serrano, L. M., Sulis, S., Ulmer Moll, S., Van Grootel, V., Alibert, Y., Alonso, R., Anglada, G., Bárczy, T., Barrado y Navascues, D., Barros, S. C. C., Baumjohann, W., Beck, M., Beck, T., Benz, W., Billot, N., Bonfanti, A., Bonfils, X., Broeg, C., Cabrera, J., Charnoz, S., Collier Cameron, A., Csizmadia, S., Davies, M. B., Deleuil, M., Delrez, L., Demangeon, O., Demory, B. O., Ehrenreich, D., Erikson, A., Fossati, L., Fridlund, M., Gillon, M., Güdel, M., Heng, K., Hoyer, S., Isaak, K. G., Kiss, L. L., Laskar, J., Lovis, C., Magrin, D., Maxted, P. F. L., Mecina, M., Nascimbeni, V., Ottensamer, R., Pagano, I., Pallé, E., Peter, G., Piotto, G., Pollacco, D., Ragazzoni, R., Rando, N., Rauer, H., Ribas, I., Santos, N. C., Sarajlic, M., Scandariato, G., Ségransan, D., Simon, A. E., Smith, A. M. S., Sousa, S. G., Steller, M., Thomas, N., Udry, S., Verrecchia, F., Walton, N., & Wolter, D., 2022, Transit timing variations of AU Microscopii b and c, *A&A*, 659, L7.

Tarter, J. C., Backus, P. R., Mancinelli, R. L., Aurnou, J. M., Backman, D. E., Basri, G. S., Boss, A. P., Clarke, A., Deming, D., Doyle, L. R., Feigelson, E. D., Freund, F., Grinspoon, D. H., Haberle, R. M., Hauck, S. A., Heath, M. J., Henry, T. J., Hollingsworth, J. L., Joshi, M. M., Kilston, S., Liu, M. C., Meikle, E., Reid, I. N., Rothschild, L. J., Scalo, J., Segura, A., Tang, C. M., Tiedje, J. M., Turnbull, M. C., Walkowicz, L. M., Weber, A. L., & Young, R. E., 2007, A

Reappraisal of The Habitability of Planets around M Dwarf Stars, *Astrobiology*, 7(1), 30–65.
URL: *http://www.liebertonline.com/doi/abs/10.1089/ast.2006.0124*

Thao, P. C., Mann, A. W., Gao, P., Owens, D. A., Vanderburg, A., Newton, E. R., Tang, Y., Fields, M. J., David, T. J., Irwin, J. M., Husser, T.-O., Charbonneau, D., & Ballard, S., 2023, Hazy with a Chance of Star Spots: Constraining the Atmosphere of Young Planet K2-33b, *AJ*, 165(1), 23.

The LUVOIR Team, 2019, The LUVOIR Mission Concept Study Final Report, *arXiv e-prints*, p. arXiv:1912.06219.

Tian, F. & Ida, S., 2015, Water contents of Earth-mass planets around M dwarfs, *Nature Geoscience*, 8(3), 177–180.
URL: *http://www.nature.com/articles/ngeo2372*

Tian, F., France, K., Linsky, J. L., Mauas, P. J. D., & Vieytes, M. C., 2014, High stellar FUV/NUV ratio and oxygen contents in the atmospheres of potentially habitable planets, *Earth and Planetary Science Letters*, 385, 22–27.

Tilley, M. A., Segura, A., Meadows, V. S., Hawley, S., & Davenport, J., 2017, Modeling Repeated M-dwarf Flaring at an Earth-like Planet in the Habitable Zone: I. Atmospheric Effects for an Unmagnetized Planet, *arXiv e-prints*, .

Tofflemire, B. M., Mathieu, R. D., & Johns-Krull, C. M., 2019, Accretion Kinematics in the T Tauri Binary TWA 3A: Evidence for Preferential Accretion onto the TWA 3A Primary, *AJ*, 158(6), 245.

Tokovinin, A., 2018, Ten Years of Speckle Interferometry at SOAR, *PASP*, 130(985), 035002.

Torres, C. A. O. & Ferraz Mello, S., 1973, On variable dM stars., *A&A*, 27, 231.

Twicken, J. D., Catanzarite, J. H., Clarke, B. D., Girouard, F., Jenkins, J. M., Klaus, T. C., Li, J., McCauliff, S. D., Seader, S. E., Tenenbaum, P., Wohler, B., Bryson, S. T., Burke, C. J., Caldwell, D. A., Haas, M. R., Henze, C. E., & Sanderfer, D. T., 2018, Kepler Data Validation I: Architecture, Diagnostic Tests, and Data Products for Vetting Transiting Planet Candidates, *PASP*, 130(6), 064502.

VanderPlas, J. T., 2018, Understanding the Lomb-Scargle Periodogram, *ApJS*, 236(1), 16.

Vanderspek, R., Huang, C. X., Vanderburg, A., Ricker, G. R., Latham, D. W., Seager, S., Winn, J. N., Jenkins, J. M., Burt, J., Dittmann, J., Newton, E., Quinn, S. N., Shporer, A., Charbonneau, D., Irwin, J., Ment, K., Winters, J. G., Collins, K. A., Evans, P., Gan, T., Hart, R., Jensen, E. L. N., Kielkopf, J., Mao, S., Waalkes, W., Bouchy, F., Marmier, M., Nielsen, L. D., Ottoni, G., Pepe, F., Ségransan, D., Udry, S., Henry, T., Paredes, L. A., James, H.-S., Hinojosa, R. H., Silverstein, M. L., Palle, E., Berta-Thompson, Z., Crossfield, I., Davies, M. D., Dragomir, D., Fausnaugh, M., Glidden, A., Pepper, J., Morgan, E. H., Rose, M., Twicken, J. D., Villaseñor, J. N. S., Yu, L., Bakos, G., Bean, J., Buchhave, L. A., Christensen-Dalsgaard, J., Christiansen, J. L., Ciardi, D. R., Clampin, M., De Lee, N., Deming, D., Doty, J., Jernigan, J. G., Kaltenegger, L., Lissauer, J. J., McCullough, P. R., Narita, N., Paegert, M., Pal, A., Rinehart, S., Sasselov, D., Sato, B., Sozzetti, A., Stassun, K. G., & Torres, G., 2019, TESS Discovery of an Ultra-short-period Planet around the Nearby M Dwarf LHS 3844, *The Astrophysical Journal*, 871(2), L24.

Vidal-Madjar, A., des Etangs, A. L., Désert, J.-M., Ballester, G. E., Ferlet, R., Hébrard, G., & Mayor, M., 2003, An extended upper atmosphere around the extrasolar planet HD209458b, *Nature*, 422(6928), 143–146.
URL: *http://www.nature.com/articles/nature01448*

Vidal-Madjar, A., Sing, D. K., Lecavelier Des Etangs, A., Ferlet, R., Désert, J. M., Hébrard, G., Boisse, I., Ehrenreich, D., & Moutou, C., 2011, The upper atmosphere of the exoplanet HD 209458 b revealed by the sodium D lines. Temperature-pressure profile, ionization layer, and thermosphere, *A&A*, 527, A110.

Vogt, S. S., 1979, A spectroscopic and photometric study of the star spot on HD 224085., *PASP*, 91, 616.

Vogt, S. S., 1981, A method for unambiguous determination of starspot temperatures and areas : application to II Peg, BY Dra, and HD 209813., *ApJ*, 250, 327–340.

Waalkes, W. C., Berta-Thompson, Z., Bourrier, V., Newton, E., Ehrenreich, D., Kempton, E. M. R., Charbonneau, D., Irwin, J., & Dittmann, J., 2019, Lyα in the GJ 1132 System: Stellar Emission and Planetary Atmospheric Evolution, *AJ*, 158(1), 50.

Wakeford, H. R., Lewis, N. K., Fowler, J., Bruno, G., Wilson, T. J., Moran, S. E., Valenti, J., Batalha, N. E., Filippazzo, J., Bourrier, V., Hörst, S. M., Lederer, S. M., & de Wit, J., 2019, Disentangling the Planet from the Star in Late-Type M Dwarfs: A Case Study of TRAPPIST-1g, *AJ*, 157(1), 11.

West, A. A., Hawley, S. L., Bochanski, J. J., Covey, K. R., Reid, I. N., Dhital, S., Hilton, E. J., & Masuda, M., 2008, Constraining the Age-Activity Relation for Cool Stars: The Sloan Digital Sky Survey Data Release 5 Low-Mass Star Spectroscopic Sample, *AJ*, 135(3), 785–795.

West, A. A., Weisenburger, K. L., Irwin, J., Berta-Thompson, Z. K., Charbonneau, D., Dittmann, J., & Pineda, J. S., 2015, An Activity-Rotation Relationship and Kinematic Analysis of Nearby Mid-to-Late-Type M Dwarfs, *ApJ*, 812(1), 3.

Wing, R. F., Peimbert, M., & Spinrad, H., 1967, Potassium Flares, *PASP*, 79(469), 351.

Winn, J. N., Fabrycky, D., Albrecht, S., & Johnson, J. A., 2010, Hot Stars with Hot Jupiters Have High Obliquities, *ApJ*, 718(2), L145–L149.

Winters, J. G., Medina, A. A., Irwin, J. M., Charbonneau, D., Astudillo-Defru, N., Horch, E. P., Eastman, J. D., Vrijmoet, E. H., Henry, T. J., Diamond-Lowe, H., Winston, E., Barclay, T., Bonfils, X., Ricker, G. R., Vanderspek, R., Latham, D. W., Seager, S., Winn, J. N., Jenkins, J. M., Udry, S., Twicken, J. D., Teske, J. K., Tenenbaum, P., Pepe, F., Murgas, F., Muirhead, P. S., Mink, J., Lovis, C., Levine, A. M., Lépine, S., Jao, W.-C., Henze, C. E., Furész, G., Forveille, T., Figueira, P., Esquerdo, G. A., Dressing, C. D., Díaz, R. F., Delfosse, X., Burke, C. J., Bouchy, F., Berlind, P., & Almenara, J.-M., 2019, Three Red Suns in the Sky: A Transiting, Terrestrial Planet in a Triple M-dwarf System at 6.9 pc, *AJ*, 158(4), 152.

Wittrock, J. M., Dreizler, S., Reefe, M. A., Morris, B. M., Plavchan, P. P., Lowrance, P. J., Demory, B.-O., Ingalls, J. G., Gilbert, E. A., Barclay, T., Cale, B. L., Collins, K. A., Collins, K. I., Crossfield, I. J. M., Dragomir, D., Eastman, J. D., Mufti, M. E., Feliz, D., Gagné, J., Gaidos, E., Gao, P., Geneser, C. S., Hebb, L., Henze, C. E., Horne, K. D., Jenkins, J. M., Jensen, E. L. N., Kane, S. R., Kaye, L., Martioli, E., Monsue, T. A., Pallé, E., Quintana, E. V., Radford, D. J., Roccatagliata, V., Schlieder, J. E., Schwarz, R. P., Shporer, A., Stassun, K. G., Stockdale, C., Tan, T.-G., Tanner, A. M., Vanderburg, A., Vega, L. D., & Wang, S., 2022, Transit Timing Variations for AU Microscopii b and c, *AJ*, 164(1), 27.

Wittrock, J. M., Plavchan, P., Cale, B. L., Barclay, T., Gilbert, E. A., Ludwig, M. R., Schwarz, R. P., Mekarnia, D., Triaud, A., Abe, L., Suarez, O., Guillot, T., Conti, D. M., Collins, K. A., Waite, I. A., Kielkopf, J. F., Collins, K. I., Dreizler, S., El Mufti, M., Feliz, D., Gaidos, E., Geneser, C., Horne, K., Kane, S. R., Lowrance, P. J., Martioli, E., Radford, D. J., Reefe, M. A., Roccatagliata, V., Shporer, A., Stassun, K. G., Stockdale, C., Tan, T.-G., Tanner, A., & Vega, L. D., 2023, Validating AU Microscopii d with Transit Timing Variations, *arXiv e-prints*, p. arXiv:2302.04922.

Wood, B. E., Linsky, J. L., Hebrard, G., Williger, G. M., Moos, H. W., & Blair, W. P., 2004, Two New Low Galactic D/H Measurements from the Far Ultraviolet Spectroscopic Explorer, *The Astrophysical Journal*, 609(2), 838–853.
URL: *http://stacks.iop.org/0004-637X/609/i=2/a=838*

Wood, B. E., Müller, H.-R., Zank, G. P., Linsky, J. L., & Redfield, S., 2005, New Mass-Loss Measurements from Astrospheric Lyα Absorption, *ApJ*, 628, L143–L146.

Wordsworth, R. D. & Pierrehumbert, R. T., 2013, Water Loss from Terrestrial Planets with CO_2-rich Atmospheres, *ApJ*, 778(2), 154.

Yamashita, M., Itoh, Y., & Oasa, Y., 2022, Starspots, chromospheric emission lines, and flares of zero-age main-sequence stars, *PASJ*, 74(6), 1295–1308.

Youngblood, A., France, K., Loyd, R. O. P., Brown, A., Mason, J. P., Schneider, P. C., Tilley, M. A., Berta-Thompson, Z. K., Buccino, A., Froning, C. S., Hawley, S. L., Linsky, J., Mauas, P. J. D., Redfield, S., Kowalski, A., Miguel, Y., Newton, E. R., Rugheimer, S., Segura, A., Roberge, A., & Vieytes, M., 2017, The MUSCLES Treasury Survey. IV. Scaling Relations for Ultraviolet, Ca II H K, and Energetic Particle Fluxes from M Dwarfs, *The Astrophysical Journal*, 843, 31.
URL: *https://doi.org/10.3847/1538-4357/aa76dd*

Youngblood, A., France, K., Loyd, R. O. P., Linsky, J. L., Redfield, S., Schneider, P. C., Wood, B. E., Brown, A., Froning, C., Miguel, Y., Rugheimer, S., & Walkowicz, L., 2016, The MUSCLES Treasury Survey II: Intrinsic Lyman Alpha and Extreme Ultraviolet Spectra of K and M Dwarfs with Exoplanets, , (2003).
URL: *http://arxiv.org/abs/1604.01032*

Zacharias, N., Finch, C. T., Girard, T. M., Henden, A., Bartlett, J. L., Monet, D. G., & Zacharias, M. I., 2012, VizieR Online Data Catalog: UCAC4 Catalogue (Zacharias+, 2012), *VizieR Online Data Catalog*, p. I/322A.

Zahnle, K., Haberle, R. M., Catling, D. C., & Kasting, J. F., 2008, Photochemical instability of the ancient Martian atmosphere, *Journal of Geophysical Research (Planets)*, 113(12), E11004.

Zahnle, K. J. & Catling, D. C., 2017, The Cosmic Shoreline: The Evidence that Escape Determines which Planets Have Atmospheres, and what this May Mean for Proxima Centauri B, *ApJ*, 843(2), 122.

Zhang, Z., Zhou, Y., Rackham, B. V., & Apai, D., 2018, The Near-infrared Transmission Spectra of TRAPPIST-1 Planets b, c, d, e, f, and g and Stellar Contamination in Multi-epoch Transit Spectra, *AJ*, 156(4), 178.

Zhitnitsky, A., 2018, Solar flares and the axion quark nugget dark matter model, *Physics of the Dark Universe*, 22, 1–15.

Zicher, N., Barragán, O., Klein, B., Aigrain, S., Owen, J. E., Gandolfi, D., Lagrange, A.-M., Serrano, L. M., Kaye, L., Nielsen, L. D., Rajpaul, V. M., Grandjean, A., Goffo, E., & Nicholson, B., 2022, One year of AU Mic with HARPS - I. Measuring the masses of the two transiting planets, *MNRAS*, 512(2), 3060–3078.

Ziegler, C., Tokovinin, A., Briceño, C., Mang, J., Law, N., & Mann, A. W., 2020, SOAR TESS Survey. I. Sculpting of TESS Planetary Systems by Stellar Companions, *AJ*, 159(1), 19.